Diss. ETH No. 16397

VORTEX PHYSICS IN LAYERED SUPERCONDUCTORS OF FINITE GEOMETRY

A dissertation submitted to the

SWISS FEDERAL INSTITUTE OF TECHNOLOGY ZURICH
(ETH ZÜRICH)

for the degree of
Doctor of Natural Sciences

presented by

ALVISE DE COL

Laurea in Fisica, Università di Padova, Italy
born 03.02.1977
Italian citizen

accepted on the recommendation of
Prof. Dr. J. W. Blatter, examiner
PD. Dr. V. B. Geshkenbein, co-examiner
Prof. Dr. E. Tosatti, co-examiner

2006

A Chiara e ai miei genitori

Cover drawing:
Nazca line, Peru

Abstract

This thesis is focused on the finite temperature behavior of vortices in type II superconductors. While thermal fluctuations are usually weak in standard low temperature superconductors, their effect is boosted in the new high temperature compounds. The reason is two-fold: on the one hand, the small coherence length enhances the impact of fluctuations, on the other hand these compounds are characterized by an extreme anisotropy which renders the vortex system softer than in standard isotropic materials. The thermal fluctuations manifest themselves in the zero magnetic field superconducting transition and, at finite fields, in the melting of the vortex lattice. The goal of this thesis is to shed light on the relevance of dimensionality or, more generally, of geometric constraints in the context of these phase transitions. Novel and interesting features emerge from the results of our analysis, e.g. the appearance of non-standard topological excitations ('fractional-flux' vortices) in systems with a finite number of superconducting layers and an intriguingly rich surface behavior at the melting transition of the vortex lattice.

It is well known that the effect of thermal fluctuations is strongly enhanced when the dimensionality of the system is reduced. For example, in a zero magnetic field a single film, strictly speaking, cannot be superconducting, since two-dimensional (Pearl) vortices involve a finite self-energy, and thus are excited at any finite temperature, breaking the phase coherence of the superconductor. On the other hand, for a three-dimensional bulk layered superconductor, in the limit of vanishingly small Josephson coupling, the transition into the normal phase takes place at a finite temperature and is induced by the Berezinskii-Kosterlitz-Thouless (BKT) type unbinding of pairs of (pancake) vortices. The huge difference in behavior observed in these two limiting cases is the motivation to study intermediate systems composed of a finite number N of layers. In a first part of the thesis, we examine how the magnetic properties of two-dimensional vortices depend on the number of layers N. We find that when more than one layer is present, a single two-dimensional vortex traps a magnetic flux which is only a fraction of a flux quantum $\Phi_0 = hc/2e$. The appearance of such 'fractional-flux' vortices has important consequences for the finite temperature behavior of samples with a finite number of layers. While the true thermodynamic transition in a multi-layer system takes place at $T = 0$ and is associated with vortex stacks, the analog of the Pearl vortices in a single film, the superconducting transition in the individual layers is due to the BKT unbinding transition of fractional-flux vortices. This BKT transition occurs at a finite temperature which depends on the total number N of layers via the value of the trapped fractional flux. By means of renormalization group techniques, we analyze the BKT unbinding transition for a bi-layer system and discuss its potential observation in a specific experimental setup with a counterflow geometry. We point out interesting analogies with the bi-layer quantum Hall system at total filling $\nu = 1$.

The second part of the thesis is devoted to the study of the thermodynamic behavior of a vortex system at finite magnetic fields. In particular, we concentrate on the effect of an *ab*-surface on the melting transition of the vortex lattice in a layered superconducting material. It is known that in standard solids the surface can assist the nucleation of the liquid phase and may lead to the suppression of the overheated solid phase ('surface melting'). However, this behavior is not generic and there are experimental systems where the surface remains solid up to the bulk melting transition ('surface non-melting'). We study the impact of the surface on the melting transition of the vortex system in two different ways. We first tackle the problem starting from the solid phase by means of a self-consistent analysis of the stability of the two-dimensional lattices. We find that for a large part of the phase diagram the lattice on the surface becomes unstable below the bulk melting transition, while it remains stable above the melting line for very large and very low magnetic fields. Then, we use a novel approach based on the combination of a mean-field substrate model and the classical density functional theory to obtain a more complete description of the problem. We first check the validity of this new approach by studying the melting transition in a bulk system. We then include the presence of the surface and obtain that, depending on the magnetic field, both the 'surface melting' and the 'surface non-melting' scenarios are realized. We find that the 'surface melting' regime occupies the major part of the low-field phase diagram in agreement with the experiments, which show no evidence for the overheated solid phase. Finally, we locate the multi-critical point which marks the crossover between the 'surface melting' and 'surface non-melting' regimes at low magnetic fields.

Sintesi

Questa tesi è incentrata sul comportamento a temperature finite di vortici nei superconduttori di tipo II. Se da un lato le fluttuazioni termiche sono generalmente deboli nei superconduttori con bassa temperatura critica, il loro effetto è potenziato nei nuovi materiali ad alta temperatura. I motivi sono due: da una parte la piccola lunghezza di correlazione accresce l'impatto delle fluttuazioni, dall'altra questi composti sono caratterizzati da un'estrema anisotropia che accentua la mobilità del sistema di vortici rispetto a materiali isotropi. Le fluttuazioni termiche sono responsabili, a campo magnetico nullo, della transizione di fase nello stato superconduttore e, a campi magnetici finiti, della fusione del reticolo di vortici. L'obiettivo di questa tesi è di chiarire l'effetto della dimensionalità o, più generalmente, di restrizioni geometriche su queste transizioni di fase. Dalla nostra analisi sono emersi risultati nuovi ed interessanti, ad esempio la presenza di eccitazioni topologiche non-standard (vortici con flusso frazionario) in sistemi composti da un numero finito di strati superconduttori e la varietà di comportamento delle superfici quando il reticolo di vortici fonde.

È ben noto che l'effetto delle fluttuazioni termiche è fortemente accentuato quando la dimensionalità del sistema è ridotta. Per esempio, strettamente parlando, un film non può essere nello stato superconduttore, perchè i vortici due dimensionali (vortici di Pearl) sono caratterizzati da un'energia finita e vengono eccitati termicamente a qualsiasi temperatura finita, distruggendo la coerenza della fase superconduttrice. In superconduttori a strati composti da un numero infinito di film senza accoppiamento Josephson la transizione nella fase normale avviene a temperatura finita ed è indotta dalla transizione di Berezinskii-Kosterlitz-Thouless (BKT) alla quale coppie neutre di vortici due dimensionali ('*pancake vortices*') si separano. La sostanziale differenza di comportamento in questi due casi limite giustifica lo studio, svolto in questa tesi, di sistemi composti da un numero finito N di strati superconduttori. Nella prima parte della tesi si esamina come le proprietà magnetiche dei vortici due dimensionali dipendono dal numero N di strati. Quando è presente più di un film, si osserva che ad un vortice è associato un flusso magnetico che è solo una frazione di un quanto di flusso $\Phi_0 = hc/2e$. La presenza di questi vortici con flusso frazionario ha importanti conseguenze sul comportamento a temperatura finita. Anche se la vera transizione nello stato superconduttore avviene a $T = 0$ ed è associata a pile di vortici ('*vortex stacks*'), l'analogo dei vortici di Pearl in un unico film, la transizione nei singoli film è dovuta al disaccoppiamento di tipo BKT dei vortici con flusso frazionario. Questa transizione BKT si manifesta ad una temperatura finita che dipende dal numero N totale di strati. Per mezzo di un'analisi basata sul gruppo di rinormalizzazione, si studia la transizione BKT per un sistema composto da due film e si esamina un particolare setup sperimentale che ne permette l'osservazione. Infine, si evidenziano analogie interessanti con il sistema Hall quantistico a doppio film e *filling* totale $\nu = 1$.

La seconda parte della tesi è dedicata allo studio del comportamento termodinamico del sistema di vortici a campi magnetici finiti. In particolare, si studia l'effetto di una superficie con orientazione *ab* sulla fusione del reticolo di vortici nei superconduttori a strati. È noto che in solidi convenzionali la superficie può assistere la nucleazione della fase liquida e può di conseguenza determinare l'eliminazione delle fase solida surriscaldata ('*surface melting*'). Tuttavia, questo comportamento non è l'unico possibile ed esistono sistemi sperimentali in cui la superficie resta solida fino alla transizione di fusione ('*surface non-melting*'). In questa tesi si esamina l'impatto della superficie sulla transizione di fusione del reticolo di vortici con due tecniche differenti. In un primo momento si affronta il problema basando l'analisi sulla fase solida per mezzo di uno studio autoconsistente della stabilità dei reticoli due dimensionali. In una grande porzione del diagramma di fase il reticolo sulla superficie diventa instabile prima che il sistema fonda al suo interno, mentre rimane stabile al di sopra della linea di fusione per campi magnetici molto elevati e molto deboli. In seguito, si è adottato un nuovo approccio fondato sulla combinazione di un modello di campo medio e della teoria classica del funzionale densità allo scopo di ottenere una descrizione più completa del problema. Si è dapprima verificata la validità di questo nuovo approccio studiando la transizione di fusione in un sistema infinito. Si è poi introdotta la presenza di una superficie e si è così ottenuto che, in funzione del campo magnetico, si verificano entrambi gli scenari *surface melting* e *surface non-melting*. La maggior parte del diagramma di fase a campi magnetici deboli è occupata dal regime di *surface melting* come provato dagli esperimenti che hanno dimostrato l'assenza della fase solida surriscaldata. Infine, si è analizzato il punto multi-critico che determina il *crossover* tra i regimi di *surface melting* e di *surface non-melting* a campi magnetici deboli.

Contents

Abstract v

Sintesi vii

1 Introduction 1

2 Basic Concepts 7
- 2.1 Introduction 7
- 2.2 Ginzburg-Landau and London theories 8
- 2.3 Vortices 11
- 2.4 Vortex lattice and elasticity 16
- 2.5 Melting of the vortex lattice 19
- 2.6 Layered systems 21
  - 2.6.1 Josephson vortices 24
  - 2.6.2 Pancake vortices 25
  - 2.6.3 Magnetically coupled layers ($\varepsilon \to 0$ limit) 28

3 Vortices in finite layered systems 31
- 3.1 Introduction 31
- 3.2 Pearl vortex (single film) 32
- 3.3 Finite number of superconducting layers 33
- 3.4 Semi-infinite geometry 37
  - 3.4.1 Out-of-plane interaction 39
  - 3.4.2 Semi-infinite stack 41

4 Thermodynamic behavior at zero magnetic field 45
- 4.1 Introduction 46
- 4.2 Thermodynamics of N superconducting layers 48
  - 4.2.1 Other multicomponent systems 50

4.3 Bi-layer system and I-V measurement 52
4.3.1 Pancake-vortex unbinding transition 54
4.3.2 Vortex stacks and their evaporation 67
4.3.3 Summary of the results of the analysis 70
4.3.4 I-V characteristic 71
4.3.5 Experimental requirements 75
4.3.6 Effects of disorder 77
4.3.7 Analogy with the bi-layer quantum Hall system 79
4.4 Conclusions 83

5 Melting of the Vortex Lattice: Bulk 85
5.1 Introduction 85
5.2 Classical Density Functional Theory 88
5.3 DFT-substrate approach 92
5.4 Free energy in Fourier space 94
5.5 Constrained theory 98
5.6 Incompressible limit and melting line 100
5.7 Density jump and Clausius-Clapeyron relation 104
5.8 Solid-liquid interface 107
5.9 Conclusions 111

6 Melting of the Vortex Lattice: Surface 113
6.1 Introduction 113
6.2 Stability analysis 116
6.2.1 Substrate model 116
6.2.2 Evaporation of an infinite and of a semi-infinite vortex stack 118
6.2.3 Surface instability of the pancake vortex lattice 120
6.3 DFT analysis of the surface melting 126
6.3.1 Large magnetic field and $B \approx 0$ limits 127
6.3.2 Low magnetic fields 128
6.3.3 Analysis of the continuous surface melting and of the multi-critical point 135
6.4 Numerical analysis 140
6.5 Conclusions 144

7 Conclusions 147
7.1 Observing fractional-flux vortices 147
7.2 Surface melting vs. surface non-melting 149

A RG equations for the bi-layer 151
A.1 Derivation of the RG equations 151
A.2 Alternative derivation 153
A.3 Solution of the RG equations 155

B Calculation of the core energy 157

C Gradient expansion 159
C.1 Kernel in Fourier space 159
C.2 Linearised saddle-point equation 161

List of Figures

2.1 Mean field phase diagram of a type II superconductor 12
2.2 Deformations of the vortex lattice: compression, shear, and tilt 17
2.3 Phase diagram of a type II superconductor 20
2.4 Topological excitations in layered systems: pancake and Josephson vortices 23
2.5 Sketch: magnetic field lines of a pancake vortex 24
2.6 Melting line for a bulk layered system 30

3.1 Sketch: magnetic field lines of a Pearl 33
3.2 Geometry of the model 35
3.3 Magnetic field lines of a pancake vortex placed on the surface 38
3.4 Semi-infinite geometry: in-plane and out-of-plane interactions 39
3.5 Sketch: out-of-plane interaction, small in-plane distances . . . 41
3.6 Sketch: out-of-plane interaction, large in-plane distances . . . 42
3.7 Magnetic field lines of a semi-infinite vortex stack 43

4.1 Sketch: magnetic field lines of a fractional-flux vortex and a vortex line 48
4.2 Total flux and T_{BKT} as functions of the number of layers 49
4.3 Topological defects in bi-layer systems 53
4.4 Screening function for the bi-layer 55
4.5 RG flows for the unscreened system 58
4.6 RG flows for the bi-layer system 60
4.7 RG flow, numerical solutions of renormalised y and K^{-1} . . . 61
4.8 Sketch of the RG flow close to the critical point 64
4.9 Correlation length 66
4.10 RG flow with vortex stacks 70
4.11 Phase diagram of the bi-later system at zero magnetic field . . 71

4.12 I-V characteristic 74

5.1 Direct correlation functions: OCP plasma and OCP with substrate 95
5.2 Two dimensional free energy density as a function of the order parameter μ 101
5.3 DFT Melting line: comparison with full numerical solution . . 103
5.4 Jumps in density across the transition 108
5.5 Solid-liquid interface 110

6.1 Stability of the vortex lattice: surface and bulk 125
6.2 Graphical solution for μ_0 133
6.3 Values of μ_0 at the transition. Comparison of analytical and numerical approaches 134
6.4 Surface melting: solid-liquid interface 136
6.5 Energy as a function of the soliton position 139
6.6 Numerical profiles of the order parameter: surface melting O_2 scenario 142
6.7 Numerical profiles of the order parameter: surface non-melting O_1 scenario 143

C.1 Solitons: comparison of local and non-local theories 162

Chapter 1

Introduction

The discovery of high temperature superconductivity by Bednorz and Müller back in 1986 [1] has triggered an enormous experimental and theoretical research activity in condensed matter physics. Since then, the study of high temperature superconductors has developed in three main directions with different but interconnected goals: understanding the microscopic mechanism producing such high transition temperatures, unravelling the phenomenological properties of these new materials, and developing compounds ready for new technological applications. This thesis deals with the phenomenology of high temperature superconductors and in particular with the properties of strongly fluctuating vortex systems.

The phenomenology of the high temperature superconductors (HTSC) is by itself a heterogeneous and fascinating field [2]. The research endeavors have been manyfold and have covered different aspects, such as the structure of vortices, their dynamical behavior and the impact of quenched disorder due to the material defects. However, probably the major focus of the recent phenomenological studies of the properties of HTSC has been on the effect of thermal fluctuations. In fact, due to the high transition temperature and the large anisotropy of these new materials, HTSC show an intriguing finite temperature behavior and a rather complex phase diagram.

Thermal fluctuations are usually small in isotropic bulk superconductors, while they are strongly enhanced in systems with a strong anisotropy. In HTSC, a clear example of this effect is given by the Bi- and Tl- based compounds, e.g. $\mathrm{Bi_2Sr_2Ca_1Cu_2O_{8+y}}$ (BiSCCO), which are characterized by an extreme anisotropy due to their pronounced layered structure. In layered materials, vortex lines are described in terms of two-dimensional vortices (pancake vortices) [3–5], residing in the superconducting layers, joined together by Josephson vortices between the layers. In the limit of infinitely large anisotropy, the inter-layer Josephson coupling vanishes and only pancake vortices remain. The relevant thermal fluctuations have a two-dimensional nature and lead to features which are typically found in two-dimensional fluctuating systems. For example, the superconducting transition in zero magnetic field occurs via a Berezinskii-Kosterlitz-Thouless (BKT) [6, 7] type transition, which is described in terms of the unbinding of pancake, i.e., two-dimensional, vortices.

Thermal fluctuations are also relevant in the description of the finite field behavior of HTSC. In fact, the regular vortex lattice predicted by Abrikosov [8] cannot withstand the enhanced vortex motions at large temperatures and melts into a vortex liquid phase over a wide portion of the phase diagram. The melting transition of the vortex lattice has been intensively investigated in the last 15 years. Although first theoretical proposals trace back to the pre-HTSC era, with the works by Eilenberger [9], by Huberman and Doniach [10] and by Fisher [11] (the latter two for thin superconducting films), attention to the relevance of this transition for HTSC has been drawn by the works of Nelson [12] for low-field regime and by Houghton, Pelcovits, and Sudbø and by Brandt [13, 14] for higher fields.

The melting transition is most prominent in highly anisotropic materials like BiSCCO. While the first approaches to this problem were based on the Lindemann analysis of the stability of the solid phase [2, 15], a more detailed picture of the transition has been obtained by means of more sophisticated techniques such as the classical density functional theory (DFT) [16] or a mean-field type 'substrate model' [17]. The layered structure of these materials strongly influences the characteristics of the melting transition. A remarkable consequence is the appearance of a wide regime in the phase diagram which is essentially described in terms of (quasi)-two-dimensional fluctuations. In fact, at high values of the external magnetic field the three-dimensional vortex system splits into weakly coupled two-dimensional vortex lattices in each layer. In this limit the melting line approaches the melting temperature $T_{\mathrm{m}}^{\mathrm{2D}}$ of a vortex system in a single superconducting layer. Going to lower magnetic fields, the three-dimensional nature of the problem is relevant and the melting of the vortex system is due to three-dimensional fluctuations. As a result, the lattice becomes stiffer and the transition temperature is pushed to values higher than $T_{\mathrm{m}}^{\mathrm{2D}}$. Finally, at vanishingly small fields, the melting line approaches the BKT unbinding temperature. Again two-dimensional fluctuations become the prominent ones; in this case two-dimensional vortex–anti-vortex fluctuating pairs. Hence, the melting line of the layered superconductors interpolates between the two-dimensional melting transition at high-fields and the two-dimensional BKT transition at very low fields, while it is determined by three-dimensional vortex fluctuations in between.

The work in this thesis is motivated by this interplay between two-dimensional and three-dimensional fluctuations. The main and new emphasis of this thesis is the study of systems with a finite number of superconducting layers, which represent the intermediate case between a single film in two dimensions and a bulk layered system in three dimensions. Our goal is to shed light on the relevance of dimensionality or, more generally, of geometric constraints in the finite temperature behavior of layered superconductors. Astonishingly, very interesting and novel results come out of this apparently simple problem.

A first example is given by the appearance of non-standard topological excitations. We find that two-dimensional vortices in systems with a finite number of layers trap only a fraction of a flux quantum $\Phi_0 = hc/2e$ (thus the name 'fractional-flux' vortices) [18–21]. The reduced trapped flux associated with these vortices is due to the presence of the additional layers which modify the magnetic screening properties in multi-layered systems. These non-standard topological excitations play a central role in the zero-field transition. They involve a self-energy which diverges logarithmically with the system size and, thus, they can only be excited in neutral pairs. These pairs undergo a BKT unbinding transition at a finite temperature. However, this transition is not associated with the superconducting transition, as it is in bulk layered systems. In fact, in samples with a finite number of layers, besides fractional-flux vortices, vortex stacks penetrating through the full array of layers also appear. They involve a finite self-energy, and thus are thermally excited at any finite temperature. Free vortices break the superconducting coherence and thus the transition into the normal phase occurs at $T = 0$ in multi-layer systems and it is due to thermally activated vortex stacks. However, this transition is weak and further decreases in relevance the larger the number of layers is. Instead, the BKT transition gains in relevance and transforms into the bulk superconducting transition as the number of layers increases. By means of a real space renormalization group analysis we study the interplay between the unbinding transition of fractional-flux vortices and the thermally activated vortex stacks. Below the BKT unbinding transition counterflow currents, i.e., currents with opposite orientations in different layers, can flow without dissipating energy. The BKT transition is then associated with the destruction of superconductivity in the individual planes as manifested in the counterflow superconducting response. We show how to trace this transition in a transport experiments.

The finite geometry has also a strong impact on the melting transition at finite magnetic fields. Melting is a first order phase transition. Like any other discontinuous transitions, it involves the appearance of metastable phases and thus exhibits hysteretic behavior in cycling through the transition. However, in ordinary crystals it is known that, while it is possible to undercool the liquid, it is usually impossible to overheat the solid above the transition temperature. This remarkable asymmetry is due to the unavoidable presence of surfaces [22–24]. In a first-order transition, to escape from a local metastable minimum, the system must overcome an activation barrier, usually via nucleation of a small germ of the thermodynamically stable phase. For the melting transition, the nucleus of the liquid phase is omnipresent and it is given by the surface. Hence, on approaching the transition temperature melting starts from the surface, removing the metastable solid phase. Even if the bulk transition is discontinuous, the surface melts in a continuous fashion and favors a smooth glide of the liquid phase into the bulk ('surface melting'). However, this behavior is non-generic and there are examples of surfaces which can remain solid up to the melting transition ('surface non-melting'), such as for example the (111) surface of lead. The question if the surface of vortex solid undergoes a continuous (surface-melting) or a discontinuous (surface non-melting) transition does not have a unique answer, since, as we will see, both scenarios are possible for this system. We have studied the problem in two different ways, firstly we have analyzed the stability of the solid phase in a semi-infinite system by means of a self-consistent elastic theory and, secondly, we have refined our analysis with the help of the classical density functional theory [25, 26], which offers a reliable order parameter theory of the melting transition. As a result, we have found that both discontinuous or continuous surface melting are predicted for this system, depending on the value of the magnetic field. We obtain a discontinuous transition for very high and very low magnetic fields and a continuous surface melting in the intermediate regime. This remarkable result is accompanied by the appearance of surface multi-critical points on the melting line, marking the crossover point from one scenario to the other. The reason for this complex surface behavior lies in the different nature of fluctuations along the melting line. While in the limits of low and large magnetic fields the relevant fluctuations are two-dimensional and the surface is ineffective, in the intermediate regime the full three dimensional nature of the problem becomes relevant and the surface effects are prominent.

The outline of this thesis is as follows: we start in Chapter 2 by describing the basic concepts of vortex physics, putting the major emphasis on the aspects which are relevant for the specific topics that we analyze in the thesis. In Chapter 3, after the description of (Pearl) vortices in isolated superconducting films, we present new results about the magnetic properties of vortices in systems with a finite number of magnetically coupled layers. These results are the basis for the analysis of Chapter 4, where we study the thermodynamic behavior of systems with a finite number of layers in zero magnetic field. In Chapters 5 and 6, we concentrate on the melting transition of the vortex system at finite magnetic fields. To prepare the discussion of surface melting, we present in Chapter 5 a novel analysis of the bulk melting transition which is based on the combination of a mean-field substrate model and the classical density functional theory. We prove the thermodynamic consistency of the approach by deriving the Clausius-Clapeyron equation, resolving inconsistencies of previous studies [27]. The effect of the surface is then considered in Chapter 6. We begin with an analysis of the properties of the solid phase and study the stability of the vortex lattices close to the surface. Secondly, we adapt the DFT analysis of Chapter 5 to include the effects of the surface. We study this problem both analytically and numerically and demonstrate the existence of both surface-melting and surface-non-melting scenarios for the vortex system. In order not to break the flow of the discussion, we have moved few technical details of the calculations to the appendices. In Appendix A we present two different derivations of the renormalization flow equation which we use in Chapter 4 to describe the zero-field behavior of the bi-layer system. In Appendix B we calculate the vortex core energy, which we use to determine the starting points of the renormalization flow in Chapter 4. In Appendix C we present an analysis of the gradient approximation used in the DFT analysis of surface melting.

Chapter 2

Basic Concepts

2.1 Introduction

The aim of this chapter is to introduce the basic concepts in the physics of type II superconductors, reserving particular attention to the properties which are relevant for the issues that we analyze in the thesis. We start in Sec. 2.2 by presenting the Ginzburg-Landau and London descriptions of anisotropic superconductors. Subsequently, in Sec. 2.3 we concentrate on type II superconductors and on the properties of a single vortex line. We then present in Sec. 2.4 the elastic description of the vortex lattice, focusing on the special case treated in this thesis where the external magnetic field **H** is oriented along the symmetry axis (the c-axis) of the superconductor. We continue in Sec. 2.5 by discussing the effect of thermal fluctuations on the mean-field phase diagram and in particular the melting transition of the vortex lattice. Section 2.6 is devoted to the analysis of the properties of layered materials with an infinite number of superconducting layers. We introduce the Lawrence-Doniach model and we discuss the basic topological defects of these layered materials: Josephson vortices (in Sec. 2.6.1) and pancake vortices (in Sec. 2.6.2). Finally in Sec. 2.6.3, we introduce the limiting case of magnetically coupled superconducting layers, which describes the extremely anisotropic materials on which this thesis is focused.

2.2 Ginzburg-Landau and London theories

The transition from the normal to the superconducting state is a second order phase transition which is brought about by the breaking of the $U(1)$ gauge symmetry associated with the conducting electrons. The quantum liquid which arises from this phase transition is conveniently described in terms of a complex order parameter field, i.e., a macroscopic wave function, $\psi(\mathbf{r}) = |\psi(\mathbf{r})|e^{i\varphi(\mathbf{r})}$, where the modulus $|\psi(\mathbf{r})|$ is proportional to the density of superconducting electrons and the phase $\varphi(\mathbf{r})$ describes the broken gauge symmetry. Similar to the ordinary Landau theory of second order phase transitions, the Ginzburg-Landau theory is based on the postulate that the free energy functional $\mathcal{F}$ for the superconducting state can be expressed through an expansion of the complex order parameter $\psi(\mathbf{r})$, which is assumed small near the critical temperature T_c. Requiring a free energy which remains invariant under gauge transformations of the electromagnetic field, Ginzburg and Landau proposed the expression [28]

$$\mathcal{F} = \int d^3\mathbf{r} \left[\alpha|\psi|^2 + \frac{\beta}{2}|\psi|^4 + \sum_{\mu=1}^{3} \frac{1}{2m_\mu} \left| \left(\frac{\hbar}{i}\nabla - \frac{e^*}{c}\mathbf{A} \right) \psi \right|^2 + \frac{B^2}{8\pi} \right], \tag{2.1}$$

where $\mathbf{A}$ is the vector potential of the microscopic magnetic field (magnetic induction) $\mathbf{B} = \nabla \times \mathbf{A}$ in Gaussian units. The Ginzburg-Landau parameter $\beta > 0$ is assumed temperature independent, whereas $\alpha(T) = -|\alpha(0)|\,(1 - T/T_c)$ changes sign at the transition temperature T_c. The effective charge is given by $e^* = -2e$, according to the microscopic theory of Bardeen, Cooper, and Schrieffer (BCS) [29] about the formation of Cooper pairs. We choose the unit charge $e > 0$ to be positive. The three parameters m_μ denote the effective masses along the main axes of the crystal. In our analysis we consider the two different cases of isotropic, $m_\mu = m$ for $\mu = 1, 2, 3$, and uniaxially anisotropic materials, $m_x = m_y = m$ and $m_z = M$. For the latter we introduce the mass anisotropy ratio

$$\varepsilon^2 = m/M < 1. \tag{2.2}$$

While the isotropic case serves mainly to introduce the basic concepts of vortex physics, high-temperature superconductors, and in particular the layered materials which we will consider in this thesis, are characterized by a strong anisotropy. In this thesis the coordinate system is chosen with the z-axis parallel to the c-axis of the material and the x- and y-axes in the isotropic ab-plane.

In the absence of an external magnetic field, the minimum of the free energy functional occurs at $\psi = 0$ for $T > T_c$ $(\alpha > 0)$ or for $T < T_c$ at

$$|\psi_0|^2 = -\frac{\alpha}{\beta}, \quad (\alpha < 0).$$

The difference in the free energy density $f \equiv \mathcal{F}/V$ (with V the volume) between the superconducting $(\psi = \psi_0)$ and normal states $(\psi = 0)$, by definition, is equal to the opposite of the condensation energy, which is expressed through the critical thermodynamic magnetic field as [30]

$$f_\mathrm{s} - f_\mathrm{n} = -\frac{\alpha^2}{2\beta} = -\frac{H_c^2(T)}{8\pi}. \tag{2.3}$$

Let us consider for the moment the isotropic case, i.e., $\varepsilon = 1$. By minimizing the free energy (2.1) with respect to the order parameter $\psi^*(\mathbf{r})$ and applying the Maxwell equation $\mathbf{j}_\mathrm{s} = c/4\pi\,(\nabla \times \mathbf{B})$, the Ginzburg-Landau equations are obtained

$$\alpha\psi + \beta|\psi|^2\psi + \frac{\hbar^2}{2m}\left(\nabla + \frac{2\pi i}{\Phi_0}\mathbf{A}\right)^2\psi = 0, \tag{2.4}$$

$$\mathbf{j}_\mathrm{s} = -\frac{2e\hbar}{m}\left(\nabla\varphi + \frac{2\pi}{\Phi_0}\mathbf{A}\right)|\psi|^2, \tag{2.5}$$

where we introduced the quantum flux unit $\Phi_0 = hc/2e \approx 2.068 \cdot 10^{-7}\mathrm{Gcm}^2$. The second equation describes the diamagnetic supercurrent $\mathbf{j}_\mathrm{s}$ of the superconductor. The equations are governed by the two characteristic lengths for a superconductor: the coherence length ξ and the penetration depth λ. The meaning of these fundamentals parameters can be understood easily from the equations (2.4) and (2.5). In a situation with no magnetic fields we can restrict the analysis to a real function $g(r) = 1 - |\psi(r)|/\psi_0$, describing the relative variation of the condensate density from its asymptotic value; the equation (2.4) becomes

$$\xi^2\nabla^2 g - 2g = 0, \quad \xi^2 = \frac{\hbar^2}{2m|\alpha(T)|} = \frac{\xi_0^2}{1 - T/T_c}. \tag{2.6}$$

The relation above shows that the order parameter decays with a length of the order of the coherence length ξ which diverges at T_c, as expected for a second order phase transition.

Similarly, the penetration depth λ comes into play when we consider the response of the system to an external magnetic field. For a weak magnetic field we can neglect variations of the modulus of the order parameter, i.e., $|\psi| = \psi_0$. Taking the curl on both sides of Eq. (2.5), we obtain the London equation

$$[1 - \lambda^2 \nabla^2]\mathbf{B} = 0, \tag{2.7}$$

where we used the relation $\nabla \times (\nabla \times \mathbf{B}) = \nabla(\nabla \cdot \mathbf{B}) - \nabla^2 \mathbf{B}$ and the Maxwell equation $\nabla \cdot \mathbf{B} = 0$. The most important consequence of Eq. (2.7) is that magnetic fields are screened from the interior of a superconductor (Meissner effect) over a distance given by the penetration depth

$$\lambda^2(T) = \frac{mc^2}{16\pi e^2 |\psi_0(T)|^2} = \frac{\lambda_0^2}{1 - T/T_c}. \tag{2.8}$$

The penetration depth diverges when the critical temperature is approached from below, due to the vanishing density of superconducting electrons.

The thermodynamic field H_c can be expressed through the two characteristic lengths

$$H_c = \frac{\Phi_0}{2\sqrt{2}\pi\lambda\xi}. \tag{2.9}$$

The superconductor can hold currents without dissipating energy up to the maximal value given by the depairing current density [30]

$$j_0 = \frac{cH_c}{3\sqrt{6}\pi\lambda}; \tag{2.10}$$

for larger currents Cooper pairs unbind and the motion of normal electrons produces a finite dissipation.

Alternatively, Eq. (2.7) can be derived within the framework of the London theory, which is based on the assumption that the energy of a superconducting system is fully described by the kinetic energy of the supercurrents $\mathbf{j}_\mathrm{s}$ and the magnetic energy associated with the field $\mathbf{B}$. Combining these two terms we obtain the London free energy functional

$$\mathcal{E} = \mathcal{E}_0 + \frac{1}{8\pi} \int d^3r \, \left[\mathbf{B}^2 + \lambda_\mathrm{L}^2 (\nabla \times \mathbf{B})^2\right], \tag{2.11}$$

where λ_L is the London penetration depth, which is defined by

$$\lambda_\mathrm{L}^2 = \frac{mc^2}{4\pi n_\mathrm{s} e^2}, \tag{2.12}$$

where n_{s} is the density of superconducting electrons. The first term in the integral is the magnetic field energy, while the second term is the kinetic energy due to the supercurrents. Varying $\mathcal{E}$ with respect to $\mathbf{B}$, we obtain the (second) London equation, which has the same form as (2.7), with λ_{L} instead of λ. The London theory is valid within the whole temperature range $0 < T < T_c$ as long as the magnetic field does not significantly suppress the order parameter. For systems with $\lambda/\xi \gg 1$, (strongly type II, see next section), the latter condition is fulfilled for a large portion of the phase diagram and, therefore, the London theory provides an adequate description.

Note that we distinguish between the extrapolated zero temperature parameter λ_0 and the BCS expression $\lambda(0) \approx \sqrt{2}\lambda_0$ at $T = 0$. In this thesis we will use the interpolation formula for the penetration depth

$$\lambda^2(T) = \frac{\lambda^2(0)}{1 - T^2/T_c^2}, \tag{2.13}$$

which describes accurately both $T \to 0$ and $T \to T_c$ limits. Finally, connecting the London and Ginzburg-Landau theories near T_c requires the definition $|\psi_0(T)| = (n_{\mathrm{s}}(0)/4)(1 - T^2/T_c^2)$. At $T = 0$ the density of superconducting electrons $n_{\mathrm{s}}(0)$ is equal to the electronic density n and $|\psi_0(0)|$ is the density of (Cooper)-paired electrons.

The analysis which we have carried out in this section can be extended to anisotropic materials, by considering the tensorial dependence of the correlation length and the penetration depth. As a consequence of the uniaxial asymmetry, the out-of-plane components $\lambda_c = \lambda/\varepsilon$ and $\xi_c = \varepsilon\xi$ are related through the anisotropy factor to the respective in-plane components $\lambda = \lambda_{ab}$ and $\xi = \xi_{ab}$. Both Ginzburg-Landau and London equations are modified accordingly, we refer to [31] for details.

2.3 Vortices

Ginzburg and Landau pointed out in their seminal paper that the ratio,

$$\kappa = \frac{\lambda(T)}{\xi(T)}, \tag{2.14}$$

which is nowadays referred as the Ginzburg-Landau parameter, plays an important role on the phenomenological properties of superconductors. They noted that while going from $\kappa < 1/\sqrt{2}$ to $\kappa > 1/\sqrt{2}$ the interfacial energy of

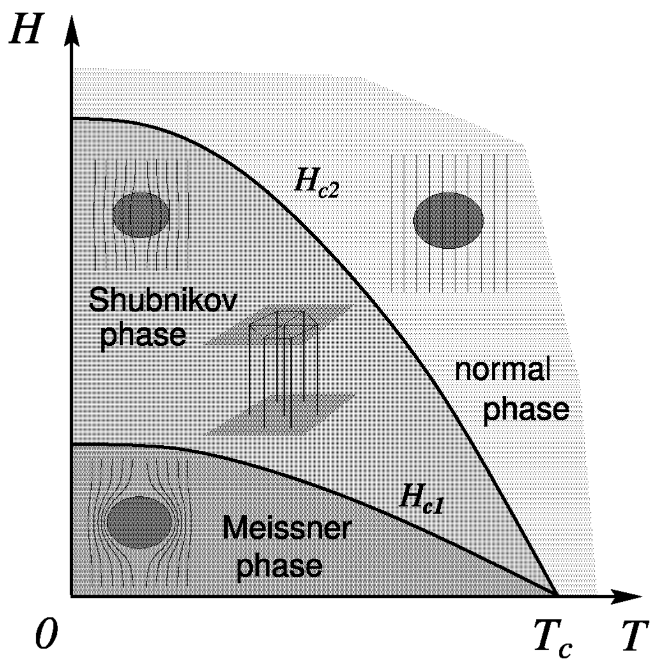

Figure 2.1: Mean field phase diagram for a type II superconductor. Below the lower critical field H_{c1} the magnetic field is expelled from the sample (Meissner-Ochsenfeld effect). In the intermediate regime $H_{c1} < H < H_{c2}$ the magnetic field penetrates the sample in the form of a regular triangular array of vortices carrying each a magnetic flux Φ_0 (Schubnikov phase). Above the upper critical field H_{c2}, superconductivity is destroyed and the system is in the normal phase.

a normal metal-superconductor interface changes sign and becomes negative in the latter case. The full consequences of this remark were subsequently analyzed in depth by Abrikosov [8] who showed that systems with $\kappa > 1/\sqrt{2}$ exhibit a highly non trivial (mean-field) phase-diagram and proposed to classify the materials according to their value of κ: type I for $\kappa < 1/\sqrt{2}$ and type II for $\kappa > 1/\sqrt{2}$. Whereas for type I materials the mean-field phase diagram is composed of two phases, the superconducting state below the line $(T,H_c(T))$ and normal metal above it, in type II systems the full destruction of the superconducting order parameter occurs in two stages. At the first critical magnetic field $H_{c1}(T)$,

$$H_{c1}(T) \approx \frac{\Phi_0}{4\pi\lambda^2} \ln \kappa, \tag{2.15}$$

the external magnetic field starts penetrating into the superconducting system in the form of vortices carrying a quantized magnetic flux $\Phi_0 = hc/2e$. Going to large values of the external magnetic field, the density of vortices increases up to the second critical field,

$$H_{c2}(T) = \frac{\Phi_0}{2\pi\xi^2}, \tag{2.16}$$

at which vortices overlap and superconductivity is completely destroyed. Hence, the phase diagram of a type II material is composed of three phases (cf. Fig. 2.1): *i)* the Meissner phase for $H < H_{c1}$, *ii)* the Schubnikov phase for $H_{c1} < H < H_{c2}$, and *iii)* the normal phase for $H > H_{c2}$.

In order to describe the properties of the Schubnikov phase we start with the analysis of a single vortex. The latter is characterized by a non trivial structure of the order parameter field $\psi = |\psi| \exp(-i\phi)$, with $\phi = \mathbf{e}_z \times \mathbf{R}/R$ the azimuthal unit vector. The phase $\varphi = -\phi$ turns by an angle 2π, driving a circulating current (from (2.5) and (2.8)),

$$j_\phi(R) = \frac{c}{4\pi\lambda^2}\Big(\frac{\Phi_0}{2\pi R} - A_\phi(R)\Big), \tag{2.17}$$

where the phase twist is described by the singular gradient $\nabla\varphi = -\mathbf{e}_z \times \mathbf{R}/R^2$. Near the center of the phase twist the currents are large and suppress the order parameter to zero at the center. This core region extends radially up to a distance of order ξ and cuts the divergence of (2.17) for $R \to 0$. The rotating currents generate a magnetic field and thus bind a finite magnetic flux to the vortex within a distance λ where it saturates to the flux unit Φ_0. This property can be easily obtained by integrating (2.17) along a circular loop γ_R of radius R

$$\int_{\gamma_R} d\mathbf{l} \cdot \mathbf{j} = \frac{c}{4\pi\lambda^2}\Big[\Phi_0 - \Phi_\mathrm{t}(R)\Big], \tag{2.18}$$

where $\Phi_\mathrm{t}(R) = 2\pi A_\phi(R)$ is the magnetic flux accumulated by the vortex within the distance R. For distances $R \gg \lambda$, transverse magnetic screening suppresses the circulating currents and

$$\Phi_\mathrm{t}(R \to \infty) = \Phi_0, \tag{2.19}$$

resulting in the so called 'flux quantization'. Note however, that this condition is not general and it is only valid when the left hand side of (2.18) vanishes; hence, the quantity which is *always* quantized is the fluxoid

$$\Phi_{\mathrm{t}}(R) + \frac{4\pi\lambda^2}{c}\int_{\gamma_R} d\mathbf{l}\cdot\mathbf{j} = \Phi_0. \tag{2.20}$$

If we neglect the vortex core region, we can obtain a good description of the vortex properties within the London theory. The presence of the quantized flux is enforced in the London equation (2.7) by introducing a source term

$$[1-\lambda^2\nabla^2]\mathbf{B}(\mathbf{R}) = \Phi_0\delta^2(\mathbf{R})\mathbf{e}_z. \tag{2.21}$$

Within the London theory the vortex core is neglected and vortex lines are modeled as one dimensional objects. Here we assume a straight vortex line, pointing along the **z**-axis. For this special case the analysis remains valid also when anisotropic materials are considered, with λ being the in-plane penetration depth. The solution of this equation is given by the zero-order Bessel function K_0 ($\mathbf{B} = B\mathbf{e}_z$)

$$B(R) = \frac{\Phi_0}{2\pi\lambda^2}K_0(R/\lambda), \tag{2.22}$$

which has the asymptotics

$$B(R) \approx \frac{\Phi_0}{2\pi\lambda^2}\ln(R/\lambda),\ \ \xi < R \ll \lambda, \tag{2.23}$$

$$B(R) \approx \frac{\Phi_0}{2\pi\lambda^2}\sqrt{\frac{\pi\lambda}{2R}}e^{-R/\lambda},\ \ R \gg \lambda. \tag{2.24}$$

For smaller distances $R < \xi$, the London theory is no longer applicable and a solution of the Ginzburg-Landau equations is required.

From the form of the magnetic field **B** we can easily derive the self-energy per unit length ε_{v} of an isolated vortex line within London theory. Inserting the vortex solution in the total free energy (2.11), one obtains that for strongly type II materials ($\kappa \gg 1$) the largest contribution to the energy comes from the kinetic energy associated with the rotating currents

$$\varepsilon_{\mathrm{kin}} = \frac{\lambda^2}{8\pi}\int d^2\mathbf{R}(\nabla\times\mathbf{B})^2 \approx \Big(\frac{\Phi_0}{4\pi\lambda}\Big)^2\int_{\xi}^{\lambda}\frac{dR}{R} = \varepsilon_0 d\ln\kappa, \tag{2.25}$$

where in the last equality we have defined the line energy

$$\varepsilon_0 = \Big(\frac{\Phi_0}{4\pi\lambda}\Big)^2. \tag{2.26}$$

Accounting for the total vortex energy requires to add the contributions due to the magnetic field and the normal-core condensation energy. A precise estimation of all terms can be done only within the framework of the Ginzburg-Landau approach and gives [32]

$$\varepsilon_\mathrm{v} = \varepsilon_0 \Big[\ln\kappa + 0.497\Big]. \tag{2.27}$$

For a detailed description of each term entering in the total energy see Appendix B.

Next, let us consider the interaction energy of two straight vortex lines at $\mathbf{R}_1$ and $\mathbf{R}_2$ at a distance $R = |\mathbf{R}_2 - \mathbf{R}_1| \gg \xi$. Due to the linearity of the London equation, the total local magnetic field at a point $\mathbf{R}$ can be written as a superposition of the magnetic fields associated with each of the two vortices, i.e., $B(\mathbf{R}) = B_1(\mathbf{R}) + B_2(\mathbf{R})$. Substituting this expression into the (2.11), the total line energy of the two-vortex system can be written as a sum of two distinct terms

$$\varepsilon = 2\varepsilon_\mathrm{v} + V(R). \tag{2.28}$$

The first term in this expression is the self energy of the vortices. The second term is the interaction we are looking for,

$$V(R) = \frac{\lambda^2}{4\pi} \oint \mathbf{B}_1 \times (\nabla \times \mathbf{B}_2) \cdot d\mathbf{s}_2, \tag{2.29}$$

where we used the Stokes' theorem and the integration is along a loop encircling the vortex at position $\mathbf{R}_2$. Finally, the integral is simply expressed as

$$V(R) = \frac{\Phi_0}{4\pi} B(R). \tag{2.30}$$

Therefore, the interaction energy between the vortices is proportional to the magnetic field $B(R)$ produced by any of the two vortices and tested at the core location of the second one. We obtain a logarithmic repulsive potential for short distances, which dies off exponentially for separations larger than the penetration depth:

$$V(R) \approx 2\varepsilon_0 \begin{cases} -\ln\dfrac{R}{\lambda}, & R \ll \lambda, \\ \sqrt{\dfrac{\pi\lambda}{2R}} e^{-R/\lambda}, & \lambda \ll R. \end{cases} \tag{2.31}$$

Differentiating Eq. (2.30) yields the corresponding force F which acts on the vortex; in vector form one obtains the transverse Lorentz force

$$\mathbf{F} = \frac{\Phi_0}{c}\,\mathbf{j} \times \mathbf{e}_z, \tag{2.32}$$

where again we have used the Maxwell equation to express the spatial derivative of the magnetic field in terms of the current $\mathbf{j}$ produced by the first vortex at the core location of the second one. Eq. (2.32) is valid in general and describes the effect of any arbitrary current $\mathbf{j}$ on a vortex line.

2.4 Vortex lattice and elasticity

In the mixed phase, i.e., for magnetic fields in the range $H_{c1} < H < H_{c2}$, a finite density $n_\mathrm{v} = B/\Phi_0 = a_0^{-2}$ of vortices penetrates into the superconductor (Schubnikov phase). The equilibrium state, which minimizes the total energy as given by the sum of all pairwise repulsive interactions, corresponds to a triangular lattice with lattice constant $a_\triangle = (2/\sqrt{3})^{1/2} a_0$. In this thesis we will only consider external magnetic fields which are directed along the z-axis. In this case the equilibrium positions are parametrized in the ab-planes as ($\nu = (\mathbf{m}, \mathbf{n})$)

$$\mathbf{R}_\nu = \Big[\frac{\sqrt{3}}{2} n a_\triangle, \frac{2m+n}{2} a_\triangle\Big], \quad \mathbf{K}_\nu = 2\pi\Big[\frac{2n-m}{\sqrt{3}a_\triangle}, \frac{m}{a_\triangle}\Big], \tag{2.33}$$

in real ($\mathbf{R}_\nu$) and Fourier ($\mathbf{K}_\nu$) space. To describe the vortex system outside its equilibrium configuration we introduce the two-dimensional displacement field $\mathbf{u}$,

$$\mathbf{u}_\nu(z) = \int_\mathrm{BZ} \frac{d^3\mathbf{k}}{(2\pi)^3} e^{i\mathbf{k}\cdot\mathbf{r}_\nu} \mathbf{u}(\mathbf{k}), \tag{2.34}$$

where $\mathbf{k} = (\mathbf{K}, k_z)$ and $\mathbf{r}_\nu = (\mathbf{R}_\nu, z)$ and the integral extends over the two-dimensional Brillouin zone in the plane and is cut off along k_z for $|k_z| > \pi/\xi$. A convenient approximation is to replace the hexagonal Brillioun zone by a circular one with radius $K_\mathrm{BZ} = \sqrt{4\pi}/a_0$, preserving the correct vortex density. The London free energy of a distorted lattice with vortex positions $\mathbf{s}_\nu(z) = \mathbf{r}_\nu + \mathbf{u}_\nu(z)$ is [2]

$$\mathcal{F}[\{\mathbf{s}_\nu\}] = \frac{\varepsilon_0}{2} \sum_{\mu,\nu} \int d\mathbf{s}_\mu \cdot d\mathbf{s}_\nu \bar{V}(|\mathbf{s}_\mu - \mathbf{s}_\nu|). \tag{2.35}$$

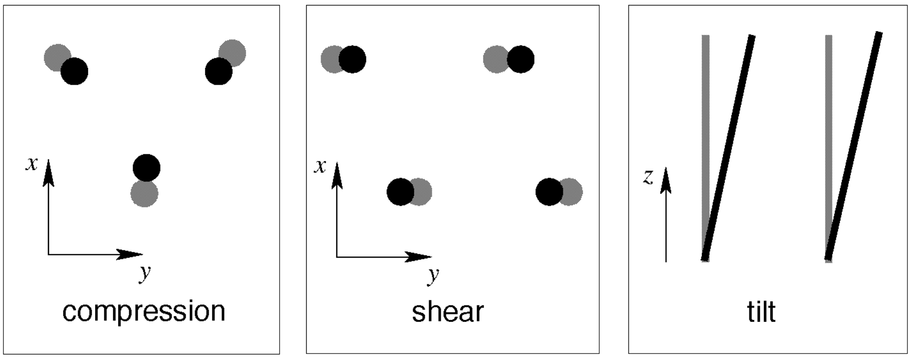

Figure 2.2: Possible elastic deformations of the vortex lattice: compression, shear, and tilt. The equilibrium positions of the vortices are plotted in grey, the distorted ones in black.

where the integration is understood over the line segments $d\mathbf{s}_\nu$ and $d\mathbf{s}_\mu$ and $\bar{V}(r)$ is the interaction between two vortex segments

$$\bar{V}(r) = \frac{1}{r} e^{-r/\lambda}, \tag{2.36}$$

with an appropriate short distance cut-off for $r < \xi$. This cut-off can be provided, for example, by the model potential

$$\bar{V}(r) = 4\pi\lambda^2 \int \frac{d^3\mathbf{k}}{2\pi^3} e^{i\mathbf{k}\cdot\mathbf{r}} \bar{V}(k), \qquad \bar{V}(k) = \frac{e^{-\xi^2 k^2}}{1+\lambda^2 k^2}. \tag{2.37}$$

Within elastic theory, the free energy (2.35) is expanded to quadratic order in the displacement fields $\mathbf{u}_\nu$ and the free energy difference of a distorted configuration relative to the equilibrium state becomes [33]

$$\mathcal{F}_{\mathrm{el}}[\mathbf{u}] = \frac{1}{2} \int_{\mathrm{BZ}} \frac{d^3\mathbf{k}}{(2\pi)^3} \sum_{\alpha,\beta} u_\alpha(\mathbf{k}) \Phi_{\alpha\beta}(\mathbf{k}) u_\beta(\mathbf{k}), \tag{2.38}$$

where the elastic matrix Φ is related to the microscopic potential via

$$\Phi_{\alpha\beta}(\mathbf{k}) = \frac{B^2}{4\pi} \sum_\nu [f_{\alpha\beta}(\mathbf{k}+\mathbf{K}_\nu) - f_{\alpha\beta}(\mathbf{K})], \tag{2.39}$$

and

$$f_{\alpha\beta}(\mathbf{k}) = (k_\alpha k_\beta + \delta_{\alpha\beta} k_z^2) \bar{V}(k). \tag{2.40}$$

Due to the symmetries of the triangular lattice the only non vanishing elastic moduli turn out to be those associated with compression, tilt, and shear deformations (see Fig. 2.2); the elastic free energy then contains only three terms

$$\begin{aligned}\mathcal{F}_{\mathrm{el}}[\mathbf{u}] = & \frac{1}{2}\int\frac{d^3\mathbf{k}}{(2\pi)^3}\left[c_{11}(\mathbf{k})|\mathbf{K}\cdot\mathbf{u}(\mathbf{k})|^2\right. \\ & \left. +c_{66}|\mathbf{K}_\perp\cdot\mathbf{u}(\mathbf{k})|^2 + c_{44}(\mathbf{k})k_z^2|\mathbf{u}(\mathbf{k})|^2\right],\end{aligned} \tag{2.41}$$

where c_{11}, c_{44}, and c_{66} denote the compression, tilt, and shear modulus respectively. The elastic matrix follows directly from comparing (2.38) and (2.41),

$$\Phi_{\alpha\beta}(\mathbf{k}) = [c_{11}(\mathbf{k}) - c_{66}]\,K_\alpha K_\beta + \delta_{\alpha\beta}\left[c_{66}K^2 + c_{44}(\mathbf{k})k_z^2\right]. \tag{2.42}$$

Whereas the shear modulus c_{66} turns out to be non-dispersive, i.e., $\mathbf{k}$ independent [33, 34]

$$c_{66} = \frac{\Phi_0 B}{(8\pi\lambda)^2} = \frac{\varepsilon_0}{4a_0^2}, \tag{2.43}$$

both the compression $c_{11}(\mathbf{k})$ and the tilt $c_{44}(\mathbf{k})$ moduli are strongly dispersive (non-local in real space) due to the long range nature of the vortex interaction [33]

$$c_{11}(\mathbf{k}) \approx c_{44}(\mathbf{k}) \approx \frac{B^2}{4\pi}\,\frac{1}{1+\lambda^2k^2}. \tag{2.44}$$

These expressions for c_{11} and c_{44} are obtained within the continuum isotropic approximation, which neglects the periodic structure of the vortex lattice and treats it as a continuous elastic manifold. From a technical point of view this approximation corresponds to retaining only the term $\nu = 0$ in (2.39). Finally, for low vortex density the vortex interaction is exponentially small, leading to an exponential softening of the shear and compression moduli

$$\begin{aligned} c_{11} &\approx 3c_{66}, \\ c_{66} &\approx \left(\frac{\pi\lambda}{6a_0}\right)^{1/2}\frac{\varepsilon_0}{\lambda^2}e^{-a_0/\lambda}. \end{aligned} \tag{2.45}$$

Including the effects of anisotropy and terms $\nu \neq 0$ in the elastic sum, one obtains important modifications close to the boundary of the Brillouin zone. We are particularly interested in the tilt modulus which is conveniently split into two different contributions [13, 35]

$$c_{44}(\mathbf{k}) = c_{44}^0(\mathbf{k}) + c_{44}^c(\mathbf{k}), \tag{2.46}$$

where $c_{44}^0(\mathbf{k})$ is the non-local contribution (cf. (2.44) for $\varepsilon = 1$)

$$c_{44}^0(\mathbf{k}) = \frac{B^2}{4\pi}\,\frac{1}{1+\lambda_c^2 K^2 + \lambda^2 k_z^2} \tag{2.47}$$

and the correction $\propto B$ is due to the vortex line energies

$$c_{44}^c(\mathbf{k}) \approx \frac{\varepsilon_0}{2a_0^2}\Big[\varepsilon^2 \ln \frac{\kappa\varepsilon^2}{1+\lambda_c^2 K_{\mathrm{BZ}}^2 + \lambda^2 k_z^2} + \frac{1}{\lambda^2 k_z^2}\ln\Big(1+\frac{\lambda^2 k_z^2}{1+\lambda^2 K_{\mathrm{BZ}}^2}\Big)\Big]. \tag{2.48}$$

2.5 Melting of the vortex lattice

The mean-field phase diagram is based on the assumption that fluctuations of the order parameter are small and therefore can be neglected. A quantitative measure of the importance of thermal fluctuations is given by the dimensionless Ginzburg number Gi which derives from a comparison of T_c with the ($T = 0$) condensation energy in the coherence volume (the Boltzmann constant is set to unity throughout the thesis, $k_{\mathrm{B}} = 1$); in an anisotropic material it reads

$$Gi = \frac{1}{2}\Big(\frac{T_c}{H_{c0}^2 \varepsilon \xi_0^3}\Big)^2, \tag{2.49}$$

where H_{c0} and ξ_0 are the extrapolated values at $T = 0$ of the critical field and the in-plane correlation length. Within the temperature window $1 - T/T_c < Gi$, thermal fluctuations become important and the mean field approach of the Ginzburg-Landau type fails to describe the system. In conventional low-T_c materials, due to the large value of the correlation length, the Ginzburg number is small (of order $\approx 10^{-8}$ typically) and the mean-field theory turns out to be extremely accurate. However, in high-T_c materials fluctuations gain dramatically in importance ($Gi \approx 0.01$ in YBCO) due to the small values of the correlation length ξ_0 and of the anisotropy parameter ε. For these materials the mean-field description becomes inadequate for a large portion of the phase diagram. Moreover, note that the width of the fluctuation regime increases with field, $Gi(H) = Gi^{1/3}[H/H_{c20}]^{2/3}$.

One of the most prominent effects of fluctuations is the appearance of the melting transition of the vortex lattice at fields below H_{c2}. Above melting, while vortices are still present, the translational symmetry associated with the Abrikosov lattice is broken. The resulting vortex liquid phase shows features characteristic of the normal state, such as an ohmic response under the driving action of an external current. Hence, the superconducting-normal

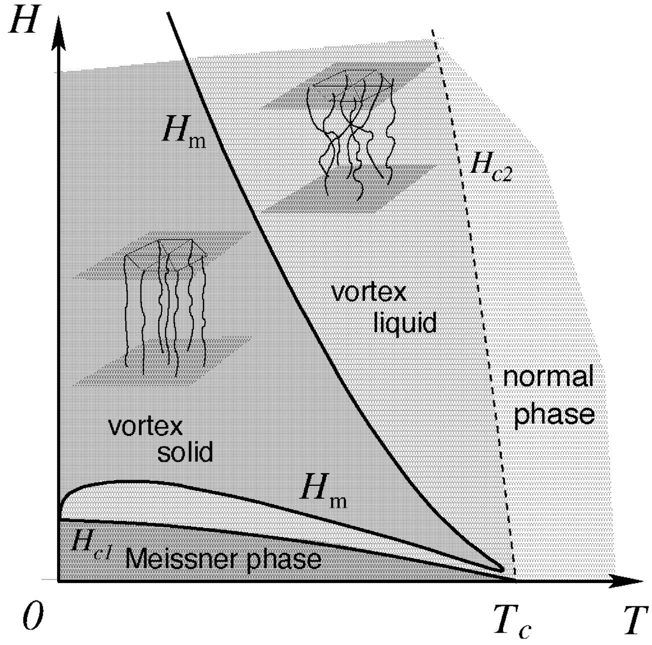

Figure 2.3: Schematic phase diagram of a strongly fluctuating type II superconductor. The vortex lattice undergoes a melting transition at a field H_{m}, below the upper critical field H_{c2}. At low magnetic fields, magnetic screening turns the vortex interaction exponentially weak and the melting line re-enters. The vortex liquid exhibits an ohmic response and the vortex-liquid and normal-metal phases are separated only by a crossover at H_{c2}.

transition is associated with the melting of the vortex lattice. The H_{c2}-line marks only a crossover from a normal phase with zero order parameter (above) to a normal phase which is characterized by a finite but strongly fluctuating order parameter (below).

Although the first suggestion that the vortex lattice may undergo a melting transition is due to Eilenberger [9] back in 1967, this transition has attracted real attention only after the discovery of high temperature superconductors [12–14]. From the experimental side, a first evidence of jumps in magnetization and entropy have been provided by Zeldov *et al.* and Schilling *et al.* [36, 37].

Gaining a full theoretical understanding of the melting transition is a difficult issue and parts of this thesis will deal with this problem in detail. However, a first rough idea of the location of the melting line in the phase diagram can be obtained from a Lindemann analysis of the stability of the solid phase. Starting from the continuum description of the vortex lattice, one calculates the mean thermal fluctuation $\langle u^2\rangle$ and compares it with the lattice spacing a_0. If these quantities become comparable, i.e., when $\langle u^2\rangle \approx c_{\mathrm{L}}^2 a_0^2$, then the lattice undergoes a melting transition. The parameter c_{L} is usually chosen to be a constant of order $c_{\mathrm{L}} \approx 0.1 - 0.3$. The mean-squared thermal fluctuation $\langle u^2\rangle$ is easily calculated from the equipartition theorem:

$$\langle u^2\rangle \approx \int \frac{d^3\mathbf{k}}{(2\pi)^3}\Big[\frac{T}{c_{66}K^2 + c_{44}(\mathbf{k})k_z^2} + \frac{T}{c_{11}(\mathbf{k})K^2 + c_{44}(\mathbf{k})k_z^2}\Big]. \tag{2.50}$$

Here we concentrate on the first term which describes the shear/tilt modes; the second term involving the compression modes produces a smaller contribution and, hence, can be neglected. For an anisotropic material we use the expression $c_{66} = \varepsilon_0/4a_0^2$ and approximate the tilt modulus with $c_{44} \approx 4\pi\varepsilon^2\varepsilon_0/a_0^4K^2$. From the Lindemann criterion we obtain the melting line

$$B_{\mathrm{m}} = \frac{\pi^2 c_{\mathrm{L}}^4}{Gi} H_{c2}(0)\frac{T_c^2}{T^2}\Big(1 - \frac{T^2}{T_c^2}\Big). \tag{2.51}$$

Approaching low magnetic fields, $a_0 \gg \lambda$, the shear and compression moduli become exponentially small, cf. (2.45). As a consequence the melting line re-enters at low magnetic fields towards small temperatures, see Fig. 2.3.

2.6 Layered systems

Up to now we have used a continuum description of the material, which is a good assumption as long as the anisotropy is not too large. However, the high temperature superconductors are characterized by a markedly layered structure and, hence, by a large anisotropy (small ε). In particular, for materials like Bi- al Tl- based compounds the discreteness of the structure becomes a crucial property and a description in terms of weakly coupled superconductors is more appropriate. The commonly used model to describe these systems was introduced by Lawrence and Doniach [38]. They consider a set of superconducting layers with order parameter ψ_n separated by a distance d,

$$\begin{aligned}\mathcal{F}[\psi_n,\mathbf{A}] = d\int d^2\mathbf{R}\sum_n \Bigg[\alpha|\psi_n|^2 + \frac{\beta}{2}|\psi_n|^4 + \frac{\hbar^2}{2m}\Bigg|\Big(\nabla^{(2)} - \frac{2\pi i}{\Phi_0}\mathbf{A}^{(2)}\Big)\psi_n\Bigg|^2 \\ + \frac{\hbar^2}{2Md^2}\Big|\psi_{n+1}e^{\frac{2\pi i}{\Phi_0}\int_{nd}^{(n+1)d} dz A_z} - \psi_n\Big|^2\Bigg] + \int d^3\mathbf{r}\,\frac{B^2}{8\pi},\end{aligned} \tag{2.52}$$

where the first term in the second line describes the (Josephson) coupling between neighboring layers. The anisotropic GL functional is recovered as a special case by approximating this coupling term as a derivative along z. The expressions $\nabla^{(2)}$ and $\mathbf{A}^{(2)}$ denote the planar component of ∇ and $\mathbf{A}$ respectively. Neglecting variations of the modulus of the order parameters, we go over to the corresponding London theory describing coupled superconducting planes

$$\begin{aligned}\mathcal{F}[\phi_n, \mathbf{A}] = \int d^2\mathbf{R}\frac{\varepsilon_0 d}{2\pi}\sum_n\Big[\Big(\nabla^{(2)}\varphi_n + \frac{2\pi}{\Phi_0}\mathbf{A}^{(2)}\Big)^2 \\ +\frac{2m}{Md^2}(1-\cos\Phi_{n,n+1})\Big] + \int d^3\mathbf{r}\,\frac{B^2}{8\pi},\end{aligned} \tag{2.53}$$

where we have defined the gauge invariant phase difference $\Phi_{n,n+1}$ between layers n and $n+1$,

$$\Phi_{n,n+1} = \varphi_{n+1} - \varphi_n + \frac{2\pi}{\Phi_0}\int_{nd}^{(n+1)d} dz A_z. \tag{2.54}$$

The saddle-point equations which are associated with the functional (2.53) read (throughout the thesis we fix the gauge of the vector potential so that $\nabla\cdot\mathbf{A} = 0$)

$$\lambda^2\Delta\mathbf{A}^{(2)} = d\sum_n\delta(z-nd)\Big[\mathbf{A}^{(2)} + \frac{\Phi_0}{2\pi}\nabla^{(2)}\varphi_n\Big], \tag{2.55}$$

$$\Delta A_z = \frac{4\pi}{c}j_\mathrm{J}\sin\Phi_{n+1,n}, \tag{2.56}$$

$$\Lambda^2\Big[\Delta^{(2)}\varphi_n + \frac{2\pi}{\Phi_0}\nabla^{(2)}\mathbf{A}^{(2)}\Big] = \sin\Phi_{n,n-1} - \sin\Phi_{n+1,n}, \tag{2.57}$$

where $\Delta^{(2)}$ denote the planar component of $\Delta = \nabla^2$ and we have defined the Josephson length $\Lambda = d/\varepsilon$ and the Josephson current density

$$j_\mathrm{J} = \frac{c\Phi_0\varepsilon^2}{8\pi^2\lambda^2 d} \approx j_0\varepsilon^2\frac{\xi}{d}. \tag{2.58}$$

Equation (2.56) is in fact the Josephson equation [39]. It describes the z component of the superconducting current j_z arising from the tunneling of Coopers pairs between adjacent layers.

Here we have chosen to describe the system in terms of the period d of the layered structure and the planar *bulk* penetration depth λ. Alternatively, one

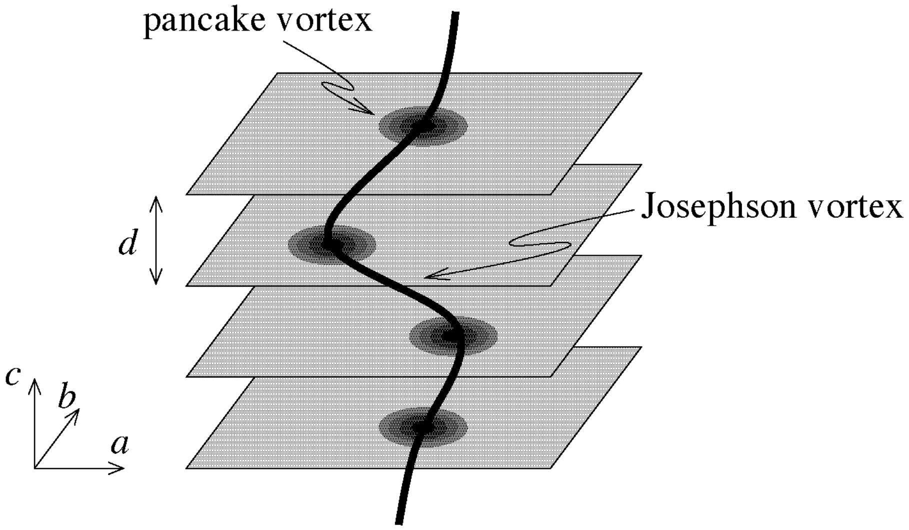

Figure 2.4: Structure of layered superconductors. Conducting layers (drawn as planes) are separated by non metallic barriers. The layering produces strong uniaxial anisotropy with a symmetry axis c (small ε). Vortex lines break up into pancake vortices threading the layers, joined by Josephson vortices between the planes.

can use the thickness d_s of the superconducting layers and the penetration depth λ_s of the planes. These two description are equivalent if $d_\mathrm{s}/\lambda_\mathrm{s}^2 = d/\lambda^2$ which guarantees equal superfluid sheet densities.

In a theory described by the free energy (2.53), there exist more complicated topological excitations than the vortex lines we have presented in the discussion of continuous materials. Due to the layered discrete structure, two elementary species of vortices come into play: 2D pancake vortices [3–5], for which the phase twist is restricted to one superconducting plane, and Josephson vortices, which are described in terms of 2π-turns of the phase-difference between neighboring planes. As a result, a distorted vortex line is composed of pancake vortices directed along the c-axis joined by Josephson vortices threading through the junctions between the superconducting layers, cf. Fig. 2.4. In the following we first shortly analyze a single Josephson vortex and then continue with the discussion of the properties of pancake vortices.

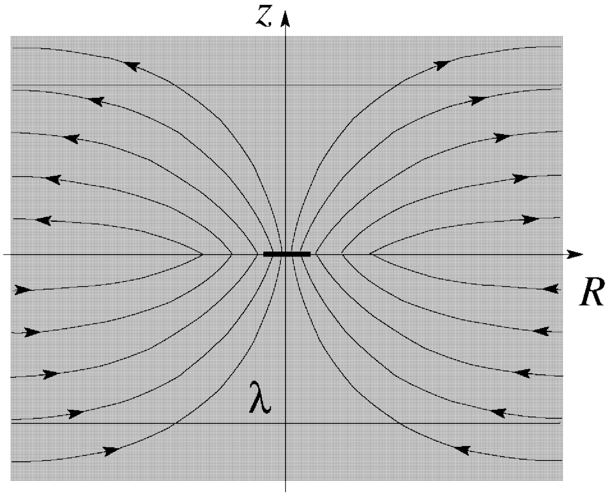

Figure 2.5: Sketch of the magnetic field lines of a pancake vortex. The magnetic field is screened on a distance $z \sim \lambda$ perpendicular to the planes.

2.6.1 Josephson vortices

Applying a magnetic field along the *ab*-plane, the flux lines are described in terms of Josephson vortices. The vortex is associated with a 2π-phase twist between neighboring superconducting planes and by a strongly anisotropic pattern of the circulating currents. The Josephson vortex is described from a set of coupled differential equations that are obtained from the phase equation (2.57),

$$\Lambda^2 \partial_x^2 \Phi_{n+1,n} = \left(2 + \frac{d^2}{\lambda^2}\right) \sin \Phi_{n+1,n} - \sin \Phi_{n+2,n+1} - \sin \Phi_{n,n-1}. \qquad (2.59)$$

The core region is elliptic with extensions Λ in the planes and d perpendicular to them. Therefore, for in-plane distances $R \ll \Lambda$ the tunneling currents are small and the Josephson vortex has not built up yet. Outside the core region, the discreteness and non-linearity of (2.59) is irrelevant and one obtains that the driving phase difference and, hence, the Josephson currents vanish beyond a length $\lambda_c = \lambda/\epsilon$ in the *ab*-plane and λ along z. Hence, whereas Λ and d describe the size of the anisotropic core, λ_c and λ determine the magnetic size of the Josephson vortex.

2.6.2 Pancake vortices

We now consider a magnetic field along the c-axis and discuss the structure of a vortex starting from its two dimensional constituents (pancake vortices). We discuss the case of an infinite array of Josephson uncoupled ($\varepsilon = 0$) superconducting layers and derive the magnetic field generated by a 2D pancake vortex placed at the layer $n = 0$. The vector potential has only in-plane components ($\mathbf{A} = \mathbf{A}^{(2)}$) which satisfy the London equation

$$\nabla^2 \mathbf{A} - \frac{1}{\lambda^2}\mathbf{A} = \frac{d}{\lambda^2}\frac{\Phi_0}{2\pi}\nabla\varphi\,\delta(z), \tag{2.60}$$

where the phase twist generates the source term in the right hand side, $\nabla\varphi = -\mathbf{e}_z \times \mathbf{R}/R^2$. Here, we treat the layered superconductor within a continuum approximation, neglecting small modulations of order d/λ across the layers and we write $\sum_n d\delta(z - nd)\mathbf{A}(z) = \mathbf{A}(z)$ in (2.55), (see [5] for a solution accounting for the discrete structure). In layered materials like BiSCCO, d/λ is typically $\approx 10^{-2}$. Due to the radial symmetry of the source term, the solution of Eq. (2.60) has only an azimuthal component which takes the form [5]

$$A_\phi(R, z) = \frac{\Phi_0 d}{2\lambda}\int_0^\infty \frac{dK}{2\pi}\frac{J_1(KR)}{\sqrt{\lambda^2 K^2 + 1}}e^{-\sqrt{K^2+1/\lambda^2}|z|}. \tag{2.61}$$

The associated magnetic field

$$\begin{aligned} B_z(\mathbf{r}) &= \frac{\Phi_0}{4\pi\lambda^2}\frac{d}{r}e^{-r/\lambda}, \\ \mathbf{B}^{(2)}(\mathbf{r}) &= \frac{\Phi_0}{4\pi\lambda^2}\frac{d\mathbf{R}}{R^2}\frac{z}{|z|}\Big(e^{-|z|/\lambda} - \frac{|z|}{r}e^{-r/\lambda}\Big) \end{aligned} \tag{2.62}$$

decays exponentially on a distance $z \sim \lambda$ perpendicular to the layers, resulting in field lines which escape to the side, see Fig. 2.5.

Next, let us consider the interaction between pancake vortices. We start with the Lorentz force between two vortices

$$F = \Phi_0 j_\phi / c, \tag{2.63}$$

which, as it has been shown in [3], remains valid in layered systems. The current j_ϕ in (2.63) is the current produced by one pancake vortex at the location of the (two-dimensional) core of the second one. Equation (2.63) yields a strongly anisotropic force and, thus, interaction between pancake vortices. The force (2.63) exhibits drastically different properties depending if the pancake vortices reside on the same layer or on different ones.

When the two pancake vortices reside in the same layer, the force is obtained from the supercurrent density at $z = 0$. The latter obeys the expression

$$j_\phi(R, z=0) = \frac{c}{4\pi\lambda^2}\Big[\frac{\Phi_0}{2\pi R} - A_\phi(R, z=0)\Big], \tag{2.64}$$

and it is driven by the 2π-twist of the phase φ of the complex order parameter (first term). We obtain the second term taking $z = 0$ in (2.61) and performing the integration over K,

$$A_\phi(R, z=0) = \frac{d}{2\lambda}\frac{\Phi_0}{2\pi R}(1 - e^{-R/\lambda}). \tag{2.65}$$

As a consequence of this result, the limiting value of the magnetic flux $\Phi_\mathrm{t}(R) = 2\pi R A_\phi(R, z=0)$ trapped by a pancake vortex is much less than Φ_0

$$\Phi_\mathrm{t} = \Phi_\mathrm{t}(R \to \infty) = (d/2\lambda)\Phi_0 < \Phi_0. \tag{2.66}$$

This result is a clear evidence that ‘flux quantization’ is not fulfilled. However, the fluxoid is always quantized. In fact, combining (2.65) and (2.64), we find that the superconducting current $j_\phi(R)$ decays as $1/R$ up to infinity and thus gives a finite contribution in the fluxoid (2.20). This current term compensates the small magnetic flux $\Phi_\mathrm{t} < \Phi_0$, yielding the exact value Φ_0 for the fluxoid. Another consequence of $\Phi_\mathrm{t} < \Phi_0$ is that the self-energy (2.25) of a single pancake vortex turns out to be logarithmically divergent due to the asymptotic behavior $\propto 1/R$ of the currents (L is the system size),

$$E_\mathrm{pv} \approx \varepsilon_0 d \ln\frac{L}{\lambda}. \tag{2.67}$$

Therefore a single pancake vortex is not an allowed excitation in an infinite system, i.e., $L \to \infty$. Going back to the Lorentz force, the two vortices repel with a force

$$F(R) = \frac{2\varepsilon_0 d}{R}\Big(1 - \frac{\Phi_\mathrm{t}(R)}{\Phi_0}\Big). \tag{2.68}$$

Integrating the force along R we obtain that the nearly unscreened currents produce a logarithmic interaction out to all distances

$$V_{z=0}(R) \approx -2\varepsilon_0 d \begin{cases} \ln\dfrac{R}{\xi}, & R \ll \lambda, \\ \ln\dfrac{\lambda}{\xi} + \Big(1 - \dfrac{d}{2\lambda}\Big)\ln\dfrac{R}{\lambda}, & \lambda \ll R. \end{cases} \tag{2.69}$$

The latter expression has to be compared with the strongly screened interaction between vortex lines (2.31). If we neglect the small modification of the prefactor of the logarithm at large scales, i.e., if we write $1 - d/2\lambda \approx 1$, we obtain that in-plane pancake vortices interact with a repulsive potential

$$V_{z=0}(R) = -2\varepsilon_0 d \ln \frac{R}{\xi}, \tag{2.70}$$

like charged particles in two dimensions (2D Coulomb gas or one component plasma, OCP).

Considering two pancake vortices in different planes, the current (2.64) which enters the Lorentz force (2.32) does not contain the driving phase $\nabla\varphi$ term

$$j_\phi(R, z \neq 0) = -\frac{c}{4\pi\lambda^2} A_\phi(R, z). \tag{2.71}$$

Hence, the force in (2.63) is due to the vector potential alone, Eq. (2.61). Integrating the force on R back from infinity, using (2.61), we find the out-of-plane interaction

$$V_{z\neq 0}(R) = -\varepsilon_0 d \frac{d}{\lambda} \int_0^\infty \frac{dK}{2\pi} \frac{J_0(KR)}{K\sqrt{\lambda^2 K^2 + 1}} e^{-\sqrt{K^2+1/\lambda^2}|z|}. \tag{2.72}$$

This potential has the asymptotic limits

$$V_z(R) \approx \varepsilon_0 d \frac{d}{\lambda} \begin{cases} \dfrac{R^2}{4|z|\lambda}, & R \ll |z| \ll \lambda, \\ \dfrac{R}{\lambda}, & |z| \ll R \ll \lambda, \\ \ln \dfrac{R}{\lambda}, & \lambda \ll R. \end{cases} \tag{2.73}$$

For separations $|z| > \lambda$ the interactions decay exponentially $\propto \exp(-|z|/\lambda)$.

In-plane (2.69) and out-of-plane (2.73) components of the interaction are drastically different. While vortices residing in the same plane interact repulsively, the interaction turns out to be attractive between different layers. Moreover, the out-of-plane interaction is an order $d/\lambda \approx 1/100$ weaker than the in-plane one and it extends over a large number $\lambda/d = 100$ of layers. This attractive potential is responsible for the formation of vortex stacks, which are the analogue of vortex lines in continuous materials. Flux quantization is recovered for a vortex stacks by summing the small fluxes $\approx (d/\lambda)\,\Phi_0$ trapped by each pancake vortex over the $\approx \lambda/d$ vortices which reside within a distance λ perpendicular to the planes. The difference between in-plane and out-of-plane components can be traced back to the expressions for the vortex current (2.64) and (2.71). The superconductor reacts to the presence of the phase twist $\propto \nabla\varphi$ by producing opposite, i.e., diamagnetic, currents $\propto A$. Hence, whereas the phase twist generates a repulsive interaction which is the relevant contribution in the plane, the out-of-plane interaction is weak and attractive due to the diamagnetic currents $\propto A$.

A finite Josephson coupling between the layers further penalizes the introduction of a single pancake vortex. In addition to the electromagnetic energy, the interlayer Josephson coupling contributes an infinite energy, now linear in the system size L. Thus, the logarithmic vortex interaction will turn linear (vortex confinement) for distances $R > \Lambda$, due to the formation of a Josephson vortex between the two vortices. The expressions for the pancake vortex interactions (2.69) and (2.72), which we have derived by accounting only for the magnetic energy, remain valid for distances smaller than the Josephson length Λ. For highly anisotropic materials with $\Lambda = d/\varepsilon \gg \lambda$, this magnetic interaction applies for a wide range of inter-vortex distances.

2.6.3 Magnetically coupled layers ($\varepsilon \to 0$ limit)

In this thesis, we will consider the limit of infinite anisotropy ($\varepsilon \to 0$) which describes magnetically coupled layered superconductors with vanishingly small Josephson coupling. Such an analysis is aimed at materials like BiSSCO ($\varepsilon < 1/500$, cf. [40]) or artificial layered systems, for which the Josephson coupling can be made arbitrarily small with an appropriate choice of the material parameters. Within this limit, a finite phase difference between adjacent layers does not contribute to the energy and does not induce inter-plane tunneling currents. Josephson vortices are ruled out and the allowed topological excitations are given by combinations of pancake vortices (and anti-vortices). Due to the absence of Josephson coupling, the remaining interactions between pancake vortices are of a pure magnetic origin, cf. the last section.

The impact of thermal fluctuations is enhanced by anisotropy, cf. (2.49), making the thermodynamic behavior of such magnetically coupled layered systems of particular interest. The fluctuations assume a two dimensional character and their relevance is quantified by the two dimensional Ginzburg number

$$Gi^{(2\mathrm{D})} = \frac{T_c}{2\varepsilon_{00} d}, \tag{2.74}$$

where $\varepsilon_{00} = 2\varepsilon_0(T = 0)$ is the Ginzburg-Landau expression for ε_0 extrapolated to $T \to 0$. For BiSSCO one obtains $Gi^{(2\mathrm{D})} \sim 0.03$.

The two dimensional nature of fluctuations has several interesting consequences [2]. For example, at zero external magnetic field, neutral pairs of pancake vortices and anti-vortices are the relevant thermal fluctuations. The transition into the normal state is of the Berezinskii-Kosterlitz-Thouless type [6, 7] and is triggered by the unbinding of vortex–anti-vortex pairs at the transition temperature $T_{\mathrm{BKT}} = \varepsilon_0 d/2$. Going to finite magnetic fields, the relevant thermal fluctuations are the deformations of the vortex lattice which trigger the melting transition into the vortex liquid state. At large magnetic fields the strong in-plane vortex repulsion dominates over the out-of-plane interactions and the melting line approaches the 2D melting temperature $T_{\mathrm{m}}^{2\mathrm{D}} \approx 0.014\,\varepsilon_0 d$ of each individual plane [42]. The third dimension becomes relevant at low magnetic fields, stiffing up the two-dimensional lattices and pushing the melting transition to higher temperatures, see Fig. 2.6. The melting line then interpolates between $T_{\mathrm{m}}^{2\mathrm{D}}$ at large B and T_{BKT} at $B = 0$. The liquid phase occupies a much wider portion of the phase diagram as compared to a continuous anisotropic material, see Fig. 2.3.

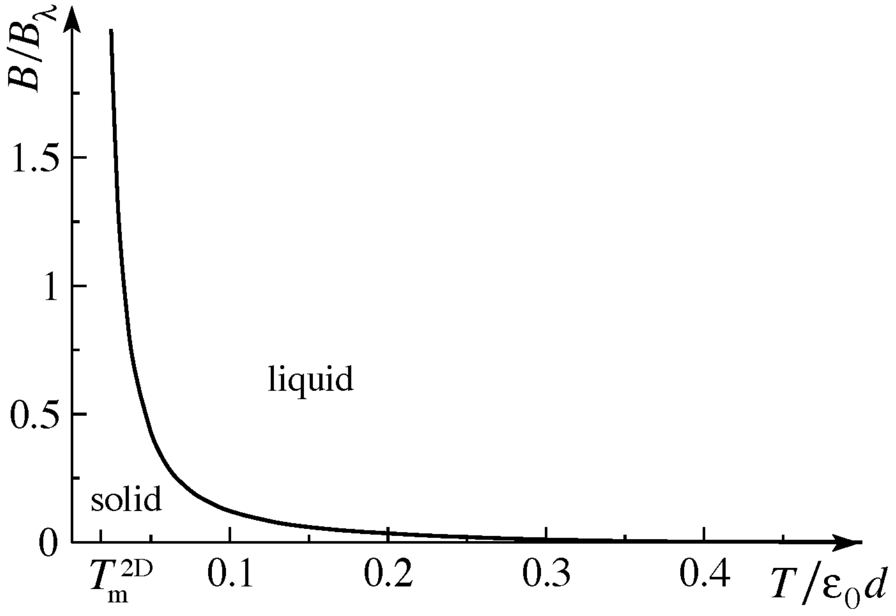

Figure 2.6: Melting line in a magnetically coupled layered superconductor (after [41]). The unit of the magnetic field is $B_\lambda = \Phi_0/\lambda^2$. The melting line interpolates between $T_m^{2D} \approx 0.014\,\varepsilon_0 d$ at large magnetic fields and $T_{\rm BKT} = \varepsilon_0 d/2$ at $B = 0$ (see also Chapter 5), delimiting a wide liquid region.

Chapter 3

Vortices in finite layered systems

3.1 Introduction

As we have seen in the previous chapter, in going from a continuous superconductor to a layered one, the properties of vortices are strongly modified. Continuous vortex lines split into two dimensional pancake vortices with extremely anisotropic interactions. Whilst these defects are restricted to a single layer, the whole superconductor provides an embedding in three dimensions and the (dia)magnetic response involves *all* superconducting planes. As a consequence, changing the geometry of the superconductor, the magnetic response of the system and, hence, the properties of the vortices are modified. In this chapter, we present a thorough analysis of the properties of two-dimensional vortices in the general situation when the system is composed of a finite number of superconducting layers. We start out in Sec. 3.2 with the known case of a vortex in an isolated superconducting film, which was originally studied by Pearl [43]. Then, we continue the analysis by considering an arbitrary number of layers in Sec. 3.3. We devote particular attention to the modification of the value of the total flux Φ_{t} trapped by a vortex as this determines its self-energy and the interaction properties. This result is the key point in the discussion about the $B = 0$ thermodynamic behavior which we present in Chapter 4. Finally, in Sec. 3.4 we describe in detail how the interactions between pancake vortices are modified in a semi-infinite sample; this will provide the basis for the analysis of the surface melting of the vortex lattice in Chapter 6.

3.2 Pearl vortex (single film)

Let us consider a thin film superconductor (single layer at $z = 0$) of thickness d_s and penetration depth $\lambda_\mathrm{s} \gg d_\mathrm{s}$ with a vortex centered in the origin. Combining Eq. (2.64) with the Maxwell equation for the vector potential $\mathbf{A}$ we have to solve

$$\nabla^2 \mathbf{A} = \frac{d_s}{\lambda_s^2}\Big(\frac{\Phi_0}{2\pi}\nabla\varphi + \mathbf{A}\Big)\delta(z) \tag{3.1}$$

in free space [44]. Exploiting the cylindrical symmetry, we find the azimuthal component of the vector potential describing a Pearl vortex,

$$A_\phi(R,z) = \Phi_0 \int_0^\infty \frac{dK}{2\pi}\frac{J_1(KR)}{1+\lambda_\mathrm{Pearl}K}e^{-K|z|}, \tag{3.2}$$

where $\lambda_\mathrm{Pearl} = 2\lambda_\mathrm{s}^2/d_\mathrm{s} \gg \lambda_\mathrm{s}$ is the Pearl length and J_1 is a Bessel function. The associated magnetic field decays like $\mathbf{r}/r^3$, resembling the field of a positively charged magnetic monopole in the upper half space (a negative one in the lower half space, see Fig. 3.1). For $z = 0$, we can carry out the integration and obtain

$$A_\phi(R, z=0) = \frac{\Phi_0}{2\pi R} + \frac{\Phi_0}{4\lambda_\mathrm{Pearl}}\Big[Y_1(R/\lambda_\mathrm{Pearl}) + H_{-1}(R/\lambda_\mathrm{Pearl})\Big], \tag{3.3}$$

where H_{-1} is the Struve function and Y_1 the Bessel function of the second type. The vector potential admits the following asymptotic behavior in the plane

$$A_\phi(R \gg \lambda_\mathrm{Pearl}, z=0) \sim \frac{\Phi_0}{2\pi R}\Big(1 - \frac{\lambda_\mathrm{Pearl}}{R}\Big). \tag{3.4}$$

The magnetic flux trapped within a distance R adds up to a full flux quantum $\Phi_\mathrm{t} = \Phi_0$ within the distance $\sim \lambda_\mathrm{Pearl}$, leading to a decaying current $j \propto 1/R^2$ at large distances $R \gg \lambda_\mathrm{Pearl}$, cf. Eq. (2.64). Hence, an isolated Pearl vortex involves a finite self-energy

$$E_\mathrm{Pearl} \approx \varepsilon_0 d \ln(\lambda_\mathrm{Pearl}/\xi) \tag{3.5}$$

and represents an elementary topological excitation of the system ($\varepsilon_0 d = (\Phi_0/4\pi\lambda)^2$, since $d_\mathrm{s}/\lambda_\mathrm{s}^2 = d/\lambda^2$, cf. Sec. 2.6). This expression has to be compared with the corresponding self-energies of a vortex line (2.27) and a

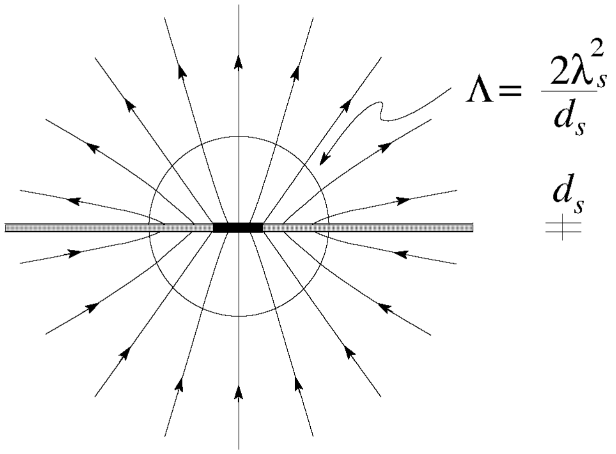

Figure 3.1: Sketch of the magnetic field lines for a Pearl vortex. The shaded area corresponds to the thin superconducting film.

single pancake vortex in an infinite system (2.67). The trapped magnetic flux reaches an entire quantum flux, hence the self energy is finite. However, currents are present up to the distance $\lambda_{\mathrm{Pearl}} \gg \lambda_{\mathrm{s}}$ and the self-energy is (logarithmically) larger than the one associated with a line vortex.

The current produces a screened logarithmic interaction $V(R)$ between two Pearl vortices, attractive for a vortex–anti-vortex pair,

$$V(R) \approx 2\varepsilon_0 d \begin{cases} \ln \dfrac{R}{\xi}, & R \ll \lambda_{\mathrm{Pearl}}, \\ \ln \dfrac{\lambda_{\mathrm{Pearl}}}{\xi} - \dfrac{\lambda_{\mathrm{Pearl}}}{R}, & \lambda_{\mathrm{Pearl}} \ll R, \end{cases} \tag{3.6}$$

where ξ is the coherence length. Transverse screening cuts the logarithmic interaction at large distances $R \gg \lambda_{\mathrm{Pearl}}$. Note, that the asymptotic value is reached algebraically $\propto 1/R$ and not exponentially like for a bulk vortex line (2.31). This is an effect of the presence of stray magnetic fields due to the finite geometry of the system.

3.3 Finite number of superconducting layers

We turn to the case of an arbitrary but finite number N of layers [20,21] and derive the properties of a pancake vortex placed on the n-th layer ($n = 1$ corresponds to the top surface layer). The equation for the vector potential

A reads

$$\begin{aligned}
&\nabla^2\mathbf{A}-\frac{1}{\lambda^2}\mathbf{A}=\frac{d}{\lambda^2}\Big(\frac{\Phi_0}{2\pi}\nabla\varphi+\mathbf{A}\Big)\delta(z), \quad -d^{<}<z<d^{>},\\
&\nabla^2\mathbf{A}=0, \qquad\qquad z<-d^{<} \text{ and } z>d^{>},
\end{aligned}\tag{3.7}$$

where $d^{<}=(N-n)d$, $d^{>}=(n-1)d$ denote the overall thickness of the protecting layers above and below the plane containing the vortex, see Fig. 3.2; the total thickness of the system is $(N-1)d$ and $\lambda^2=\lambda_{\mathrm{s}}^2 d/d_{\mathrm{s}}$. In Eq. (3.7) the three dimensional space is split in three regions: *i)* the layer at $z=0$, where the vortex resides (source term $\propto\delta(z)$); *ii)* the superconductor which is described by the London equation (2.7) for $-d^{<}<z<d^{>}$; finally, *iii)* the free space where the vector potential is governed by the Maxwell equation. The presence of the additional screening term $\propto\mathbf{A}$ in current density on the right hand side of (3.7) depends on the implementation of the continuum description; its effect is of subleading order in d/λ for thick samples, i.e., with $Nd\gg\lambda$, but it is required to obtain the correct limit in the case of an isolated superconducting film (see previous section). The vector potential associated with the vortex assumes the form

$$A_\phi(R,z)=\frac{\Phi_0 d}{\lambda^2}\int_0^\infty\frac{dK}{2\pi}\frac{J_1(KR)}{C(K)}f(K,z),\tag{3.8}$$

where

$$f(K,z)=\big[1-\alpha_{d'}(K)\big]e^{-K_+|z|}+\alpha_{d'}(K)e^{K_+|z|},\tag{3.9}$$

describes the z-dependence within the superconductor, i.e., in the region $-d^{<}<z<0$ if we set $d'=d^{<}$ and in the region $0<z<d^{>}$ if we choose $d'=d^{>}$; here,

$$\alpha_{d'}(K)=\frac{K_+-K}{(K_++K)e^{2K_+d'}+(K_+-K)},\tag{3.10}$$

and $K_+=\sqrt{K^2+1/\lambda^2}$ is the screened wave number. The denominator $C(K)$ assumes the form

$$C(K)=[1-2\alpha_{d^{<}}(K)]K_++[1-2\alpha_{d^{>}}(K)]K_++\frac{2}{\lambda_{\mathrm{Pearl}}}.\tag{3.11}$$

The field outside the superconductor is obtained by replacing d' and $z>0$ (d' and $z<0$) by $d^{>}$ ($-d^{<}$) in (3.9) and correcting by the additional factor $\exp[K(d^{>}-z)]$ ($\exp[K(d^{<}+z)]$). The Pearl vortex and the pancake vortex

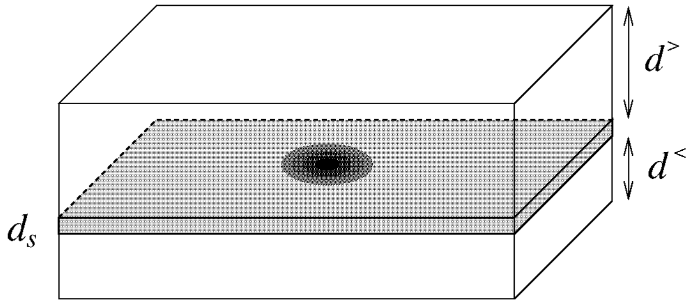

Figure 3.2: A vortex in a 2D superconducting layer of thickness d is placed between two superconductors of finite thickness $d^>$ and $d^<$.

discussed in Sec. 3.2 and Sec. 2.6.2 are recovered respectively with $d^< = d^> = 0$ and $d^< = d^> = \infty$.

First we use (3.8) at $z = 0$ in order to calculate the value of the total magnetic flux $\Phi_{\mathrm{t}} = \Phi(R \to \infty)$ trapped by a vortex. At distances R larger than λ, $A(R, z = 0)$ assumes the asymptotic form

$$\begin{aligned} A_\phi(R \gg \lambda, z = 0) &\sim \Phi_{\mathrm{t}} \int_0^\infty \frac{dK}{2\pi} \frac{J_1(KR)}{1 + \lambda_{\mathrm{eff}} K} \\ &= \frac{\Phi_{\mathrm{t}}}{2\pi R} + \frac{\Phi_{\mathrm{t}}}{4\lambda_{\mathrm{eff}}} \Big[Y_1\Big(\frac{R}{\lambda_{\mathrm{eff}}}\Big) + H_{-1}\Big(\frac{R}{\lambda_{\mathrm{eff}}}\Big) \Big], \end{aligned} \tag{3.12}$$

where, in comparison with the solution for the thin film of Eq. (3.2),

$$\lambda_{\mathrm{eff}}(N, n) = \lambda \, \frac{2 - \tanh^2(d^</\lambda) - \tanh^2(d^>/\lambda)}{\tanh(d^</\lambda) + \tanh(d^>/\lambda) + d/\lambda} \tag{3.13}$$

is the effective penetration depth and

$$\Phi_{\mathrm{t}}(N, n) = \frac{\Phi_0 d/\lambda}{\tanh(d^</\lambda) + \tanh(d^>/\lambda) + d/\lambda} \tag{3.14}$$

is the trapped flux (see also [18,19]). At distances larger than λ_{eff}, the vector potential $A_\phi(R, z = 0)$ takes the asymptotic form

$$A_\phi(R \gg \lambda_{\mathrm{eff}}, z = 0) \sim \frac{\Phi_{\mathrm{t}}}{2\pi R} \Big(1 - \frac{\lambda_{\mathrm{eff}}}{R}\Big). \tag{3.15}$$

Eq. (3.15) generalizes the expressions (3.4) and (2.65) obtained previously for the single layer film and the bulk infinite stack. The penetration depth λ_{eff} and the trapped flux Φ_{t} are strongly affected by stray fields; the expressions

(3.13) and (3.14) interpolate between the values $\Phi_\mathrm{t} = \Phi_0$ and $\lambda_\mathrm{eff} = \lambda_\mathrm{Pearl}$ for a thin film and $\Phi_\mathrm{t} = d\Phi_0/2\lambda$ and $\lambda_\mathrm{eff} = 0$ for an infinite layer bulk superconductor. Note that in thick samples λ_eff drops to values smaller than λ and approaches zero in the bulk, consistent with Eq. (2.65), where the corrections to the asymptotic value of the flux are exponentially small for $R \gg \lambda$.

For a thin N-layer system, with $(N-1)d \ll \lambda$, the trapped flux of Eq. (3.14) is easily rewritten into the simpler form [18–21]

$$\Phi_\mathrm{t}(N) \approx \frac{\Phi_0}{N} \tag{3.16}$$

and the dependence on the layer position n cancels out. The decrease $\Phi_\mathrm{t} = \Phi_0/N$ in the trapped flux with an increasing number of layers can be easily understood with the following simple argument: consider the case of a single pancake vortex in a bi-layer system. The magnetic field produced by the vortex varies on scale λ. In the limit of a small layer spacing, $d \ll \lambda$, the magnetic field penetrating both layers is approximately the same and so is the flux. Furthermore, a vortex stack penetrating both layers corresponds to a Pearl vortex and carries a full flux quantum Φ_0. The flux associated with one pancake vortex in a bi-layer system is then half the value trapped by the Pearl vortex and thus $\Phi_\mathrm{t} = \Phi_0/2$, in agreement with (3.16). This argument is easily extended to the multi-layer case as long as the thickness $(N-1)d$ of the system remains smaller than λ. To stress the important property $\Phi_\mathrm{t} < \Phi_0$, we will introduce the name 'fractional-flux' vortices for this kind of topological objects.

With the appearance of additional protecting layers, the transverse screening of the vortex singularity becomes incomplete, i.e., $\Phi_\mathrm{t} < \Phi_0$. As a consequence of the fluxoid quantization, the $(1/R)$-behavior of the currents extends to infinite distances and the attraction between oppositely charged vortices residing in the same layer is logarithmic to all scales,

$$V(R) \approx 2\varepsilon_0 d \begin{cases} \ln \dfrac{R}{\xi}, & R \ll \lambda_\mathrm{eff}, \\ \ln \dfrac{\lambda_\mathrm{eff}}{\xi} + \Big(1 - \dfrac{\Phi_\mathrm{t}}{\Phi_0}\Big) \ln \dfrac{R}{\lambda_\mathrm{eff}}, & \lambda_\mathrm{eff} \ll R, \end{cases} \tag{3.17}$$

but involves a reduced prefactor $\propto 1 - \Phi_\mathrm{t}/\Phi_0$ at large distances $R \gg \lambda_\mathrm{eff}$. Within the terminology adopted for the 2D Coulomb gas problem, we observe that the screening parameter $1 - \Phi_\mathrm{t}/\Phi_0$ acts as a renormalization of the effective 'charge' at distances $R \gg \lambda_{\rm eff}$. Hence a vortex carries a full 'charge' for $R \ll \lambda_{\rm eff}$ and a reduced one for $R \gg \lambda_{\rm eff}$.

3.4 Semi-infinite geometry

We consider now a semi-infinite geometry with the superconductor filling the upper half-space $z \geq 0$. This discussion is particularly relevant for the analysis of the surface effects on the melting of the vortex lattice (Chapter 6). A pancake vortex placed at z' generates a vector potential field satisfying the following set of equations, (cf. Eq. (3.7) with $d^> = z'$ and $d^> = \infty$, the additional term $\propto \mathbf{A}$ in the right hand side is irrelevant in this limit)

$$\begin{aligned} &\nabla^2\mathbf{A} - \frac{1}{\lambda^2}\mathbf{A} = \frac{d}{\lambda^2}\nabla\varphi\;\delta(z-z'), \quad z>0,\\ &\nabla^2\mathbf{A} = 0, \qquad\qquad\qquad z<0. \end{aligned} \tag{3.18}$$

In a semi-infinite system, the modification from bulk properties is largest at the surface. To give an idea of this modification, we first solve Eq. (3.18) for a pancake vortex placed on the surface $z' = 0$. The associated vector potential within the superconductor ($z > 0$) is

$$A_\phi(R, z \geq 0) = \frac{\Phi_0 d}{\lambda^2}\int_0^{+\infty}\frac{dK}{2\pi}\frac{J_1(KR)}{K+K_+}e^{-K_+ z}, \tag{3.19}$$

where $K_+ = \sqrt{\lambda^{-2}+K^2}$; a similar expression with the replacement $-K_+z \to -K|z|$ in the exponent describes the potential within the vacuum $z < 0$. The corresponding magnetic field resembles that of a Pearl vortex in the vacuum (half magnetic monopole) and takes the form characteristic of a bulk pancake-vortex within the superconducting region ($z > 0$), see Fig. 3.3. For $z = 0$, the integral in (3.19) can be carried out

$$A_\phi(R, z = 0) = \frac{d}{\lambda}\frac{\Phi_0}{2\pi R}\left[1 - \frac{\lambda}{R}\left(1 - e^{-R/\lambda}\right)\right]. \tag{3.20}$$

The total flux trapped by the surface pancake vortex is $\Phi_{\rm t}(0) = d\Phi_0/\lambda$, twice the bulk value, cf. also (3.14). Comparing (3.20) with the corresponding expressions for the Pearl vortex (3.4) and the bulk pancake vortex (2.65), one sees that the magnetic length is the bulk penetration depth λ and both the exponential and algebraic decay are present, with the latter dominating

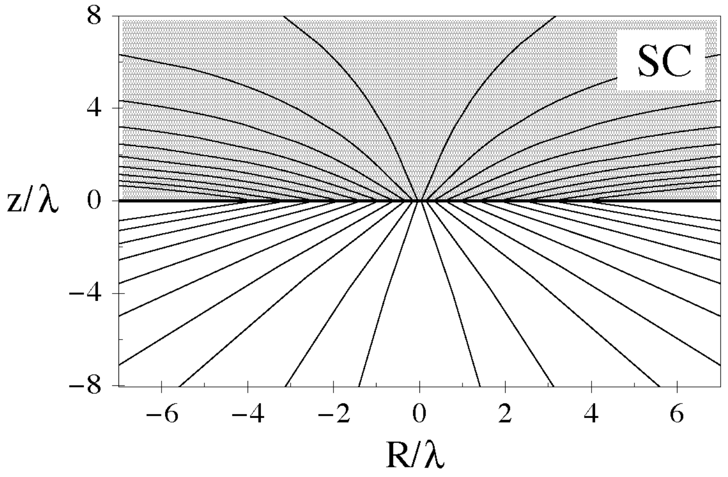

Figure 3.3: Magnetic field lines of a pancake vortex placed on the surface. The shaded half-space corresponds to the superconducting region.

at large scales. As we will see, this slow $1/R$ dependence becomes important in the discussion of surface melting of the vortex lattice.

Next, we consider two pancake vortices residing on the same layer, cf. Fig. 3.4(a). As we have argued before, their interaction includes the contributions from both terms in Eq. (2.64), the driving source $\nabla\varphi$ and the vector potential $\mathbf{A}$ and it obeys the expression

$$V_{z',z'}(R) \approx -2\varepsilon_0 d \begin{cases} \ln\dfrac{R}{\xi}, & R \ll \lambda, \\ \ln\dfrac{\lambda}{\xi} + \Big(1 - \dfrac{\Phi_{\rm t}(z')}{\Phi_0}\Big)\ln\dfrac{R}{\lambda}, & \lambda \ll R, \end{cases} \tag{3.21}$$

where $\Phi_{\rm t}(z)$ is the magnetic flux trapped by a pancake vortex placed at a distance z away from the surface. The surrounding layers affect the vortex properties via their (dia)-magnetic response, by reducing the value of the total trapped flux $\Phi_{\rm t}(z) < \Phi_0$. From (3.14) with $d^> = \infty$, $d^< = z'$, we obtain the interpolating formula $\Phi_{\rm t}(z)$ between the values $(d/\lambda)\Phi_0$ on the surface and $(d/2\lambda)\Phi_0$ in the bulk,

$$\Phi_{\rm t}(z') = \frac{\Phi_0 d}{2\lambda}\Big(1 + e^{-2z'/\lambda}\Big). \tag{3.22}$$

The combination of (3.22) with (3.21) confirms that the modification of the strength of the in-plane interaction is only of order d/λ. If we ignore contributions of this order arising from magnetic screening, the in-plane interaction

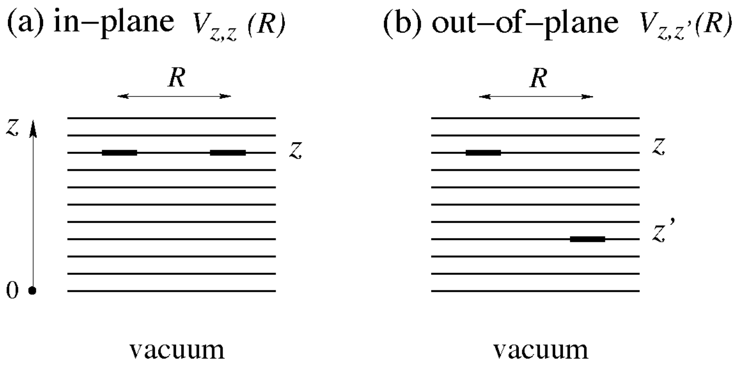

Figure 3.4: Geometry of the model. A layered superconductor fills the half space with $z > 0$. The interaction between two pancake vortices is affected by the semi-infinite geometry and by the strong anisotropy, leading to a strong logarithmic repulsion between pancake vortices which reside within the same layer (a) or to a weak logarithmic attraction between pancake vortices in different layers (b).

is independent of z. Within this approximation, vortices in the same layer feel a repulsive logarithmic interaction,

$$V_{z,z}(R) \approx -2\varepsilon_0 d \ln\frac{R}{\xi}, \tag{3.23}$$

a potential corresponding to the two-dimensional Coulomb gas (one component plasma) with charge $e^2 \to 2\varepsilon_0 d$.

3.4.1 Out-of-plane interaction

For two pancake vortices in different layers (cf. Fig. 3.4(b)), the current (2.71) which enters the Lorentz force (2.63) does not contain the contribution from the driving phase $\nabla\varphi$. Hence, the force in (2.64) is due to the vector potential A alone. The central quantity in the discussion is the magnetic field which is produced by a single pancake vortex placed in a semi-infinite sample. By solving Eq. (3.18), we obtain the vector potential at the point $(\mathbf{R}, z)$ inside the superconductor produced by a pancake vortex placed at the origin of the layer at z',

$$A_\phi(R, z \geq 0, z' \geq 0) = \frac{\Phi_0 d}{2\lambda^2}\int_0^{+\infty}\frac{dK}{2\pi}\frac{J_1(KR)}{K_+}\times$$
$$\times \left(e^{-K_+|z-z'|} + \frac{K_+ - K}{K_+ + K}e^{-K_+(z+z')}\right). \tag{3.24}$$

Note again the symmetry $z \leftrightarrow z'$. We first extract the total flux $\Phi_{\mathrm{t}}(z,z')$ induced in the layer at z by a pancake placed at a distance z' from the surface

$$\Phi_{\mathrm{t}}(z,z') = \frac{\Phi_0 d}{2\lambda}\Big(e^{-|z-z'|/\lambda} + e^{-(z+z')/\lambda}\Big). \tag{3.25}$$

The trapped flux $\Phi_{\mathrm{t}}(z) \equiv \Phi_{\mathrm{t}}(z,z)$ recovers the expression of Eq. (3.22). If we add pancake vortices in a stack, the trapped flux is quantized and equal to Φ_0, i.e.,

$$\int_0^{\infty} dz' \Phi_{\mathrm{t}}(z,z') = \Phi_0. \tag{3.26}$$

The symmetry $z \leftrightarrow z'$ allows us to interpret (3.26) equivalently as the sum over all layers of the magnetic fluxes produced by a single pancake vortex. By inserting the vector potential (3.24) in (2.32) and (2.64), we obtain an expression for the force between two pancake vortices residing in different layers $z \neq z'$. By integrating it over R we arrive at the out-of-plane interaction

$$\begin{aligned} V_{z,z'}(R) = &-\frac{\varepsilon_0 d^2}{\lambda^2}\int_0^{+\infty} dK \frac{J_0(KR)}{KK_+} \\ &\times \left(e^{-K_+|z-z'|} + \frac{K_+ - K}{K_+ + K} e^{-K_+(z+z')}\right). \end{aligned} \tag{3.27}$$

The interaction is given by the sum of a bulk- (first) $V^{\mathrm{b}}_{z-z'}(R)$ and a stray-field term (second) $V^{\mathrm{s}}_{z,z'}(R)$, where the latter becomes negligible at a distance $\sim \lambda$ away from the surface.

For small in-plane distances, i.e., $R \ll \lambda$, the contribution of the stray field potential to the overall vortex interaction energy can be neglected: $V^{\mathrm{s}}_{z,z'}(R) \ll V^{\mathrm{b}}_{z-z'}(R)$, see Fig. 3.5. Thus, for $R \ll \lambda$, the potential coincides with the bulk one (2.73)

$$V_{z,z'}(R) \approx \varepsilon_0 d \frac{d}{\lambda} \begin{cases} \dfrac{R^2}{4|z-z'|\lambda}, & R \ll |z-z'| \ll \lambda, \\ \dfrac{R}{\lambda}, & |z-z'| \ll R \ll \lambda. \end{cases} \tag{3.28}$$

As expected, the out-of-plane interaction is weaker with respect to the in-plane case (3.23) due to the small pre-factor d/λ. However, this interaction extends over many (λ/d) layers.

On the other hand, for larger in-plane distances, i.e., for $R \gg \lambda$, we find relevant modifications of the out-of-plane interaction at the surface

$$V_{z,z'}(R) \approx \varepsilon_0 d \frac{d}{\lambda} e^{-|z-z'|/\lambda} \ln\frac{R}{\lambda} + \varepsilon_0 d \frac{d}{\lambda} e^{-(z+z')/\lambda}\Big(\ln\frac{R}{\lambda} + \frac{2\lambda}{R}\Big). \tag{3.29}$$

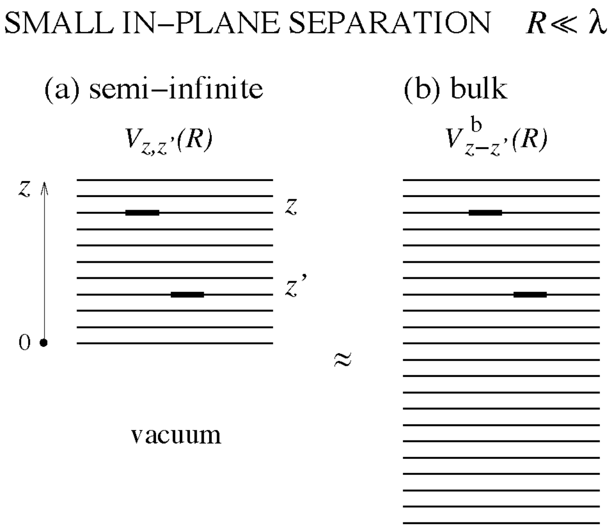
SMALL IN–PLANE SEPARATION $R \ll \lambda$
(a) semi–infinite
$V_{z,z'}(R)$
(b) bulk
$V^{\mathrm{b}}_{z-z'}(R)$
z
0
z
z'
≈
vacuum

Figure 3.5: For small in-plane separations, i.e., $R \ll \lambda$, the total energy for the out-of-plane interaction in a semi-infinite system (a) is equivalent to the one of a translation invariant bulk (b) system $V^{\mathrm{b}}_{z-z'}(R)$.

The first term has a bulk origin (2.73), whereas the terms which follow vanish away from the surface. Combining the terms, we can rewrite (3.30) in the more convenient form

$$V_{z,z'}(R) = 2\varepsilon_0 d\Big[\frac{\Phi_{\mathrm{t}}(z,z')}{\Phi_0}\ln\frac{R}{\lambda} + \frac{d}{\lambda}e^{-(z+z')/\lambda}\frac{\lambda}{R}\Big]. \qquad (3.30)$$

We identify two different terms: a logarithmic attractive interaction (first) and an algebraic repulsive potential (second). The logarithmic interaction can be analyzed in terms of mirror vortices (see Fig. 3.6): a test vortex at z then effectively experiences a logarithmic attraction from *two* bulk-type vortices, the real one at z' and a fake mirror vortex with equal sign at $-z'$, see Fig. 3.6. Finally the algebraic repulsion associated with the second term in (3.30) is again due to the stray magnetic field and produces a surface softening (cf. the discussion in Chapter 6 of the melting of the vortex lattice in the presence of a surface).

3.4.2 Semi-infinite stack

In this section, we calculate the magnetic field produced by a complete vortex stack close to the surface, by adding the contributions of aligned pancake

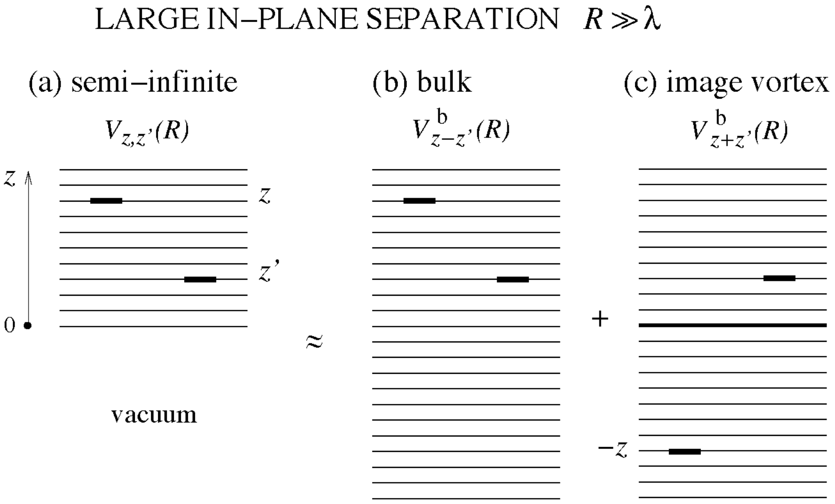
LARGE IN–PLANE SEPARATION $R \gg \lambda$
(a) semi–infinite
$V_{z,z'}(R)$
z
z
z'
0
vacuum
≈
(b) bulk
$V^{\mathrm{b}}_{z-z'}(R)$
+
(c) image vortex
$V^{\mathrm{b}}_{z+z'}(R)$
$-z$

Figure 3.6: For large in-plane separations, i.e., $R \gg \lambda$, the total energy for the out-of-plane interaction in a semi-infinite system (a) can be split in (b) a translation invariant bulk term $V^{\mathrm{b}}_{z-z'}(R)$ and (c) an additional one $V^{\mathrm{b}}_{z+z'}(R)$ that can be interpreted in terms of an image vortex placed in $-z$.

vortices. Integrating up Eq. (3.24) on z', we obtain the total vector potential due to a vortex stack ($z \geq 0$) [45]

$$A_{\mathrm{stack}}(R,z) = \frac{\Phi_0}{\lambda^2}\int_0^\infty \frac{dK}{2\pi}\frac{J_1(KR)}{K_+^2}\left[1 - \frac{K\,e^{-K_+ z}}{K+K_+}\right]. \tag{3.31}$$

In the bulk $z \longrightarrow +\infty$ one recovers the standard expression

$$\begin{aligned} A_{\mathrm{stack}}(R, z \gg \lambda) &= \frac{\Phi_0}{\lambda^2}\int_0^\infty \frac{dK}{2\pi}\frac{J_1(KR)}{K_+^2} && (3.32)\\ &= \frac{\Phi_0}{2\pi R}\left[1 - K_1\Big(\frac{R}{\lambda}\Big)\right], && (3.33)\end{aligned}$$

which leads to an interaction $\propto K_0(R/\lambda)$, cf. (2.30) (with (2.24)). On the other hand, at the surface ($z=0$) the integration over K gives

$$A_{\mathrm{stack}}(R, z=0) = \frac{\Phi_0}{2\pi\lambda} I_1\Big(\frac{R}{2\lambda}\Big) K_0\Big(\frac{R}{2\lambda}\Big), \tag{3.34}$$

where I_1 and K_0 are modified Bessel functions, of the first and zero order respectively. At large distances we obtain

$$A_{\mathrm{stack}}(R \gg \lambda, z=0) \sim \frac{\Phi_0}{2\pi R}\Big(1 - \frac{\lambda}{R}\Big); \tag{3.35}$$

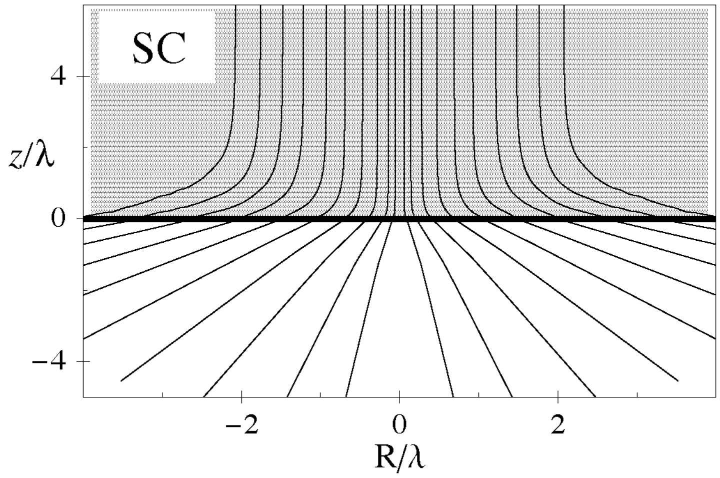

Figure 3.7: Magnetic field lines of an aligned pancake vortex stack near the surface of a semi-infinite sample. The shaded area corresponds to the superconducting region.

this expression can also be derived from the integral of (3.30) over z'. From the first term in (3.30) we obtain that a full vortex line traps a whole flux quantum Φ_0, like in the bulk (the mirror term in (3.30) compensates the lack of superconducting planes in $z < 0$). At the surface, modifications appear due to the residual algebraic potential in (3.30) which adds up to yield the second term in (3.35). The stray field in the free half-space takes the form ($z \leq 0$)

$$A_{\text{stack}}(R, z) = \frac{\Phi_0}{2\pi\lambda^2} \int_0^{\infty} dK \frac{J_1(KR)e^{-Kz}}{K_+(K + K_+)}. \tag{3.36}$$

The flux lines of the corresponding magnetic field are shown in Fig. 3.7.

Combining (3.31) with (2.71) and (2.63), we obtain the magnetic component of the Lorentz force (without the contribution from the source term $\propto \nabla\varphi$). Integrating over R back from infinity the associated line interaction is derived,

$$V_{\text{stack}}(R, z) = -\frac{2\varepsilon_0 d}{\lambda^2} \int_0^{+\infty} dK \, \frac{J_0(KR)}{KK_+^2} \Big(1 - \frac{Ke^{-K_+ z}}{K + K_+}\Big). \tag{3.37}$$

From this expression at $z = 0$, including the contribution of the source term, we obtain the interaction per unit length between the tips of two vortices at the surface ($z = 0$)

$$V(R, z = 0) \approx 2\varepsilon_0 \begin{cases} -\ln \dfrac{R}{\xi}, & R \ll \lambda, \\ \dfrac{\lambda}{R}, & \lambda \ll R. \end{cases} \tag{3.38}$$

The logarithmic interaction at short scales turns to an $1/R$-algebraic behavior at large distances [44]. This long range interaction is not present in the bulk, cf. (2.31), and it is due to the stray magnetic fields.

Chapter 4

Thermodynamic behavior at zero magnetic field

We discuss the zero-field thermodynamic behavior of superconducting systems with a finite number of magnetically coupled layers. We assume an ideal situation with no Josephson coupling. Pancake vortices, i.e., two-dimensional vortices residing within individual layers, trap a fraction of a full quantum flux and involve a self-energy which diverges logarithmically with the system size. On the other hand, full pancake vortex stacks, which correspond to Pearl vortices in a single layer setup, involve a finite self-energy and are thermally excited at any finite temperature. Their presence suppresses the superconductivity in all layers together, while the counterflow superconductivity, i.e., relative to different layers, is preserved. This remaining superconducting response is finally destroyed via the unbinding of intra-layer neutral pairs of pancake vortices. They undergo an unbinding transition of the Berezinskii-Kosterlitz-Thouless type at a given finite temperature which depends on the total number of layers. This unbinding transition also affects the thermally excited vortex stacks, triggering their dissociation. By means of renormalization group techniques, we analyze the dissociation transition for a bi-layer system and discuss its potential observation in a specific experimental setup with a counterflow geometry. We point out interesting analogies with the bi-layer quantum Hall system at total filling $\nu = 1$.

4.1 Introduction

Topological excitations play a central role in statistical physics. The unbinding of topological defects, e.g. phase slips in superconducting wires [46], vortices in thin superfluid films [47], and dislocations in two dimensional crystals [48], drive specific phase transitions which have attracted much interest. Similarly, the transition of layered superconductors into the normal state in zero magnetic field is due to the proliferation of two dimensional vortices [2]. In fact, in the absence of pinning forces, under the action of an external current the vortices move and dissipate energy, producing a finite linear resistivity like in a normal metal [49]. Many studies, both theoretical and experimental [50–52], concentrated on thin films or on bulk layered superconductors and investigated these systems in relation with the Berezinskii-Kosterlitz-Thouless [6,7] (BKT) pair unbinding transition. Here, we extend the analysis to systems with a finite number of layers and show that new interesting properties emerge in these systems.

The basic prerequisite [6] for the appearance of a BKT transition is the logarithmic interaction between topological defects. In uncharged superfluids, e.g. ^{4}He, this logarithmic interaction extends to infinity and the system undergoes a BKT transition at a finite temperature [6]. In a superconducting film the charged currents couple to the vector potential $\mathbf{A}$. Magnetic screening leads to the suppression of the currents at the Pearl length λ_{Pearl}. Pearl vortices trap a full flux Φ_0 and acquire a finite, although large, self energy $E_{\mathrm{Pearl}} = \varepsilon_0 d \ln \lambda_{\mathrm{Pearl}}/\xi$, cf. (3.5). At distances larger than λ_{Pearl}, the logarithmic interaction is cut off and vortices interact only via a weak algebraic potential. At any non-zero temperature, free Pearl vortices are thermally generated at a finite density $n_{\mathrm{Pearl}} \propto \exp(-E_{\mathrm{Pearl}}/T)$. The putative BKT transition at $T_{\mathrm{BKT}}^{\mathrm{x}} = \tilde{\varepsilon}_0 d/2$ ($\tilde{\varepsilon}_0$ is the appropriate [53] renormalized value of ε_0) then is preempted by the thermal activation of Pearl vortices. Therefore, in a single superconducting film the superconducting to normal transition is shifted to $T = 0$. However, due to the large value of the self-energy E_{Pearl}, the number of thermally excited Pearl vortices is small [54]. The unbinding of vortices on scales smaller than λ_{Pearl} produces a sharp crossover at $T_{\mathrm{BKT}}^{\mathrm{x}}$, which has been observed in many experimental studies, e.g. [51,52].

Going to a bulk layered system with $N \gg \lambda/d$, two dimensional topological excitations transform from Pearl vortices to pancake vortices. The additional layers produce further magnetic screening and expel the magnetic field associated with a pancake vortex in the transverse direction (see Fig. 2.5); a pancake vortex traps a reduced flux, $\Phi_{\mathrm{t}} = d\Phi_0/2\lambda$. The in-plane logarithmic interaction between pancake vortices extends to arbitrary lengths, resulting into a true pancake vortex unbinding transition of BKT type at $T_{\mathrm{BKT}}^{(\infty)} \approx \tilde{\varepsilon}_0 d/2$. In a bulk layered system the role of vortex lines is played by vortex stacks. They involve a self-energy $E_{\mathrm{s}} = N\varepsilon_0 d \ln \lambda/\xi$ which grows linearly with the thickness Nd and, hence, for large N they can penetrate into the system only under the action of a finite external magnetic field. Hence, at zero magnetic field, as no thermally excited vortex stacks are present, the superconducting to normal transition is induced by the proliferation of pancake vortices within the individual layers and it occurs at the finite temperature $T_{\mathrm{BKT}}^{(\infty)}$ [50]. As it was pointed out in Ref. [5], this unbinding transition can also be interpreted in terms of the dissociation of vortex stacks. Both transitions are based on the in-plane logarithmic pancake vortex interaction; removing a single pancake vortex out of an aligned vortex stack by a distance R involves the same logarithmic energy cost as the creation of a pancake vortex–anti-vortex pair of size R. As a consequence, at $T_{\mathrm{BKT}}^{(\infty)}$ the vortex stacks break apart and dissolve into unbound pancake vortices.

The difference between the thermodynamic behavior of a single film and a bulk layered superconductor motivates our study of the intermediate case of systems composed of a finite number N of superconducting layers. We start in Sec. 4.2 with the analysis of the intra-layer vortex unbinding transition temperature $T_{\mathrm{BKT}}^{(N)}$ and discuss its dependence on the value Φ_{t} of the total trapped magnetic flux. We then concentrate in Sec. 4.3 on the bi-layer system and discuss, using a renormalization group analysis, the competition between the $T = 0$ transition induced by thermally excited vortex stacks and the finite temperature pancake vortex unbinding transition in individual layers. We determine the I-V characteristic and show how to track the dissociation of the vortex molecules in a counterflow geometry in Sec. 4.3.4. We discuss the experimental requirement and the impact of disorder on the phase transition in Secs. 4.3.5 and 4.3.6. Finally, in Sec. 4.3.7 we propose an interesting analogy with the bi-layer quantum Hall system at filling $\nu = 1$.

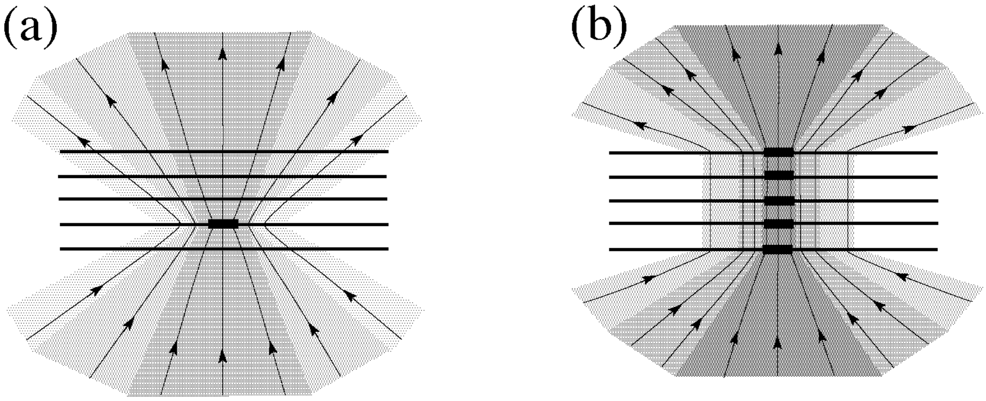

Figure 4.1: Sketch of the magnetic field lines for (a) a single fractional-flux vortes ($\Phi_{\rm t} = \Phi_0/N$) and (b) a pancake vortex stack ($\Phi_{\rm t} = \Phi_0$) in a system composed of five superconducting layerd ($N = 5$). The shading intensity relates to the intensity of the magnetic field.

4.2 Thermodynamics of N superconducting layers

Systems which are composed of a finite number N of layers exhibit a rather rich thermodynamic behavior, somewhat intermediate between the single film ($N = 1$) and the bulk layered superconductor ($N = \infty$). In N-layered systems, we encounter different types of topological defects: pancake vortex stacks (see Fig. 4.1(b)) and two dimensional vortices (see Fig. 4.1(a)).

Pancake vortex stacks involve, like Pearl vortices in an isolated film, a full flux quantum Φ_0, and thus a finite self energy $E_{\rm s} = N\varepsilon_0 d \ln(\lambda_{\rm eff}/\xi)$ (from (3.5)). Hence, free vortex stacks are thermally generated at any non-zero temperature in a finite density $n_{\rm s} \propto \exp(-E_{\rm s}/T)$ and destroy superconductivity in *all layers together*. Given the linear dependence on the number of layers N, in thick samples this transition becomes exponentially weak and disappears altogether in a bulk system.

On the other hand, single pancake vortices trap a magnetic flux Φ_0/N (cf. Eq. (3.16)), which is a fraction of a complete quantum flux (see Fig. 4.1(a)). This reduction in trapped flux is the result of the modified transverse screening which depends on the number of protecting layers. The incomplete screening due to $\Phi_{\rm t}(N) < \Phi_0$ implies an infinite interaction range for $N > 1$ and hence vortex-unbinding establishes a finite temperature BKT transition

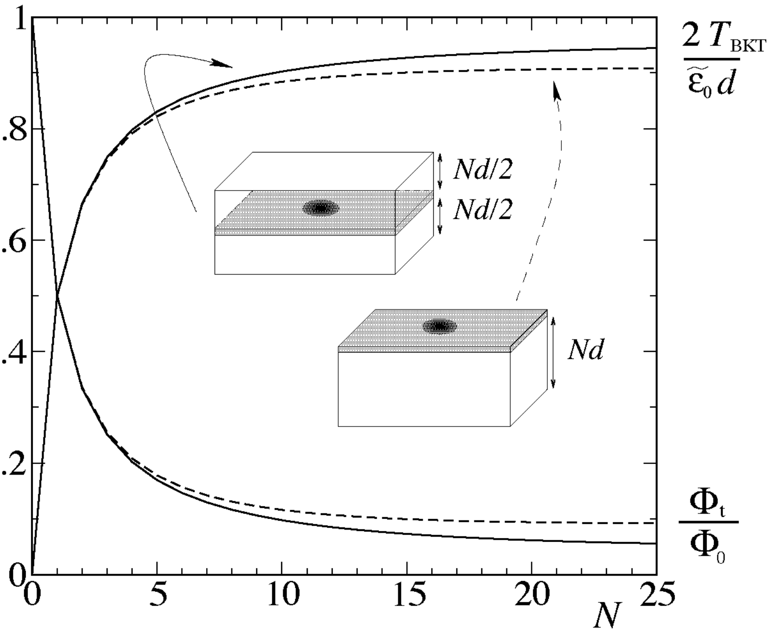

Figure 4.2: Dependence of the total flux and the superfluid density jump at the transition on the total number of layers for the surface (dashed line) and the bulk (solid line). A large value $\lambda/d = 10$ has been chosen for illustrative reasons.

[18, 19] which depends on N

$$T^{(N)}_{\rm BKT} = \frac{\tilde{\varepsilon}_0 d}{2}\Big(1 - \frac{\Phi_{\rm t}(N)}{\Phi_0}\Big). \tag{4.1}$$

As usual [53], the line energy ε_0 undergoes renormalization due to thermal fluctuations and we have to make use of the proper renormalized value $\tilde{\varepsilon}_0 = \varepsilon_0^{\infty}(T_{\rm BKT})$ (depending on the number N of superconducting layers). At this unbinding transition, free pancake vortices proliferate within the individual layers, suppressing superconductivity in the *individual layers*. The finite range of the interaction in the thin film ($N = 1$) transforms the transition into a crossover; this is consistent with (4.1) as a full flux quantum Φ_0 is trapped by the Pearl vortex, $\Phi_{\rm t} = \Phi_0$. However, differently from the case of a single superconducting film, for $N > 1$ fractional flux vortices undergo a true finite temperature Berezinskii-Kosterlitz-Thouless [6, 7] (BKT) transition. The presence of one additional 'protecting' layer changes the situation dramatically: transverse screening reduces the trapped flux to half its value,

$\Phi_{\rm t} = \Phi_0/2$, thus extending the range of the logarithmic interaction to infinity and pushing the transition temperature to a finite value $\tilde{\varepsilon}_0 d/4$. Adding more layers (N), the trapped flux $\Phi_{\rm t} = \Phi_0/N$ decreases further until assuming the asymptotic value $\Phi_{\rm t} = d\Phi_0/2\lambda$ in a bulk superconductor where $T_{\rm BKT}^{(\infty)} \approx \tilde{\varepsilon}_0 d/2$ is largest, see Fig. 4.2. Similarly, the jump in the superfluid density [47] at the phase transition depends on the number of layers via the screening factor $1 - \Phi_{\rm t}/\Phi_0$; the maximal jump is realized in the bulk case where it assumes the value of an uncharged superfluid, $T_{\rm BKT}^{(\infty)} \approx 8m/n^{\rm 2D}\hbar^2\pi$ (enhanced by a factor 4 due to pairing).

Summarizing in systems with a finite number of layers, two different transition take place: *i)* a $T = 0$ transition, which is induced by vortex stacks in all layers and *ii)* a finite temperature transition at $T_{\rm BKT}^{(N)}$ due to the unbinding of pancake vortices in the individual layers. Whereas the superconducting transition is associated with the first (like in a single superconducting film), the latter suppresses the superconductivity in the individual layers. As it was pointed out in [5] for the case of a bulk system (see discussion above), the pair unbinding at $T_{\rm BKT}^{(N)}$ can be equivalently viewed as the stack dissociation. Therefore, the intra-layer BKT transition is associated with the dissociation of vortex stacks into fractional flux vortices, rather than describing the transition into the normal phase. However, at this point it is natural to rise the question whether this finite temperature pairs-unbinding/stack-dissociation BKT transition can be detected or it is completely preempted by the presence of vortex stacks. In the next sections we will show how one can remove the effect of vortex stacks for current-sensitive experiments with the help of an appropriate experimental setup, thus allowing to observe the finite temperature BKT transition.

4.2.1 Other multicomponent systems

The appearance of a finite temperature phase transition due to the protecting action of additional superconducting layers has its counterpart in multigap superconductors [55–57] and is often associated with the term ‘flux fractionalization’ (similar results were also found in the context of microscopic studies of high-T_c superconductivity in Refs. [58, 59], see also [60]). In the case of multi-gap superconductors, different superconducting components correspond to disconnected sheets of the Fermi surface; beside normal vortices, involving a rotation of all components together, one can consider vortices with a core limited to one component alone, the analogue of pancake vortices in the layered system. Therefore, the creation of a topological defect in one superconducting component or layer induces screening currents in the other components/layers via coupling to the common gauge field A. The additional screening provided by these 'protecting' components/layers inhibits the trapping of a full flux quantum Φ_0 needed in order to screen the driving field associated with the vortex singularity at long distances. As a result, the effect of the singularity persists up to infinite distances (though with a 'charge' renormalized by the factor $(1-\Phi_\mathrm{t}/\Phi_0)$), similar to the situation in a neutral superfluid where screening is entirely absent. We note that the Josephson coupling between the superconducting layers or the internal coupling between the components of a multigap superconductor spoils this phenomenon: the Josephson coupling introduces a new length scale $\Lambda = d/\varepsilon$ beyond which pancake vortex pairs are confined with a potential rising linear with distance (cf. Sec. 2.6.1), thus inhibiting their unbinding and quenching the BKT transition. The Josephson coupling can be (made) small in artificial layered material; on the other hand, the internal Josephson effect in a multi-component superconductor cannot be tuned and is not necessarily small [61].

A more promising proposal [62], albeit only theoretical so far, is hydrogen which, at low temperatures and under the effect of an elevated pressure, is supposed to become a two-component superconductor (with components respectively associated with paired electrons and protons). For this system, tunneling between the electronic and protonic components is naturally excluded. However, the large pressure which is required to liquify hydrogen has not been achieved yet.

Finally, another systems which shows interesting analogies with the systems that we are studying is the bi-layer quantum Hall system at total filling $\nu = 1$ [63, 64]. This system hosts 'fractional' topological excitations, called merons. They are composed of vortices which carry a fractionalized electronic charge $\pm e/2$ and are associated with oppositely flowing currents in the two layers. We will come back to describe this analogy in detail in Sec. 4.3.7.

4.3 Bi-layer system and I-V measurement

Here, we are interested in the possibility to observe the particular effects due to the presence of incomplete transverse screening in multi-layer systems in an experiment. The setup where the fractional-flux vortices make their most prominent appearance is the bi-layer system with $N = 2$. This configuration has attracted much attention in the past in the context of the flux-transformer which was originally proposed by Giaever [65–67]. Here, rather than studying the magnetic coupling between the layers at finite external applied magnetic field, we discuss the modifications of the BKT transition due to the presence of fractional-flux vortices.

A vortex which resides in only one layer traps half a flux quantum $\Phi_0/2$ and the associated BKT unbinding transition occurs at $T_{\rm BKT}^{(2)} = \tilde{\varepsilon}_0 d/4$. The bi-layer system hosts two different kinds of topological excitations: *i)* half-flux vortex–anti-vortex pairs within the individual layers (cf. Fig. 4.3(b) for a single vortex) and *ii)* full vortex stacks, cf. Fig. 4.3(a). On the one hand, the loss of superconductivity in both layers is related to the appearance of full vortex stacks, which involve a finite self-energy and are thermally excited at any finite temperature. On the other hand, at $T_{\rm BKT}^{(2)}$ individual fractional-flux vortices unbind and thermally excited vortex stacks dissociate. As we will see below, this transition is associated with the destruction of the *counterflow* superconducting response.

A convenient tool that allows to probe the nature of the superconducting and normal phases as well as the transition itself is the measurement of the current-voltage characteristic. In the bi-layer system, the shape of the I-V characteristic is determined by both full vortex stacks, which play the role of Pearl vortices in the film and are present at any finite temperature, and half-flux vortex–anti-vortex pairs in individual layers, which undergo an unbinding transition at $T_{\rm BKT}^{(2)} = \tilde{\varepsilon}_0 d/4$. In a standard geometry where the current flows in parallel through the two layers, the drag motion of thermally activated full vortex stacks produces an ohmic response at small drive for any finite temperature. However, the particular topology where the two superconducting layers are connected at one edge, see Fig. 4.3(c), preserves the special screening properties of the bi-layer system, while 'shortcircuiting' the ohmic response of full vortex stacks. Feeding and removing the current at the remaining free ends of the film, the forces acting on the two half-flux vortices of one stack compensate one another and thus they do not produce

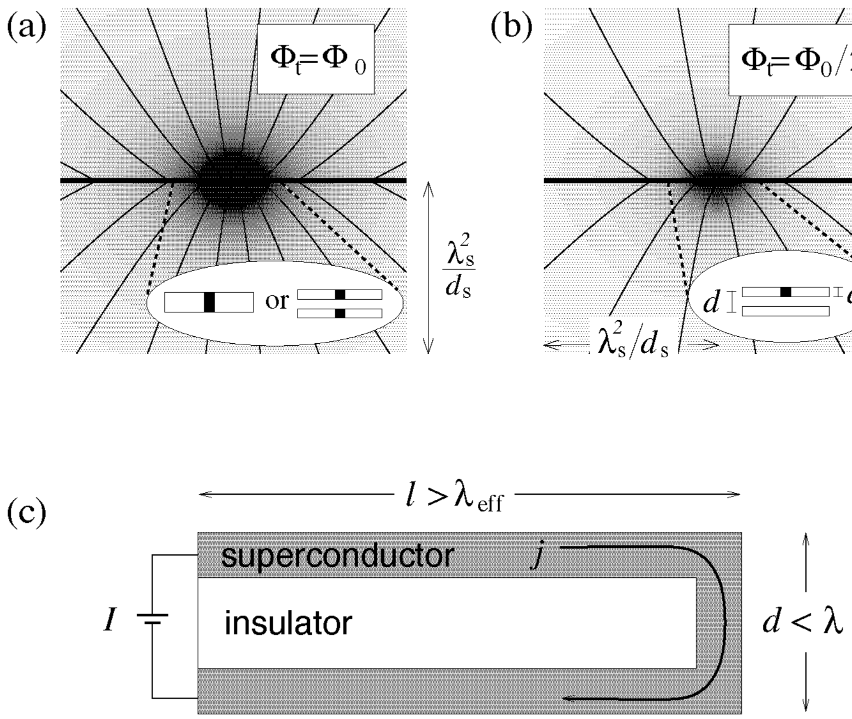

Figure 4.3: Topological defects in bi-layer systems (we assume the same material with penetration depth λ_s): (a) Pearl vortex in a film or vortex stack in a bi-layer superconductor, (b) half-flux (hf) vortex in a bi-layer superconductor. The density of field lines and the shading proportional to the field intensity B illustrate the difference in trapped flux. Both the interlayer distance and the film thickness are $d, d_\mathrm{s} \ll \lambda_\mathrm{eff}$, hence the geometric structure, e.g. single or double layer, is not visible on scales of the order of the magnetic length λ_eff. (c) Experimental setup suppressing the impact of full vortex stacks on the current-voltage characteristic and allowing for the identification of half-flux vortices.

a linear resistivity. In this way, the stack dissociation transition is associated with the suppression of the superconducting (superfluid) response in the counterflow channel. The non-linear current-voltage characteristic $V \propto I^\alpha$ then is determined by the current-induced unbinding of half-flux vortex–anti-vortex pairs residing in the individual layers and an additional contribution from current-assisted evaporation of stacks. The *I*-*V* characteristic then carries the signature of fractional-(i.e., half-)flux vortices and their unbinding at $T_{\mathrm{BKT}}^{(2)}$. The specific properties of the bi-layer system produce a modified *I*-*V* curve; half-flux vortices manifest themselves at currents lower than a typical small value I_{eff}. At the transition temperature $T_{\mathrm{BKT}}^{(2)}$, the exponent changes from $\alpha = 3$ to $\alpha = 5$ with increasing current, a consequence of the half-quantum flux trapped by the individual vortices.

Note that this experiment can be generalized to the case of any even number of layers by connecting alternatively opposite edges in the layer array. The total sheet current, which is given by the sum of the sheet currents in individual layers adds up to zero and thus does not exert a net force on the vortex stacks.

In the following, we first present a quantitative analysis of the thermodynamic properties of the bi-layer system, in particular, the crossover from unscreened to half-flux vortices and their unbinding at $T_{\mathrm{BKT}}^{(2)}$. We then make use of these results in the determination of the current-voltage characteristic and identify the specific features signalling the presence of half-flux vortices.

4.3.1 Pancake-vortex unbinding transition

The thermodynamic properties of two-dimensional superfluids are conveniently described by a renormalization group analysis. Here, we extend the conventional discussion in a thin film [6, 68] to a bi-layer system. We concentrate on configurations where both vortices reside in the same layer, see section 4.3.2 below for a discussion of vortex-stacks involving vortices in different layers. The interaction energy between a pair of half-flux vortices derives from the vector potential $A(R)$ with the trapped flux $\Phi_{\mathrm{t}} = \Phi_0/2$, see Eq. (3.12), and the effective penetration depth $\lambda_{\mathrm{eff}} = \lambda^2/d$ of the double layer, cf. Eq. (3.13). The $T = 0$ interaction energy of a half-flux vortex pair separated by R derives from integrating the force (2.68),

$$V(R) = 2\varepsilon_0 d \int_\xi^R \frac{q(R')}{R'} dR', \tag{4.2}$$

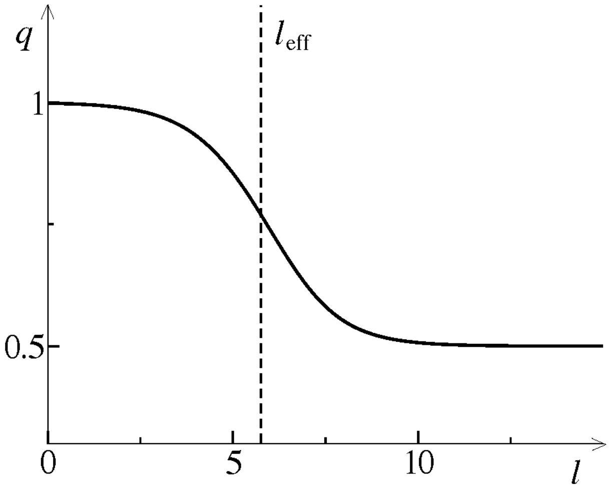

Figure 4.4: Screening factor $q(l = \ln R/\xi)$ for the bi-layer system. We use the parameter $\lambda_{\text{eff}}/\xi = 10^{2.5}$ (see section 4.3.5), producing a screening length $l_{\text{eff}} = \ln(\lambda_{\text{eff}}/\xi) \approx 5.76$. Pancake vortices interact with only half the original strength at distances beyond l_{eff}.

where the dimensionless parameter

$$q(R) = 1 - \frac{\Phi(R)}{\Phi_0} \xrightarrow{R \gg \lambda_{\text{eff}}} \frac{1}{2} \tag{4.3}$$

includes the effects of magnetic screening and acts as a space dependent dielectric function interpolating between $q \approx 1$ at distances $R \ll \lambda_{\text{eff}}$ and $q \approx 1/2$ for $R \gg \lambda_{\text{eff}}$. The interaction potential in (4.2) crosses over to half its value at the scale λ_{eff} when the flux reaches the asymptotic value $\Phi_0/2$ (see Fig. 4.4). In the following, in analogy with the two-dimensional Coulomb gas, we can view the function $q(R)$ as a scale dependent dielectric function, which screens the 'full charge' of the vortices to half its value at scales $R \ll \lambda_{\text{eff}}$. With this terminology $q(R)$ describes the crossover from 'full-charged' at short scales to 'half-charged' (or equivalently half-flux) vortices at large distances.

In the following, we perform a simple scaling analysis which relies on the (quasi)-logarithmic R dependence of the potential $V(R)$. This scheme is then accurate for slowly varying functions $q(R)$ without scale. Here, $q(R)$ changes on the screening length λ_{eff} and our analysis is accurate only on small and large scales, while it is interpolating in between.

At finite temperatures, the interaction $V(R)$ is renormalised by the presence of fluctuating vortex–anti-vortex pairs of size smaller than R. The effective interaction

$$\tilde{V}(R) = 2\pi T \int_{\xi}^{R} \frac{q(R')K(R')}{R'} dR', \tag{4.4}$$

accounts for these fluctuations via the scale dependent superfluid density $K(R)$ with $K(\xi) = K_0 = \varepsilon_0 d/\pi T$. The function $K(R)$ derives from a scaling analysis adapting the standard Kosterlitz scaling scheme [69, 70], which exploits the analogy to the Coulomb gas, to the bi-layer system. Up to an additional factor $q(R)$ describing the particular screening properties of the bi-layer system, the scaling equations take the usual form (see Appendix A),

$$\begin{aligned} \partial_l K^{-1}(l) &= 4\pi^3 q(l)\, y^2(l), \\ \partial_l y(l) &= [2 - \pi q(l) K(l)]\, y(l), \end{aligned} \tag{4.5}$$

where $l = \ln(R/\xi)$. The auxiliary function $y(R)$ is the renormalised vortex fugacity at the distance R. Integrating the second equation of (4.5), we obtain the expression

$$y(R) = y_0 \Big(\frac{R}{\xi}\Big)^2 \exp\Big[-\pi \int_{\xi}^{R} \frac{K(R')q(R')}{R'} dR'\Big], \tag{4.6}$$

where $y^2(R)$ is the number of vortex–anti-vortex pairs of extension R in a system of linear size R. Here, $y(\xi) = y_0 = \exp(-E_c/T)$ is the fugacity due to the vortex core with energy $E_c \sim \eta\varepsilon_0 d$ and η is a number of order unity. By estimating the condensation energy lost in the vortex core we obtain the value $\eta = 0.38$, cf. Appendix B. A real space RG analysis of the vortex partition function makes the approximations in (4.5) more explicit (see Appendix A.2): integrating out small vortex pairs of (log)-size $[l, l + \delta l]$, the renormalized interaction involves a new shape function $q_l(R)$. However, in order to close the RG scheme, we have to neglect the new terms $\propto \partial_R q$ and approximate $\nabla^2 V_l(R) = 2\pi[q_l(\xi_l)\delta^{(2)}(R) + \partial_R q_l(R)/2\pi R] \approx 2\pi q_l(\xi_l)\delta^{(2)}(R)$. This approximation then preserves the shape of the function $q_l(R)$, $q_l(R) = q(R)K_l/K_0$, yielding the recursion relations Eqs. (4.5) as a final result. The above approximation is unproblematic at the critical point $T_{\mathrm{BKT}}^{(2)} = \tilde{\varepsilon}_0 d/4$ where large (half-flux) vortex pairs unbind. On the other hand, corrections may become relevant near the crossover temperature $T_{\mathrm{BKT}}^{x} = \tilde{\varepsilon}_0 d/2$: the results describing the crossover in the unbinding of 'half-charged'- and 'fully-charged' vortices at λ_{eff} should be considered as an interpolation only. In the following, we proceed with the analysis of the flow equations (4.5).

Conventional Kosterlitz scaling

Assuming a constant $q = 1$ (i.e., ignoring transverse screening), the usual Kosterlitz scaling equations produce the well known RG flow shown in the upper graph of Fig. 4.5. The temperature T defines a starting point for the flow on the line $y_0 = \exp(-\pi\eta K_0)$ through the temperature dependence of $K_0 = \varepsilon_0 d/\pi T$. At low temperatures the flow approaches the line of fixed points $y = 0$ with $K \to \bar{K}$ describing the superfluid density at large distances. At high temperatures the lines escape to $K = 0$ and high fugacity, describing a normal state with free vortices. The transition between these two regimes takes place at the universal value of the (renormalised) superfluid density $K_c^x = 2/\pi$; the corresponding transition temperature $T_{\mathrm{BKT}}^x = \tilde{\varepsilon}_0 d/2$ has to account for the renormalization in the line energy $\tilde{\varepsilon}_0$. Introducing the difference variable $x_1 = 2 - \pi K$ close to the critical point, the scaling equations become

$$\begin{aligned} \partial_l x_1(l) &= 4\pi^2 \, y^2(l)[2 - x_1(l)]^2 \approx 16\pi^2 \, y^2(l), \\ \partial_l y(l) &= x_1(l) y(l). \end{aligned} \tag{4.7}$$

Multiplying the first equation by $x_1(l)$ and the second by $y(l)$ and taking their difference, one obtains

$$\partial_l[16\pi^2 y^2(l) - x_1^2(l)] = 0. \tag{4.8}$$

Integrating this expression over l, one finds scaling trajectories in the form of hyperbolae $16\pi^2 y^2 - x_1^2 = c_0$. The parameter c_0 is the integration constant, its value depends on the starting point for the flow and, thus, on temperature. Away from the critical point the hyperbolae approach the asymptotics $16\pi^2 y^2 = x_1^2$, i.e., $4\pi^2 y^2 = (2K^{-1}/\pi - 1)^2$. Close to the critical point, we can distinguish three different kinds of trajectories, see Fig. 4.5: *i)* collapsing semi-hyperbolae, $x = -\sqrt{16\pi^2 y^2 - c_0}$, with $c_0 < 0$ *ii)* diverging full hyperbolae, $4\pi y = \sqrt{x^2 + c_0}$, with $c_0 > 0$ and *iii)* diverging semi-hyperbolae, $x = +\sqrt{16\pi^2 y^2 - c_0}$, with $c_0 < 0$.

The trajectories which follow the collapsing semi-hyperbolae converge on the line of fixed points and describe a state with a finite effective superfluid density. On the other hand, the diverging hyperbolae escape towards $K = 0$, describing a normal state. The typical length $\xi_{\mathrm{KT}} = \xi \exp(l_{\mathrm{KT}})$ at which free vortices are present (correlation length) is related to the distance at which the fugacity assumes a value of order unity. Close to the critical transition

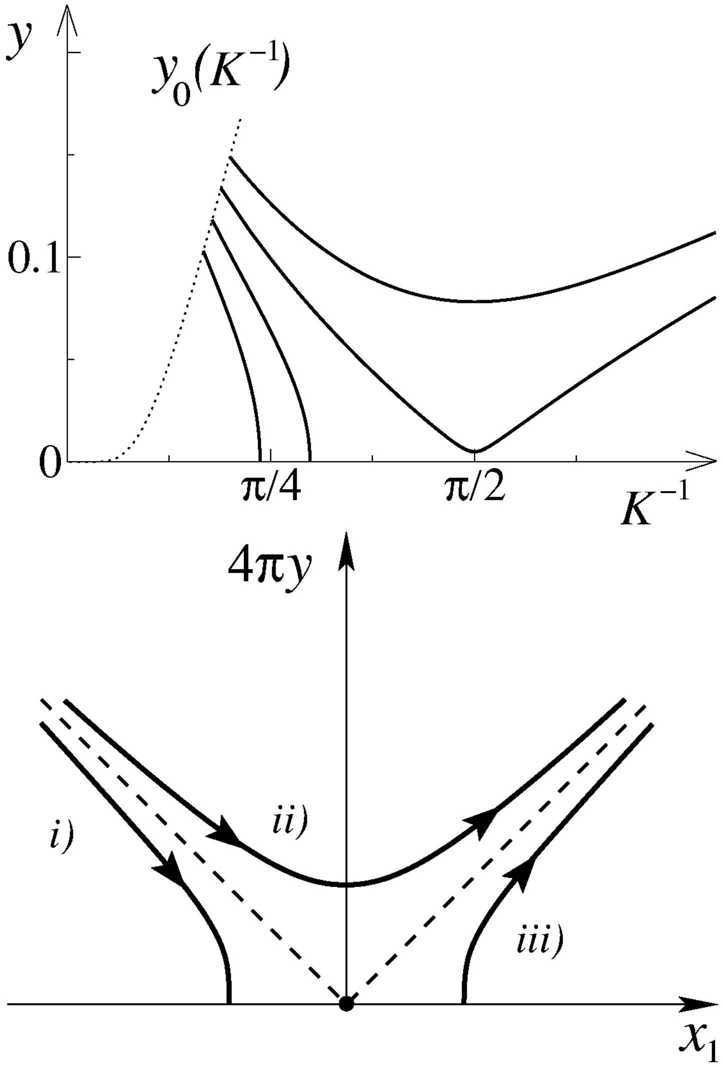

Figure 4.5: Upper graph: numerical solution of the RG flow trajectories for a conventional KT scenario ($q = 1$). The critical point is at $K_c^x = 2/\pi$. The dotted line corresponds to the possible initial points $y_0 = \exp(-0.38\pi/K_0^{-1})$, with $\eta = 0.38$ (see text and Appendix B). Trajectories which remain below $[K_c^x]^{-1}$ converge towards $y = 0$ and $K \to \bar{K}$. At high temperatures the lines escape to $K = 0$ and high fugacity, describing a normal state with free vortices. Lower graph: sketch of the trajectories close to the critical point $K_c^x = 2/\pi$, $16\pi^2y^2 - x_1^2 = c_0$, with $x_1 = 2 - \pi K$. We can distinguish three different kinds of trajectories: *i)* collapsing semi-hyperbolae, $x = -\sqrt{16\pi^2y^2 - c_0}$, with $c_0 < 0$ *ii)* diverging full hyperbolae, $4\pi y = \sqrt{x^2 + c_0}$, with $c_0 > 0$ and *iii)* diverging semi-hyperbolae, $x = +\sqrt{16\pi^2y^2 - c_0}$, with $c_0 < 0$.

temperature the parameter c_0 is small $c_0 \ll 1$. Combining the first equation in (4.7) with the expression defining the hyperbolic trajectory, one obtains

$$l_{\mathrm{BKT}} = \int_{x_1(0)}^{16\pi^2 - c_0} \frac{dx_1}{16\pi^2 y^2} \approx \int_{-\infty}^{+\infty} \frac{dx_1}{x_1^2 + c_0} = \sqrt{\frac{\pi}{c_0}}, \tag{4.9}$$

where in the evaluation of the integral we have extended the integral to the whole axis, since the main contribution comes from the vicinity of the critical point, i.e., from $x_1^2 \lesssim c_0$. For temperatures close to the critical temperature T^x_{BKT}, one can expand $c_0 \sim (T - T^x_{\mathrm{BKT}})/T^x_{\mathrm{BKT}}$ and one obtains the temperature dependence of the correlation length $\xi_{\mathrm{BKT}}(T) \sim \xi \exp[1/\sqrt{(T - T^x_{\mathrm{BKT}})/T^x_{\mathrm{BKT}}}]$. Critical fluctuations close T^x_{BKT} produce a correlation length which exhibits a non-analytical dependence on temperature. Beside the collapsing semi-hyperbolae and and the diverging full-hyperbolae which we have just discussed, also the diverging semi-infinite hyperbolae (cf. lines *iii)* in Fig. 4.5) are possible trajectories of the RG flow in the vicinity of the critical point. They are symmetric to the collapsing semi-hyperbolae, but their flow is towards the $y \to \infty$ fixed point rather than towards $y = 0$. These lines do not enter in the description of a standard BKT transition, which is analyzed only by means of the collapsing semi-hyperbolae and the diverging full-hyperbolae. However, trajectories which follow the diverging semi-hyperbolae become important in the analysis of the bi-layer system and describe the unbinding of half-flux vortices for a wide range of temperatures (see below).

Description of the RG flow

Accounting for the non-trivial screening properties in the bi-layer as described by the screening factor $q(l)$, the flow lines are modified as shown in Fig. 4.6 (cf. also Ref. [68] for an RG analysis of the transition in a superconducting film accounting for transverse screening). A new transition appears at the universal value of the (renormalised) superfluid density $K_c^{(2)} = 4/\pi$, corresponding to a transition temperature $T^{(2)}_{\mathrm{BKT}}$. For temperatures lower than the critical value $T^{(2)}_{\mathrm{BKT}}$, i.e., for trajectories with K^{-1} remaining below $[K_c^{(2)}]^{-1} = \pi/4$, the flow coincides with the standard one for $q = 1$, with the fugacity $y \to 0$, see line (a) in Fig. 4.6; we can ignore the small modifications appearing beyond the screening length λ_{eff}. At high temperatures $T > T^{(2)}_{\mathrm{BKT}}$, the flow first follows the $q = 1$ trajectory until screening reduces the interaction between vortices to half its value at λ_{eff}. The flow then turns

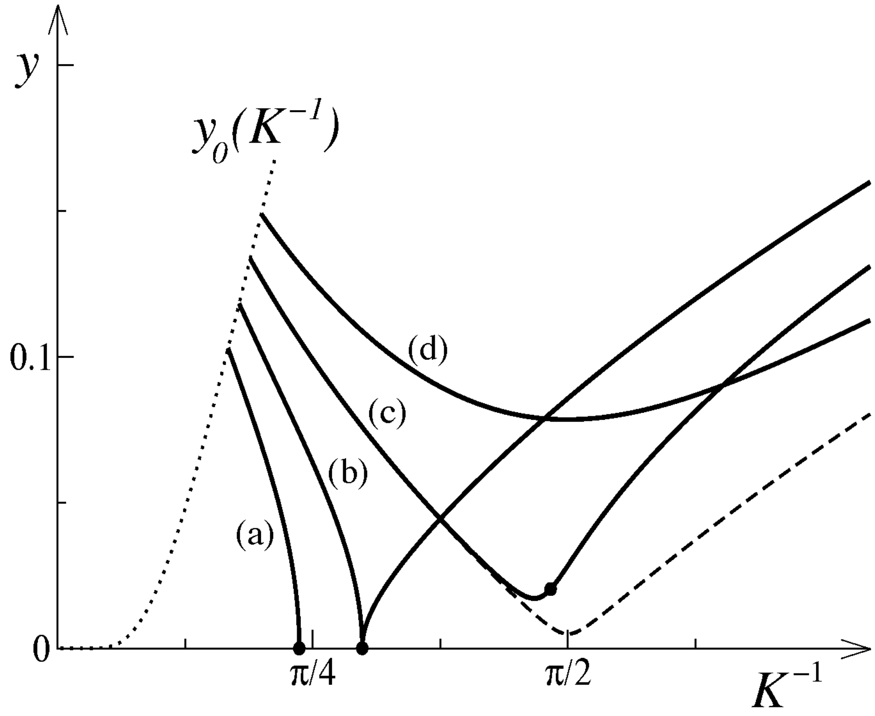

Figure 4.6: RG flow for the bi-layer system with $\lambda_{\text{eff}}/\xi = 10^{2.5}$, and $\eta = 0.38$ (see Appendix B), restricting the possible initial points to the line $y_0 = \exp(-0.38\pi/K_0^{-1})$. The critical point is located at $K_c^{(2)} = 4/\pi$. Scaling trajectories first follow the conventional flow with $q = 1$ until screening reduces the 'charge' to a value 1/2 at the scale λ_{eff} (marked with a bullet). At low temperatures, 'half-charged' vortex pairs remain bound and the fugacity y flows to zero, while the superconducting density K renormalizes to $\bar{K} > 4/\pi$. For temperatures $T > T_{\text{BKT}}^{(2)}$ vortex-pairs unbind ($y \to \infty$, $K \to 0$) following the scaling trajectories associated with 'half-charged' vortices ($q = 1/2$). The dashed lines describe the flow trajectories with $q = 1$. While for the trajectories (a), (b), and (d) these lines are not visible because they are masked by the RG flow with the full function $q(l)$ (solid lines), for (c) the two trajectories split (for this line the correlation length is of the same order of the effective penetration depth, $\xi_{\text{hf}} \sim \lambda_{\text{eff}}$).

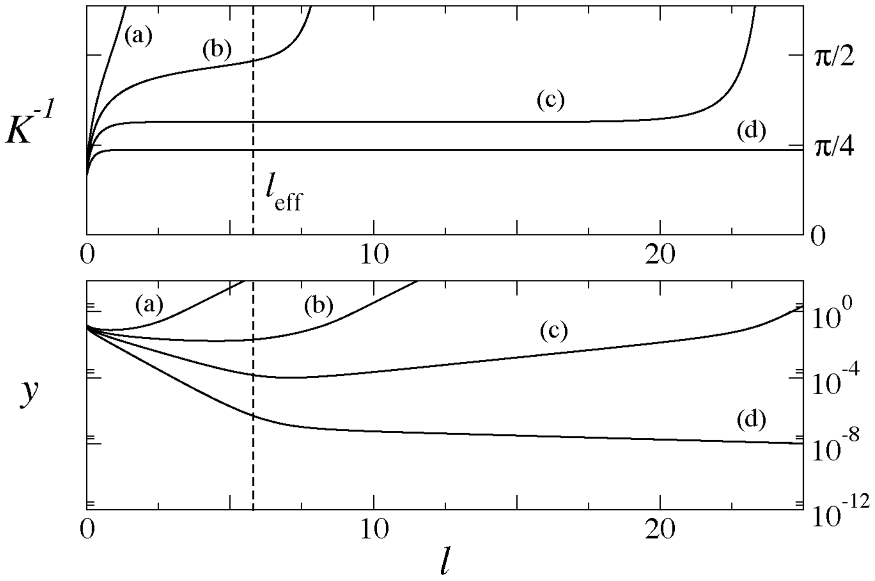

Figure 4.7: Numerical solution of (4.5) for different initial values (K_0^{-1}, y_0), (d) below $T_{\text{BKT}}^{(2)}$, (c) and (b) above $T_{\text{BKT}}^{(2)}$, and (a) above T_{BKT}^{x}. Note the linear dependence of $y(l)$ and the extended plateaux for K^{-1}, justifying the two-stage RG procedure with a restart at $(\bar{K}^{-1}, \bar{y})$. The change in slope (from $2 - \pi\bar{K}$ to $2 - \pi\bar{K}/2$) appearing in $y(l)$ is located at the scale l_{eff}, where half of the 'charge' is stripped.

around to follow the trajectory describing free 'half-charged' vortices above the unbinding transition at $T_{\text{BKT}}^{(2)}$, see line (b) in Fig. 4.6. Finally, at higher temperatures $T > T_{\text{BKT}}^{x}$ (corresponding to $K_c^x = 2/\pi$) the trajectories diverge along the conventional ones with $q = 1$, see line (d) in Fig. 4.6. The screening length λ_{eff} introduces a scale in the problem, producing a different behavior at short and large scales and allowing trajectories associated with different values of q to cross, see, e.g., lines (c) and (d) in Fig. 4.6.

'Full-charged' vortices, $l < l_{\text{eff}}$

For a quantitative analysis we approximate the flows in the two regimes: for $l < l_{\text{eff}} \equiv \ln(\lambda_{\text{eff}}/\xi)$ we replace $q(l)$ with the constant $q = 1$ ('full-charged' vortices) and for $l > l_{\text{eff}}$ with $q = 1/2$ and combine them afterwards, see Fig. 4.8. Analytical estimates (see below) and numerical integration of the full flow equations (cf. Fig. 4.7) confirm the validity of this approximation scheme for temperatures $T < T_{\text{BKT}}^{x}$.

Integrating the flow equations (4.5), the superconducting density K first undergoes a (small) renormalization (on the scale $l_r = 1/(\pi K - 2)$), while the fugacity y collapses. Sufficiently below T^x_{BKT}, this transitory regime extends over a short scale $l_r \ll l_{\mathrm{eff}}$. Beyond l_r the fugacity is small and from the first equation in (4.5) we obtain that the superfluid density assumes a constant value $K(l_{\mathrm{eff}}) \approx K^{\infty}_{q=1} \equiv \bar{K}$. The value of the renormalised fugacity is estimated with the help of the second equation in (4.5)

$$\partial_l y(l) = \left[2 - \pi\bar{K}\right] y(l). \tag{4.10}$$

From the integral of this equation we find the new starting point $(\bar{K}^{-1}, \bar{y} = y(\lambda_{\mathrm{eff}}))$ at the scale λ_{eff}, where

$$\bar{y} \approx y_0 \Big(\frac{\xi}{\lambda_{\mathrm{eff}}}\Big)^{\pi\bar{K}-2}. \tag{4.11}$$

Rewriting (4.11) in the form $\bar{y} = y_0(\lambda_{\mathrm{eff}}/\xi)^2 \exp[-E(\lambda_{\mathrm{eff}})/T]$ and comparing with (4.6) then tells us that vortices acquire an additional self-energy $E(\lambda_{\mathrm{eff}}) = \tilde{\varepsilon}_0 d \ln(\lambda_{\mathrm{eff}}/\xi) \gg E_c$ from the kinetic energy of supercurrents.

'Half-charged' vortices, $l > l_{\mathrm{eff}}$: 1) mean field regime

Second, we restart the flow at $(\bar{K}^{-1}, \bar{y})$ using (4.5) with $q = 1/2$. Following step by step the analysis of Eqs. (4.7) and (4.8), we obtain that the trajectories close to the critical point $(K^{(2)}_c = \pi/4, 0)$ correspond to the family of hyperbolae

$$(2\pi y)^2 - (4/\pi K - 1)^2 = c. \tag{4.12}$$

At low temperatures $T < T^{(2)}_{\mathrm{BKT}}$ the factor $2 - \pi\bar{K}/2 < 0$ and the fugacity y continues to decrease, hence 'half-charge' vortices remain bound, cf. line (a) in Fig. 4.8. The flow line passing through $(\pi/4, 0)$ (dashed-dotted in Fig. 4.8 with $(2\pi y)^2 = (4/\pi K - 1)^2$) defines the critical temperature $T^{(2)}_{\mathrm{BKT}}$. On this line the flows of full- and 'half-charged' vortices join at the point $([\bar{K}^{(2)}]^{-1}, \bar{y}^{(2)} \approx y_0(\xi/\lambda_{\mathrm{eff}})^2)$, where $[\bar{K}^{(2)}]^{-1} = \pi/4 - \pi^2\bar{y}^{(2)}/2$. Above $T^{(2)}_{\mathrm{BKT}}$, the $q = 1/2$ lines diverge towards $K^{-1} \to \infty$ and describe the collapse of the superfluid density. The typical scale $\xi_{\mathrm{hf}} = \xi \exp(l_{\mathrm{hf}})$ where free half-flux appear then is related (cf. Eqs. (4.5)) with the distance at which the renormalised fugacity assumes a value of order unity.

Above but close to the transition temperature $T^{(2)}_{\mathrm{BKT}}$, the correlation length ξ_{hf} of the system derives from the integration of the diverging full hyperbolae between the two separatrixes (cf. line (b) in Fig. 4.8) and (line *ii)* in the lower graph of Fig. 4.5). In this regime the trajectory is directly influenced by the critical point ($K_c^{(2)} = \pi/4, 0$). However, this critical regime is very narrow, $|4/\pi\bar{K} - 1| < 2\pi\bar{y}^{(2)}$, since $\bar{y}^{(2)} \ll 1$ (anyhow, we will analyze this regime below).

Away from this narrow critical regime, i.e., for temperatures corresponding to $4/\pi\bar{K} - 1 \gg 2\pi\bar{y}$ (line (c) in Fig. 4.8) the flow is not affected by the critical fluctuations at $\pi/4$, but is rather described by the diverging semi-hyperbolae (cf. lines *iii)* in lower graph in Fig. 4.5) which yield a mean-field type unbinding of the half-flux vortices. Integrating (4.5) from ($\bar{K}^{-1} > \pi/4, \bar{y}$) with a constant value for $K = \bar{K}$ we obtain the fugacity (see Fig. 4.7)

$$y(l) = \bar{y}\, \exp\Big[(2 - \pi\bar{K}/2)(l - l_{\rm eff})\Big] \tag{4.13}$$

(the same result follows from integrating $y(l)$ with the $q(l)$ as given by (4.3), $y(l) = y_0 \exp[2l - \pi\bar{K}\int_0^l dl' q(l')$). Using (4.13) with $y(l_{\rm hf}) \sim 1$, we find the correlation scale [71, 72]

$$l_{\rm hf} \approx l_{\rm eff} - \frac{2}{4 - \pi\bar{K}} \log \bar{y} \tag{4.14}$$

and combining this result with (4.11), we obtain the density $n_{\rm hf} \sim 1/\xi_{\rm hf}^2$ of free half-flux vortices

$$n_{\rm hf} \approx \frac{1}{\xi^2}\Big(\frac{\xi y_0^{2/\pi\bar{K}}}{\lambda_{\rm eff}}\Big)^{\frac{2\pi\bar{K}}{4-\pi\bar{K}}}. \tag{4.15}$$

Summarizing, we find that the density of free $q = 1/2$ vortices at the transition temperature $T_{\rm BKT}^{(2)}$ (and below $T_{\rm BKT}^{x}$) is low, a consequence of the small parameter $\xi/\lambda_{\rm eff}$. Moreover, critical fluctuations are only relevant very close to the critical temperature. Away from this narrow critical regime the transition is well described by the mean-field expression (4.15). On approaching $T_{\rm BKT}^{x}$ we have $\bar{K} = 2/\pi$ and the correlation length becomes comparable to the screening length, cf. (4.15).

In order to express the above results in terms of the temperature deviation $\Delta t = (T - T_{\rm BKT}^{(2)})/T_{\rm BKT}^{(2)}$, we have to establish the connection $\bar{K}(T)$. We define the new variable $x_2(T) = 2 - \pi\bar{K}(T)/2$ and write $x_2(T) \approx [2 - \pi\bar{K}^{(2)}/2] + a_2\Delta t$ with the coefficient a_2 of order unity whose precise value depends on the core energy $E_c = \eta\varepsilon_0 d$. Within the mean-field regime at temperatures larger than $\Delta t \gg 8\pi\bar{y}^{(2)}/a_2$ the corresponding result reads (cf. (4.15), we approximate

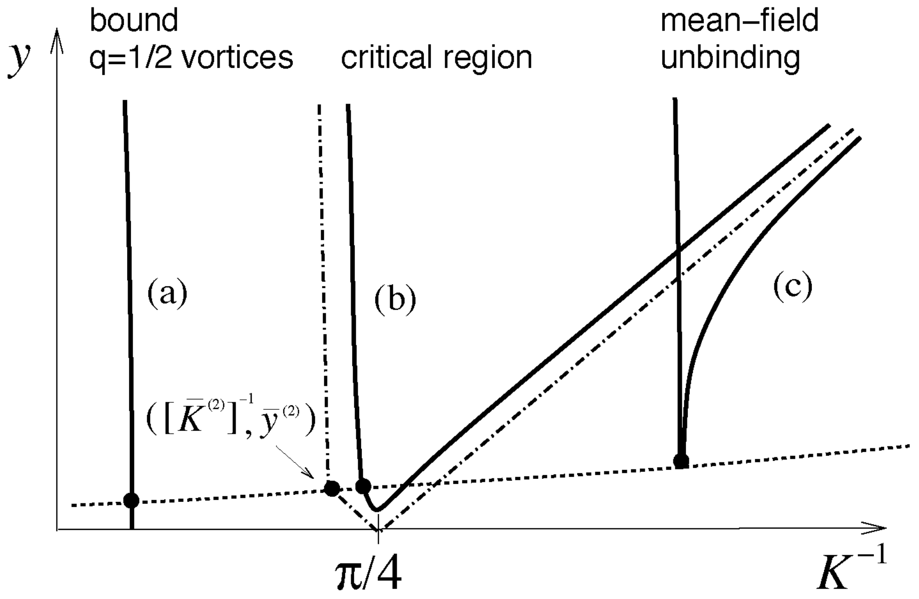

Figure 4.8: Sketch of the RG flow close to the critical point $K_c^{(2)} = 4/\pi$. The dotted line represents the renormalised values $(\bar{K}^{-1}, \bar{y})$ evaluated at the screening length λ_{eff} where half of the 'charge' is stripped. At this location the flow lines for $l < l_{\text{eff}}$ with $q = 1$ change over to those for 'half-charge' vortices valid at large distances $l > l_{\text{eff}}$. Pancake-vortices remain bound at low temperatures with $K^{-1} < \pi/4$, see curve (a). In the critical region near $K_c^{(2)}$ the trajectory follows hyperbolae with $(2\pi y)^2 - (4/\pi K - 1)^2 = c > 0$, see (b), while K flows to zero along trajectories with $c < 0$ when vortices have lost half of their charge, see (c). The dashed-dotted line marks the separatrix with $c = 0$. The point $([\bar{K}^{(2)}]^{-1}, \bar{y}^{(2)})$ defines the critical temperature $T_{\text{BKT}}^{(2)}$. The plot is largely magnified for illustrative reasons.

$2 - \pi\bar{K}^{(2)}/2 = -4\pi\bar{y}^{(2)} \approx 0$ and thus $x_2(T) \approx a_2\Delta t$)

$$n_{\rm hf}(T) \approx \frac{\lambda_{\rm eff}^2}{\xi^4}\Big(\frac{\xi\sqrt{y_0}}{\lambda_{\rm eff}}\Big)^{4/a_2\Delta t}. \tag{4.16}$$

Finally, we comment on the effect of fluctuating pairs on the screening function $q(R)$: thermally activated vortex–anti-vortex pairs modify the screening properties of the superconducting layers, changing the penetration depth $\lambda_{\rm eff}$. Below $T^x_{\rm BKT}$, the renormalised value $\bar{K}$ plays the role of the effective superfluid stiffness at distances shorter than the correlation length $\xi_{\rm hf} > \lambda_{\rm eff}$, see Fig. 4.7. Substituting $\lambda_{\rm eff} \to (K_0/\bar{K})\lambda_{\rm eff}$ we can account for the modification of screening due to vortex–anti-vortex pairs.

‘Half-charged’ vortices, $l > l_{\rm eff}$: 2) critical regime

The unbinding of ‘half-charge’ vortices just above $T^{(2)}_{\rm BKT}$ is described by the hyperbolae $(2\pi y)^2 - (4/\pi K - 1)^2 = c$. Above but close to the transition temperature $T^{(2)}_{\rm BKT}$, the correlation length $\xi_{\rm hf}$ of the system derives from the integration of the hyperbolic solution and follows the standard critical KT behavior with $l_{\rm hf} \sim l_{\rm eff} + \pi/(2\sqrt{|c|})$, cf. Eq. (4.9). This critical behavior of the correlation length is restricted to the narrow regime where $|4/\pi\bar{K} - 1| < 2\pi\bar{y}^{(2)}$ close to the critical point (line (b) in Fig. 4.8); at the right boundary the correlation length assumes the value $\xi_{\rm hf} \sim \lambda_{\rm eff}\exp[1/(4\pi\bar{y}^{(2)})]$, a large value indeed (see Appendix A.3, where we analyze the crossover between the critical and the mean-field regimes). The narrowness of this critical regime is a consequence of the exponentially small value of the renormalised fugacity which strongly suppresses critical fluctuations.

In terms of the temperature variable we obtain a critical regime of width $\Delta t \sim 8\pi\bar{y}^{(2)}/a_2$ where the density of half-flux vortices is given by the standard expression

$$n_{\rm hf}(T) \approx \frac{1}{\lambda_{\rm eff}^2}\exp(-2\sqrt{b_2/\Delta t}) \tag{4.17}$$

with $b_2 = \pi/2\sqrt{2}\bar{y}^{(2)}a_2$. Therefore, the critical regime shows the standard behavior associated with a BKT transition. However, the large value of the (renormalized) fugacity restrict the regime of validity to a very narrow window of temperatures. The unbinding is then described within the the mean field unbinding (4.16), which exhibits a modified temperature dependence.

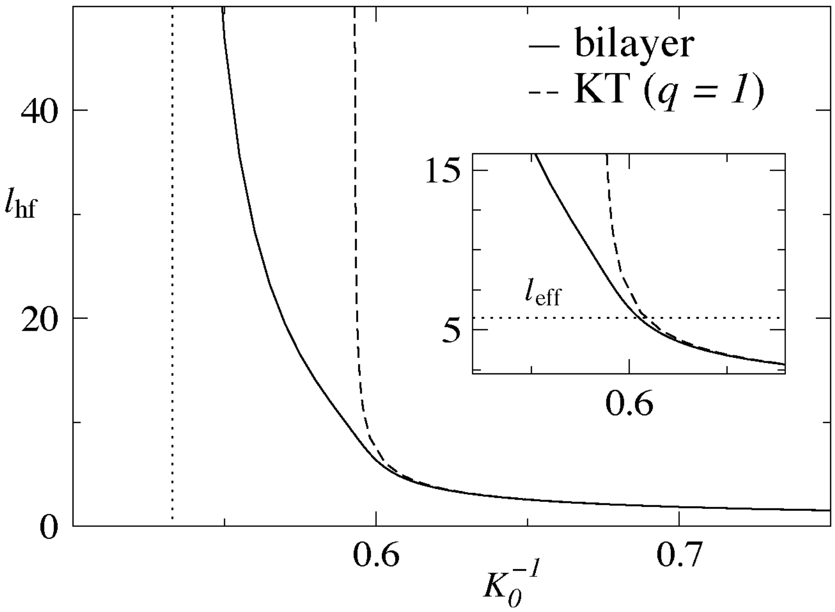

Figure 4.9: The correlation length $l_{\mathrm{hf}} = \ln(\xi_{\mathrm{hf}}/\xi)$ of the bi-layer system as a function of K_0^{-1}. The length has been extracted from the numerical solutions of (4.5) with initial values $(K_0^{-1}, y_0(K_0^{-1})) = (K_0^{-1}, \exp(-\eta\pi/K_0^{-1}))$, with $\eta = 0.38$, by imposing the condition $y(l_{\mathrm{hf}}) = 1$. The correlation length (bulk line) diverges on approaching the critical temperature of the by-layer system $T_{\mathrm{BKT}}^{(2)} = \tilde{\varepsilon}_0 d/4$ (dotted vertical line). The line interpolates between the mean-field unbinding of half-screened vortices (4.14) and the standard KT correlation length of an unscreened system (with constant $q = 1$) at large temperatures. The dashed line in the graph corresponds to the correlation length of the unscreened system, with a transition temperature $T_{\mathrm{BKT}}^{x} = \tilde{\varepsilon}_0 d/2$. The inset shows a close up of the larger graph for values of $\ell_{\mathrm{hf}} \sim \ell_{\mathrm{eff}}$, i.e., for temperatures around T_{BKT}^{x}. Note the linear dependence (4.18) on temperature of ℓ_{hf} below T_{BKT}^{x}.

‘Half-charged’ vortices, $l > l_{\text{eff}}$: 3) close to $T^x_{\text{BKT}} = \tilde{\varepsilon}_0 d/2$

At higher temperatures, close to but below $T^x_{\text{BKT}} = \tilde{\varepsilon}_0 d/2$, we reexpress the result (4.14) in terms of the new temperature difference $\Delta t_1 = (T - T^x_{\text{BKT}})/T^x_{\text{BKT}}$. Using the expansion $x_1(T) = 2 - \pi \bar{K}(T) \sim a_1 \Delta t_1$, we obtain the density of half-flux vortices

$$n_{\text{hf}}(T) \approx \frac{1}{\xi^2} y_0^{2+a_1|\Delta t_1|} \Big(\frac{\xi}{\lambda_{\text{eff}}}\Big)^{2+2a_1|\Delta t_1|}. \tag{4.18}$$

The result (4.18) is valid provided that the renormalised superfluid density K shows a broad plateau, i.e., as long as $l_{\text{eff}} \gg l_r$; this translates into a temperature regime $a_1 \Delta t_1 < -1/l_{\text{eff}}$. The half-flux vortex density at the upper edge of this regime assumes the value $n_{\text{hf}} \approx y_0^2/(e\lambda_{\text{eff}})^2$. At higher temperatures beyond T^x_{BKT} the correlation length first decreases till $\xi_{\text{hf}} < \lambda_{\text{eff}}$. For even higher temperatures the vortices unbind before losing their ‘charge’ and the half-flux vortex density is given by the standard expression

$$n_{\text{hf}}(T) \approx \frac{1}{\xi^2} \exp\Big(-2\sqrt{b_1/\Delta t_1}\Big), \tag{4.19}$$

where the constant b_1 relates to a_1 via $b_1 = \pi/8\bar{y}_1 a_1$ (here $\bar{y}_1 \approx 1/4\pi l_{\text{eff}}$ is the value of the fugacity on the separatrix). In experiments on thin superconducting films [51, 52] typical values $b_1 \sim 2 - 16$ have been found. The validity of (4.19) extends down to temperatures for which $\xi_{\text{hf}} \sim \lambda_{\text{eff}}$ which translates into deviations $a_1 \Delta t_1 \geq \pi^2/2l_{\text{eff}}$. This leaves us with a narrow temperature window $|\Delta t_1| < 1/a_1 l_{\text{eff}}$ for which we cannot provide a simple and accurate expression for the density of half-flux vortices. We note that in this problematic regime, magnetic screening and vortex unbinding occur at the same scale and the scaling equations (4.5) are only approximately valid.

4.3.2 Vortex stacks and their evaporation

Thermally activated stacks, i.e., bound pairs of half-flux vortices residing in different layers, preempt the superconducting phase transition of the bi-layer system at $T^{(2)}_{\text{BKT}}$. Given the large self-energy $E_s = 2E_c + 2\varepsilon_0 d \ln(\lambda_{\text{eff}}/\xi)$ of a vortex stack, the transition at $T = 0$ is a very weak one, with only few stacks present at finite temperature. Accounting for renormalisation due to bound half-flux vortex pairs, we obtain the stack density

$$n_{\text{s}} = \frac{1}{\xi^2} e^{-\tilde{E}_s/T} \approx \frac{1}{\xi^2} \Big(\frac{\xi y_0^{1/\pi \bar{K}}}{\lambda_{\text{eff}}}\Big)^{2\pi \bar{K}}, \tag{4.20}$$

where $\tilde{E}_s$ denotes the properly renormalized self-energy. The stack density (4.20) determines the correlation length $\xi_\mathrm{s} \sim 1/\sqrt{n_\mathrm{s}}$ beyond which superconductivity is lost in the bi-layer system. However, superconductivity is still preserved within the individual layers, as stacks do not screen the interaction between pancake vortices; indeed, considering the force of a pancake vortex acting on a straight stack we find it to vanish rapidly beyond the effective screening length λ_eff. This is easily understood from the force expression (2.32) (together with (2.64) and (2.71)): while the pancake vortices in the same layer repel with a force $\propto (1 - \Phi(R)/\Phi_0)$, the second pancake vortex in the stack is attracted with a force $\propto -\Phi(R)/\Phi_0$. Beyond λ_eff the trapped flux equals $\Phi_\mathrm{t} = \Phi_0/2$ and the forces compensate. The same argument applies to a system of $N < \lambda/d$ layers, where the stack vortex residing in the same layer as the pancake vortex experiences a repulsive force $\propto (1 - 1/N)$, while the $N-1$ other vortices in the stack are attracted with a force $\propto 1/N$. Also, this is consistent with the bulk situation, where a single pancake vortex does not drive a vortex stack beyond the scale λ. Hence, individual pancake vortices in a layer do not move stacks at distances beyond λ_eff and there is no screening due to stacks.

Let us next study the thermodynamics of individual stacks in the bi-layer setup. The interaction between the two half-flux vortices constituting the stacks is due to screening currents induced in the opposite layer [73, 74]. As compared to the intra-planar interaction, the inter-plane interaction misses the singular phase term driving the current density and hence the force is due to the induced flux $\Phi(R)/\Phi_0 = [1 - q(R)]$ alone, thus leading to the interaction potential (cf. Eq. (4.4))

$$\tilde{V}_{\mathrm{p-p}}(R) = 2\pi T \int_\xi^R \frac{[1 - q(R')]K(R')}{R'} dR'. \tag{4.21}$$

In (4.21) we have assumed that $A(R, d) = A(R, 0)$ since the magnetic field escaping in between the two planes is of order d/λ. Note the slow growth of the potential $\tilde{V}_{\mathrm{p-p}}$ at small distances $R \ll \lambda_\mathrm{eff}$ which goes over into a strong logarithmic attraction between half-flux vortices at large distances. Hence the long-distance interaction between half-flux vortices constituting a stack is identical to the logarithmic interaction between half-flux vortex–anti-vortex pairs in individual layers; the unbinding of the latter at $T_\mathrm{BKT}^{(2)}$ is equivalent to the evaporation of the former [5].

Although vortex stacks do not destroy superconductivity in the individual layers of the bi-layer structure, they do contribute to the downward renormalization of the superfluid stiffness K. Similar to half-flux vortex–anti-vortex pairs in individual layers, the thermal fluctuations of stacks generate dipoles screening the interaction between other vortices; pairs separated by a distance R correspond to stacks misaligned by R and contribute to the screening on scales larger then R. Accounting for the polarizability of stacks in the derivation of the RG equations, we obtain the modified set (see Appendix A)

$$\begin{aligned}
\partial_l K^{-1}(l) &= 4\pi^3 y^2(l) q(l) + 4\pi^3 y_{\mathrm{s}}^2(l) q(l), \\
\partial_l y(l) &= [2 - \pi q(l) K(l)]\, y(l), \\
\partial_l y_{\mathrm{s}}(l) &= \{2 - \pi[1 - q(l)] K(l)\}\, y_{\mathrm{s}}(l),
\end{aligned} \tag{4.22}$$

where $y_{\mathrm{s}}(l)$ is the fugacity of a vortex in a stack displaced a distance $R = \xi \exp(l)$ from its partner vortex in the opposite layer. Such distorted stacks contribute a dipole moment equal to the one of vortex pairs with separation R and thus contribute equally to the renormalization of the superfluid density K (cf. (4.22)). Note the different screening factors $q(l)$ and $[1 - q(l)]$ in the equations for the pair- and stack-fugacities $\partial_l y$ and $\partial_l y_{\mathrm{s}}$ accounting for the different interactions $\tilde{V}$ and $\tilde{V}_{\mathrm{p-p}}$, cf. Eqs. (4.4) and (4.21).

The density of vortex stacks is small due to their large self energy E_{s}, hence the fugacity y_{s} starts out with a small value

$$y_{\mathrm{s}}(0) = e^{-\tilde{E}_{\mathrm{s}}/2T} = y_0 \Big(\frac{\xi}{\lambda_{\mathrm{eff}}}\Big)^{\pi \bar{K}}, \tag{4.23}$$

and thus its effect on the flow of K^{-1} is negligible at small scales. Assuming $K^{-1} < \pi/2$, y renormalizes downward with increasing l, while $y_{\mathrm{s}}(l) \approx y_{\mathrm{s}}(0)\exp(2l)$ increases until both fugacities meet at the screening length λ_{eff}. At larger scales $l > l_{\mathrm{eff}}$, $q(l) \approx 1/2$ and the two fugacities flow in parallel with (we use $\bar{y} = y_{\mathrm{s}}(0)\exp(2l_{\mathrm{eff}})$, cf. (4.11) and (4.23), and assume a constant $K = \bar{K}$, cf. Fig. 4.7)

$$y(l) = y_{\mathrm{s}}(l) = \bar{y} e^{(2-\pi\bar{K}/2)(l-l_{\mathrm{eff}})}, \tag{4.24}$$

producing a twice larger renormalization of K^{-1}. Hence we find that stacks equally contribute to the renormalization of the superfluid density K at distances beyond λ_{eff}. Vortex stacks simply reduce the correlation length ξ_{hf} by a factor $2^{1/(4-\pi\bar{K})}$, weakly enhancing the vortex density, without modifying the nature of the unbinding transition at $T_{\mathrm{BKT}}^{(2)} = \tilde{\varepsilon}_0 d/4$.

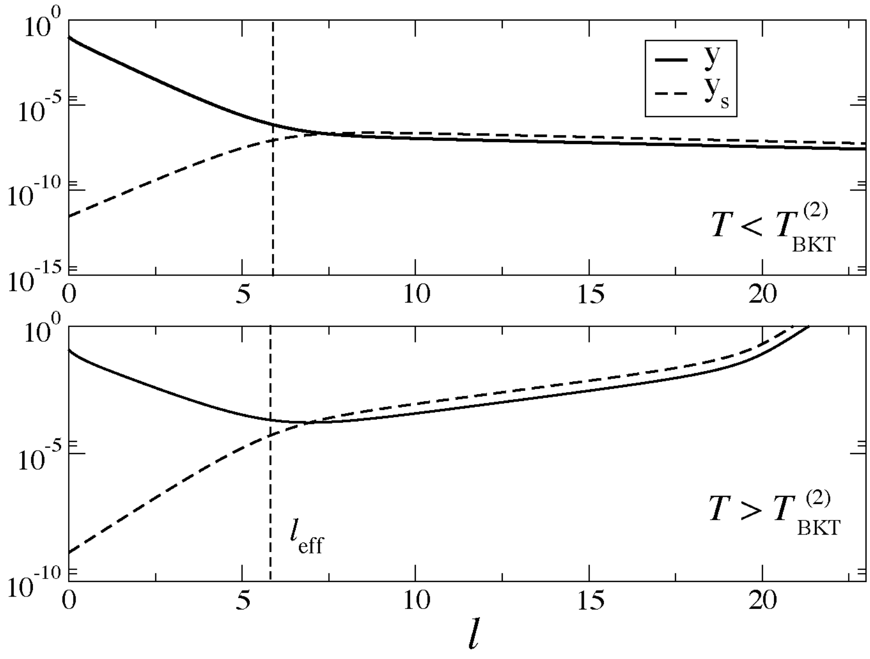

Figure 4.10: Numerical solution of (4.22) for two different initial values (K_0^{-1}, y_0) below (upper) and above (lower) the transition temperature $T^{(2)}_{\rm BKT}$; the two fugacities y_0 and $y_s(0)$ are related via Eq. (4.23). Note the linear dependence of $y(l)$ and the change in slope, from $2 - \pi\bar{K} < 0$ to $2 - \pi\bar{K}/2$ for y and from 2 to $2 - \pi\bar{K}/2$ for y_s, at the scale $l_{\rm eff}$, where the 'charge' is stripped.

4.3.3 Summary of the results of the analysis

We summarize here the main results of the renormalization group analysis, cf. Fig. 4.11. Thermally activated vortex stacks are present in the system at any finite temperature. However, their self-energy is large and their density is small, cf. the small factor $\xi/\lambda_{\rm eff}$ in (4.20). Hence, this $T = 0$ transition is a weak one. The effect of free vortex stacks is to destroy superconductivity in the composed system, by suppressing the stiffness of the double-layer system.

On the other hand, below $T^{(2)}_{\rm BKT} = \tilde{\varepsilon}_0 d/4$ the superconductivity in the individual layer is preserved. The effect of this remaining superfluid stiffness is reflected in the properties of sustaining counterflow currents without dissipating energy. In fact, under the action of opposite currents in the two layers the vortex stacks do not move and the superconductive response is preserved. Above the BKT temperature $T^{(2)}_{\rm BKT} = \tilde{\varepsilon}_0 d/4$ free 'half-charged'

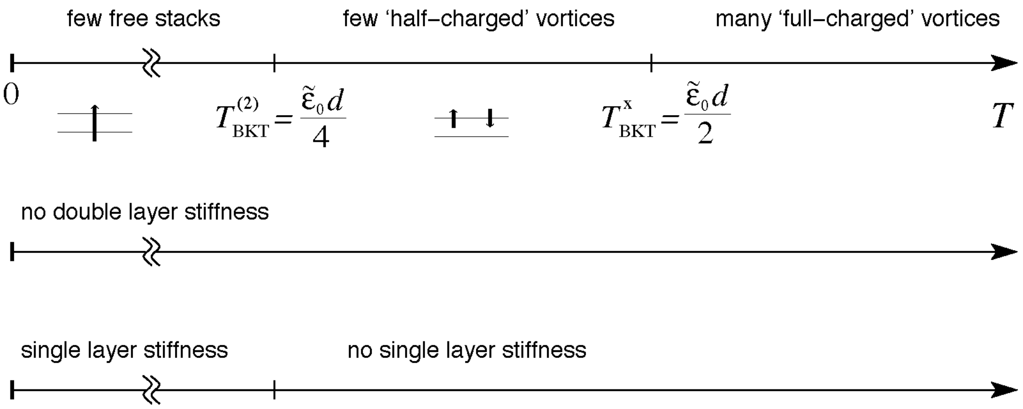
few free stacks
few 'half-charged' vortices
many 'full-charged' vortices
0
$T_{\mathrm{BKT}}^{(2)} = \frac{\tilde{\varepsilon}_0 d}{4}$
$T_{\mathrm{BKT}}^{x} = \frac{\tilde{\varepsilon}_0 d}{2}$
T
no double layer stiffness
single layer stiffness
no single layer stiffness

Figure 4.11: Phase diagram of the bi-layer system at zero external magnetic field. For temperatures between 0 and $\tilde{\varepsilon}_0 d/4$ only complete vortex stacks appear, suppressing superconductivity in the two layers together. Above $T_{\mathrm{BKT}}^{(2)} = \tilde{\varepsilon}_0 d/4$ half-flux vortices with $q = 1/2$ unbind, destroying the superconductivity in each layer alone. At the crossover transition temperature $\tilde{\varepsilon}_0 d/2$, vortices with $q = 1$ proliferate boosting the value of the linear resistance.

(i.e., half flux) vortices unbind. They suppress the single layer stiffness and destroy the counterflow superconducting response. However, also this transition is weak, since the half-flux vortices are characterized by a big magnetic 'core' and thus appear just above $T_{\mathrm{BKT}}^{(2)}$ with a low density, due to the small factor $\xi/\lambda_{\mathrm{eff}}$ in (4.15). Increasing the temperature above the crossover value $T_{\mathrm{BKT}}^{x} = \tilde{\varepsilon}_0 d/4$, vortices unbind on a scale smaller than the effective penetration depth λ_{eff}. Magnetic screening is therefore ineffective and 'full-charged' vortices proliferate in a large density in the system, cf. (4.19).

4.3.4 I-V characteristic

The presence of half-flux vortices can be traced in an experiment measuring the current-voltage characteristic. In the connected geometry of Fig. 4.3, the effect of an applied dc current is to stretch pairs and full vortex stacks, while the drag motion of complete vortex stacks is inhibited by the counterflow geometry. In the following, we proceed with an analysis of the current-induced unbinding of half-flux vortex pairs residing in one layer; the contribution from the evaporation of full vortex stacks is either smaller (at small distances) or equal to the one produced by the pair-unbinding in individual layers and does not modify the results of this section.

An applied dc sheet current $I = jd$ modifies the energy of the vortex–anti-vortex pairs in a individual layer,

$$U(R) = 2\pi \int_{\xi}^{R} \frac{K(R')q(R')}{R'}\, dR' - I\Phi_0 \frac{R}{c}. \tag{4.25}$$

Below the unbinding temperature $T^{(2)}_{\mathrm{BKT}}$, free half-flux vortices are created by thermal fluctuations once the pair overcomes the activation barrier

$$U_c \approx 2\tilde{\varepsilon}_0 d \begin{cases} \ln \dfrac{R_c}{\xi}, & R_c \ll \lambda_{\mathrm{eff}}, \\ \ln \dfrac{\lambda_{\mathrm{eff}}}{\xi} + \dfrac{1}{2} \ln \dfrac{R_c}{\lambda_{\mathrm{eff}}}, & R_c \gg \lambda_{\mathrm{eff}}, \end{cases}$$

where

$$R_c = \frac{I_0}{I} q(R_c)\, \xi \approx \frac{I_0}{I}\, \xi \tag{4.26}$$

is the distance at which the maximum of U_c occurs and $I_0 = 2\tilde{\varepsilon}_0 dc/\Phi_0\xi$ is the sheet depairing current (2.10), up to the factor $2/(3\sqrt{3})$. Applied currents smaller than

$$I_{\mathrm{eff}} = I_0 \frac{\xi}{\lambda_{\mathrm{eff}}}, \tag{4.27}$$

probe lengths larger than the magnetic length λ_{eff} and the effects of half-flux vortices become accessible.

The equilibrium density n_{hf} of free half-flux vortices is derived from the steady state solution of the rate equation [75]

$$\partial_t n_{\mathrm{hf}} = \Gamma - \frac{\xi^2}{\tau_{\mathrm{rec}}} n_{\mathrm{hf}}^2, \tag{4.28}$$

where $\Gamma \propto \exp(-U_c/T)$ is the production rate of free half-flux vortices and $\xi^2/\tau_{\mathrm{rec}}$ is the recombination parameter. The applied sheet current I drags the free half-flux vortices, resulting in a finite Bardeen-Stephen resistivity [49] $\rho = 2\pi\xi^2\rho_{\mathrm{n}} n_{\mathrm{hf}}$ scaling as

$$\rho \sim \rho_{\mathrm{n}} \begin{cases} \left(\dfrac{I_{\mathrm{eff}}}{I_0}\right)^{\pi\bar{K}} \left(\dfrac{I}{I_{\mathrm{eff}}}\right)^{\pi\bar{K}/2}, & I < I_{\mathrm{eff}}, \\ \left(\dfrac{I}{I_0}\right)^{\pi\bar{K}}, & I > I_{\mathrm{eff}}, \end{cases}$$

where ρ_n is the resistance of the normal state. The strong current dependence of the dissociated pair density then yields an algebraic I-V characteristic of the form

$$\frac{V}{V_0} \sim \Big(\frac{I}{I_0}\Big)^{\alpha(T,I)}, \tag{4.29}$$

with an exponent which depends on the temperature T and the driving sheet current I via

$$\alpha(T,I) = 1 + \pi \bar{K}(T) q(I). \tag{4.30}$$

The exponent α depends explicitly on the 'charge' associated with the vortices: at short scales, conventional $q = 1$ vortices are probed and $\alpha = 1 + \pi\bar{K}$. On the other hand, large distances probe 'charge' $q = 1/2$ vortices and the exponent α is reduced to $\alpha = 1 + \pi\bar{K}/2$. The crossover between these two regimes appears at the sheet current $I_\mathrm{eff} \ll I_0$ where the density of free half-flux vortices is already quite small, $n_\mathrm{hf} \sim 1/\lambda_\mathrm{eff}^2$ at $T_\mathrm{BKT}^x = \tilde{\varepsilon}_0 d/2$ and $n_\mathrm{hf} \sim \xi^2/\lambda_\mathrm{eff}^4$ at the true transition point $T_\mathrm{BKT}^{(2)} = \tilde{\varepsilon}_0 d/4$. At these two temperatures, the exponent α assumes the universal values 3 at T_BKT^x and large currents and 3(5) at $T_\mathrm{BKT}^{(2)}$ and small(large) currents.

The temperature $T_\mathrm{BKT}^{(2)}$ defines a resistive transition due to the proliferation of unbound free half-flux vortices. Above $T_\mathrm{BKT}^{(2)}$ the exponent α then jumps to unity for currents smaller than

$$I_\mathrm{hf} \approx I_0 \frac{\xi}{\xi_\mathrm{hf}}, \tag{4.31}$$

probing distances larger than the correlation length ξ_hf. The ohmic resistance at low currents is determined by the density of free half-flux vortices

$$\rho \approx \rho_\mathrm{n} \Big(\frac{\xi}{\xi_\mathrm{hf}}\Big)^2. \tag{4.32}$$

For larger currents the probing length is shorter than ξ_hf and pairs are still bound, resulting in an algebraic characteristic.

In the mean-field regime above $T_\mathrm{BKT}^{(2)}$ we can make use of (4.15) and find the location of the crossover at

$$I_\mathrm{hf} \approx I_0 \frac{\lambda_\mathrm{eff}}{\xi} \Big(\frac{\xi\sqrt{y_0}}{\lambda_\mathrm{eff}}\Big)^{2/a_2 \Delta t}, \tag{4.33}$$

as well as the temperature dependent resistivity

$$\rho(T) \approx \rho_\mathrm{n} \Big(\frac{\lambda_\mathrm{eff}}{\xi}\Big)^2 \Big(\frac{\xi\sqrt{y_0}}{\lambda_\mathrm{eff}}\Big)^{4/a_2 \Delta t}, \tag{4.34}$$

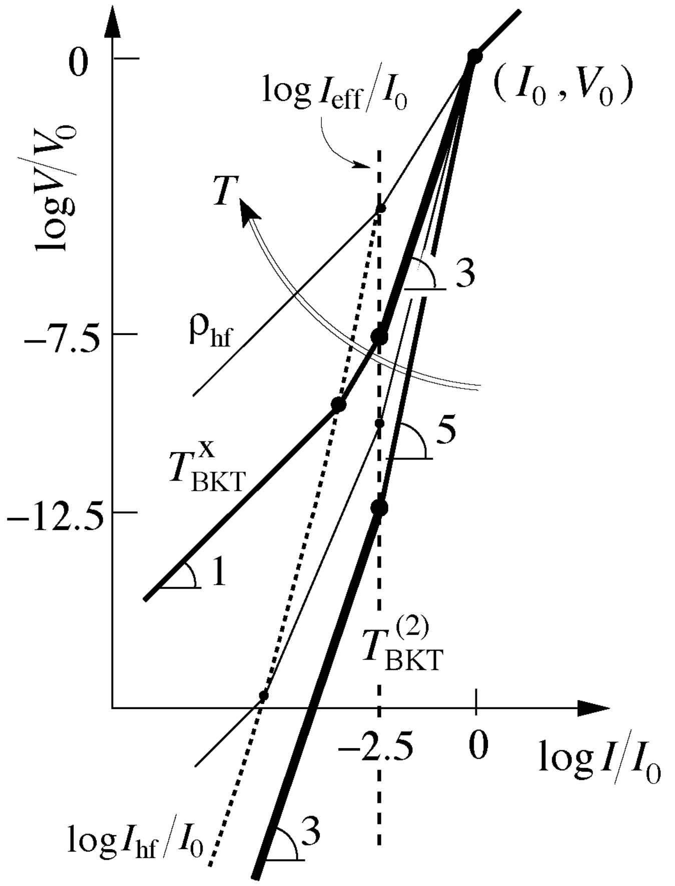

Figure 4.12: Qualitative sketch of the I-V characteristic. At low temperatures (right hand side) the voltage depends algebraically on the applied current with an exponent $\alpha > 3$, while the characteristic turns ohmic at high temperatures (left hand side). The regime close to the critical temperatures $T^x_{\rm BKT}$ and $T^{(2)}_{\rm BKT}$ contains the interesting features associated with half-flux vortices. The current scale $I_{\rm eff} \sim I_0(\xi/\lambda_{\rm eff})$ (vertical dashed line) separates the physics of conventional ($I > I_{\rm eff}$ probing lengths $R < \lambda_{\rm eff}$) from 'half-charged' vortices ($I < I_{\rm eff}$ probing lengths $R > \lambda_{\rm eff}$). At $T^{(2)}_{\rm BKT}$ the I-V curve exhibits the characteristic exponents 3 and 5 at small and large currents; the crossover from 5 to 3 traces the crossover from $q = 1$ conventional vortices to half-flux vortices with $q = 1/2$. At intermediate temperatures $T^{(2)}_{\rm BKT} < T < T^x_{\rm BKT}$ the slopes decrease and an additional ohmic regime due to free 'half-charged' vortices appears at low currents when distances beyond $\xi_{\rm hf}$ are probed (the dotted line marks the corresponding current $I_{\rm hf}$). At temperatures $T > T^x_{\rm BKT}$ the ohmic regime takes over and leaves only a small non-linear region at high currents probing conventional $q = 1$ vortices.

due to free 'half-charged' vortices. Hence the measurement of $I_{\rm hf}$ or ρ in this regime provides direct access to the correlation length $\xi_{\rm hf}$ and its mean-field like temperature dependence.

4.3.5 Experimental requirements

In order to observe the finite temperature BKT transition at $T_{\rm BKT}^{(2)}$, the system size must be larger than the effective penetration length $\lambda_{\rm eff}$, since only at this length the magnetic flux saturates to its value $\Phi_0/2$. Accounting for the temperature dependence of the penetration depth and using the relation (4.1) which fixes the jump in the superfluid density at the transition, we obtain [54]

$$\lambda_{\rm eff}(T_{\rm BKT}^{(2)}) \approx \frac{0.5\ {\rm cm}}{T_{\rm BKT}^{(2)}\ {\rm in\ K}}. \tag{4.35}$$

Hence, a typical value for low $T_{\rm c}$ materials is $\lambda_{\rm eff} \approx 1{\rm mm}$, whereas it is reduced by an order of magnitude in high $T_{\rm c}$ superconductors. The largeness of this transverse screening length is the major and most critical hurdle against the observation of fractional-flux vortices.

A second issue is the separation between the two layers: on the one hand it should be large enough to prevent Josephson coupling producing linear confinement of vortex–anti-vortex pairs, on the other hand, a large distance d_i between the layers would promote leaking of the magnetic field, thus modifying the value of the trapped flux $\Phi_{\rm t}$. Hence, in order to observe $\Phi_0/2$ vortices, both the interlayer distance d and the layer thickness $d_{\rm s}$ have to be small compared to the bulk penetration depth λ. Separating the two superconducting layers by an insulator, the Josephson current density $j_{\rm J}$ can be made arbitrarily small and the Josephson length $\Lambda = \sqrt{(j_0/j_{\rm J})\xi d}$ (from (2.58)), beyond which vortex pairs are linearly confined, arbitrarily large. Hence, an insulator of a few nm thickness is sufficient to push Λ beyond $\lambda_{\rm eff}$ and the two apparently contradictory requirements can still be satisfied simultaneously.

A further complication arises from the mean-field temperature dependence $\propto (1 - T^2/T_c^2)^{1/2}$ of the Ginzburg-Landau parameters λ and ξ. As a result, the Kosterlitz-Thouless temperatures $T_{\rm BKT}^{(2)}$ and $T_{\rm BKT}^{x}$ are pushed closer to the mean-field critical temperature T_c. The parameter quantifying the strength of fluctuations is the two-dimensional Ginzburg number (2.74), $Gi^{(2{\rm D})} = T_c/(2\varepsilon_{00}d) \ll 1$; as a result one finds that $(T_{\rm BKT}^{x} - T_{\rm BKT}^{(2)})/T_{\rm BKT}^{x} \approx$

$4Gi^{(2D)}$, $(T_c - T^x_{\rm BKT})/T_c \approx 4Gi^{(2D)}$. The Ginzburg number thus fixes the relative distance between the transition temperatures and its value must be larger than the experimental temperature sensitivity in order to distinguish between the different transition temperatures.

Finally, we have to discuss the high voltage sensitivity required for the observation of the characteristic features in the *I*-*V* curves. As we have seen above, all signals related to 'half-charged' vortices are compromised by the small factor $\xi/\lambda_{\rm eff}$, which is a consequence of the large self-energy associated with the screening currents extending out to $\lambda_{\rm eff}$. This small factor determines the density of half-flux vortices in the relevant regime and thus fixes the required voltage sensitivity. Its correct estimate must account for the intrinsic dirtiness of the thin film. First, a small electronic mean free path ℓ reduces [76] the value of the coherence length: at zero temperature it becomes $\xi_{\rm d0} \sim \sqrt{\xi_{\rm c0}\ell}$, with $\xi_{\rm c0}$ the corresponding value of the pure bulk material at zero temperature. At the same time, the penetration depth is increased, $\lambda_{\rm d0} \approx \lambda_{\rm c0}\sqrt{\xi_{\rm c0}/\ell}$. In a thin film, the mean free path is of the order of the layer thickness, $\ell \sim d_{\rm s}$ and we obtain the estimates

$$\frac{\xi}{\lambda_{\rm eff}}(T^{(2)}_{\rm BKT}) \approx 1.5 \cdot 10^{-4}\; T_c^{1/2}\frac{d_{\rm s}^{3/2}}{\lambda_{\rm c0}}, \tag{4.36}$$

$$Gi^{(2D)} \approx 3.2 \cdot 10^{-9}\; T_c\frac{\lambda_{\rm c0}^2\xi_{\rm c0}}{d_{\rm s}^2}, \tag{4.37}$$

where all lengths are measured in Å and temperatures in Kelvin; here the penetration length $\lambda_{\rm c0}$ is the film penetration and not the corresponding bulk value $\lambda^{\rm b}_{\rm c0}$ ($\lambda^2_{\rm c0} = [\lambda^{\rm b}_{\rm c0}]^2 d_{\rm s}/d$). The results (4.36) and (4.37) tell us that given the (clean) material parameters $\lambda_{\rm c0}$ and $\xi_{\rm c0}$ it is not possible to maximize both parameters $Gi^{(2D)}$ and $\xi/\lambda_{\rm eff}$ simultaneously by varying the remaining free parameter $d_{\rm s}$. A reasonable compromize can be achieved if we choose a material with $\lambda_{\rm c0} \sim \xi_{\rm c0} \sim 1000$ Å, $T_{\rm c} \sim 10$ K, and a thickness $d_{\rm s} \sim 500$ Å; this yields $\xi/\lambda_{\rm eff} \approx 10^{-2.5}$ and $Gi^{(2D)} \sim 10^{-4}$. With an experimental sensitivity for voltage measurements in the pico-Volt range [77] and $V_0 \sim \rho_{\rm n} j_0 L \approx 10$ mV (we assume $\rho_{\rm n} \sim 100\ \mu\Omega$cm, $j_0 \sim 10^2$ A/cm^2, and a system size $L \sim 1$ cm) we can extend the voltage axis in Fig. 4.12 down to $\log(V/V_0) \approx -10$. At $T^{(2)}_{\rm BKT}$ the small parameter $\xi/\lambda_{\rm eff} \sim 10^{-2.5}$ pushes the 'slope 5' regime down to $\log(V/V_0) \approx -5 \cdot 2.5 = -12.5$; hence the observation of the upturn to a slope 3 at lower currents pushes the resolution limit of present days experiments (see Fig. 4.12). It is this 'double appearance' of a 'slope 3' characteristic at high temperatures/high currents and at low temperatures/low currents which is the most clear signature of fractional-flux vortex unbinding. Alternative ways to trace the presence of fractional-flux vortices are *i)* to look for the characteristic mean-field type resistivity below T^x_{BKT}, cf. (4.34), or *ii)* to identify the algebraic upturn in the I-V characteristic at temperatures below T^x_{BKT} and currents smaller than I_{eff} (note that the temperature T^x_{BKT} is identified through its characteristic 'slope 3' regime at large currents; in the conventional scenario, the I-V characteristic exhibits only a downturn at temperatures below T^x_{BKT}).

Alternatively, one can access directly the value of the flux at low temperatures, for example with a scanning SQUID microscope [78]. In a finite perpendicular magnetic field vortex stacks penetrate into the bi-layer and arrange in a regular two dimensional lattice. A dc counterflow current in the proposed experimental setup of Fig. 4.3(c) separates each vortex stack into two half-flux vortices. If the two half-flux vortices can be kept at a fixed distance $R \gg \lambda_{\mathrm{eff}}$, the total trapped flux $\Phi_0/2$ of each half-flux vortex can be measured.

4.3.6 Effects of disorder

The above derivation of the I-V characteristic does not account for the effects of disorder on the unbinding transition. Thermally generated vortices experience a disordered energy landscape and may remain stuck around favorable pinning sites rather than move and dissipate. However, the main properties of the I-V characteristic considered here are derived close to the mean-field critical temperature where thermal fluctuations are large and pinning is expected to be irrelevant.

The effect of the material defects is usually two-fold [2]: on the one hand inhomogeneities produce a variation of the electronic mean free path ℓ ($\delta\ell$ pinning); on the other hand, particularly in high temperature materials, the value of critical temperature is not constant throughout the sample (δT_c pinning). Within the framework of the Ginzburg-Landau theory, the effect of $\delta\ell$ pinning is described by variations of the effective mass m, whereas δT_c pinning produces fluctuations of the coefficient α of the quadratic term in ψ, cf. Eq. (2.1). Here, we are mainly interested in the first of these two, since our experimental proposal is based on low T_c materials, for which variations of T_c are usually absent or extremely weak, since defects should not produce modifications in T_c (cf. Anderson's theorem [79]).

In the theory of weak collective pinning [80] the total energy $\mathcal{E}_{\rm pin}$ of competing pinning centers averages to zero. On the other hand the fluctuations of the pinning energy do not vanish and lead to a finite contribution

$$U_{\rm p} \equiv \langle \mathcal{E}_{\rm pin}^2 \rangle^{1/2}. \tag{4.38}$$

Let us characterize the disorder potential by the three-dimensional density n_i and the individual pinning forces $f_{\rm pin}$ and consider their effect on a single vortex. The mean free path ℓ is related to the impurity density and the scattering cross section through the relation $\ell = 1/n_i\sigma$. Thus, this analysis applies to the case of $\delta\ell$ pinning. Only defects within a distance ξ away from the vortex center contribute to the pinning energy. Due to the competition between different pins, the individual pinning forces add up only within the volume $\xi^2 d$ and the (fluctuations in the) pinning energy can be written as

$$U_{\rm p} = \sqrt{n_i d} f_{\rm pin} \xi^2. \tag{4.39}$$

Comparing the Lorentz force with the total pinning force one obtains that vortices remain pinned for currents smaller than a typical critical value I_c,

$$\frac{I_c}{I_0} \approx \frac{U_c}{\varepsilon_0 d}. \tag{4.40}$$

The individual pinning force can be related to the defect cross-section σ by means of $f_{\rm pin} = H_c^2 \sigma(\xi_0/\xi) \approx \varepsilon_0(\xi_0/\xi)(\sigma/\xi^2)$ [81]. Hence, the critical current becomes

$$\frac{I_c}{I_0} \approx \sqrt{\frac{\sigma}{\ell d}} (1 - T/T_c)^{1/2}. \tag{4.41}$$

By means of the quasi-classical expression of the resistivity R of the film in the normal state

$$R \approx \frac{m_e}{dne^2\tau}, \tag{4.42}$$

with m_e the electronic mass, n the electronic density, and τ the relaxation time, we can rewrite the mean free path as

$$\ell \approx \tau v_F \approx \frac{1}{k_F^2 d} \frac{R_Q}{R}, \tag{4.43}$$

where $R_Q = \hbar/e^2$ is the quantum resistance, v_F the Fermi velocity and k_F the Fermi momentum. In dirty superconductors the ratio R/R_Q is of the order of the two-dimensional Ginzburg number [54], $R/R_Q \approx Gi^{(2\mathrm{D})}$. Hence, using (4.43) in (4.41), we recast the result in the following form

$$\frac{I_c}{I_0} \approx Gi^{(2\mathrm{D})}\sqrt{\sigma k_F^2}, \tag{4.44}$$

from which we obtain that the critical current I_c is suppressed by a factor $Gi^{(2\mathrm{D})}$ with respect to the depairing current I_0 near T_c. With $Gi^{(2\mathrm{D})} \sim 10^{-4}$, $1 - T/T_c \sim 4Gi^{(2\mathrm{D})}$, and σk_F^2 of order unity [81] we have I_c/I_0 of order 10^{-4}, which is smaller than $I_{\mathrm{eff}}/I_0 \sim 10^{-2.5}$. Hence, pinning due to variations of the mean free path does not mask the features of the I-V characteristic below I_{eff}.

Microscopically, beside modifying the mean free path, disorder can also produce spatial fluctuations of the critical temperature T_c. Even if these fluctuations are usually small in low T_c materials, the consequences of this different microscopic pinning mechanism must be careful accounted for, since close to T_c even extremely small δT_c fluctuations may become relevant. In fact, if the typical T_c fluctuation are of the order of $Gi^{(2\mathrm{D})}$, different regions of the system may become normal, producing a 'percolated' granular superconductor. Introducing the parameter γ_T which describes the δT_c fluctuations ($\langle \delta T_c(r)\delta T_c(r')\rangle = \gamma_T T_c^2 \delta(r - r')$), the critical current obeys the relation [2]

$$\frac{I_c}{I_0} \sim \sqrt{\frac{\gamma_T}{d\xi_0^2}}\frac{1}{(1 - T/T_c)^{1/2}}, \tag{4.45}$$

and diverges when T approaches T_c. To avoid that this δT_c pinning could mask the main features of the I-V characteristics, one needs a small critical current $I_c \ll I_{\mathrm{eff}}$ and hence a small γ_T. This requires a largely uniform critical temperature within the sample, and, hence, a good quality of the film.

4.3.7 Analogy with the bi-layer quantum Hall system

An interesting analogy appears when comparing the present system with the bi-layer quantum Hall setup at total filling $\nu = 1$. For small interlayer separations ($d/\ell \sim 2$, with $\ell = \sqrt{\hbar c/(eB)} = \sqrt{\Phi_0/\pi B}$ the characteristic magnetic length) the bi-layer quantum Hall system shows a remarkable coherent state, which is nowadays well established both experimentally [82,83] and theoretically [63,64]. Due to strong quantum fluctuations, even in the absence of interlayer tunneling, each electron lowers its energy by going into a coherent superposition, i.e., with a well-defined relative phase, of states with a fixed layer index. The broken coherent phase can be described in different ways, such as an interlayer excitonic Bose condensate [84] or as a planar ferromagnet [85] in the pseudo-spin variable, describing the layer occupation. In this last formalism one defines the z-component of the pseudo-spin to label the layer occupation, i.e., spin-up ($\uparrow$) corresponds to the upper layer and spin-down ($\downarrow$) to the lower one. Hence, $S_z = (N_\uparrow - N_\downarrow)/2$ is proportional to the charge imbalance between the two layers. A finite value $\langle S_z \rangle$ is penalized by the charging energy ('easy-plane' anisotropy)

$$H_c = \frac{e^2}{2C} S_z^2, \tag{4.46}$$

where C is the capacity of the double layer. Thus, this 'easy-plane' term prefers a pseudo-spin pointing in the xy plane, i.e., $\langle S_z \rangle = 0$. The coherent phase φ is associated with the angle of the pseudo-spin in the xy plane with respect to the x axis. In the coherent state the full electronic wave function Ψ is described by a BCS-type wave function [86]

$$|\Psi\rangle = \prod_k \frac{1}{\sqrt{2}} \Big(c^\dagger_{k,\uparrow} + e^{i\varphi} c^\dagger_{k,\downarrow} \Big) |0\rangle, \tag{4.47}$$

where $c^\dagger_{k,\uparrow}$ ($c^\dagger_{k,\downarrow}$) is the creation operator of an electron with momentum k in the upper (lower) layer and $|0\rangle$ is the vacuum state. In the absence of tunneling the total energy does not depend on the value of the global phase φ and thus the system exhibits a broken $U(1)$ symmetry, which is associated with the phase φ. One can define the order parameter

$$\psi(\mathbf{R}) \equiv \langle \Psi^\dagger_\uparrow(\mathbf{R}) \Psi^\dagger_\downarrow(\mathbf{R}) \rangle = \frac{n_0}{2} e^{i\varphi}, \tag{4.48}$$

where $\Psi^\dagger_\uparrow(\mathbf{R})$ ($\Psi^\dagger_\downarrow(\mathbf{R})$) creates an electron in the upper (lower) layer at the position $\mathbf{R}$ and $n_0 = 1/2\pi\ell^2$ is the electronic density.

Let us now consider the topological excitations in this system. While the energy does not depend on the value of φ, it depends on the spatial gradient $\nabla\varphi$. When the fluctuations of the out-of-plane component of the pseudo-spin are small, the energy can be written as [87]

$$H = \int d^2\mathbf{R} \Big[\frac{\rho_s}{2} (\nabla\varphi)^2 + \frac{(\hbar n_0 e/2)^2}{2C_\mu} m_z^2 \Big], \tag{4.49}$$

where the second term comes from the capacity energy (4.46), $m_z = \langle S_z \rangle$, and C_μ is related to the capacity per unit area [64]. The superfluid stiffness ρ_s arises from the loss of optimal Coulomb exchange in the presence of a phase gradient [64]. Topological excitations associated with the vortices in this interlayer phase φ are called merons [64]. They are characterized by a non-singular core. Close to the core position, the three-dimensional pseudo-spin can exit out of the xy plane paying a finite capacity energy (due to the second term) instead of a singular contribution coming from the first term. Due to the (half)-flip of the pseudo-spin along the z-axis, a meron carries a finite charge $\pm e/2$, which is a fraction of the electronic charge e. Merons in the bi-layer setup appear in four different species and can be identified by the value of the charge $\pm e/2$ and vorticity ± 1. Each meron alone involves a logarithmically divergent self-energy and therefore, like in the case of a multilayered superconductor, excitations correspond to neutral topological objects. Combining merons with opposite vorticity in pairs can give rise to charged ($\pm e$) or uncharged configurations, corresponding to pairs of equally or opposite charged merons. Due to the underlying broken $U(1)$ symmetry, the unbinding of meron-pairs is supposed to be of the BKT type and leads to the suppression of the interlayer phase coherence at high enough temperatures.

Let us now consider the bi-layer superconductor in order to shed light on the similarities with the bi-layer quantum Hall setup. Also in the superconductor system the half-flux vortices appear in four species, with ± 1 vorticity in each layer. The analogy between these topological objects and the merons in the quantum Hall setup can be made clear by means of an opportune variable change in the superconducting system. Instead of the phases φ_1 and φ_2 in the individual layers, we consider the phase difference $\varphi(\mathbf{R}) \equiv \varphi_1(\mathbf{R}) - \varphi_2(\mathbf{R})$ and the phase average $\varphi_+(\mathbf{R}) \equiv [\varphi_1(\mathbf{R}) + \varphi_2(\mathbf{R})]/2$. The presence of a conventional vortex stack is induced by a phase twist in the φ_+, while the phase difference φ remains constant. On the other hand, half-flux vortices are associated with a finite vorticity of φ. We can therefore distinguish vortices and anti-vortices in the phase difference φ. In order to obtain a full description of the four possible kinds of half-flux vortices we need another variable. To this end, we can choose[1] the value of the trapped magnetic flux $\pm\Phi_0/2$. In this way, we obtain a full description of the four kinds of vortices: a (anti)-vortex in the upper layer corresponds to vorticity $+1$ (-1) and flux $+\Phi_0/2$ $(-\Phi_0/2)$, while a (anti)-vortex in the second layer corresponds to vorticity -1 $(+1)$ and flux $-\Phi_0/2$ $(+\Phi_0/2)$. Hence, the formal analogy to the bi-layer superconducting system is achieved by going from magnetically charged vortices to vortices carrying an effective electronic charge (thus, by replacing the elementary flux with the elementary charge $\Phi_0 \to e$). Moreover, in both systems one obtains that the first correction to the logarithmic interaction between half-flux vortices/merons is algebraic $\propto 1/R$, due to the Coulomb interaction for the quantum Hall setup and to the stray-fields for the bi-layer superconductor (from the second term in (3.15)).

---

[1] Another possibility is to define the variable $m_z(\mathbf{R}) = [n_1(\mathbf{R}) - n_2(\mathbf{R})]/2n_\infty$, where n_1 (n_2) is the superfluid density and n_∞ the asymptotic value of both n_1 and n_2 in the first (second layer). For equivalent layers is $m_z = 0$ except at the location of the core of a

From the experimental point of view both the physics of fractional flux vortices and merons can be accessed in basically two ways. First, by testing the interlayer coherence/correlation by a drag experiment. This idea in the context of bi-layer superconductors goes back to the flux transformer firstly developed by Giaever [65], where the current is pushed through one layer only (primary) and the induced voltage is measured in the opposite one (secondary). In the quantum Hall setup electrons move together coherently and a voltage drop appears also in the secondary layer, even though no external current is applied [82]. In the superconductor system the voltage appears due to the motion of vortices in the primary layer, which drag along vortices in the secondary layer due to the attractive magnetic interaction [65, 67]. Clearly this effect is enhanced with an applied magnetic field by increasing the density of vortex stacks. A second experiment requires the counterflow geometry we have proposed to trace the appearance of half-flux vortices. Opposite currents do not couple with charged excitations (charged merons pairs/stacks) but only with the relative displacement of its (fractionalised) components, yielding no linear contribution to the resistivity. Hence, in the counterflow geometry both the bi-layer quantum Hall system and the bi-layer superconductor show a superfluid response [83] (i.e., dissipationless flow), allowing a direct access to the specific properties of merons/fractional flux vortices.

---

half-flux vortex. In terms of these variables one can obtain a free-energy similar to (4.49), cf. also Ref. [88].

4.4 Conclusions

Summarizing, in this Chapter we have presented a detailed analysis of the BKT transition in superconducting systems with a finite number of layers. The effectiveness of magnetic screening depends on the number of layers, producing qualitative differences in the thermodynamic behavior. The reduced (fractional) magnetic flux Φ_{t} trapped by a two-dimensional vortex extends the logarithmic inter-vortex interaction to infinite distances, like in neutral superfluids where magnetic screening is absent. The main consequence is the appearance of a finite temperature BKT transition at which fractional-flux vortices–anti-vortex pairs unbind. However, to describe the full thermodynamic behavior of these multi-layered superconductors one also has to account for the effect of vortex stacks, which like Pearl vortices in a single film, are thermally excited at any finite temperature and push the superconducting transition to $T = 0$. We have discussed how to eliminate in an experiment the effect of these thermally activated vortex stacks, in order to access the finite temperature BKT transition. In the connected experimental setup of Fig. 4.3 stacked vortices do not move, inhibiting the appearance of a linear resistivity at low applied currents. The effect of stray fields modifies the standard BKT scenario for the vortex unbinding transition; within an RG approach we have shown how the density of free vortices above the transition increases slowly with temperature, due to the large kinetic energy acquired below the effective penetration depth λ_{eff}, see Fig. 4.11. We have discussed in detail the precise form of the I-V characteristic, including the effects of magnetic screening. The presence of fractional-flux vortices can be accessed by probing the system with small currents and it is associated, for example, with the change of the exponent α at $T_{\mathrm{BKT}}^{(2)}$ ($V \propto I^{\alpha}$): $\alpha = 3$ at low currents to $\alpha = 5$ at larger currents. The value of the current which distinguishes between these two different regimes is at $I_{\mathrm{eff}} = (\xi/\lambda_{\mathrm{eff}})I_0$. The requirement of having a large factor $\xi/\lambda_{\mathrm{eff}}$ contradicts the demand of a sufficient large separation between the transition temperatures T_{BKT}^{x} and $T_{\mathrm{BKT}}^{(2)}$, i.e. of a large Ginzburg number. We have shown how to optimally compromise between these two opposite requirements in order to observe the main features of the I-V characteristic with nowadays voltage and temperature sensitivities.

We have pointed out rather striking analogies with the properties of the bi-layer quantum Hall setup at filling $\nu = 1$. In both systems the second layer leads to the appearance of vortices carrying a fractionalized flux (charge).

Combination of these elementary vortices into topological neutral pairs yields finite energy excitations with unit or zero flux (charge). Charged excitations correspond to standard vortices (vortex stacks), which describe the physics of single film systems. The internal degrees of freedom can be experimentally accessed in a counterflow geometry. In this manner charged vortex pairs (stacks) are left inert, allowing to study the properties of neutral vortex pairs and their unbinding into fractional flux vortices (merons).

Chapter 5

Melting of the Vortex Lattice: Bulk

We study the melting of the pancake vortex lattice in the limit of vanishingly small Josephson coupling, implementing the idea of the substrate model within the framework of the classical density functional theory. We obtain a simple free energy functional in terms of a scalar order-parameter profile and analyze the properties of the solid-liquid transition. Restricting the analysis to density configurations with an integer number of vortices, the free energy describes correctly the negative magnetization jump found in the experiments. We demonstrate the thermodynamic consistency of the theory by deriving the Clausius-Clapeyron relation from our free energy. Finally, we study the properties of a solid-liquid interface.

5.1 Introduction

The melting transition of the vortex lattice is one of the most remarkable aspects of the phenomenology of high-temperature superconductors. It is now both theoretically [12–14,16] and experimentally [36,37] well established that enhanced thermal fluctuations make the Abrikosov lattice unstable towards the formation of a vortex liquid over a large part of the B-T phase diagram. The impact of thermal fluctuations is boosted in layered materials like BiSCCO due to their extreme anisotropy, cf. (2.49), favoring the appearance of the liquid phase over an even wider portion of the phase diagram, see Sec. 2.6.3. Here, we concentrate our analysis on the limiting case $\varepsilon \to 0$ of magnetically coupled layers, which serves as a guideline to understand these materials and allows for an accurate theoretical analysis.

The first theories for the melting of the vortex lattice were based on the Lindemann analysis (cf. Sec. 2.5 and [13, 89]), which provides a stability criterion for the solid phase. Although being not rigorous, the Lindemann melting scenario has been reasonably accurate in predicting the position of the first-oder melting transition. However, a more detailed description is needed to characterize the transition completely.

Even if only the electromagnetic interaction is considered, a precise analysis of the melting transition is a challenging task due to the long-range character of the interactions between pancake vortices, cf. (2.70) and (2.73). At large magnetic fields the strong in-plane vortex repulsion dominates over the out-of-plane interactions and the melting line approaches the 2D melting temperature $T_{\mathrm{m}}^{\mathrm{2D}}$ of isolated planes. On the other hand, ignoring the possibility of low-field reentrance [12], at vanishingly small magnetic fields only few pancake vortex stacks are present in the system. Thermal fluctuations trigger the evaporation of isolated vortex stacks at T_{BKT}, in correspondence with the zero-field two-dimensional Berezinskii-Kosterlitz-Thouless (BKT) transition (cf. last Chapter $T_{\mathrm{BKT}} = T_{\mathrm{BKT}}^{(\infty)} \approx \tilde{\varepsilon}_0 d/2$). For intermediate values of the external magnetic field the melting line interpolates between the BKT transition temperature $T_{\mathrm{BKT}} \lesssim T_c$ close to the critical temperature T_c and the two-dimensional lattice melting temperature $T_{\mathrm{m}}^{\mathrm{2D}} \ll T_c$ and the full three-dimensional character of the system comes into play.

From a theoretical point of view, the particular properties of the potential (2.69) and (2.73) allow for an elegant 'mean-field' approach [17] which has been successfully used to describe the fluctuations of the pancake vortex lattice. Due to the large difference between the in-plane and out-of-plane components of the interaction, one can proceed with a dimensional reduction of the problem to an effective two dimensional one. In the $\varepsilon \to 0$ limit, the tilt modulus becomes strongly dispersive, cf. (2.48), $c_{44}(k_z) \propto 1/k_z^2$, and the tilt elastic energy $\propto c_{44}(k_z) k_z^2 |u(\mathbf{k})|^2$ in (2.41) generates a simple harmonic potential $\propto u^2$. Each pancake vortex feels this harmonic potential arising from the vortex stack to which it belongs, in addition to the in-plane interaction. As a result, the system can be analysed in terms of a two-dimensional Coulomb gas under the effect of this substrate potential. One can then study the stability of this effective two dimensional system by means of standard techniques, such as the self-harmonic elastic approximation [90], and locate the solid instability line (see also Chapter 6). Finally, the determination of the melting line requires information of the liquid phase as well. In [17], the melting line has been located via a comparison of the free energies of the solid phase with numerical estimates of the free energy of the liquid (from Monte Carlo simulations of the two dimensional one component plasma). Extensive Monte Carlo and molecular dynamics simulations [41] of the three-dimensional pancake vortex system have confirmed the validity of this ‘substrate’ model and the accuracy of its results.

The extreme anisotropic limit of zero Josephson coupling between the layers has also been analyzed by means of classical Density Functional Theories (DFT) [16, 27, 91] . If we compare the results of these previous DFT approaches to the melting line obtained numerically, we find consistent results at large magnetic fields larger than $B \approx 0.5B_\lambda$ ($B_\lambda = \Phi_0/\lambda^2$). However, going to the low field regime the disagreement between the two theories is substantial, since the DFT melting line lies at much higher temperatures. Another problem of previous DFT studies is the value of the magnetization jump across the transition. It is experimentally well known [36] that the vortex lattice shows a negative jump in magnetization, leading to a solid phase which is less dense than the liquid, similar to the situation in the ice-water transition. Besides direct observation of the magnetization jump itself, this feature is also consistent with the negative slope of the melting line in the B-T phase diagram and the Clausius-Clapeyron relation. However, previous DFT analyses of the freezing transition led to a physical inconsistent picture with a positive density change but a negative slope of the melting line.

In this Chapter, we adapt the DFT analysis to include the main ideas from the substrate approach. The difference with the previous DFT approaches lies in the determination of the direct correlation function. Whereas in the previous analyses this was derived *ab initio* from the microscopic vortex interactions using the hypernetted chain approach or more elaborate extensions, here we use a direct correlation function which combines results from Monte Carlo simulations of 2D logarithmically interacting particles with the substrate potential. Within this new approach we obtain a simple expression for the free energy which can be extendend to the study of inhomogeneous cases. Moreover, we prove the thermodynamic consistency of our approach by showing how to obtain the negative density jump across the transition, by including a constraint which enforces an integer number of particles per unit cell [92]. Contrary to former claims [27], we demonstrate that no higher order correlation function (three point or more) is needed in order to obtain this negative density jump. Moreover, we demonstrate the thermodynamic consistency of the theory, by deriving the Clausius-Clapeyron relation from the DFT free energy. Finally, we extend the analysis to study non-homogeneous states. We derive a fully three dimensional free energy which is capable of describing the coexistence of solid and liquid phase. We discuss the properties of the interface, in particular its width and the free energy cost.

5.2 Classical Density Functional Theory

In this section, we introduce the classical density functional theory. For simplicity, we consider here a generic three-dimensional system of point-like particles interacting via a two-body potential $V(r)$; the modifications needed to describe the pancake vortex system are presented in the next section. The convenient thermodynamic potential to study the melting transition is the grand canonical free energy $\Omega(\mu, T, V)$ which is obtained from the partition function

$$e^{-\Omega/T} = \sum_{N=0}^{\infty} \frac{1}{N!} \int e^{[\mu N - \sum_{i>j} V(|\mathbf{r}_i - \mathbf{r}_j|)]/T} \prod_{i=1}^{N} \frac{d^3\mathbf{r}_i}{\Lambda_{\mathrm{th}}^3}, \tag{5.1}$$

where N is the total number of particles, μ the chemical potential ($\mu = \Phi_0 HL/4\pi$ for a 3D vortex system with L the thickness) and Λ_{th} the thermal length. The determination of Λ_{th} is only required to fix the additive constant in the entropy. However, in our following analysis we only deal with energy differences and terms containing Λ_{th} will drop out.

Following the classical Density Functional Theory of freezing outlined by Ramakrishnan and Yussouff [25, 93], we choose the uniform liquid as the reference state and consider the difference in free energy due to the appearance of finite density modulations. The spatial arrangement of vortices is described in terms of the density field defined through

$$\rho_\mu(\mathbf{r}) = \sum_{i=1}^{N} \delta(\mathbf{r} - \mathbf{r}_i), \tag{5.2}$$

where $\mathbf{r}_i$ is the position of the i-th particle (the index μ emphasizes that $\rho_\mu(\mathbf{r})$ describes the microscopic density, i.e., non averaged, cf. see below) To analyze the finite temperature behavior of the system we consider the density

$\rho(\mathbf{r})$, averaged over thermal fluctuations

$$\rho(\mathbf{r}) = \langle \rho_\mu(\mathbf{r}) \rangle, \tag{5.3}$$

where the brackets $\langle \ldots \rangle$ denote the thermal average. The liquid and the solid phases are characterized by qualitatively different density fields $\rho(\mathbf{r})$: in the liquid phase the vortices are delocalized across the system and the averaged density is constant $\rho(\mathbf{r}) = \bar{\rho}^{\mathrm{3D}}$; on the other hand the solid phase is characterized by a strongly modulated $\rho(\mathbf{r})$, with pronounced peaks at the lattice points. The appearance of finite density modulations is a consequence of particle-particle correlations arising from the microscopic interactions $V(\mathbf{r})$.

The simplest way to include the effects of the two body potential is via the virial expansion [94]: one begins with the ideal gas partition function and accounts for interactions in a systematic perturbative high temperature expansion in terms of the Mayer function $f(\mathbf{r}) = \exp[-V(\mathbf{r})/T] - 1$. The disadvantage of this approach is that the virial expansion remains analytic to all finite orders. Hence, it cannot describe the melting transition which is associated with the appearance of a singularity in the free energy.

On the other hand, the classical DFT is based on the assumption that the free energy can be written as a functional of the averaged density $\rho(\mathbf{r})$, which plays the role of the order parameter of the transition. Again, one starts from the ideal gas free energy describing a non interacting liquid, but the correlations are included via an effective quadratic term in the density modulations $\delta\rho(\mathbf{r}) = \rho(\mathbf{r}) - \bar{\rho}^{\mathrm{3D}}$. Within this approximation the grand canonical free energy difference relative to the uniform liquid reads

$$\begin{aligned}\frac{\delta\Omega[\rho(\mathbf{r})]}{T} = \int d^3\mathbf{r} \Big[\rho(\mathbf{r}) \ln \frac{\rho(\mathbf{r})}{\bar{\rho}^{\mathrm{3D}}} - \delta\rho(\mathbf{r}) \\ - \frac{1}{2} \int d^3\mathbf{r}' \delta\rho(\mathbf{r}) c(|\mathbf{r} - \mathbf{r}'|) \delta\rho(\mathbf{r}') \Big].\end{aligned} \tag{5.4}$$

The first two terms generalize the standard free energy of an ideal gas to the case of non-homogeneous systems [95]. The double integral term incorporates the effects of interactions up to second order in the density difference $\delta\rho$. This is the term which is responsible for the appearance of finite density modulations, which are absent in a non-interacting system. Therefore, the key input in this theory is the function $c(r)$, so-called direct pair correlation function, which has to be calculated to account for the correlations in the reference liquid.

The direct pair correlation function can be related to more transparent physical quantities such as the static structure factor [93,94]. We start from the microscopic density-density correlator

$$\langle \delta\rho_\mu(\mathbf{r}_1)\delta\rho_\mu(\mathbf{r}_2)\rangle \equiv \sum_{i,j} \langle [\delta(\mathbf{r}_1 - \mathbf{r}_i) - \bar{\rho}^{\mathrm{3D}}][\delta(\mathbf{r}_2 - \mathbf{r}_j) - \bar{\rho}^{\mathrm{3D}}]\rangle. \tag{5.5}$$

where $\delta\rho_\mu(\mathbf{r}) \equiv \rho_\mu(\mathbf{r}) - \bar{\rho}^{\mathrm{3D}}$. The Fourier transform of the density-density correlator defines the structure factor[1] [94]

$$S(\mathbf{q}) = \frac{1}{\bar{\rho}^{\mathrm{3D}} V} \int d^3\mathbf{r}_1\, d^3\mathbf{r}_2\, e^{-i\mathbf{q}\cdot(\mathbf{r}_1 - \mathbf{r}_2)} \langle \delta\rho_\mu(\mathbf{r}_1)\delta\rho_\mu(\mathbf{r}_2)\rangle. \tag{5.6}$$

An important physical quantity related to the structure factor is the pair *correlation* function

$$\begin{aligned} h(\mathbf{r}) &= \frac{1}{(\bar{\rho}^{\mathrm{3D}})^2 V} \int d^3\mathbf{r}' \sum_{i\neq j} \langle [\delta(\mathbf{r}' + \mathbf{r} - \mathbf{r}_i) - \bar{\rho}^{\mathrm{3D}}][\delta(\mathbf{r}' - \mathbf{r}_j) - \bar{\rho}^{\mathrm{3D}}]\rangle \\ &= \frac{1}{(\bar{\rho}^{\mathrm{3D}})^2 V} \int d^3\mathbf{r}' \langle \delta\rho_\mu(\mathbf{r}' + \mathbf{r})\delta\rho_\mu(\mathbf{r}')\rangle - \frac{\delta(\mathbf{r})}{\bar{\rho}^{\mathrm{3D}}}, \end{aligned} \tag{5.7}$$

in the last line the delta function term comes from the diagonal terms in the sum ($i = j$), which are present in the definition of the density-density correlator, but not in the pair correlation function. The structure factor can then be rewritten in terms of the pair correlation function

$$S(\mathbf{q}) = 1 + \bar{\rho}^{\mathrm{3D}} h(\mathbf{q}). \tag{5.8}$$

Another function which is commonly used to describe the correlation in the liquid phase is the so-called pair *distribution* function, which is defined through

$$\begin{aligned} g(\mathbf{r}) &= \frac{1}{(\bar{\rho}^{\mathrm{3D}})^2 V} \int d^3\mathbf{r}' \sum_{i\neq j} \langle \delta(\mathbf{r}' + \mathbf{r} - \mathbf{r}_i)\delta(\mathbf{r}' - \mathbf{r}_j)\rangle \\ &= 1 + h(\mathbf{r}). \end{aligned} \tag{5.9}$$

The Fourier transform of $g(\mathbf{r})$ produces an additional term $(2\pi)^3\delta(\mathbf{q})$ when compared to the Fourier transform of $h(\mathbf{r})$. This term is sometimes included in the definition of the structure factor, e.g. in [93].

---

[1] In [93] this expression is named Ursell function (up to a factor $1/\bar{\rho}^{\mathrm{3D}}$). The structure factor contains an irrelevant additional $(2\pi)^3\delta(\mathbf{q})$.

Next, we calculate the structure factor from the free energy (5.4). The second functional derivative of the free energy with respect to $\rho(\mathbf{r})$ evaluated at $\rho(\mathbf{r}) = \bar{\rho}^{\mathrm{3D}}$ is the (functional) inverse of the density-density correlator (see also [93])

$$\begin{aligned} \frac{\delta^2[\delta\Omega]}{\delta[\delta\rho(\mathbf{r}_1)]\delta[\delta\rho(\mathbf{r}_2)]} &= [\langle\delta\rho_\mu(\mathbf{r}_1)\delta\rho_\mu(\mathbf{r}_2)\rangle]^{-1} \\ &= \frac{1}{\bar{\rho}^{\mathrm{3D}}}\delta(\mathbf{r}_2 - \mathbf{r}_1) - c(|\mathbf{r}_2 - \mathbf{r}_1|) \qquad (5.10) \end{aligned}$$

The functional inverse can be easily calculated in Fourier space. Using (5.6) we find the relation between the structure factor and the direct correlation function

$$S(\mathbf{q}) = \frac{1}{1 - c(\mathbf{q})}. \qquad (5.11)$$

Therefore, apart from additive constants (or delta functions in real space), the direct correlation function $c(\mathbf{q})$ is the functional inverse of the structure factor $S(\mathbf{q})$ (or, in real space, of $h(\mathbf{r})$ or $g(\mathbf{r})$). In Eq. (5.11), following standard practice of liquid-state theory, we have defined the Fourier transform of the direct correlation function $c(\mathbf{q})$ with an explicit factor $\bar{\rho}^{\mathrm{3D}}$ (dimensionless Fourier transform)

$$c(\mathbf{q}) = \bar{\rho}^{\mathrm{3D}} \int d^3\mathbf{r}\, c(\mathbf{r}) e^{-i\mathbf{q}\cdot\mathbf{r}}. \qquad (5.12)$$

The $q = 0$ mode of the structure factor is related through the fluctuation-dissipation theorem to the isothermal compressibility of the system, i.e., $S(q = 0) = (\langle N^2\rangle - \langle N\rangle^2)/\langle N\rangle^2 = \bar{\rho}^{\mathrm{3D}} T\kappa_T$ (the isothermal compressibility of the ideal gas is $\kappa_T^0 = 1/(\bar{\rho}^{\mathrm{3D}} T)$) and

$$1 - c(q = 0) = \frac{1}{\bar{\rho}^{\mathrm{3D}} T\kappa_T}. \qquad (5.13)$$

The study of the free energy functional (5.4) requires knowledge of the direct correlation function $c(r)$, a quantity which is usually obtained from the liquid state theory. As in the virial expansion, it is possible to write a diagrammatic expansion for $c(r)$ in terms of the Mayer function $f(r)$. For weak potentials, high-order correlations can be neglected and $c(r)$ is given by the first (unperturbed) term [94]

$$c(r) \approx f(r) \approx -\frac{V(r)}{T}. \qquad (5.14)$$

In order to obtain a better estimate for $c(r)$, higher order terms in the perturbation expansion must also be included. This is usually done by selecting specific classes of diagrams out of the complete perturbative series. The approach that is most widely used is the hypernetted chain (HNC) closure, an approximation scheme which, however, is known to underestimate liquid-state correlations. The strategy we pursue here is different: we exploit the specific properties of the pancake vortex lattice by considering the system as a collection of two dimensional systems of log-interacting particles subject to a periodic modulated substrate potential due to the other layers, similarly to the substrate model approach [17]. The correlator $c(r)$ then combines an in-plane correlator $c_{z,z}(R)$, arising from the strong in-plane logarithmic interaction, and the weak out-of-plane potential $-V_{z,z'}(R)/T$.

5.3 DFT-substrate approach

With respect to standard liquids, the pancake vortex system exhibits a strong uniaxial anisotropy. Hence, we consider separately the in-plane ($\mathbf{R}$) and out-of-plane (z) dependencies: in particular $\rho(\mathbf{r}) \to \rho_z(\mathbf{R})$ becomes a sequence (in z) of two dimensional densities and similarly we define the density variations $\delta\rho_z(\mathbf{R}) = \rho_z(\mathbf{R}) - \bar{\rho}$ and the direct pair correlation function $c_{z,z'}(|\mathbf{R}-\mathbf{R}'|)$ (note that $\bar{\rho}$ is a 2D density). The DFT free energy of Eq. (5.4) can be adapted to the anisotropic vortex liquid

$$\begin{aligned}\frac{\delta\Omega[\rho_z(\mathbf{R})]}{T} = & \int \frac{dz}{d} d^2\mathbf{R} \Big[\rho_z(\mathbf{R}) \ln \frac{\rho_z(\mathbf{R})}{\bar{\rho}} - \delta\rho_z(\mathbf{R}) \\ & -\frac{1}{2}\int \frac{dz'}{d} d^2\mathbf{R}' \delta\rho_z(\mathbf{R}) c_{z,z'}(|\mathbf{R}-\mathbf{R}'|)\delta\rho_{z'}(\mathbf{R}')\Big].\end{aligned} \tag{5.15}$$

The only input needed in the DFT free energy is the direct correlation function $c_{z,z'}(R)$. Our approach implements the substrate model for the determination of the pair correlation function, by separating the contributions of the strong in-plane logarithmic repulsion from the weak out-of-plane but long-range attraction,

$$c_{z,z'}(R) = d c^{\mathrm{2D}}(R)\delta(z-z') - \frac{V_{z,z'}(R)}{T}. \tag{5.16}$$

where $V_{z,z'}(R)$ is the out-of-plane interaction (cf. Eq. (2.72) for a bulk system or Eq. (3.27) for a semi-infinite system).

Within the planes, vortices are strongly correlated due to the repulsive logarithmic interactions (we neglect the small contributions of order d/λ and use (2.70)). Hence, we can approximate $c_{z,z}(R)$ with the direct correlation function $c^{\text{2D}}(R)$ of the two dimensional logarithmically interacting particles (also known as one component plasma, OCP). The effect of the out-of-plane interaction on the in-plane component $c_{z,z}(R)$ is small, since $V_{z,z'\neq z}(R)$ appears in the perturbative expansion at least to quadratic order $\propto [f_{z,z'\neq z}(R)]^2 \sim [V_{z,z'\neq z}(R)/T]^2 \sim (d/\lambda)^2$ [94]. Instead of using an approximate scheme, such as the HNC equation, we used results of Monte Carlo simulations of the two-dimensional OCP at various coupling constants $\Gamma = 2\varepsilon_0 d/T$ to extract $c^{\text{2D}}(R)$. These simulations have been performed by Gautam Menon on a system of 256 particles, using an alternative to the traditional Ewald summation method proposed recently by Tyagi [96]. Thermodynamic data and correlations were averaged over $\sim 3\times 10^3$ independent measurements following equilibration. The program was benchmarked using available numerical results for correlations and thermodynamic functions. In the simulations, the pair correlation function $h(R) = g(R) - 1$ was calculated and then Fourier transformed to yield the structure factor $S(K)$ and finally the direct correlation function $c(K) = 1 - 1/S(K)$.

In the determination of the out-of-plane direct correlation function $c_{z,z'}(R)$ we neglect the higher order correlations and approximate it with the leading unperturbed value $-V_{z,z'}(R)/T$ (cf. Eq. (5.14)). This is consistent with the approximation we have used for the in-plane part, since higher orders in $c_{z,z'}(R)$ involve at least terms of the type $[f_{z,z'\neq z}(R)]^2 \sim (d/\lambda)^2$.

At a mean-field level the thermodynamically stable state corresponds to the minimal free energy configuration of the functional (5.15). Then, the density functions $\rho_z(R)$ must obeys the saddle point equation

$$\ln\frac{\rho_z(\mathbf{R})}{\bar\rho} = \int\frac{dz'}{d}\int d^2\mathbf{R}'\, c_{z,z'}(|\mathbf{R}-\mathbf{R}'|)\delta\rho_{z'}(\mathbf{R}'). \tag{5.17}$$

A key quantity in our discussion is the molecular field $\xi_z(\mathbf{R})$ [25,26,97] defined through

$$\xi_z(\mathbf{R}) = \ln\frac{\rho_z(\mathbf{R})}{\bar\rho}. \tag{5.18}$$

At the minimum of the free energy, combining the saddle point equation (5.17) with (5.18), the molecular field becomes

$$\xi_z(\mathbf{R}) = \int\frac{dz'}{d}\int d^2\mathbf{R}'\, c_{z,z'}(|\mathbf{R}-\mathbf{R}'|)\delta\rho_{z'}(\mathbf{R}'). \tag{5.19}$$

The molecular field represents the average potential produced by the modulated density. However, whereas Eq. (5.18) defines the molecular field, Eq. (5.19) is only valid at the minimum.

5.4 Free energy in Fourier space

In thermodynamic equilibrium all superconducting planes are equal and the averaged vortex density $\rho_z(\mathbf{R})$ becomes independent of the layer position z; we write $\rho_z(\mathbf{R}) = \rho(\mathbf{R})$. Next, instead of seeking the exact form $\rho(\mathbf{R})$ which solves the non-linear integral equations (5.17), we restrict our analysis to a simple family of periodic functions which models the modulations of the density in the solid phase. In the following, we concentrate on the simplest case, retaining only the first Fourier components of the density in a triangular lattice

$$\frac{\rho(\mathbf{R})}{\bar{\rho}} = 1 + \eta + \sum_{\mathbf{K}_1} \mu e^{i\mathbf{K}_1 \cdot \mathbf{R}} = 1 + \eta + \mu g_{K_1}(\mathbf{R}), \tag{5.20}$$

where the vectors $\mathbf{K}_1$ are the first reciprocal lattice vectors of the frozen structure and depend on the area a of the unit cell, $\mu = \delta\rho(K_1)/\bar{\rho}$ is the Fourier component of the density with wave length K_1, and $\eta = \delta\rho(\mathbf{K} = 0)/\bar{\rho}$ the relative density change. In a consistent picture the size of the unit cell a in the crystalized structure and the value of the density jump are related and, thus, K_1 and η are not independent variables (we will come back to this issue in the next section). The function

$$g_{K_1}(\mathbf{R}) = \sum_{\mathbf{K}_1} e^{i\mathbf{K}_1 \cdot \mathbf{R}} = 2\cos(2\tilde{x}) + 4\cos(\tilde{x})\cos(\tilde{y}) \tag{5.21}$$

includes the sum on the six first reciprocal lattice vectors, cf. (2.33); in the last equality we have defined the dimensionless variables $\tilde{x} = xK_1/2$ and $\tilde{y} = \sqrt{3}\,yK_1/2$. We also write a similar Ansatz for the molecular field

$$\xi(\mathbf{R}) = \zeta + \xi g_{K_1}(\mathbf{R}), \tag{5.22}$$

retaining only the zeroth and first Fourier components, ζ and ξ respectively. This Ansatz for $\xi(R)$ is justified by noting that the saddle point equation for $\rho(R)$ involves the convolution of the density and the direct correlator. However, in the liquid phase $c(K)$ decays rapidly to zero (cf. Fig. 5.1) and the full Fourier series of $\rho(R)$ can be truncated after few terms. In a fully

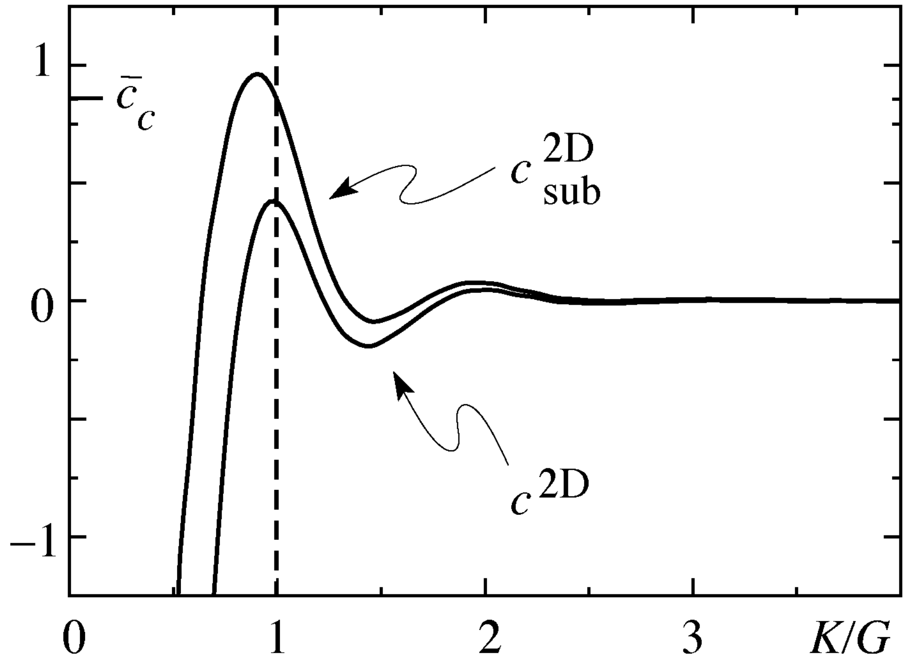

Figure 5.1: Direct correlation function at $T/\varepsilon_0 d = 0.1$ ($\Gamma = 20$) for the two-dimensional OCP, $c^{2D}(K)$ from MC simulations and $c^{2D}_{\rm sub}(K) = c^{2D}(K) - V_{\rm stack}(K)/T = c^{2D}(K) + 2\alpha(K)/dK_+$ (cf. (5.28)) for the full three-dimensional pancake vortex system at the melting magnetic field $B_{\rm m}$ ($B_{\rm m}/B_\lambda \approx 0.099$ for $T/\varepsilon_0 d = 0.1$). We define our unit of length $G = (8\pi^2\bar{\rho}/\sqrt{3})^{1/2}$. At melting the full three-dimensional correlator assumes the value $\bar{c}^{2D}_{\rm sub} \equiv c^{2D}_{\rm sub}(G) = \bar{c}_c \approx 0.856$, cf. (5.47). The substrate potential $V_{\rm stack}(K)$ modifies the full correlator $c^{2D}_{\rm sub}(K)$ in two different ways as compared to the in-plane correlation function $c^{2D}(K)$: *i)* it enhances the correlations of the liquid, pushing the melting to temperatures larger than $T^{2D}_{\rm m}$ and *ii)* it shifts the peak of the correlation function to a value of K which is smaller than G, and therefore it leads to a cristallized structure with a density smaller than the liquid one, i.e., $n_{\rm v} < \bar{\rho}$.

consistent theory, the term $\xi g_{K_1}(\mathbf{R})$ generates higher components $\delta\rho(\mathbf{K}_n)$, which however are irrelevant for a rapidly decaying $c(K)$.

The Fourier components of $\rho(\mathbf{R})$ and $\xi(\mathbf{R})$ are not independent and can be related through (5.18). With the help of the following relations (from the orthogonality of the Fourier basis)

$$\frac{1}{a}\int_a d^2\mathbf{R} g(\mathbf{R}) = 0, \qquad \frac{1}{a}\int_a d^2\mathbf{R}[g(\mathbf{R})]^2 = 6, \tag{5.23}$$

by filtering out the zeroth and first Fourier components of $\rho(\mathbf{R}) = \bar{\rho}\exp(\zeta + \xi g_{K_1}(\mathbf{R}))$, we obtain the relations

$$\begin{aligned} \zeta &= -\Phi(\xi) + \ln(1+\eta), \\ \mu &= \frac{1+\eta}{6}\,\Phi'(\xi), \end{aligned} \tag{5.24}$$

where we have defined the function

$$\Phi(\xi) = \ln\left[\frac{1}{a}\int_a d^2\mathbf{R}\, e^{\xi g(\mathbf{R})}\right]. \tag{5.25}$$

This function is unaffected by rescaling of the unit cell area a (equivalently, does not depend on the length of the vector K_1).

Substituting the Ansätze (5.20) and (5.22) in the DFT free energy (5.15), one obtains the two-dimensional free energy density (d is the interlayer spacing)

$$\frac{\delta\omega^{\mathrm{2D}}_{\mathrm{sub}}}{T} \equiv \frac{d}{\bar{\rho}V}\,\frac{\delta\Omega}{T} \tag{5.26}$$

as a function of the order parameters η and μ

$$\begin{aligned} \frac{\delta\omega^{\mathrm{2D}}_{\mathrm{sub}}(\eta,\mu,K_1)}{T} &= (1+\eta)[\ln(1+\eta) - \Phi(\xi)] - \eta \\ &\quad + 6\xi\mu - \frac{c^{\mathrm{2D}}_{\mathrm{sub}}(0)\eta^2}{2} - 3c^{\mathrm{2D}}_{\mathrm{sub}}(K_1)\mu^2, \end{aligned} \tag{5.27}$$

where ξ has to be understood as a function of η and μ through (5.24). In (5.27) we have defined the correlator

$$c^{\mathrm{2D}}_{\mathrm{sub}}(K) = \int \frac{dz}{d}\, c_z(K) = c^{\mathrm{2D}}(K) - \int \frac{dz}{d}\,\frac{V_z(K)}{T}, \tag{5.28}$$

where $c_z(K) \equiv c_{z,0}(K)$ and $V_z(K)$ is the dimensionless Fourier transform of the bulk out-of-plane pancake vortex interaction (2.72)

$$\frac{V_z(K)}{T} = -\frac{2\pi\varepsilon_0\bar{\rho}d^2}{TK^2\lambda^2K_+}e^{-K_+|z|} = -\alpha(K)f_z(K), \tag{5.29}$$

with $K_+ = \sqrt{K^2 + \lambda^{-2}}$ (cf. Chapter 3), $\alpha(K) = 2\pi\varepsilon_0\bar{\rho}d^2/TK^2\lambda^2K_+$ and $f_z(K) = \exp(-K_+|z|)$. Note the additional $\bar{\rho}$ factor due to the dimensionless definition of the Fourier transform, cf. (5.12). The out-of-plane interactions contribute to the correlator through the total stack potential

$$\frac{V_{\text{stack}}(K)}{T} = \int_{-\infty}^{+\infty} \frac{dz}{d} \frac{V_z(K)}{T} = -\frac{2\alpha(K)}{dK_+}, \tag{5.30}$$

which enhances the nearest neighbors correlations, cf. Fig. 5.1.

Within this approach only the $K = 0$ and the $K = K_1$ components of the correlator are present in the expression for the free energy (5.27). Particular care must be taken when considering $c^{\text{2D}}_{\text{sub}}(0)$, which should reproduce the compressibility of the system as we know from (5.13). In the limit of small K, it is known that the OCP correlation function shows the asymptotic behavior [42]

$$c^{\text{2D}}(K \to 0) \approx -\frac{2\bar{\rho}\varepsilon_0 d}{TK^2} + \frac{\varepsilon_0 d}{2}, \tag{5.31}$$

where the first (divergent) term is simply the Fourier transform of the logarithmic potential and describes the incompressibility of the OCP. The second term is due to the liquid correlations and can be derived from the virial equation [94]. In the full correlator $c^{\text{2D}}_{\text{sub}}(K)$, the divergent term of $c^{\text{2D}}(K)$ cancels out with an opposite term in the stack potential. This assures the charge neutrality of the full three dimensional system; in the usual OCP charge neutrality is due to the oppositely charged uniform background, here, this effect is due to the third dimension, i.e., to the presence of full vortex stacks. Including the second term in the expansion of the stack potential in $c^{\text{2D}}_{\text{sub}}(0)$, we obtain

$$1 - c^{\text{2D}}_{\text{sub}}(0) \approx \frac{4\pi\varepsilon_0}{T}\frac{B}{B_\lambda} = \frac{\Phi_0 Bd}{4\pi T}, \tag{5.32}$$

with $B_\lambda = \Phi_0/\lambda^2$. We have neglected the correlation (second) term in c^{2D} (5.31), this approximation is valid down to fields $B/B_\lambda \sim 0.05$. The results in (5.32) is consistent with (5.13) and the compressibility of the vortex system. In fact using the relation between compressibility and compression modulus $\kappa_T = 1/c_{11}(0)$, where from (2.44) $c_{11}(0) = B^2/4\pi$, Eq. (5.13) yields $1 - c^{\text{2D}}_{\text{sub}}(0) = \Phi_0 dc_{11}/BT = \Phi_0 Bd/4\pi T$. Therefore, the substrate model discussed reproduces prior results correctly. Only at very low fields ($B \lesssim 0.05B_\lambda$), the correlation term in c^{2D} becomes relevant leading to an incorrect result. Hence, in this particular limit, one should also include the effects of the higher order out-of-plane correlations, which are neglected in our substrate model. In the forthcoming analysis, we neglect the effect of the correlation term in (5.31) and use (5.32) for $c_{\rm sub}^{\rm 2D}(0)$ for any value of the magnetic field. However, as we will see, $c_{\rm sub}^{\rm 2D}(0)$ affects only weakly the location of the melting line, which can be derived essentially from $c_{\rm sub}^{\rm 2D}(K_1)$, i.e., at a finite value of $K = K_1$.

The equation (5.27) is one of the fundamental results in this Chapter. The thermodynamic state of the system is associated with the minimum of (5.27) with respect to η and μ. The liquid state is always a minimum and corresponds to an uncompressed and homogeneous state, i.e., with $\eta = 0$ and $\mu = 0$. Depending on the values of the magnetic field B and of the temperature T, a second minimum may appear at a finite value of $\mu \neq 0$, describing a solid phase. If the free energy value of this second minimum is less than the free energy of the liquid, i.e., if at the solid minimum $\delta\omega_{\rm sub}^{\rm 2D} < 0$, then the system freezes.

5.5 Constrained theory

Within our approximation for $\rho(R)$, the state of the system is characterized only by two parameters: the density modulation μ at the first reciprocal lattice vector and the density change η across the transition. However, a theory based on the Ansatz (5.20) and the functional (5.15) is not fully consistent. The problem, as it was pointed out in [92], is that in (5.20) the size of the unit cell a and the density jump η are independent variables. This theory therefore may lead to the appearance of states with a non-integer occupancy per unit cell and, hence, not to a correct description of the solidification of the liquid. To solve this inconsistency only states with a fixed and integer total number of particles per unit cell should be considered. Hence, one has to proceed with a constrained minimization of the free energy, introducing a Lagrange multiplier χ which enforces the so-called 'perfect crystal' condition [92]

$$\int_a d^2\mathbf{R}\,\rho(\mathbf{R}) = 1, \tag{5.33}$$

i.e., each unit cell contains exactly one vortex. With this additional term the free energy density becomes

$$\frac{\delta\tilde{\omega}_{\rm sub}^{\rm 2D}(\eta,\mu,K_1,\chi)}{T} = \frac{\delta\omega_{\rm sub}^{\rm 2D}(\eta,\mu,K_1)}{T} - \frac{\chi}{\bar{\rho}a}\Big[\int_a d^2\mathbf{R}\,\rho(\mathbf{R}) - 1\Big], \tag{5.34}$$

where $\delta\omega_{\rm sub}^{\rm 2D}(\eta,\mu,K_1)$ is (5.27). Substituting the Fourier Ansatz in the Lagrange multiplier term, we obtain the expression for the constrained free energy

$$\frac{\delta\tilde{\omega}^{\rm 2D}_{\rm sub}(\eta,\mu,K_1,\chi)}{T} = \frac{\delta\omega^{\rm 2D}_{\rm sub}(\eta,\mu,K_1)}{T} - \chi\left[(1+\eta) - \left(\frac{K_1}{G}\right)^2\right], \tag{5.35}$$

where G is the length of the first reciprocal lattice vector associated with a solid with the same density of the liquid ($G^2 = 8\pi^2\bar{\rho}/\sqrt{3}$). The 'perfect crystal' constraint of (5.33) yields a relation between η and K_1 (last term in square brackets in (5.35))

$$\eta(K_1) = \left(\frac{K_1}{G}\right)^2 - 1. \tag{5.36}$$

The case $K_1 = G$ describes an incompressible system, since the solid and the liquid have the same density. However, an ordinary first order phase transition is characterized by a finite jump of the density, and hence by a non-zero η. Consistently with our constrained theory, a finite η corresponds to the crystallization into a solid with a first reciprocal lattice vector $K_1^2 \equiv 8\pi^2 n_{\rm v}/\sqrt{3}$ which is not related to the liquid density, $K_1^2 \neq G^2$. When $K_1 > G$ the solid is denser than the liquid, like in standard materials, whereas $K_1 < G$ leads to an anomalous density jump with a solid which is less dense than the liquid, similarly to what happens in the water-ice transition.

Minimizing (5.35) with respect to μ, η, and K_1, we obtain the following relations

$$\xi = c^{\rm 2D}_{\rm sub}(K_1)\mu, \tag{5.37}$$

$$\chi = -\Phi(\xi) + (1 - c^{\rm 2D}_{\rm sub}(0))\eta, \tag{5.38}$$

$$\chi = \frac{3G^2\mu^2}{2K_1}\frac{\partial c^{\rm 2D}_{\rm sub}(K)}{\partial K}\bigg|_{K_1}, \tag{5.39}$$

which have to be completed with the constraint (5.36) coming from the minimum with respect to χ and the equation (5.24) relating ξ with μ. Combining (5.37)-(5.39) and (5.24), we can eliminate ξ and χ. The saddle point equations for η and μ can be written as

$$\mu = \frac{[1+\eta]}{6}\frac{\displaystyle\int_v d^2\mathbf{R}\, g(\mathbf{R})\exp\Big[\mu c^{\rm 2D}_{\rm sub}(K_1) g(\mathbf{R})\Big]}{\displaystyle\int_v d^2\mathbf{R}\exp\Big[\mu c^{\rm 2D}_{\rm sub}(K_1) g(\mathbf{R})\Big]}, \tag{5.40}$$

$$\eta = \frac{1}{1 - c^{\rm 2D}_{\rm sub}(0)}\left[\Phi(c^{\rm 2D}_{\rm sub}(K_1)\mu) + \frac{3G^2\mu^2}{2K_1}\frac{\partial c^{\rm 2D}_{\rm sub}(K)}{\partial K}\bigg|_{K_1}\right], \tag{5.41}$$

where η and K_1 are related by (5.36). The homogeneous ($\mu = 0$) and uncompressed ($\eta = 0$) liquid always solves these equations. However, at low temperatures, other non-uniform solutions ($\mu \neq 0$) may appear. If their corresponding free energy is smaller than the liquid, $\delta\omega_{\text{sub}}^{\text{2D}} < 0$ the system freezes into the periodic (crystal) structure.

The equations (5.40) and (5.41) can also be obtained directly from the free energy (5.27),

$$\frac{\delta\omega_{\text{sub}}^{\text{2D}}(\eta,\mu)}{T} \equiv \frac{\delta\omega_{\text{sub}}^{\text{2D}}(\eta,\mu,K_1(\eta))}{T}, \tag{5.42}$$

where K_1 is written as a function of η via (5.36). The minimization of $\delta\omega_{\text{sub}}^{\text{2D}}(\eta,\mu)/T$ with respect to η and μ yields the saddle point equations (5.40) and (5.41).

5.6 Incompressible limit and melting line

The pancake vortex system is incompressible ($|c_{\text{sub}}^{\text{2D}}(0)| \gg 1$) for a wide portion of the phase diagram and the corresponding value of the density jump is small, i.e., $\eta \ll 1$. In this limit, the free energy becomes a function of μ alone,

$$\frac{\delta\omega_{\text{sub}}^{\text{2D}}(\mu)}{T} \equiv \frac{\delta\omega_{\text{sub}}^{\text{2D}}(\eta=0,\mu)}{T} = 6\xi(\mu)\mu - 3\bar{c}_{\text{sub}}^{\text{2D}}\mu^2 - \Phi(\xi(\mu)), \tag{5.43}$$

where $\bar{c}_{\text{sub}}^{\text{2D}} \equiv c_{\text{sub}}^{\text{2D}}(G)$ and $\xi(\mu)$ is implicitly defined by

$$\mu(\xi) = \Phi'(\xi)/6. \tag{5.44}$$

For the 3D vortex system, the whole effective three dimensional function $\bar{c}_{\text{sub}}^{\text{2D}}$ is given by the sum of two contributions: the OCP correlation function $\bar{c}^{\text{2D}}$ and the stack potential $V_{\text{stack}}(G)$ (5.30). Whereas the first depends only on the temperature, the latter depends also on the vortex density and thus on the magnetic field

$$\begin{aligned}\bar{c}_{\text{sub}}^{\text{2D}}(T,B) &= \bar{c}^{\text{2D}}(T) + \frac{4\pi\bar{\rho}\varepsilon_0 d}{TG^2}\frac{1}{1+\lambda^2G^2} \\ &= \bar{c}^{\text{2D}}(T) + \frac{\sqrt{3}\varepsilon_0 d}{2\pi T}\frac{1}{[1+(8\pi^2/\sqrt{3})B/B_\lambda]},\end{aligned} \tag{5.45}$$

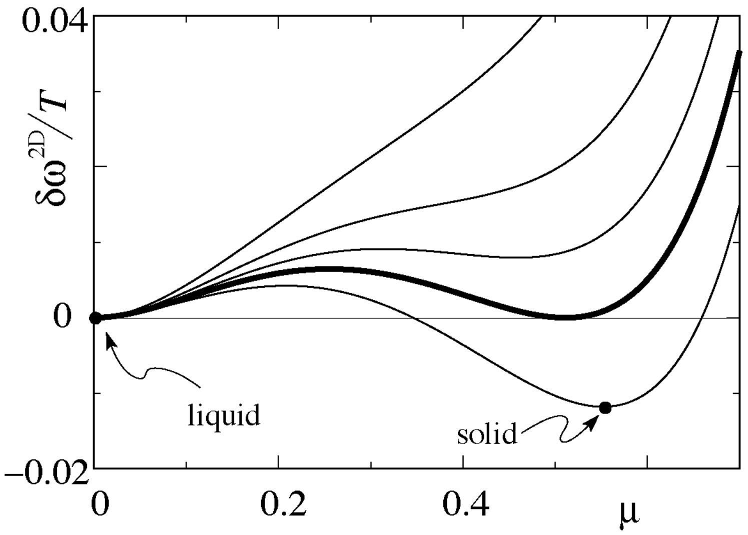

Figure 5.2: Profiles of the two dimensional free energy difference $\partial\omega^{2\mathrm{D}}(\mu)$ (5.43) as a function of the order parameter μ, in correspondence to the values (from above to below) $\bar{c}^{2\mathrm{D}} \equiv \bar{c}^{2\mathrm{D}}(G) = 0.80$, 0.83, 0.845, 0.856 ($= \bar{c}_c$ critical, thicker line), 0.87. At melting the order parameter jumps from the solid minimum at $\mu_\mathrm{s} \approx 0.51$ to $\mu_\mathrm{l} = 0$, overcoming the activation barrier $\delta\omega^{2\mathrm{D}}_{\mathrm{max}} \approx 0.0065\,T$.

where we use $\bar{\rho}/G^2 = \sqrt{3}/(8\pi^2)$ and $\lambda^2 G^2 = (8\pi^2/\sqrt{3})B/B_\lambda$, with $B_\lambda = \Phi_0/\lambda^2$.

At large values of B, the inter-plane interaction is negligible and the full correlator reduces to the 2D-OCP component $\bar{c}^{2\mathrm{D}}$. The temperature enters via the T-dependence of the direct correlation function $\bar{c}^{2\mathrm{D}}(T)$, changing the coefficient of the quadratic term (like in the ϕ^4 Landau theory). We obtain this quantity directly from MC simulations; the results are shown in the upper plot of Fig. 5.3. Increasing the temperature, the liquid loses its correlation, $S(G)$ decreases, and so does $\bar{c}^{2\mathrm{D}}$, cf. Eq. (5.11). As a function of μ, the free energy exhibits the shape of a Landau theory describing a first order phase transition. In Fig. 5.2 we plot the free energy as a function of μ for different values of $\bar{c}^{2\mathrm{D}}$. At large temperatures, the correlator $\bar{c}^{2\mathrm{D}}$ is small and $\delta\omega^{2\mathrm{D}}(\mu)$ exhibits only one minimum at $\mu = 0$ with a value $\delta\omega^{2\mathrm{D}}(0)/T = 0$, in correspondence with the (homogeneous) liquid phase. Decreasing the temperature (which corresponds to increasing values of $\bar{c}^{2\mathrm{D}}$), a second local minimum $\mu_{\rm s}$ (metastable solid) with energy

$$\frac{\delta\omega^{\rm 2D}(\mu_{\rm s})}{T} = 3\bar{c}^{\rm 2D}\mu_{\rm s}^2 - \Phi(\bar{c}^{\rm 2D}\mu_{\rm s}) \tag{5.46}$$

appears in addition to the liquid one at $\mu_{\rm l} = 0$. Freezing occurs when the liquid and solid minima assume the same value of the free energy, i.e., when $\delta\omega^{\rm 2D}(\mu_{\rm s}) = 0$. Within our one component theory, this condition is equivalent to a simple equation for the correlator [26]

$$\bar{c}^{\rm 2D} = \bar{c}_c \approx 0.856. \tag{5.47}$$

Going to even lower temperatures, $\bar{c}^{\rm 2D}$ further increases, the solid minimum goes down $\delta\omega^{\rm 2D}(\mu_{\rm s})/T < 0$, and the crystal becomes the only thermodynamically stable phase. Monte Carlo simulation [42] show that the 2D-OCP freezes at $T_{\rm m}^{\rm 2D} \approx \varepsilon_0 d/70$ where however the correlator assumes the value $\bar{c}^{\rm 2D} \approx 0.77 < \bar{c}_c$ ($\Gamma = 2\varepsilon_0 d/T = 140$). This disagreement is due to the approximations we have adapted in our analysis. In particular, at low temperatures, the higher order peaks become important and more terms in the Fourier expansion have to be retained [95].

At lower magnetic fields, the inter-plane correlation becomes important and the 2D correlations $\bar{c}^{\rm 2D}$ are augmented by the stack potential $V_{\rm stack}(G)$. The critical condition $\bar{c}^{\rm 2D}_{\rm sub}(T,B) = \bar{c}_c$ can be solved together with (5.45) and yields a simple expression for the melting line $B_{\rm m}(T)$

$$\frac{B_{\rm m}(T)}{B_\lambda} = \frac{\sqrt{3}}{8\pi^2}\Big[\frac{\sqrt{3}\Gamma}{4\pi(\bar{c}_c - \bar{c}^{\rm 2D}(T))} - 1\Big]. \tag{5.48}$$

This melting line is plotted in Fig. 5.3 (lower) together with the numerical results of the MC/MD simulations [41]. We find a better agreement when compared with the previous DFT studies where the direct correlation function has been derived *ab initio* through approximative closure schemes such as the hypernetted chain or the more elaborate Rogers-Young approach [16,91]. In particular this novel approach approximates well the numerical results for small values of the magnetic fields ($B \lesssim 0.5\,B_\lambda$), for which previous studies show a substantial disagreement.

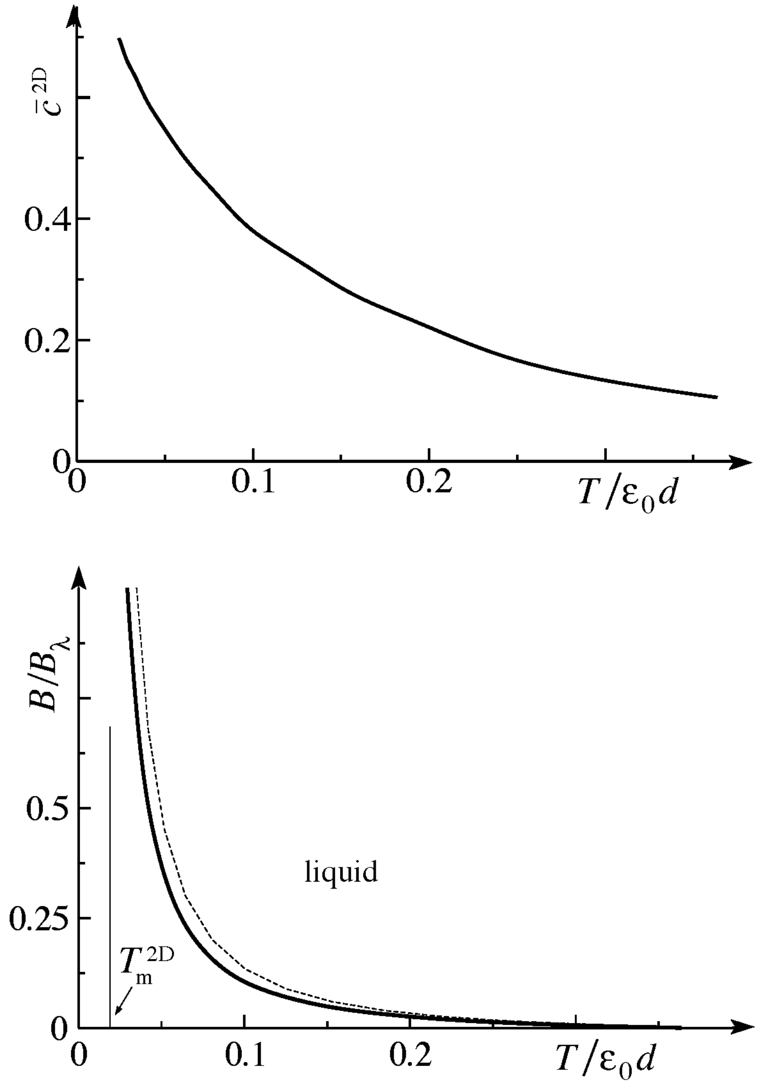

Figure 5.3: Upper graph: values of the first peak at $K_{\rm max} \approx G$ of the in-plane two-point direct correlator $c^{\rm 2D}(K)$ as a function of $T/\varepsilon_0 d = 2/\Gamma$, from Monte Carlo simulations of the two dimensional one component plasma (OCP). Lower graph: comparison of the melting line obtained from the substrate-DFT analysis (solid line) with the result of full numerical simulations [17] (dashed line).

5.7 Density jump and Clausius-Clapeyron relation

If we want to quantify the density jump across the transition, we need to consider the saddle point equation (5.41) for η

$$\eta = \frac{1}{1 - c^{\mathrm{2D}}_{\mathrm{sub}}(0)} \Big[\Phi(c^{\mathrm{2D}}_{\mathrm{sub}}(K_1)\mu) + \frac{3G\mu^2}{2(1+\eta/2)} \frac{\partial c^{\mathrm{2D}}_{\mathrm{sub}}(K)}{\partial K}\Big|_{K_1} \Big], \tag{5.49}$$

where we have used $K_1 = G\sqrt{1+\eta} \approx G(1+\eta/2)$ to linear order in η from (5.36). Previous analyses of the freezing of the pancake vortex system were based on the unconstrained free energy (5.27), by fixing K_1 in correspondence to the value of K at which the first peak of in-plane correlation function takes place. In the unconstrained theory, the equation for η contains only the first term in (5.49), since the second term is due to the Lagrange multiplier, cf. (5.39); hence, within the unconstrained theory, one obtains ('nc' stands for not-constrained)

$$\eta_{\mathrm{nc}} = \frac{\Phi(\bar{c}^{\mathrm{2D}}_{\mathrm{sub}}\mu_{\mathrm{s}})}{1 - c^{\mathrm{2D}}_{\mathrm{sub}}(0)} \approx -\frac{\Phi(\bar{c}^{\mathrm{2D}}_{\mathrm{sub}}\mu_{\mathrm{s}})}{c^{\mathrm{2D}}_{\mathrm{sub}}(0)}, \tag{5.50}$$

where in the last line we have assumed a small compressibility, i.e., $|c^{\mathrm{2D}}_{\mathrm{sub}}(0)| \gg 1$. Given that $c^{\mathrm{2D}}_{\mathrm{sub}}(0) < 0$ and $\Phi(\bar{c}^{\mathrm{2D}}_{\mathrm{sub}}\mu_{\mathrm{s}}) > 0$, the sign of η is always positive. This result contradicts the Clausius-Clapeyron relation and the experimental evidence that vortices, like water, freeze into a solid which is less dense than the liquid. In a magnetic system the Clausius-Clapeyron relation reads [31]

$$\Delta B = -4\pi\Delta s \Big(\frac{dH_{\mathrm{m}}(T)}{dT}\Big)^{-1}, \tag{5.51}$$

where $\Delta B = B_{\mathrm{l}} - B_{\mathrm{s}} = \eta B_{\mathrm{l}} = -\eta\Phi_0\bar{\rho}$ is the jump in magnetic induction and $\Delta s = (S_{\mathrm{l}} - S_{\mathrm{s}})/V$ the jump in entropy density. Ignoring the small difference between H and B, equation (5.51) can be rewritten as ('CC' stands for Clausius-Clapeyron)

$$\eta_{\mathrm{CC}} = \frac{4\pi\Delta s}{\Phi_0\bar{\rho}} \Big(\frac{dB_{\mathrm{m}}(T)}{dT}\Big)^{-1}. \tag{5.52}$$

Combining (5.52) with the negative slope of the melting line $B_{\mathrm{m}}(T)$ of Eq. (5.48), we obtain that the density jump is negative, $\eta_{\mathrm{CC}} < 0$. Therefore, a theory with a positive η and a melting line with a negative slope is not thermodynamically consistent.

The second term in (5.49) resolves this inconsistency. In standard 2D systems the first maximum of the direct correlation function is placed at $K_{\rm max} \approx G$, and hence $\partial_K c_{\rm sub}^{\rm 2D}(G)$ (and the second term in (5.49)) is zero. However, for the 3D pancake vortex system the substrate potential shifts the first peak of $c_{\rm sub}^{\rm 2D}(K)$ to a value of K which is smaller than G, $K_{\rm max} < G$ (cf. Fig. 5.1). Hence, the derivative $\partial_K c_{\rm sub}^{\rm 2D}(K_1) \approx \partial_K c_{\rm sub}^{\rm 2D}(G)$ in the second term of (5.49) is negative and a negative solution for η becomes possible. Next, we confirm the thermodynamic consistency of the constrained theory, by showing that (5.49) and the Clausius-Clapeyron equation (5.52) are equivalent. To compare (5.52) with (5.49), we need to calculate the jump in entropy density Δs in (5.52). The latter is given by the T derivative of the free energy

$$\begin{aligned}\Delta s &= \frac{\bar\rho}{d}\frac{\partial \delta\omega_{\rm sub}^{\rm 2D}}{\partial T}\bigg|_{\eta,\mu} = \frac{\bar\rho T}{d}\frac{\partial}{\partial T}\frac{\delta\omega_{\rm sub}^{\rm 2D}}{T}\bigg|_{\eta,\mu} \\ &= -\frac{3T\bar\rho\mu^2}{d}\frac{\partial c_{\rm sub}^{\rm 2D}(K_1)}{\partial T} - \frac{T\bar\rho}{2d}\frac{\partial c_{\rm sub}^{\rm 2D}(0)}{\partial T}\eta^2 \approx -\frac{3T\bar\rho\mu^2}{d}\frac{\partial c_{\rm sub}^{\rm 2D}(K_1)}{\partial T},\end{aligned} \tag{5.53}$$

where we have used that $\delta\omega_{\rm sub}^{\rm 2D} = 0$ along the melting line. The second term is of order $\eta^2 \ll 1$ and can be neglected when compared to the first one. In order to calculate the entropy jump and $\eta_{\rm CC}$, we need to evaluate the partial derivative $\partial c_{\rm sub}^{\rm 2D}(K_1)/\partial T$ at melting. The standard way [26,27] is to extimate $\partial c_{\rm sub}^{\rm 2D}(K_1)/\partial T$ from the temperature dependence of the solid structure factor. Here we proceed in a different way. Comparing (5.49) with (5.52) and (5.53), we see that in the first equation appears the partial derivative of $c_{\rm sub}^{\rm 2D}$ with respect to K_1 whereas the second equation contains the partial derivative with respect to T. To compare the two different expressions for η we need to find a way to connect these two partial derivatives. This relation can be found from the critical condition which determines the melting line.

The system freezes when the free energy at the solid minimum vanishes. Substituting the values of the molecular field $\mu_{\rm s}$ and of $\eta_{\rm s}$ at the minimum in the free energy (5.27), the freezing condition reads

$$\frac{\delta\omega_{\rm sub}^{\rm 2D}(\eta_{\rm s},\mu_{\rm s})}{T} = 3c_{\rm sub}^{\rm 2D}(K_1)\mu_{\rm s}^2 - (1+\eta_{\rm s})\Phi(c_{\rm sub}^{\rm 2D}(K_1)\mu_{\rm s}) = 0, \tag{5.54}$$

where K_1 is related to $\eta_{\rm s}$ through (5.36) and we have neglected the term $(1-c_{\rm sub}^{\rm 2D}(0))\eta_{\rm s}^2$, which is quadratic in $\eta_{\rm s}$. At the minimum the molecular field $\xi_{\rm s}$ and the order parameter $\mu_{\rm s}$ are related through $\xi_{\rm s} = c_{\rm sub}^{\rm 2D}(K_1)\mu_{\rm s}$, so (5.54) can be rewritten as

$$3\frac{\xi_{\rm s}^2}{c_{\rm sub}^{\rm 2D}(K_1)} - (1+\eta_{\rm s})\Phi(\xi_{\rm s}) = 0. \tag{5.55}$$

For incompressible systems the same equation remains valid when one sets $\eta_\mathrm{s} = 0$

$$3\frac{\xi_\mathrm{s}^2}{\bar{c}_\mathrm{sub}^\mathrm{2D}} - \Phi(\xi_\mathrm{s}) = 0. \tag{5.56}$$

From the discussion in the last section we know that this equation is equivalent to the simple condition $\bar{c}_\mathrm{sub}^\mathrm{2D} = \bar{c}_c$, cf. (5.47). Comparing (5.56) with (5.55), it is simple to realize that the freezing equation in the compressible theory is equivalent to the one in the incompressible limit if one replaces $c_\mathrm{sub}^\mathrm{2D}(K_1)[1+\eta(K_1)]$ by $\bar{c}_\mathrm{sub}^\mathrm{2D}$. Therefore, we can write a critical condition similar to (5.47) that is valid for a compressible system

$$c_\mathrm{sub}^\mathrm{2D}(T, K_1)[1+\eta(K_1)] = \bar{c}_c, \tag{5.57}$$

where we have written explicitly both the T- and the K_1-dependences of the correlator. In (5.57), the correlator depends indirectly on the microscopic magnetic field B in the solid phase through K_1 via

$$K_1 = \left(\frac{8\pi^2}{\sqrt{3}}\frac{B}{\Phi_0}\right)^{1/2} \approx G(1+\eta/2). \tag{5.58}$$

Since the microscopic magnetic field jumps across the transition, the microscopic magnetic field in the liquid is $B_\mathrm{l} = \Phi_0\bar{\rho} = B/(1+\eta) \neq B$. Along the melting line $B_\mathrm{m}(T)$, K_1 can be written as a function of T only by using (5.58), i.e. $K_1 = K_1(B_\mathrm{m}(T))$. Hence, at melting the LHS of (5.57) can be written as a function of the temperature alone; taking the derivative of (5.57) with respect to T, we obtain

$$\begin{aligned}\frac{\partial c_\mathrm{sub}^\mathrm{2D}(T,K_1)}{\partial T} = &-\frac{c_\mathrm{sub}^\mathrm{2D}(T,K_1)}{1+\eta(K_1)}\frac{\partial\eta(K_1)}{\partial K_1}\frac{\partial K_1}{\partial B}\frac{dB_\mathrm{m}}{dT} \\ &-\frac{\partial c_\mathrm{sub}^\mathrm{2D}(T,K_1)}{\partial K_1}\frac{\partial K_1}{\partial B}\frac{dB_\mathrm{m}}{dT}.\end{aligned} \tag{5.59}$$

We need to compute the derivative

$$\frac{\partial K_1}{\partial B} = \frac{K_1}{2B} \approx \frac{G}{2B_\mathrm{l}(1+\eta/2)}, \tag{5.60}$$

where we have used $B = B_\mathrm{l}(1+\eta)$ and the linearized relation between K_1 and G in (5.58). Inserting Eq. (5.59) (with the help of (5.60) and (5.36)) in (5.53), we obtain the entropy jump across the transition

$$\Delta s = \frac{3\mu^2\bar{\rho}T}{dB_\mathrm{l}}\left[\frac{c_\mathrm{sub}^\mathrm{2D}(T,K_1)}{1+\eta} + \frac{G}{2(1+\eta/2)}\frac{\partial c_\mathrm{sub}^\mathrm{2D}(T,K)}{\partial K}\bigg|_{K_1}\right]\frac{dB_\mathrm{m}}{dT}. \tag{5.61}$$

Inserting this expression in (5.52), we obtain the density jump $\eta_{\rm CC}$ described by the Clausius-Clapeyron relation

$$\begin{aligned}\eta_{\rm CC} &= \frac{4\pi}{B_{\rm l}^2}\frac{\bar{\rho}T}{d}\left[\frac{3c^{\rm 2D}_{\rm sub}(T,K_1)\mu^2}{1+\eta} + \frac{3G\mu^2}{2(1+\eta/2)}\frac{\partial c^{\rm 2D}_{\rm sub}(T,K)}{\partial K}\bigg|_{K_1}\right]\\ &= \frac{1}{1-c^{\rm 2D}_{\rm sub}(0)}\left[\frac{3c^{\rm 2D}_{\rm sub}(T,K_1)\mu^2}{1+\eta} + \frac{3G\mu^2}{2(1+\eta/2)}\frac{\partial c^{\rm 2D}_{\rm sub}(T,K)}{\partial K}\bigg|_{K_1}\right], \qquad (5.62)\end{aligned}$$

where in the last line we have used $dB_{\rm l}^2/4\pi\bar{\rho}T = d\Phi_0 B_{\rm l}/4\pi T = 1 - c^{\rm 2D}_{\rm sub}(0)$ from (5.32). The first term in the square brackets in (5.62) can be rewritten with the help of (5.54). As a final result we obtain

$$\eta_{\rm CC} = \frac{1}{1-c^{\rm 2D}_{\rm sub}(0)}\left[\Phi(c^{\rm 2D}_{\rm sub}(K_1)\mu) + \frac{3G\mu^2}{2(1+\eta/2)}\frac{\partial c^{\rm 2D}_{\rm sub}(T,K)}{\partial K}\bigg|_{K_1}\right] = \eta, \qquad (5.63)$$

which is exactly Eq. (5.49). Thus, we conclude that the saddle point equation (5.49) is fully consistent with the Clausius-Clapeyron relation. Note that this result is valid when one considers the constrained DFT. Within the (standard) unconstrained theory, the expression which determines η is given by (5.50), which misses the second term in (5.49) and, hence, is not thermodynamically consistent.

To obtain an estimate of the density jump across the transition we have preformed a numerical minimization of the constrained free energy (5.35). The system freezes when the solid minimum exhibits the same free energy of the liquid phase, i.e., when $\delta\omega(\eta_{\rm s},\mu_{\rm s}) = 0$. In Fig. 5.4 we present the results of our numerical analysis for various values of T. For each temperature we show the density jump at the transition; as expected, we find a negative value of η. However, the modulus of the density jump η is always small, between $|\eta| \approx 10^{-4}$ at low temperatures (large magnetic fields) and $|\eta| \approx 10^{-2}$ for large temperatures (low fields). The effect of such a small η on the determination of the melting line and on the value of $\mu_{\rm s}$ in the solid phase is negligible.

5.8 Solid-liquid interface

In the last section we have shown how to obtain a consistent result for the density jump across the transition. Given the small value of $|\eta|$, however, its determination is not important for the derivation of the melting line and the discussion in Sec. 5.6 based on the incompressible limit remains valid. Moreover, within the incompressible limit we can study more complex problems,

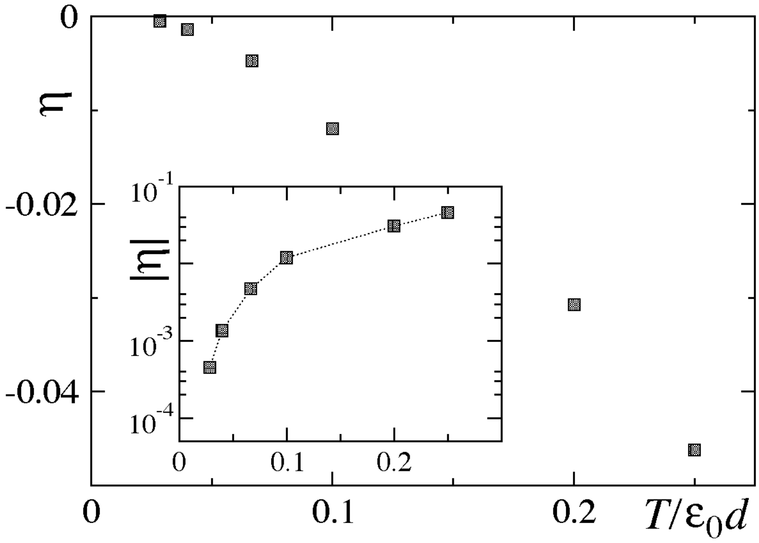

Figure 5.4: Values of the density jump η across the transition as a function of temperature for the 3D bulk vortex system. The density jump η is negative and small, of order 10^{-4} at low temperatures (large magnetic fields) rising to 10^{-2} at larger temperatures (low magnetic fields). Inset: log-plot of the absolute value of η.

such as inhomogeneous situations with a non constant order parameter along z. In the following we will consider two (related) examples: *i)* a solid-liquid interface (see below) and *ii)* the effect of surfaces on the melting transition (cf. next chapter).

Let us consider an interface parallel to the ab plane between a solid and a liquid domain. As a first step, we have to modify the Ansatz for the density in order to keep track of the z-dependence of the order parameter

$$\frac{\rho_z(\mathbf{R})}{\bar{\rho}} = 1 + \eta_z + \mu_z g(\mathbf{R}) \tag{5.64}$$

and equivalently for ξ_z. For each value of z, the Fourier components of $\rho_z(\mathbf{R})$ and $\xi_z(\mathbf{R})$ are still related via the expressions (5.24). For this inhomogeneous situation the full z-dependence in the bulk direct correlator c_z is relevant. We write

$$\bar{c}_\mathrm{z} = \bar{c}^{\mathrm{2D}} d\delta(z) + \bar{\alpha}\bar{f}_z, \tag{5.65}$$

where in the last line we have defined the function $\bar{f}_z \equiv f_z(G) = \exp(-G_+|z|)$ and the quantity $\bar{\alpha} \equiv \alpha(G) = \pi\bar{\rho}\Gamma d/G^2\lambda^2 G_+$, with $G_+ = \sqrt{G^2 + \lambda^{-2}}$. The associated DFT 3D free energy density (A is the sample area)

$$\frac{\delta\omega}{T} = \frac{1}{\bar{\rho}A}\frac{\delta\Omega}{T} \tag{5.66}$$

becomes a functional of the order parameter profile μ_z

$$\begin{aligned} \frac{\delta\omega[\mu_z]}{T} &= \int \frac{dz}{d}\Big[-\Phi(\xi_z) + 6\xi_z\mu_z - 3\int \frac{dz'}{d}\bar{c}_{z-z'}\mu_{z'}\mu_z\Big] & (5.67)\\ &= \int \frac{dz}{d}\Big[\frac{\delta\omega^{2\mathrm{D}}_{\mathrm{sub}}(\mu_z)}{T} + \frac{3\bar{\alpha}}{2}\int \frac{dz'}{d}\bar{f}_{z-z'}(\mu_{z'} - \mu_z)^2\Big]. & (5.68) \end{aligned}$$

The first term describes the local two dimensional free energy of a uniform system (5.43) with the full correlator $c^{2\mathrm{D}}_{\mathrm{sub}}$. The additional non local term in (5.68) quantifies the energy cost due to variations of the order parameter.

Along the melting line $B_{\mathrm{m}}(T)$ the solid and the liquid assume the same value of the free energy and can coexist. Below we analyze the situation when half of the system is in the liquid state and the other half is solid. The corresponding profile of μ_z takes the form of a soliton with boundary conditions $\mu_{z\to-\infty} = 0$ (liquid) and $\mu_{z\to+\infty} = \mu_{\mathrm{s}}$ (solid), where $\delta\omega^{2\mathrm{D}}_{\mathrm{sub}}(0)/T = \delta\omega^{2\mathrm{D}}_{\mathrm{sub}}(\mu_{\mathrm{s}})/T = 0$. The properties of the interface between the two phases depend on the non-local term in the free energy functional (5.68). For a large part of the phase diagram (see Appendix C), it is possible to approximate the full non-local theory with a local one, by proceeding with a gradient expansion [98,99] of the kernel (5.65); inserting $\mu_{z'} \approx \mu_z + (d\mu_z/dz)(z' - z)$ in (5.65), we obtain

$$\frac{\delta\omega[\mu_z]}{T} = \int \frac{dz}{d}\Big[\frac{\delta\omega^{2\mathrm{D}}_{\mathrm{sub}}(\mu_z)}{T} + \frac{1}{2}\ell^2\Big(\frac{d\mu_z}{dz}\Big)^2\Big], \tag{5.69}$$

with the elastic scale

$$\begin{aligned} \ell^2 &= \frac{3\bar{\alpha}}{d}\int_{-\infty}^{+\infty} dz\, \bar{f}_z z^2 = \frac{12\bar{\alpha}}{dG_+^3} = \\ &= \lambda^2\frac{3\sqrt{3}}{2\pi}\frac{\Gamma}{[1 + (8\pi^2/\sqrt{3})B_{\mathrm{m}}(T)/B_\lambda]^2}. \end{aligned} \tag{5.70}$$

This local approximation describes well the full non-local free energy if the profile μ_z varies slowly over the extension $1/G_+$ of the kernel. We have checked that this condition is fulfilled for $T \gtrsim 0.04\,\varepsilon_0 d$, which corresponds to not too high magnetic fields $B \lesssim 0.5B_\lambda$ (see Appendix C).

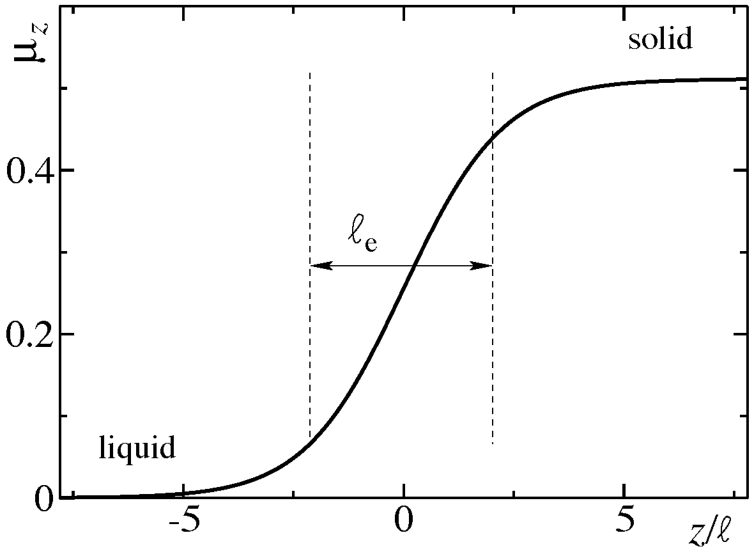

Figure 5.5: Profile of the order parameter μ_z describing an interface between a liquid ($\mu_{z\to-\infty} = 0$) and a solid ($\mu_{z\to+\infty} = \mu_s \approx 0.51$). It has been obtained numerically by solving the differential equation (5.71). The width of the interface is approximately $\ell_e \approx 4.05\ell$ (we define it as the full width at half maximum of the function $d\mu_z/dz$), where ℓ is defined in (5.70).

Now we can estimate the main properties of the solid-liquid interface, e.g. its width and free energy cost. We write the Euler-Lagrange equation of the free energy functional (5.69)

$$\ell^2 \frac{d^2\mu_z}{dz^2} = \frac{d}{d\mu}\Big(\frac{\delta\omega^{2D}_{\rm sub}(\mu_z)}{T}\Big) \tag{5.71}$$

and the corresponding energy conservation relation (the integration constant is zero for a soliton solution)

$$\frac{d\mu_z}{dz} = \frac{1}{\ell}\sqrt{\frac{2\delta\omega^{2D}_{\rm sub}(\mu_z)}{T}}. \tag{5.72}$$

The energy $E_{\rm sl}$ of the interface (soliton) is estimated as

$$\begin{aligned} E_{\rm sl} &= T\int \frac{dz}{d}\ell^2\Big(\frac{d\mu_z}{dz}\Big)^2 = T\frac{\ell}{d}\int_0^{\mu_s} d\mu\sqrt{\frac{2\delta\omega^{2D}_{\rm sub}(\mu)}{T}} \\ &\approx CT\frac{\ell}{d}\mu_s\sqrt{\frac{2\delta\omega^{2D}_{\rm max}}{T}}, \end{aligned} \tag{5.73}$$

where $\delta\omega^{\mathrm{2D}}_{\mathrm{max}} \approx 0.0065\,T$ is the barrier in the energy density between the solid and liquid minima on the melting line and $\mu_{\mathrm{s}} \approx 0.51$ (cf. thick line in Fig. 5.2). The constant C is of order unity and requires to evaluate the integral in (5.73). From a numerical analysis one obtains $C \approx 0.69$. The energy can also be estimated from the first expression in (5.73), by writing $d\mu_z/dz \approx \mu_{\mathrm{s}}/\ell_{\mathrm{e}}$ and from the consideration that the relevant part of the integration domain extends over a distance ℓ_{e}. Hence,

$$E_{\mathrm{sl}} \approx T\frac{\ell_{\mathrm{e}}}{d}\ell^2\Big(\frac{\mu_{\mathrm{s}}}{\ell_{\mathrm{e}}}\Big)^2. \tag{5.74}$$

Therefore, by combining (5.73) together with (5.74), we can extract the width ℓ_{e} of the interface between solid and liquid

$$\ell_{\mathrm{e}} \approx \ell\frac{\mu_{\mathrm{s}}}{\sqrt{2\delta\omega^{\mathrm{2D}}_{\mathrm{max}}/T}} \approx C_{\mathrm{e}}\ell. \tag{5.75}$$

Again, the value of the constant C_{e} must be obtained numerically. Defining ℓ_{e} as the full width at half maximum of the derivative $d\mu_z/dz$, we find $C_{\mathrm{e}} \approx 4.05$, see Fig. 5.5. At low fields, $B \to 0$ (and $T \to T_{\mathrm{BKT}}$), the soliton becomes wider than the bulk penetration depth $\ell_{\mathrm{e}} \approx 8\lambda$, from (5.75) and (5.70). In the limit of large fields the intra-layer interactions dominate the inter-layer ones, leading to a system of decoupled 2D planes which melt independently (cf. the vertical asymptotic of the melting line $B_{\mathrm{m}}(T)$ in correspondence to the melting temperature of the individual layers $T^{\mathrm{2D}}_{\mathrm{m}}$). For large B, ℓ_{e} agrees with this picture of independent layers, since it assumes the asymptotic behavior $\ell_{\mathrm{e}} \sim (B_\lambda/B)\lambda$ which goes to zero for $B \gg B_\lambda$. However, this final result cannot be completely trusted, since equation (5.70) is based on the gradient expansion which is not justified for $B \gg B_\lambda$. In this limit, one needs to go back to the full non-local problem. We have tackled numerically this problem and, as a result of our analysis, we have found that the full theory produces a sharper interface than the one coming from the gradient approximation (see Appendix C).

5.9 Conclusions

In this chapter we have presented an analysis of the freezing of the uncoupled pancake vortex system based on classical density functional theory. We have solved the thermodynamic inconsistency of former studies which contradicted the Clausius-Clapeyron relation, by restricting the analysis to states with an integer number of vortices per unit cell. We determine the direct correlation function of the pancake vortex liquid, combining the results from Monte Carlo simulations of the two dimensional one-component plasma for the in-plane component with the out-of-plane correlator from perturbation theory. Despite of the simplicity of this technique, we have obtained superior results when compared with previous DFT analyses. Moreover, this technique is easily extended to the study of non-homogeneous states. Besides the study of an interface between a liquid and a solid domain, our substrate-DFT approach can be used to discuss the impact of surfaces on the melting transition, which we will describe in detail in the next chapter.

Finally, our substrate-DFT approach can be applied to other problems, such as the effects of specific externally imposed surface potentials. Recent experiments investigate the response of vortices in BiSCCO to a weak perturbation induced by pinning structures created on the sample surface [100]. In our calculation, such surface pinning would be implemented as an imposed external potential acting on the first pancake vortex layer. Within our method we could then describe the response of the pancake vortex system in layers far away from the surface as well as the interplay between periodic surface pinning favoring order and thermal fluctuations favoring the liquid phase.

Chapter 6

Melting of the Vortex Lattice: Surface

In this final chapter, we study the effects of an *ab*-surface on the vortex solid to vortex liquid transition in layered superconductors. In the limit of vanishing inter-layer Josephson coupling, the weak out-of-plane but long-range interaction between pancake vortices justifies a treatment in terms of separate 2D vortex systems in the presence of a self-consistently computed substrate potential generated by neighboring layers. Due to the absence of protecting layers in the neighbourhood of the surface, the vortex lattice formed in this region is more susceptible to thermal fluctuations. Within a self-consistent elastic description, we find that the solid layer at the surface becomes unstable at temperatures below the bulk thermodynamic melting transition. Adapting the density functional theory of freezing to study the effect of the surface, we obtain that both discontinuous and continuous surface melting are possible for this system, with the latter scenario occupying the major part of the low-field phase diagram. The formation of a quasi-liquid layer below the bulk melting temperature inhibits the appearance of a superheated solid phase, yielding an asymmetric hysteretic behavior which has been seen in experiments [101].

6.1 Introduction

Melting should involve, in common with other discontinuous phase transitions, the appearance of metastable phases, namely an undercooled liquid below the transition temperature T_m and a overheated solid above it. Hence, hysteretic behavior is expected upon cycling through the transition. However, experiments on the layered, high-T_c superconductor BiSSCO [101] reveal an asymmetric hysteresis, characterized by the appearance of only the supercooled liquid and no overheated solid. Similar behavior is displayed by ordinary crystals, in particular in metals [23, 24, 102], where such an asymmetry is understood to be a consequence of surface (pre-)melting: surfaces act as nucleation centers for the liquid, thereby inhibiting a metastable solid above the melting transition. However, such surface melting is not generic and there are experimental systems, e.g. Pb(111), Al(111), and Al(110), where the surface remains solid up to the bulk melting transition [24]. Here, we study the effects of an (ab)-surface on the vortex lattice melting, showing that, as the strength of the magnetic field is varied, the same surface may exhibit either a 'surface non-melting' or a 'surface melting' behavior. The latter scenario applies to the major part of the low-field phase diagram, in agreement with experiments [101].

A first order phase transition is characterized by a finite jump of the order parameter. Within a Landau mean field theory, the free energy develops two equivalent minima at the transition. These minima correspond to the coexisting solid and liquid phases. Away from but close to the coexistence line, the free energy exhibits a local minimum which corresponds to a metastable phase in addition to the global minimum. To escape from such a local metastable minimum, the system must overcome an activation barrier. This escape from the metastable state occurs through nucleation of small droplets of the thermodynamically stable phase. If the radius of the droplets exceeds a given critical value, the stable phase propagates into the system. When the energy barrier disappears, no metastable minimum is present and the critical radius of the droplet vanishes.

A general phenomenon associated with the appearance of metastable states is the presence of hysteresis in cycling through the transition. On cooling or on heating, the system can remain trapped in the metastable state and the actual transition will occur not at the melting temperature T_m but at some temperature close to it, depending on the particular sample and the experimental conditions.

Even if locating the transition itself requires that the bulk free energies of the two phases to be compared, a criterion which is unaffected by the presence of the surface, surfaces can drastically modify the hysteretic behavior. For example, in the case of the melting of conventional solids, the atoms at the surface experience a weaker stabilizing potential. An analysis of the stability of crystals in the presence of a surface, as it was done in Ref. [103] for a semi-infinite atom chain, shows that the enhanced motion of surface atoms makes the lattice on the surface unstable at a lower temperature than in the bulk. This suggests that the surface may represent a favorable nucleation site for the liquid phase. However, the state of the system beyond the surface instability point cannot be addressed by stability arguments alone.

A better description of the melting transition in the presence of a surface requires to include the effects of both the solid and the liquid phases [104–106]. On a phenomenological level, this can be done within the framework of a Landau theory, in terms of the natural order parameter of the melting transition, i.e., the Fourier components of the particle density. The destabilizing effect of the surface can be accounted for by introducing a surface term favoring the appearance of the liquid at the interface [22, 107]. Qualitatively different scenarios are possible depending on the strength of the surface term. For relatively large perturbations the surface assists the formation of the liquid at the melting transition and removes the overheated solid. As a function of temperature, the order parameter goes continuously towards the liquid minimum at the transition temperature (named surface melting [24] or O_2 transition [22]), even if the order parameter in the bulk jumps discontinuously. For weak surface perturbations, an alternative scenario applies. As in the bulk, the order parameter at the surface jumps discontinuously to the liquid minimum across the transition, although from a reduced value (surface non-melting or O_1 transition). In this case, the surface does not inhibit the appearance of the overheated solid phase.

In the following, we start from a 'microscopic' theory which accounts for the modification of the inter-vortex interactions at the surface. The analysis of the effect of the surface proceeds into two different ways. First, in Sec. 6.2 we use the substrate model to study the stability of the pancake vortex lattice close to the surface. Whereas, in both the $B \to 0$ and $B \to \infty$ limits the surface turns out to be irrelevant, for intermediate values of B we obtain that on the first layers the lattice becomes unstable *below* the bulk melting line. Therefore, in this regime we expect important precursor effects at the surface. Then, from Sec. 6.3 on, we change our approach and study the problem within the framework of the substrate-DFT theory that we have developed in Chapter 5. We present an analytical solution of the problem and show that depending on the value of the magnetic field the system exhibits either a 'surface non-melting' or a 'surface melting' behavior. Finally, in section 6.4 we confirm the validity of our analytical approach by a direct numerical solution of the DFT equations.

6.2 Stability analysis

At large temperatures thermal fluctuations trigger the dissolution of the vortex lattice. A plausible mechanism for this effect comes from the anharmonic terms in the free energy that soften the crystal, eventually rendering it unstable above a typical temperature T_{u}. Between the melting temperature T_{m} and $T_{\mathrm{u}} > T_{\mathrm{m}}$ (spinoidal region), although the liquid is the stable minimum, the system can remain trapped in the solid phase. Experimentally, in this temperature window non reproducible effects should show up, resulting in the typical hysteretic behavior of first order phase transitions.

A study of the stability of the vortex lattice based on the substrate model was presented in [17]. The anharmonic crystal is described in the framework of an effective harmonic theory whose elastic moduli are softened by thermal fluctuations. The instability temperature of the solid is then identified with the limiting value for which a solution is possible within this self-consistent theory. Here, we generalize the analysis of [17] to the more complicated case of a semi-infinite sample, with a surface parallel to the *ab*-planes [108]. The presence of the surface modifies the elastic properties of the pancake vortex lattice in two ways: *i)* via the appearance of stray fields modifying screening and thus the interaction between pancake vortices; *ii)* via the weakening of the overall out-of-plane potential due to the absence of pancake vortices above the surface. We will see that, for a large part of the phase diagram, the softer crystals at the surface turn unstable *below* the thermodynamic melting transition. This suggests the presence of important precursor effects at the surface.

6.2.1 Substrate model

Even though a complete stability analysis of the full three-dimensional problem is very complicated, the strong anisotropy in the in-plane and out-of-plane interactions allow for an elegant and precise handling of the problem via a dimensional reduction to two dimensions. Each pancake vortex feels an overall aligning force from the remaining vortices in the stack which arises from the sum of many (λ/d) small terms ($\propto d/\lambda$). For small vortex displacements the attractive potential is quadratic,

$$V_{\text{stack}}(u_z) \approx \frac{1}{2}\alpha_0(z)u_z^2, \tag{6.1}$$

where $\alpha_0(z)$ accounts for the overall out-of-plane interaction

$$\alpha_0(z) = \sum_{z'\neq z} \partial_x^2 V_{z',z}(R)\Big|_{R=0} = \partial_x^2 V_{\text{stack}}(R,z)\Big|_{R=0} \tag{6.2}$$

where $V_{z',z}(R)$ is the out-of-plane magnetic interaction (3.27) between pancake vortices in a semi-infinite geometry and $V_{\text{stack}}(R,z)$ the magnetic interaction of a pancake vortex in a semi-infinite stack (3.37). Performing the second derivative in (6.2) with help of (3.37), we obtain

$$\alpha_0(z) = \frac{\varepsilon_0 d}{\lambda^2}\int_0^\infty dK \frac{K}{K_+^2}\Big(1 - \frac{Ke^{-K_+ z}}{K+K_+}\Big). \tag{6.3}$$

The large K divergence of the substrate strength is an artifact of the London approximation which does not account for the suppression of the superconducting density close to the vortex core. Using an upper cut-off of order $\sim 1/\xi$ with $\lambda \gg \xi$, we obtain the bulk result

$$\alpha_0(\infty) \approx \frac{\varepsilon_0 d}{\lambda^2}\ln\frac{\lambda}{\xi} \tag{6.4}$$

while at the surface

$$\alpha_0(0) \approx \frac{\varepsilon_0 d}{2\lambda^2}\ln\frac{\lambda}{\xi} = \frac{\alpha_0(\infty)}{2}. \tag{6.5}$$

This result is easily understood: for short distances the out-of-plane vortex interaction (3.28) at the surface coincides with the bulk one. Thus, the surface substrate strength is only half the bulk one, since it is due to a semi-infinite vortex stack.

At finite temperatures, the vortices still feel a quadratic potential, but its strength is reduced by the thermal fluctuations. We account for this thermal softening in a self-consistent manner by choosing the strength of the harmonic potential $\alpha(z)$ to match the thermal average $\langle\ldots\rangle$ of the real potential,

$$\alpha(z) = \sum_{z\neq z'} \partial_x^2 \langle V_{z',z}(|\mathbf{u}_z - \mathbf{u}_{z'}|)\rangle. \tag{6.6}$$

Equation (6.6) requires to evaluate the thermal average over the in-plane displacements of the vortices in (3.27). Hence, we need to calculate the term $\langle \partial^2_{u_z^x} J_0(K|\mathbf{u}_{z'} - \mathbf{u}_z|)\rangle$; for Gaussian fluctuations, we can use the identity

$$\begin{aligned}\langle \partial^2_{u_z^x} J_0(K|\mathbf{u}_{z'} - \mathbf{u}_z|)\rangle &= -\int_0^{2\pi} \frac{d\phi}{2\pi} K_x^2 \langle e^{iK|\mathbf{u}_{z'}-\mathbf{u}_z|\cos\phi}\rangle \\ &= -\frac{1}{2}K^2 e^{-K^2(\langle u_z^2\rangle + \langle u_{z'}^2\rangle)/4}, \end{aligned} \tag{6.7}$$

where $\langle u_z^2\rangle$ is the mean squared thermal displacement of vortices within the layer z. Hence, the substrate potential becomes a functional of the whole fluctuation profile

$$\begin{aligned}\alpha(z, [\langle u_z^2\rangle]) =& \frac{\varepsilon_0 d^2}{2\lambda^2} \sum_{z'\neq z} \int_0^\infty dK K \frac{e^{-K^2(\langle u_z^2\rangle + \langle u_{z'}^2\rangle)/4}}{K_+} \\ &\times \left(e^{-K_+|z-z'|} + \frac{K_+ - K}{K_+ + K} e^{-K_+(z+z')}\right). \end{aligned} \tag{6.8}$$

Again, we find that the substrate potential depends on z and, thus, it is different at the surface and in the bulk. However, we will see below that the thermal fluctuations strongly reduce this difference when compared to the $T = 0$ results (6.4) and (6.5),

6.2.2 Evaporation of an infinite and of a semi-infinite vortex stack

Before tackling the full problem of a semi-infinite system at finite magnetic fields, we study the low-field limit in detail. We show that the enhanced thermal fluctuations strongly reduce the difference between $\alpha_0(0)$ and $\alpha_0(\infty)$, and that the surface is essentially ineffective in this limit. We start the discussion with the infinite bulk case [17], which serves as a guideline to illustrate the substrate approach.

In the bulk, the system is translation invariant and the value of the pancake vortex fluctuations are independent of z. With the definition $\langle u^2\rangle \equiv \langle u_z^2\rangle$, the substrate potential becomes

$$\alpha(\langle u^2\rangle) = \frac{\varepsilon_0 d^2}{2\lambda^2} \int_0^\infty K dK \sum_{z'\neq z} \frac{e^{-K_+|z| - K^2\langle u^2\rangle/2}}{K_+}. \tag{6.9}$$

Going over to a continuous description along z', the sum over all layers can be written as

$$\sum_{z'\neq z} e^{-K_+|z-z'|} \approx \int_{-\infty}^{\infty} \frac{dz'}{d} e^{-K_+|z-z'|} - 1, \tag{6.10}$$

where we have been careful to exclude the layer with the test vortex at z. We have to retain this contribution, although it is of order d/λ, if we want to study the modifications of the vortex stack dissociation at the surface. Carrying out the integral over z', we obtain

$$\alpha(\langle u^2\rangle) = \frac{\varepsilon_0 d^2}{2\lambda^2} \int_0^{\infty} K dK \frac{e^{-K^2\langle u^2\rangle/2}}{K_+} \Big(\frac{2}{dK_+} - 1\Big). \tag{6.11}$$

As the temperature of the vortex stack dissociation transition is approached from below, vortex fluctuations become large: $\langle u^2\rangle \gg \lambda^2$. In this limit we can carry out the integral over K, yielding

$$\alpha(\langle u^2\rangle) \sim \frac{\varepsilon_0 d}{\langle u^2\rangle}\Big(1 - \frac{d}{2\lambda}\Big)\Big(1 - \frac{2\lambda^2}{\langle u^2\rangle}\Big). \tag{6.12}$$

Using the equipartition theorem for quadratic potentials, we obtain a second relation between $\langle u^2\rangle$ and α,

$$\langle u^2\rangle = \frac{2T}{\alpha(\langle u^2\rangle)}. \tag{6.13}$$

We can therefore solve for the fluctuations and obtain

$$\langle u^2\rangle \sim \frac{2\lambda^2}{1 - T/T_{\mathrm{BKT}}^{(\infty)}}, \tag{6.14}$$

where we have defined (cf. (4.1) together with (2.66))

$$T_{\mathrm{BKT}}^{(\infty)} = \frac{\varepsilon_0 d}{2}\Big(1 - \frac{d}{2\lambda}\Big). \tag{6.15}$$

Combining (6.12) together with (6.14), we see that the substrate potential collapses exactly at the BKT transition temperature $T_{\mathrm{BKT}}^{(\infty)}$. At this temperature the vortex fluctuations diverge, leading to the dissociation of the stack into unbound pancake vortices, as discussed in Chapter 4. Thus, the substrate potential is able to reproduce correctly the evaporation of the vortex stack at $T_{\mathrm{BKT}}^{(\infty)}$.

In a semi-infinite geometry, the system loses its translation invariance along z. As a consequence, the pancake vortex fluctuations $\langle u_z^2\rangle$ are not constant throughout the sample and the z dependence must be retained in the calculations. The solution of the problem in terms of the substrate potential requires to handle a coupled set of integral equations for different z. However, if we are only interested in an estimate of the substrate potential at the dissociation transition, we can equivalently look at the in-plane BKT vortex–anti-vortex pair unbinding. By combining (3.22) with (4.1), we find that the surface superconducting layer undergoes a BKT transition at

$$T_{\mathrm{BKT}}^{\mathrm{surf}} = \frac{\varepsilon_0 d}{2}\Big(1 - \frac{d}{\lambda}\Big). \tag{6.16}$$

Surface vortices dissociate at a slightly lower temperature with respect to the bulk but the effect is small, of order d/λ. Hence, the collapse of the individual vortex stack in the bulk and at the surface occurs approximately at the same temperature $T_{\mathrm{BKT}}^{(\infty)} \approx T_{\mathrm{BKT}}^{\mathrm{surf}}$, showing that, in this single stack/low-field limit, the $(T = 0)$ difference between the substrate potential at the surface and in the bulk is strongly reduced.

6.2.3 Surface instability of the pancake vortex lattice

At any finite magnetic fields, the pancake vortices arrange themselves in aligned 2D lattices, resembling the triangular lattice of vortex lines which we have described in Sec. 2.4. The relevant excitations correspond to deformations $\mathbf{u}(\mathbf{R}, z)$ of the 2D lattices which are described, for each z, by the elastic 2D free energy

$$\mathcal{F}_z^{\mathrm{2D}}[\mathbf{u}] = \frac{1}{8\pi^2}\int_{\mathrm{BZ}} d^2\mathbf{K} u_z^i(\mathbf{K})\Phi_{ij}(\mathbf{K}, z)u_z^j(-\mathbf{K}), \tag{6.17}$$

where $\Phi_{ij}(\mathbf{K}, z)$ is the elastic matrix of the lattice at z and u_z^i is the i-th component of the 2D displacement at z $(i = x, y)$.

At high magnetic fields, the in-plane interactions become the dominant ones and the system splits into independent 2D lattices. For a two dimensional triangular crystal, the in-plane elastic matrix Φ contains only the compression $(\delta_{ij} - \hat{K}_i\hat{K}_j)\Phi_{ij}^{\mathrm{2D}}(\mathbf{K}) = c_{66}K^2$ and the shear $\hat{K}_i\hat{K}_j\Phi_{ij}^{\mathrm{2D}}(\mathbf{K}) = c_{11}(K)K^2$ projections. Ignoring small contributions of order d/λ in (3.21), pancake vortices repel logarithmically on all scales, cf. Eq. (3.23). The long range interaction makes the system incompressible: retaining only the $\nu = 0$ term in (2.39), we find a strongly dispersive compression modulus

$$c_{11}(K) = \frac{4\pi\varepsilon_0 d n_{\mathrm{v}}^2}{K^2}, \tag{6.18}$$

which is divergent for long wave deformations $K \to 0$. On the other hand, due to the long range nature of the inter-vortex interactions, the calculation of the shear elastic modulus becomes a highly non-trivial task, since all terms in the elastic sum must be retained. Nevertheless a solution of this problem is available in the context of uncharged superfluid systems [34], e.g. ^{4}He. As a final result, the expression (2.43)

$$c_{66} = \frac{\varepsilon_0 d n_\mathrm{v}}{4}, \tag{6.19}$$

which was derived for the screened logarithmic potential $\propto K_0(R)$, remains valid also for unscreened logarithmically interacting particles. This result can be understood with the following simple argument. If we rewrite (6.19) $c_{66} = \varepsilon_0 d n_\mathrm{v}/4 = h^2 n_s n_\mathrm{v} d/16m$ the charge e drops out and, thus, magnetic screening does not play a role in the determination of c_{66} (n_s is the superfluid density, we have used the expression (2.26) and $\Phi_0 = hc/2e$). Hence, an unscreened logarithmic potential and a screened one (e.g. $K_0(R)$) generate the same shear modulus (2.43). In the high field limit the surface does not enter in the elastic constants. Hence, the system is composed of independent and equal 2D lattices of vortices which interact with the same logarithmic interaction. As a result, the instability temperature is equal in all layers and the surface turns out to be ineffective also in the limit $B \gg B_\lambda$.

So far we have shown that in both the low and high magnetic field limits no important effects from the surface can be expected. However, for intermediate values of B the full three dimensional nature of the problem is relevant. Each 2D lattice feels a periodic stabilizing potential from the pancake vortex stacks, which stiffens the elastic modes of the 2D logarithmically interacting vortices. Within the self-consistent harmonic approximation (SCHA) the energetic contributions associated with the elastic distortions of the lattice are described by an effective quadratic hamiltonian with renormalised elastic moduli,

$$\Phi_{ij}(\mathbf{K}, z, [\langle u_z^2 \rangle]) = \Phi_{ij}^{\mathrm{2D}}(\mathbf{K}, \langle u_z^2 \rangle) + n_\mathrm{v} \alpha(z, [\langle u_{z'}^2 \rangle]) \delta_{ij}. \tag{6.20}$$

The 2D elastic matrix, softened by pancake vortex fluctuations, is

$$\Phi_{ij}^{\mathrm{2D}}(\mathbf{K}, \langle u_z^2 \rangle) = \varepsilon_0 d n_\mathrm{v}^2 \sum_{\mathbf{K}_\nu} \Big[f_{ij}^z(\mathbf{K}_\nu + \mathbf{K}) - f_{ij}^z(\mathbf{K}_\nu) \Big], \tag{6.21}$$

where $f_{ij}^z(\mathbf{K}) = K_i K_j (4\pi/K^2) \exp[-K^2 \langle u_z^2 \rangle]$ is reduced by the vortex fluctuations via the Debye-Waller factor. It follows that the 2D shear elastic constant $c_{66}(\langle u_z^2\rangle)$ is softened within the SCHA by the thermal fluctuations $\langle u_z^2\rangle$. It recovers the usual form for the 2D vortex lattice at $T=0$, where $\langle u_z^2\rangle = 0$. The stack potential at finite magnetic field derives from the sum over the vectors of the reciprocal lattice $\mathbf{K}_\nu$

$$\begin{aligned}\alpha(z,[\langle u_{z'}^2\rangle]) = 2\pi n_\mathrm{v}\varepsilon_0 d^2 \sum_{\mathbf{K}_\nu}\int_0^\infty \frac{dz'}{d}\,\frac{e^{-K_\nu^2(\langle u_z^2\rangle+\langle u_{z'}^2\rangle)/4}}{\lambda^2 K_\nu^+}\\ \times\left(e^{-K_\nu^+|z-z'|}+\frac{K_\nu^+-K_\nu}{K_\nu^++K_\nu}e^{-K_\nu^+(z+z')}\right),\end{aligned}\qquad(6.22)$$

with $K_\nu^+ = \sqrt{K_\nu^2+1/\lambda^2}$. The difference between the bulk and the surface lattices is due to the substrate potential, which can differ appreciably when thermal fluctuations are not too large (cf. the discussion of the $T=0$ limit for $\alpha(z)$ in Sec. 6.2.2).

The surface breaks the translation symmetry in the z direction, making the determination of the substrate potential a non-trivial task. Within the SCHA, one has to solve the following set of equations (for different z) for the fluctuations $\langle u_z^2\rangle$ self-consistently,

$$\langle u_z^2\rangle = T\int_\mathrm{BZ}\frac{d^2\mathbf{K}}{(2\pi)^2}[\Phi^{-1}]_{ii}(\mathbf{K},z,\langle u_z^2\rangle),\qquad(6.23)$$

where $\langle u_z^2\rangle$ enters also in the elastic matrix. In particular, the substrate potential $\alpha(z,[\langle u_{z'}^2\rangle])$ depends on the fluctuation profile $\langle u_z^2\rangle$ and couples different positions z in (6.23). Assuming a circular Brillouin zone with $K_\mathrm{BZ} = \sqrt{4\pi}/a_0$, the integral over K yields

$$\begin{aligned}\langle u_z^2\rangle = &\frac{T}{4\pi c_{66}(\langle u_z^2\rangle)}\ln\Big(1+\frac{c_{66}(\langle u_z^2\rangle)K_\mathrm{BZ}^2}{n_\mathrm{v}\alpha(z,[\langle u_{z'}^2\rangle])}\Big)+\\ &\frac{T}{4\pi c_{11}(K_\mathrm{BZ})+\alpha(z,[\langle u_{z'}^2\rangle])}.\end{aligned}\qquad(6.24)$$

The stack evaporation and the high field limit are recovered as special cases of (6.24). At low magnetic fields the elastic moduli can be neglected in comparison to the substrate potential, giving $\langle u_z^2\rangle = 2T/\alpha(z,[\langle u_{z'}^2\rangle])$. On the other hand, at large magnetic fields the relevant modes are the shear deformations. The substrate potential acts as a large K cut-off for shear fluctuations which otherwise would diverge logarithmically. Therefore, the substrate potential provides only a small logarithmic correction to the two dimensional scenario. In this regime, even if the substrate potential at the surface is reduced with respect to the bulk (cf. Eqs. (6.4)-(6.5)), the system is effectively two dimensional and no relevant modifications appear at the surface.

To tackle the full problem at any value of the magnetic field we have solved Eq. (6.23) numerically by testing different variational Ansätze for the function $\langle u_z^2\rangle$. For a given shape of the fluctuation profile $\langle u_z^2\rangle$, we can carry out the integral in z in (6.22) and derive an expression for the substrate potential as a function of few variational parameters. Solving a convenient number (equal to the number of the variational parameters) of Eqs. (6.23) at different values of z, we can fix the values of the parameters and find an approximate solution for the function $\langle u_z^2\rangle$. The accuracy of the solution can be checked by inserting the fluctuation profile back in the right hand side of Eq. (6.23) and examining the accuracy of the solution of the self-consistent set of equations for arbitrary z.

We have found that the exponential Ansatz

$$\langle u_z^2\rangle = \langle u_\mathrm{b}^2\rangle + e^{-z/\lambda\tau}(\langle u_\mathrm{s}^2\rangle - \langle u_\mathrm{b}^2\rangle) \tag{6.25}$$

characterized by the three free parameters $\langle u_\mathrm{s}^2\rangle$, $\langle u_\mathrm{b}^2\rangle$, and τ yields results accurate to about 1.5%. Inserting this Ansatz in (6.22), we obtain an expression for the substrate potential as a function of these three parameters

$$\begin{aligned}\alpha(z) = \pi\epsilon_0 d\tau n_\mathrm{v} \sum_{K_\mu\neq 0} & \frac{e^{-K_\mu^2(\langle u^2(z)\rangle+\langle u_b^2\rangle)/4}}{\lambda K_\mu^+} \qquad (6.26)\\ & \times \Big[e^{-K_\mu^+ z}(K_u)^{\lambda K_\mu^+\tau}\,\Gamma(-\lambda K_\mu^+\tau, K_u e^{-z/\lambda\tau}, K_u)\\ & + e^{K_\mu^+ z}(K_u)^{-\lambda K_\mu^+\tau}\,\Gamma(\lambda K_\mu^+\tau, K_u e^{-z/\tau\lambda}, \infty)\\ & + e^{-K_\mu^+ z}\left(\frac{\lambda K_\mu^+ - \lambda K_\mu}{\lambda K_\mu^+ + \lambda K_\mu}\right)(K_u)^{-\lambda K_\mu^+\tau}\,\Gamma(\lambda K_\mu^+\tau, K_u, \infty)\Big],\end{aligned}$$

where $K_u = (K_\mu^2/4)(\langle u_\mathrm{s}^2\rangle - \langle u_\mathrm{b}^2\rangle)$ and Γ is the incomplete Euler Gamma function

$$\Gamma(x,a,b) = \int_a^b e^{-t}t^{x-1}dt. \tag{6.27}$$

By inserting Eq. (6.26) in (6.23) for a given value of z, one obtains an equation with the three unknown variables $\langle u_\mathrm{s}^2\rangle$ and $\langle u_\mathrm{b}^2\rangle$ and τ. Considering Eq. (6.23) for three different values of z (we choose $z = 0$, $z = \lambda/2$ and $z = \infty$), we obtain the values of $\langle u_{\rm s}^2\rangle$ and $\langle u_{\rm b}^2\rangle$ and τ. The values of these parameters depend on temperature and magnetic field. For a fixed value of T, at low fields we always find larger fluctuations at the surface $\langle u_{\rm s}^2\rangle > \langle u_{\rm b}^2\rangle$, suggesting that the surface lattices are softer than the bulk ones and, thus, more sensitive to thermal fluctuations. Increasing the value of the magnetic field, both $\langle u_{\rm s}^2\rangle$ and $\langle u_{\rm b}^2\rangle$ increase up to the field $B_{\rm surf}$ where no solution is found at the surface, $z = 0$. We interpret this results as the instability of the surface layer. The instability line $(T_{\rm surf}, B_{\rm surf})$ in the phase diagram is then obtained by calculating the value of $B_{\rm surf}$ for different temperatures T. The instability is triggered by enhanced fluctuations at the surface which produce a large $\langle u_{\rm s}^2\rangle$, cf. [103]. We obtain that along the surface instability line the mean squared displacement $\langle u_{\rm s}^2\rangle$ on the surface layer becomes comparable with the lattice constant $\langle u_{\rm s}^2\rangle \sim 0.1\, a_0^2$. This result is consistent with a Lindemann parameter $c_{\rm L} \approx 0.3$, cf. Sec. 2.5.

It is known that the SCHA usually overestimates the instability temperature [90]. A more accurate scheme is provided by the 2-Vertex SCHA (2V-SCHA) [90], which includes more anharmonic terms in the perturbation expansion about the harmonic approximation. In Fig. 6.1 we show the instability line for the surface layer calculated within a 2V-SCHA using an exponential Ansatz for the fluctuation profile. We compare this result with the bulk instability line and melting line, as obtained in [41] from Monte Carlo/molecular dynamics simulations. We find that for temperatures $T/\varepsilon_0 d \lesssim 0.205$ the surface becomes unstable below the bulk thermodynamic melting temperature. As a result, we conclude that in this temperature regime the solid phase is stable below the surface instability line, where a solution for the self-consistent set of equations can be found in all layers. We can also conclude that above the bulk instability line, no solid, not even a metastable one, can appear. However, within this analysis one cannot describe the state of the system between surface and bulk instability lines, where both the liquid and solid phases should be accounted for. To obtain a complete picture one needs a better analysis, able to treat both solid and liquid phases on equal footing, cf. the density functional theory analysis in the next sections.

At low magnetic fields, which correspond to temperatures larger than $T/\varepsilon_0 d \approx 0.205$ (see inset of Fig. 6.1), we find that the surface instability line lies above the melting line. In this regime we expect no important effects from the surface. This agrees with the analysis of the dissociation of an

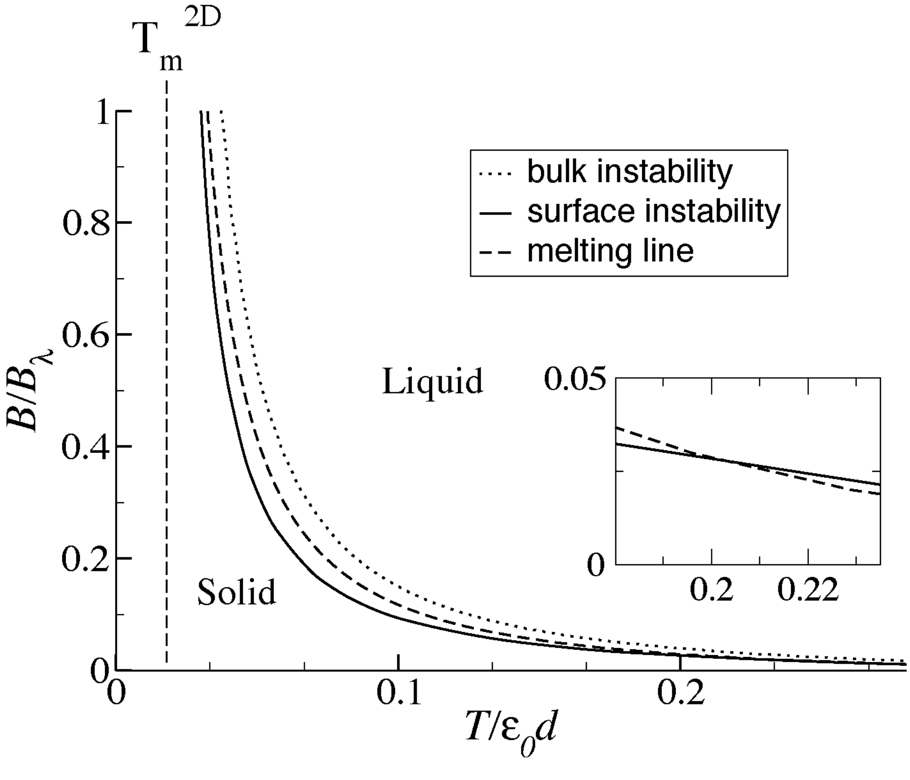

Figure 6.1: Results of the stability analysis of the vortex lattice at the surface (solid line) and comparison with the bulk instability line (dotted line) and the bulk melting line (dashed line) of Refs. [17, 41]. The magnetic field unit is $B_\lambda = \Phi_0/\lambda^2$. The melting temperature $T_{\rm m}^{\rm 2D}/\varepsilon_0 d \approx 1/70 \approx 0.014$ of the individual two dimensional layer [42] is showed by the dashed vertical line. At low magnetic fields (inset) the surface becomes unstable above the bulk melting line. In this high-temperature/low-field regime we expect no important effect from the surface.

isolated vortex stack at the beginning of this section, where we have found no modifications on the surface (up to order d/λ).

6.3 DFT analysis of the surface melting

A more detailed study of the effects of the surface on the melting transition requires an analysis which is not limited to the solid phase alone. To this end, a more convenient technique is provided by the substrate-DFT approach which we have used in Chapter 5 to study the melting transition in the bulk. This approach provides us with an accurate order parameter theory which can handle both solid and liquid phases in a unified manner [109].

The energy difference relative to the homogeneous liquid is given by the expression (5.67) for a non uniform order parameter in a bulk system. The presence of a surface modifies the bulk expression (5.67) in two ways: *i)* the superconductor occupies only a half-infinite space $z > 0$, *ii)* stray magnetic fields modify the vortex interaction and hence the direct correlation function $\bar{c}_{z,z'}$; therefore, for the present system the free energy density becomes

$$\frac{\delta\omega[\mu_z]}{T} = \int_0^\infty \frac{dz}{d}\Big[-\Phi(\xi_z) + 6\xi_z\mu_z - 3\int_0^\infty \frac{dz'}{d}\bar{c}_{z,z'}\mu_{z'}\mu_z\Big], \tag{6.28}$$

where ξ_z is understood as a function of μ_z through $\mu_z = \Phi'(\xi_z)/6$ and $\Phi(\xi)$ is defined in (5.25). In (6.28) the function

$$\bar{c}_{z,z'} = \bar{c}^{\mathrm{2D}} d\delta(z-z') - V_{z,z'}(G)/T \tag{6.29}$$

is the direct correlation function $\bar{c}_{z,z'} = c_{z,z'}(G)$ evaluated at the first reciprocal lattice vector ($G^2 = 8\pi^2\bar{\rho}/\sqrt{3} = 8\pi^2 B/\sqrt{3}\Phi_0$). It includes the effects of stray fields through the out-of-plane interaction $V_{z,z'}(G)$ of Eq. (3.27) and replaces the translation-invariant expression $\bar{c}_{z-z'} = \bar{c}^{\mathrm{2D}} d\delta(z-z') - V_{z-z'}(G)/T$ in (5.67). From (3.27), we obtain the dimensionless Fourier transform of the out-of-plane potential,

$$\begin{aligned}\frac{V_{z,z'}(G)}{T} &= -\frac{\pi\Gamma d}{G^2\lambda^2 G_+}\Big(e^{-G_+|z-z'|} + \frac{G_+ - G}{G_+ + G}e^{-G_+(z+z')}\Big)\\ &= -\bar{\alpha}(\bar{f}_{z-z'} + \bar{\beta}\bar{f}_{z+z'}),\end{aligned} \tag{6.30}$$

with $G_+ = \sqrt{G^2 + \lambda^{-2}}$ and $\Gamma = 2\varepsilon_0 d/T$ the one component plasma parameter. In (6.30) we have defined the function $\bar{f}_z = f_z(G) = \exp(-G_+|z|)$ and the quantities $\bar{\alpha} = \alpha(G) = \pi\bar{\rho}\Gamma d/G^2\lambda^2 G_+$ and $\bar{\beta} = (G_+ - G)/(G_+ + G)$. After some simple algebraic manipulations the free energy can be written in the more convenient form

$$\frac{\delta\omega[\mu_z]}{T} = \int_0^\infty \frac{dz}{d}\Big[\frac{\delta\omega^{\rm 2D}_{\rm sub}(\mu_z)}{T} + \frac{3\bar{\alpha}}{2}\int_0^\infty \frac{dz'}{d}(\bar{f}_{z-z'} + \bar{f}_{z+z'})(\mu_z - \mu_{z'})^2\Big] + \frac{6\bar{\alpha}G}{G+G_+}\int_0^\infty \frac{dz}{d}\int_0^\infty \frac{dz'}{d}\,\bar{f}_{z+z'}\mu_z\mu_{z'}, \tag{6.31}$$

where like in (5.68) the first term describes the free energy of a homogeneous system (5.43)

$$\frac{\delta\omega^{\rm 2D}_{\rm sub}(\mu)}{T} = 6\xi(\mu)\mu - 3\bar{c}^{\rm 3D}\mu^2 - \Phi(\xi(\mu)), \tag{6.32}$$

with the full correlator $\bar{c}^{\rm 3D} = \bar{c}^{\rm 2D} - V_{\rm stack}(G)/T$ (cf. (5.26)) which includes the contributions from the 2D OCP in-plane component $\bar{c}^{\rm 2D}$ and the *bulk* substrate potential $V_{\rm stack}(G)/T = -2\bar{\alpha}/G_+ d$. Comparing (6.31) with the corresponding bulk expression (5.68), we see that the surface free energy contains a mirror term (the term $\propto \bar{f}_{z+z'}$ in the first line) and a pure surface term (second line), see the discussion in Sec. 3.4.1.

The configuration of the system is derived from the saddle-point of (6.31). Minimization with respect to μ_z provides us with the integral equation

$$\frac{\partial_{\mu_z}\delta\omega^{\rm 2D}_{\rm sub}(\mu_z)}{T} + 6\bar{\alpha}\int_0^\infty \frac{dz'}{d}[\bar{f}_{z-z'} + \bar{f}_{z+z'}](\mu_z - \mu_{z'}) + \frac{12\bar{\alpha}G}{G+G_+}\int_0^\infty \frac{dz'}{d}\,\bar{f}_{z+z'}\,\mu_{z'} = 0. \tag{6.33}$$

In the following, we first acquaint ourselves with the formalism by studying the $B \approx 0$ and large field limits. Then, we present the full analysis at arbitrary values of the magnetic field.

6.3.1 Large magnetic field and $B \approx 0$ limits

Let us consider firstly large magnetic fields, i.e., $B \gg B_\lambda$. In this limit, the contribution of the out-of-plane potential vanishes ($G \approx (B/\Phi_0)^{1/2} \to \infty$ and $\bar{\alpha} \to 0$) and the system decouples into independent two-dimensional systems. Only the intra-layer interaction becomes relevant in this limit; hence, the free energy is simply

$$\frac{\delta\omega[\mu_z]}{T} \overset{B\gg B_\lambda}{\approx} \int_0^\infty \frac{dz}{d}\,\frac{\delta\omega^{\rm 2D}_{\rm sub}(\mu_z)}{T}. \tag{6.34}$$

This free energy is given by the bulk expression (cf. Fig. 5.2), which we have already studied in Sec. 5.6. In this high-field limit the correlator $\bar{c}^{\rm 3D}_{\rm sub}$ (cf. (5.45)) reduces to the 2D-OCP component $\bar{c}^{\rm 2D}$ which is z-independent. The saddle point equation $\partial_{\mu_z}\delta\omega^{\rm 2D}_{\rm sub}(\mu_z)/T = 0$ does not depend on z and the solution is given by a constant order parameter profile. Thus, no modifications occur at the surface for $B \gg B_\lambda$.

In the opposite limit of $B \approx 0$ ($G \approx 0$), $\bar{\alpha}$ remains finite. Since $G_+ \approx 1/\lambda$, the surface term in (6.31) is negligible and the free energy becomes

$$\frac{\delta\omega[\mu_z]}{T} \overset{B\approx 0}{\approx} \int_0^\infty \frac{dz}{d}\Big[\frac{\delta\omega^{\rm 2D}_{\rm sub}(\mu_z)}{T} + \frac{3\bar{\alpha}}{2}\int_0^\infty \frac{dz'}{d}(\bar{f}_{z-z'}+\bar{f}_{z+z'})(\mu_z-\mu_{z'})^2\Big]. \quad (6.35)$$

The solution of the associated saddle point equation,

$$\frac{\partial_{\mu_z}\delta\omega^{\rm 2D}_{\rm sub}(\mu_z)}{T} + 6\bar{\alpha}\int_0^\infty \frac{dz'}{d}[\bar{f}_{z-z'} + \bar{f}_{z+z'}](\mu_z - \mu_{z'}) = 0, \quad (6.36)$$

contains an additional term as compared to (6.35). However, this additional term involves the difference $\mu_z - \mu_{z'}$ and thus it is equal to zero for a constant profile of the order-parameter. As a result, the bulk constant solution is still a valid solution and the surface is irrelevant also in this limit.

We can conclude that for both $B \approx 0$ and $B \gg B_\lambda$ the surface does not lead to a modification of the bulk behavior, in agreement with the results of the stability analysis in Sec. 6.2.3

6.3.2 Low magnetic fields

At any finite magnetic fields, the $B \approx 0$ expression of the free energy functional (6.35) is modified by the presence of the additional surface term (cf. (6.31))

$$\begin{aligned}\frac{\delta\omega^{\rm s}[\mu_z]}{T} &= \frac{6\bar{\alpha}G}{G+G_+}\int_0^\infty \frac{dz}{d}\int_0^\infty \frac{dz'}{d}\,\bar{f}_{z+z'}\mu_z\mu_{z'} \\ &= \frac{6\bar{\alpha}G}{G+G_+}\Big(\int_0^\infty \frac{dz}{d}\,e^{-G_+ z}\mu_z\Big)^2. \end{aligned} \quad (6.37)$$

This new term is produced by the modifications of the pancake-vortex interactions close to the surface and acts as a destabilizing potential ($\sim \mu_0^2$) which favors the appearance of the liquid phase on the topmost layers. In real space this term is associated with the $\propto 1/R$ repulsive potential induced by the stray magnetic field, cf. the second term in (3.30). When the bulk is in the solid phase, the non-local elastic energy in (6.35) competes against this surface term (6.37) by favoring the bulk solid solution. This interplay between the surface potential and the elastic energy is the key point in the discussion of the surface melting.

Similarly to the Landau-theory description of a first order phase transition in a semi-infinite system [107], diverse scenarios may arise depending on the strength of the surface destabilizing potential. The different scenarios can be distinguished by the behavior of the order parameter on the surface at the bulk transition temperature. For weak surface modifications the order parameter on the surface μ_0 jumps across the melting line from $0 < \mu_0 < \mu_\infty = \mu_{\mathrm{s}}$ to zero, leading to a discontinuous surface melting (named surface non-melting in [24] or O_1 transition in [22]). On the other hand, for a sufficiently strong destabilizing potential the order parameter goes continuously to zero when the system melts at T_{m} (surface melting or O_2 transition) even if the transition is discontinuous in the bulk.

To make progress analytically, we have to simplify the non-local terms in (6.33). Concentrating on the bulk, i.e., $z \gg 1/G_+$, both mirror and surface terms can be ignored. For not too large values of the magnetic fields, we can adopt a gradient expansion of the non-local elastic term $\propto \bar{f}_{z-z'}$, cf. Sec. 5.8 and Appendix C. As a result we obtain the differential equation

$$\ell^2 \frac{d^2\mu_z}{dz^2} = \frac{d}{d\mu}\frac{\delta\omega^{\mathrm{2D}}_{\mathrm{sub}}(\mu_z)}{T} \tag{6.38}$$

with $\ell^2 = (6\bar{\alpha}/d)\int_0^{+\infty} dz\ \bar{f}_z z^2 = 12\bar{\alpha}/d\,G_+^3$. Equation (6.38) has to be completed with a boundary condition, which has to be provided by the surface part of the integral equation. In the following, we restrict the analysis to small values of the order parameter at the surface in order to study the interplay between continuous and discontinuous surface melting scenarios. In this regime the bulk potential can be approximated as

$$\frac{\delta\omega^{\mathrm{2D}}_{\mathrm{sub}}(\mu)}{T} \approx 3(1-\bar{c}_c)\mu^2, \tag{6.39}$$

since $\bar{c}^{\mathrm{3D}} = \bar{c}_c \approx 0.856$ at melting. The saddle point equation becomes a linear integral equation

$$\begin{aligned} 6(1-\bar{c}_c)\mu_z + 6\bar{\alpha}\int_0^\infty \frac{dz'}{d}[\bar{f}_{z-z'} + \bar{f}_{z+z'}](\mu_z - \mu_{z'}) + \\ + \frac{12\bar{\alpha}G}{G+G_+}\int_0^\infty \frac{dz'}{d}\,\bar{f}_{z+z'}\,\mu_{z'} = 0, \end{aligned} \tag{6.40}$$

which contains three terms: two dimensional potential (first), non-local elastic term (second) and the pure surface term (third). Separating the non-local terms from the local ones, we obtain

$$\left[6(1-\bar{c}_c)+\frac{12\bar{\alpha}}{dG_+}\right]\mu_z = 6\bar{\alpha}\int_0^\infty \frac{dz'}{d}[\bar{f}_{z-z'}+\bar{\beta}\bar{f}_{z+z'}]\,\mu_{z'}, \tag{6.41}$$

where we have used $\int_0^\infty (dz'/d)[\bar{f}_{z-z'}+\bar{f}_{z+z'}] = 12\bar{\alpha}/G_+d$ and again $\bar{\beta} = (G_+ - G)/(G_+ + G)$. This kind of integral equations are commonly found in the study of boundary problems, e.g. in the analysis of the surface effects on the superconducting transition [76, 110]. For the latter case, the equation which determines the superconducting gap $\Delta(r)$ is a non-local integral equation with a structure similar to (6.41). In the bulk the kernel is translation invariant. Close to T_c, a gradient expansion reduces the non-local equation into the local Ginzburg-Landau equation (2.4). The presence of the surface enters in the kernel of the original non-local theory via an additional 'mirror' term, similar to the $\propto \bar{f}_{z+z'}$ term in (6.41). However, a major difference between these two similar problems is given by the different nature of the bulk phase transitions: first order for melting and second order for the superconducting transition. In the case of a second order phase transition the coefficient of the quadratic term in the bulk free energy goes to zero at the transition point, cf. the coefficient $\alpha \sim (T - T_c)$ in (2.4). Hence, the first term in the square brackets in the LHS of (6.41) would be absent.

Equation (6.41) can be rewritten as

$$\mu_z = \frac{G_+}{2(1+r)}\int_0^\infty dz'\,[\bar{f}_{z-z'}+\bar{\beta}\bar{f}_{z+z'}]\,\mu_{z'}, \tag{6.42}$$

with $r = dG_+(1-\bar{c}_c)/2\bar{\alpha} = 6(1-\bar{c}_c)/(G_+\ell)^2$. In this formula the difference between a first and a second order bulk transition enters in the normalization of the integral in the RHS, through the parameter r, which is $r \neq 0$ for a first order transition and $r = 0$ for a second order one (due to the absence of the linear term from the bulk free energy (6.41)).

In general, the solution of an integral equation like (6.42) is a non-trivial task, which usually cannot be carried out exactly. However, in the present case a straightforward solution is possible due to the particular exponential structure of the kernel. In fact, by taking the second derivative of (6.42) and making use of the identity

$$\frac{d^2}{dz^2}e^{-G_+|z-z'|} = -2G_+\delta(z-z') + G_+^2 e^{-G_+|z-z'|}, \tag{6.43}$$

we find that the integral equation yields the *same* differential equation (6.38) derived previously in the bulk by means of a gradient expansion,

$$(1+r)\ell^2\frac{d^2\mu_z}{dz^2} \approx \ell^2\frac{d^2\mu_z}{dz^2} = 6(1-\bar{c}_c)\mu_z; \tag{6.44}$$

here we have used the linearized force $\partial_\mu \delta\omega^{\rm 2D}_{\rm sub}(\mu)/T = 6(1-\bar{c}_c)\mu_z$. We drop the small renormalization factor $(1+r)\approx 1$, which is absent in the gradient expansion of the bulk equation. This difference is due to the higher order derivatives $\partial_z^n\mu_z$ that are neglected in the gradient expansion (see Appendix C). This differential equation admits two exponential solutions. For the case of a second order bulk transition, due to the absence of a linear term in the bulk free energy, the differential equation which is obtained after derivation is $d^2\mu_z/dz^2 = 0$ which is solved by a linear function [76]. Anyway, in both cases the differential equations coincide with the linearized bulk equations (6.38) and show no trace of the surface term $\propto \bar{\beta}$. Thus, the integral equation (6.42) is equivalent to the *bulk* differential equation (6.44) and the effect of the surface terms is to provide a boundary condition at $z=0$. This is a lucky coincidence due to the particular exponential structure of the kernel. Normally, the bulk solution is not valid in the vicinity of the surface and the problem becomes much more difficult to solve.

To solve the integral equation (6.42), we need to find the boundary condition which is provided by the surface term. We first write the general solutions of the bulk differential equation

$$\mu_z = Ae^{\gamma G_+ z} + Be^{-\gamma G_+ z}, \tag{6.45}$$

where $\gamma^2 = r/(1+r)$. Here we retain the small correction $(1+r)$ in (6.44) since the following analysis is based on the linearized integral equation (dropping this term leads to results which are correct to order r, in agreement with the precision of the gradient expansion). Inserting this Ansatz back into (6.42), we obtain

$$\begin{aligned} Ae^{\gamma G_+ z} + Be^{-\gamma G_+ z} &= Ae^{\gamma G_+ z} + Be^{-\gamma G_+ z} \\ &+ \frac{e^{-G_+ z}}{2(1+r)}\Big[A\Big(\frac{\bar{\beta}}{1-\gamma} - \frac{1}{1+\gamma}\Big) + B\Big(\frac{\bar{\beta}}{1+\gamma} - \frac{1}{1-\gamma}\Big)\Big]. \end{aligned} \tag{6.46}$$

In order to fulfill this equation the term in the square brackets in the second line must be zero. This requirement selects a unique value of the ratio B/A,

$$\frac{B}{A} = \frac{\gamma(\bar{\beta}+1) - (\bar{\beta}-1)}{\gamma(\bar{\beta}+1) + (\bar{\beta}-1)}. \tag{6.47}$$

Finally, we can calculate the logarithmic derivative at $z = 0$, which is the relevant boundary condition in our forthcoming analysis (we define $\mu_z' = \partial_z \mu_z$)

$$\frac{\mu_z'}{\mu_z}\bigg|_{z=0} = G_+ \frac{1-\bar{\beta}}{1+\bar{\beta}} = G. \tag{6.48}$$

This final relation can also be derived directly without solving the differential equation at the surface. One only needs to calculate the value of the order parameter and its derivative at $z = 0$ from (6.42),

$$\begin{aligned}\mu_0 &= \frac{G_+}{2(1+r)}(1+\bar{\beta}) \int_0^\infty dz \bar{f}_z \mu_z, \\ \frac{d\mu_z}{dz}\bigg|_{z=0} &= \frac{G_+}{2(1+r)} G_+(1-\bar{\beta}) \int_0^\infty dz \bar{f}_z \mu_z.\end{aligned}$$

The ratio μ_0'/μ_0 does not depend on the function μ_z which drops out. As a result we recover (6.48), which remains valid for the case of a bulk second order phase transition ($r = 0$). In the limit $B \approx 0$ in (6.48), the boundary condition becomes $\mu_0' = 0$, since $G \approx 0$. Hence, the constant bulk solution goes though and the surface is not relevant, in agreement with the results of the last section.

The analysis of the boundary value problem (6.38) and (6.48) follows the one in Ref. [107]. Combining the boundary condition (6.48) with the expression for the 'conserved energy' originating from the bulk equation

$$\ell \frac{d\mu_z}{dz} = \sqrt{\frac{2\delta\omega_{\text{sub}}^{\text{2D}}(\mu_z)}{T}}, \tag{6.49}$$

we find an algebraic relation which determines the value of the order parameter μ_0 at the surface,

$$\mu_0 \ell G = \sqrt{\frac{2\delta\omega_{\text{sub}}^{\text{2D}}(\mu_0)}{T}}. \tag{6.50}$$

The liquid surface $\mu_0 = \mu_{\text{l}} = 0$ is always a solution and we deal with a continuous surface melting (O_2 scenario) if it is the only one. Once a second solution with $\mu_0 > 0$ is present, the surface undergoes a discontinuous (O_1) transition, see Fig. 6.2. Using the full expression for the potential on the RHS of (6.50), we find that (6.50) admits two solutions for large T (very small fields B) and only the $\mu_0 = 0$ solution for small temperatures (larger magnetic fields), cf. the solid line in Fig. 6.3. Since both the continuous and the discontinuous melting scenarios are present, a multi-critical point

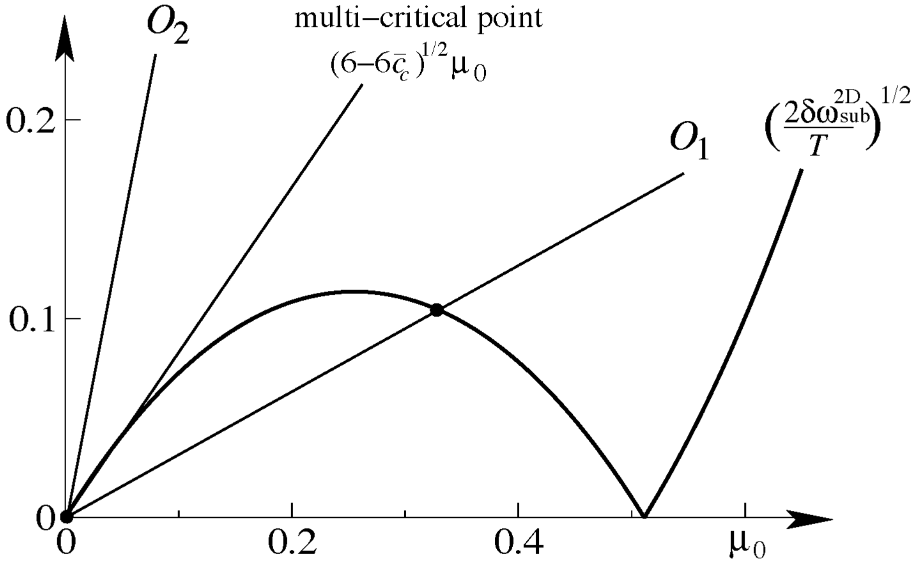

Figure 6.2: Graphical solution of (6.50) for μ_0. We plot separately the RHS of (6.50), $\sqrt{2\delta\omega^{2\mathrm{D}}_{\mathrm{sub}}(\mu_0)/T}$, and the LHS, $\ell G\mu_0$, for different values of the slope ℓG. For $\ell G < \sqrt{6(1-\bar{c}_c)}$ we find an intersection point at a $\mu_0 > 0$ (beside $\mu_0 = 0$). This finite value is the residual order parameter on the surface (O_1 scenario, surface non-melting). For $\ell G = \sqrt{6(1-\bar{c}_c)}$ the straight line is tangent to $\sqrt{2\delta\omega^{2\mathrm{D}}_{\mathrm{sub}}(\mu_0)/T}$ at $\mu_0 = 0$, the finite solution has disappeared, and only $\mu_0 = 0$ remains (multi-critical point). Again for $\ell G > \sqrt{6(1-\bar{c}_c)}$ the solution is only $\mu_0 = 0$ (O_2 scenario, surface melting).

separating the two different kinds of transitions must exist. The equation which locates the critical-point derives simply from (6.50) by considering the quadratic expansion of the potential $\delta\omega^{2\mathrm{D}}_{\mathrm{sub}}(\mu)/T$ (cf. Fig. 6.2)

$$\frac{\ell(T_{\mathrm{mc}}, B_{\mathrm{mc}})G(B_{\mathrm{mc}})}{\sqrt{6(1-\bar{c}_c)}} = 1 \longrightarrow (T_{\mathrm{mc}}, B_{\mathrm{mc}}) \approx (0.29\,\varepsilon_0 d, 0.007\,B_\lambda). \qquad (6.51)$$

Hence, for $T < T_{\mathrm{mc}}$ the surface undergoes a continuous transition. The surface then acts as a nucleus for the liquid phase, preventing the appearance of the solid metastable phase. On the other hand, for large temperatures $T > T_{\mathrm{mc}}$ the order parameter at $z = 0$ still undergoes a residual jump and the double-sided hysteretic behavior is restored, see Figs. 6.6 and 6.7.

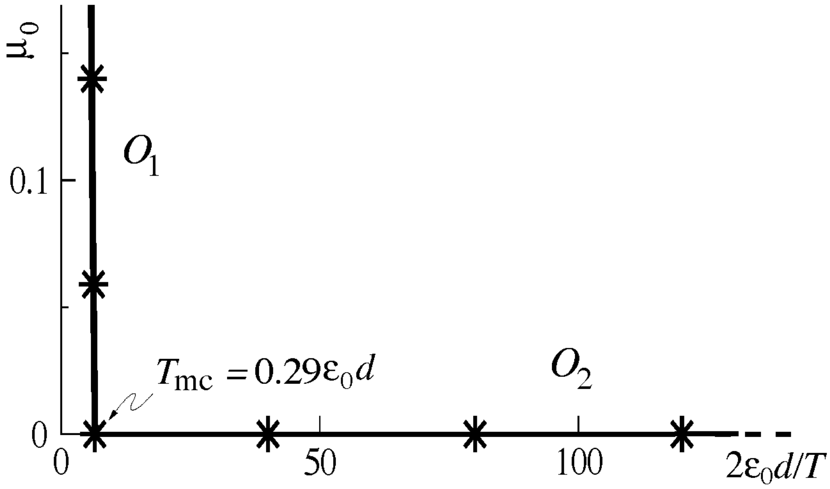

Figure 6.3: Residual value of the order parameter at the surface: analytic (solid line) from (6.50) and full numerical solution (stars) see Section 6.4. For $T < T_{\rm mc}$ the surface undergoes a continuous transition (O_2), whereas for $T > T_{\rm mc}$ the order parameter at $z = 0$ still exhibits a residual jump at melting.

High-field limit

Finally, at high magnetic fields the layers melt independently following a first-order type 2D melting scenario. The order parameter μ_0 in the topmost layer then undergoes a finite jump and the surface non-melting (O_1) scenario applies. The presence of a discontinuous O_1 regime at high fields implies the existence of a second multi-critical point. While our analytical approach is not applicable anymore, since it is based on the gradient expansion which is not justified in this regime, numerically we have found clear indications of a finite jump at high fields ($B \approx 10\, B_\lambda$). However, a more elaborate version of the DFT is required for an accurate determination of this multi-critical point [95]. In particular, approaching the melting temperature of each 2D lattice, the higher order peaks in the OCP correlation function $c^{\rm 2D}(K)$ become important ($K_n > G$). Hence, higher components in the Fourier expansion of the density have to be retained [95], in order to obtain a more precise description of the high field regime.

6.3.3 Analysis of the continuous surface melting and of the multi-critical point

The fact that a discontinuous bulk transition may turn continuous at the surface is somewhat non-trivial. To obtain a better insight into the mechanism of the continuous surface melting, we present here a slightly different, more qualitative, analysis. We describe the surface melting process in the language of the entry of the liquid through the boundary. The appearance of a liquid layer at the surface, while the bulk remains solid, implies the existence of an interface between the two phases, which is described by a soliton-like profile of the order parameter. The entry of the liquid can happen in two different ways: *i)* the soliton can slide smoothly from the boundary at $T_{\rm m}$ (surface melting, O_2) or *ii)* it starts entering the system but it remains pinned at the surface at $T_{\rm m}$ (surface non-melting, O_1). To distinguish these two scenarios we need to calculate the energy of the soliton and the pinning energy. We do this within the local theory

$$\frac{\delta\omega[\mu_z]}{T} = \int \frac{dz}{d}\Big[\frac{\delta\omega_{\rm sub}^{\rm 2D}(\mu_z)}{T} + \frac{1}{2}\ell^2\Big(\frac{d\mu_z}{dz}\Big)^2 + \frac{1}{2}\ell^2 G\mu_z^2\delta(z)\Big]. \tag{6.52}$$

This equation provides a local approximation of the full non local theory of (6.31). The saddle point equation of (6.52) reproduces the equation of state (6.38) with the boundary condition (6.48) at $z = 0$.

Like in the previous section, we concentrate on the case when the order parameter at the surface is small. Such an analysis can describe a continuous surface melting behavior or a weak discontinuous surface transition and the multi-critical point between them. In the following analysis, we estimate the energy of a liquid-solid interface as a function of its distance $z_{\rm s}$ from the surface. The bulk solution remains valid also in the vicinity of the surface, cf. last section. We can then study the problem within a variational scheme, by taking as a convenient variational function a bulk soliton $\mu_z^{\rm sl}(z_{\rm s})$ and displace it rigidly at different distances $z_{\rm s}$ from the surface ('sl' stands for solid-liquid interface), see Fig. 6.4. In the following we need the function $\mu_0^{\rm sl}(z_{\rm s})$, i.e., the relation between the value of the order parameter on the surface and the soliton position $z_{\rm s}$. For a soliton which is well inside the sample, $\mu_0^{\rm sl}(z_{\rm s})$ can be approximated as

$$\mu_0^{\rm sl}(z_{\rm s}) \approx e^{-G_+\sqrt{r}z_{\rm s}}. \tag{6.53}$$

This relation is derived by the solution of the linearized bulk equation (6.38) and thus it is valid when $\mu_0^{\rm sl}$ is in the soliton tail (here we neglect the renor-

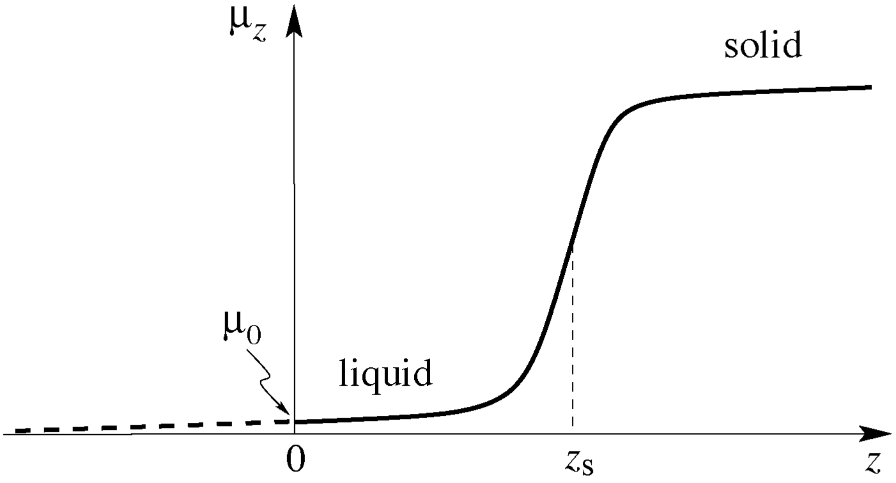

Figure 6.4: Sketch of a solid-liquid interface placed at a distance z_s away from the surface. The surface destabilizing term $E_{\text{surf}}(z_s)$ in (6.54) favors the entry of the liquid-solid interface at the surface, producing a repulsive potential on the soliton. On the other hand, the energy cost to push the soliton into the system generates an attractive potential $E_{\text{sl}}(z_s)$. Depending on which term is dominant, either a continuous or a discontinuous surface transition is realized.

malization factor $(1+r) \approx 1$ which would appear in the exponent from the solution of the non-local integral equation (6.44)); the exact $\mu_0^{\text{sl}}(z_s)$ requires to account for the full solitonic shape but is not needed in our analysis.

We proceed now to estimate the energy due to a surface liquid domain of size z_s, which is given by $\delta\omega[\mu_z^{\text{sl}}(z_s)]$. In the following, we want to calculate the soliton energy not only at the bulk transition temperature T_m but also at T close to it. However, for $T \neq T_m$, the free energy $\delta\omega[\mu_z^{\text{sl}}(z_s)]$ is not finite due to the infinite contribution coming from the bulk solid $\delta\omega_{\text{sub}}^{\text{2D}}(\mu_s) \neq 0$ ($\mu_s = \mu_{z\to\infty}^{\text{sl}}$). In order to obtain a finite energy, which correctly estimates the soliton energy $E_{\text{sl}}^{\text{surf}}(z_s)$ in the presence of the surface we have to subtract this infinite contribution. Hence, we define

$$\begin{aligned} E_{\text{sl}}^{\text{surf}}(z_s) &\equiv \delta\omega[\mu_z^{\text{sl}}(z_s)] - (L/d)\delta\omega_{\text{sub}}^{\text{2D}}(\mu_s, T) \\ &\approx E_{\text{surf}}(z_s) + E_{\text{sl}}(z_s) - (z_s/d)\delta\omega_{\text{sub}}^{\text{2D}}(\mu_s, T), \end{aligned} \tag{6.54}$$

where $L \to \infty$ is thickness of the sample. Note, that $E_{\text{sl}}^{\text{surf}}(z_s)/L \to 0$, since the thermodynamic limit accounts only for the contribution of the bulk. Here we are exactly trying to capture the effects of the surface, thus we subtract the bulk free energy in (6.54). In the last line of (6.54) we have split $E_{\rm sl}^{\rm surf}(z_{\rm s})$ in three different contributions, which we discuss separately in the following. The first term $E_{\rm surf}(z_{\rm s})$ is the energy due to the surface (third) term in (6.52). The second and third term estimate the soliton energy due to the first two terms in (6.52). Away from $T_{\rm m}$ the presence of a liquid layer of thickness $\approx z_{\rm s}$, produces a contribution linear in $z_{\rm s}$. This is due to the finite difference between the liquid and the solid free energies, $-\delta\omega_{\rm sub}^{\rm 2D}(\mu_{\rm s}, T) > 0$. We have written the additional argument T in $\delta\omega_{\rm sub}^{\rm 2D}$ to make explicit the temperature dependence: $\delta\omega_{\rm sub}^{\rm 2D}(\mu_{\rm s}, T_{\rm m}) = 0$ and $\delta\omega_{\rm sub}^{\rm 2D}(\mu_{\rm s}, T < T_{\rm m}) > 0$. Finally, $E_{\rm sl}(z_{\rm s})$ is the energy due to the interface, i.e., to the non-constant part of the order parameter profile. This energy depends on the soliton position, since for a finite $z_{\rm s}$ the soliton has not fully entered in the system and, hence, the energy due to the missing part of the tail has to be subtracted from the total energy $E_{\rm sl} \equiv E_{\rm sl}(\infty)$, see Fig. 6.4. Whereas $E_{\rm sl}(z_{\rm s})$ penalizes the entrance of the soliton and, thus, favors the solid phase, $E_{\rm surf}(z_{\rm s})$ promotes the formation of the liquid phase at the surface. Depending on which term is dominant, either a continuous or a discontinuous surface transition is realized. In the following we proceed to estimate these two terms.

The total energy of the soliton consists of potential, $\delta\omega_{\rm sub}^{\rm 2D}$, and elastic, $\propto (\mu_z')^2$, energies, which combined together yield (see Eq. (5.73))

$$\begin{aligned} E_{\rm sl}(z_{\rm s}) &= \frac{\ell T}{d}\int_{\mu_0^{\rm sl}(z_{\rm s})}^{\mu_{\rm s}} d\mu \sqrt{\frac{2\delta\omega_{\rm sub}^{\rm 2D}(\mu)}{T}} = E_{\rm sl} - \frac{\ell T}{d}\int_0^{\mu_0^{\rm sl}(z_{\rm s})} d\mu \sqrt{\frac{2\delta\omega_{\rm sub}^{\rm 2D}(\mu)}{T}} \\ &\approx E_{\rm sl} - \sqrt{6(1-\bar{c}_c)}\, T\, \frac{\ell}{d}\frac{\mu_0^2(z_{\rm s})}{2}, \end{aligned} \tag{6.55}$$

where $E_{\rm sl}$ is the total interface energy which is given by (5.73) at $T = T_{\rm m}$. In the last line of (6.55) we have expanded the 2D potential for small values of μ. Next, the surface term in (6.52) is easily calculated,

$$E_{\rm surf}(z_{\rm s}) = T\, \frac{\ell^2 G}{d}\frac{\mu_0^2(z_{\rm s})}{2}. \tag{6.56}$$

Combining all terms, we obtain the soliton energy (6.54)

$$E_{\rm sl}^{\rm surf}(z_{\rm s}) \approx E_{\rm sl} + \frac{l}{\bar{\rho}}\frac{T_{\rm m} - T}{T_{\rm m}} z_{\rm s} + \frac{\ell T_{\rm m}}{d}\frac{[\mu_0^{\rm sl}(z_{\rm s})]^2}{2}\Big[\ell G - \sqrt{6(1-\bar{c}_c)}\Big], \tag{6.57}$$

where we have expanded the solid free energy term around the melting temperature $T_{\rm m}$, $\delta\omega_{\rm sub}^{\rm 2D}(\mu_{\rm s}, T) \approx \delta\omega_{\rm sub}^{\rm 2D}(\mu_{\rm s}, T_{\rm m}) + \partial_T\delta\omega_{\rm sub}^{\rm 2D}(\mu_{\rm s}, T_{\rm m})(T - T_{\rm m})$ and we have used the definition of the latent heat $l = T_{\rm m}\Delta s = T_{\rm m}(s_{\rm l} - s_{\rm s}) = -(\bar{\rho}/d)T_{\rm m}\partial_T \delta\omega^{\rm 2D}_{\rm sub}(\mu_{\rm s}, T_{\rm m})$ and $\delta\omega^{\rm 2D}_{\rm sub}(\mu_{\rm s}, T_{\rm m}) = 0$.

Now we are ready to discuss the difference between the continuous and the discontinuous surface melting scenarios. At the melting transition, i.e., when $T = T_{\rm m}$, a finite order parameter at the surface leads to a positive or a negative energy contribution depending on the quantity in square brackets in (6.57). When is $\ell G > \sqrt{6(1-\bar{c}_c)}$, the soliton enters completely inside the sample at $T = T_{\rm m}$, leading to the propagation of the liquid phase into the bulk (surface melting). On the other hand, for weak surface potentials, $\ell G < \sqrt{6(1-\bar{c}_c)}$, the entry of the interface costs a positive energy and, thus, the soliton remains pinned at the surface at $T_{\rm m}$. However, to find the pinning location of the soliton a more detailed analysis is required, accounting for the higher order terms in (6.55) (we have solved this problem numerically, see Fig. 6.5). The two different behaviors are separated by the multicritical point, whose location is given by

$$\ell(T_{\rm mc}, B_{\rm mc})G(B_{\rm mc}) = \sqrt{6(1-\bar{c}_c)}. \tag{6.58}$$

This equation coincides with (6.51).

Since the surface melting behavior is continuous, it can be characterized by specific critical exponents upon approaching $T_{\rm m}$. In particular we can look at how the soliton position $z_{\rm s}$ depends on T. The position of the soliton is found from the minimum of (6.57)

$$\begin{aligned} z_{\rm s}(T) &\approx -\frac{1}{2G_+\sqrt{r}} \ln\left[\frac{ld(T_{\rm m}-T)}{2\sqrt{r}G_+\bar{\rho}\ell T_{\rm m}^2(\ell G - \sqrt{6(1-\bar{c}_c)})}\right] \\ &\sim |\ln(1-t)|, \end{aligned} \tag{6.59}$$

where in the last line we have defined the reduced temperature $t = T/T_{\rm m}$. Hence, the soliton slides into the system logarithmically with t [22]. Next, we study how the residual order parameter on the surface goes to zero. Combining (6.59) together with (6.53), we find

$$\mu_0(T) \sim (1-t)^{1/2}. \tag{6.60}$$

These results are standard in the theory of surface melting when only short-range interactions are present [22].

For a continuous surface melting transition the soliton propagates into the bulk at $T_{\rm m}$, leading, in a semi-infinite system, to the coexistence of the

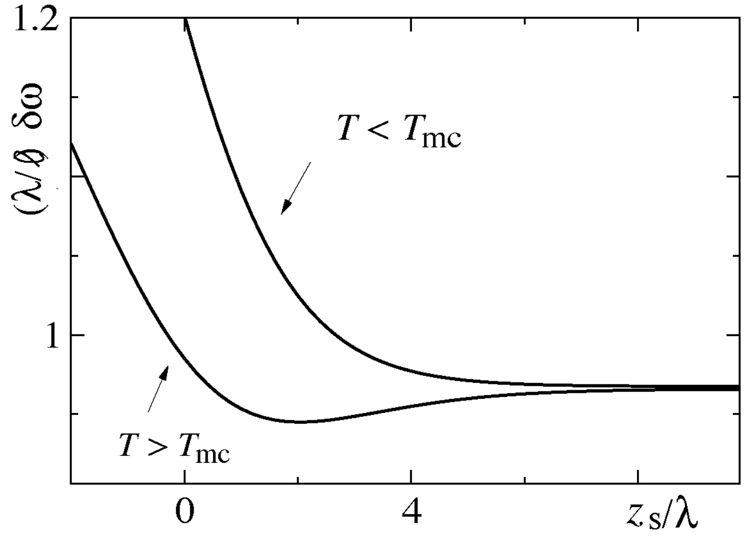

Figure 6.5: Energy as a function of the soliton position $z_{\rm s}$. Note the minimum for $T = 0.33\,\varepsilon_0 d > T_{\rm mc}$ (O_1, pinned soliton) which has disappeared at $T = 0.28\,\varepsilon_0 d < T_{\rm mc}$ (O_2, depinned soliton).

liquid and the solid. The interface deep in the bulk produces the maximum free energy cost, $E_{\rm sl}^{\rm surf}(z_{\rm s} \to \infty) = E_{\rm sl}$ (see Sec. 5.8). This energy is only an interface energy and, hence, its contribution vanishes in the thermodynamic limit. In realistic finite systems, one has to account for the effect of the opposite surface. Approaching $T_{\rm m}$ from below both surfaces undergo a continuous melting transition. The two surfaces act like two nucleation points for the liquid phase, giving rise to two opposite solitons. The system is then composed of a sequence of liquid-solid-liquid regions. At $T_{\rm m}$ the two solitons merge and the intermediate solid domain vanishes altogether. Hence, the solid cannot be overheated above the melting temperature.

Finally, the appearance of the multi-critical point ($T_{\rm mc}, B_{\rm mc}$) along the melting line can be interpreted as a surface-depinning transition of the solid-liquid interface (soliton). Whereas in the surface non-melting regime the soliton remains pinned to the surface at the melting temperature, in the surface melting regime the pinning barrier disappears, since the soliton always experiences a repulsive potential. We have calculated this potential numerically in both the surface melting and surface non-melting regimes, using the following scheme: we place a bulk soliton at different distances from the surface and evaluate numerically the total non-local energy (6.31) as a function of the position z_s of its (half-height) center. In Fig. 6.3, we present two different curves, one at $T = 0.33\,\varepsilon_0 d > T_\mathrm{mc}$ and another at $T = 0.28\,\varepsilon_0 d < T_\mathrm{mc}$. Whereas for the higher temperature the potential exhibits a stable minimum close to the surface at which the soliton remains pinned, decreasing the temperature the minimum moves deeper into the bulk and disappears altogether at T_mc.

6.4 Numerical analysis

In order to check the accuracy of our analytical approach, we have carried out a numerical solution of the saddle point equations (6.33). As a preliminary step, we write (6.33) in a slightly different form which is more convenient for our numerical study. From the variation of (6.28) with respect to μ_z, we obtain that at the saddle point ξ_z and μ_z are related by

$$\xi_z = \int_0^\infty \frac{dz'}{d}\,\bar{c}_{z,z'}\mu_{z'}. \tag{6.61}$$

Combining this expression with the relation (cf. (5.44))

$$\mu_z = \Phi'(\xi_z)/6, \tag{6.62}$$

where the function Φ is defined in (5.25), we obtain a set of integral equations which determine the order parameter profile μ_z

$$6\mu_z = \frac{\displaystyle\int_v d^2\mathbf{R}\, g(\mathbf{R}) \exp\Big[\int_0^\infty \frac{dz'}{d}\,\bar{c}_{z,z'}\mu_{z'}g(\mathbf{R})\Big]}{\displaystyle\int_v d^2\mathbf{R} \exp\Big[\int_0^\infty \frac{dz'}{d}\,\bar{c}_{z,z'}\mu_{z'}g(\mathbf{R})\Big]}, \tag{6.63}$$

where we have written explicitly Φ' and the function $g(\mathbf{R})$ is defined in (5.21). Our numerical solution is based on the recursive solution of the saddle point equations (6.63).

We first discretize the z axis in $N = 1000$ values $\{z_i\}$ with a fixed distance $z_i - z_{i-1} = \Delta z = 0.04\,\lambda$ (for $\Gamma > 40$ we use a smaller step size $\Delta z = 0.01\,\lambda \approx d$, since the soliton interface becomes sharper). We start from a constant solid phase and initialize the values of $\{\mu_i\}$ as $\mu_i = \mu_{z_i} = \mu_\mathrm{s}$, for any i. Then, from Eq. (6.61), we derive the molecular field profile ξ_i in correspondence to the values $\{z_i\}$. We calculate the RHS of equation (6.62) for $i = 1, \ldots, i_\mathrm{max}$, while keeping the last values ($i = i_\mathrm{max}+1, \ldots, 1000$) unchanged, and obtain the new

$\mu_i^{\rm n} = \Phi'(\xi_{z_i})$. We compare $\{\mu_{z_i}^{\rm n}\}$ with $\{\mu_{z_i}\}$ and if both the inequalities $\mu_0^{\rm n} - \mu_0 < 10^{-5}$ and $(1/N)\sum_i(\mu_{z_i}^{\rm n} - \mu_{z_i}) < 10^{-5}$ are satisfied, we accept $\{\mu_{z_i}^{\rm n}\}$ as the order parameter profile. Otherwise, the procedure is iterated recursively until a stable solution (fixed point) is reached. We take $i_{\rm max} = 750$; for this value we have checked that the connection between the numerical solution for $i \leqslant i_{\rm max}$ and the constant bulk value for $i > i_{\rm max}$ is smooth (we find a small jump at $i_{\rm max}$, $(\mu_{i_{\rm max}+1} - \mu_{i_{\rm max}})/\mu_{i_{\rm max}} \approx 10^{-5}$). Usually convergence is obtained after a reasonable number of iteration (< 100), however in the proximity of a continuous surface transition the convergence becomes slow and problematic. This critical slowing down makes it difficult to track the sliding of the soliton inside the bulk. To avoid this problem, for these critical cases we start our iteration from a more convenient initial state. Instead of initiating the profile in the bulk homogenous solid, we chose to start from a bulk soliton at the position which minimizes the total surface free energy (cf. Fig. 6.5 and discussion in the last section). In this case the convergence is extremely rapid.

In Figs. 6.6 and 6.7, we show two different examples of the order parameter profile for two different values of the temperature: *i)* $T = 0.08\ \varepsilon_0 d < T_{\rm mc}$ in Fig. 6.6, at which the surface undergoes a continuous transition and *ii)* $T = 0.33\ \varepsilon_0 d > T_{\rm mc}$ in Fig. 6.7 for which a discontinuous surface transition takes place.

For $T = 0.08\,\varepsilon_0 d$, the surface undergoes a continuous (O_2) transition. In Fig. 6.6, we show different order parameter profiles for different values of the magnetic field. The value of B increases from top to bottom (see also the caption of Fig. 6.6). At low magnetic fields, the profile is almost constant (cf. the topmost line), since the surface kernel $\delta\omega^{\rm s}$ is negligible and the system is translationally invariant. Going to larger values of the magnetic field, the modifications of the interlayer potential on the surface become relevant, reducing the value of the order parameter at the surface. This corresponds to the results of the stability analysis of Sec. 6.2, which indicates that the vortex solids are softer closer to the surface and thus more susceptible to thermal fluctuations. Upon increasing the magnetic field further towards the thermodynamic melting transition, vortex density modulations become vanishingly small close to the surface. The numerical solution shows that the order parameter on the surface goes continuously to zero (liquid), instead of jumping from a finite value (solid). The surface assists the penetration of the liquid phase by the formation of a quasi-liquid nucleus. The continuous tran-

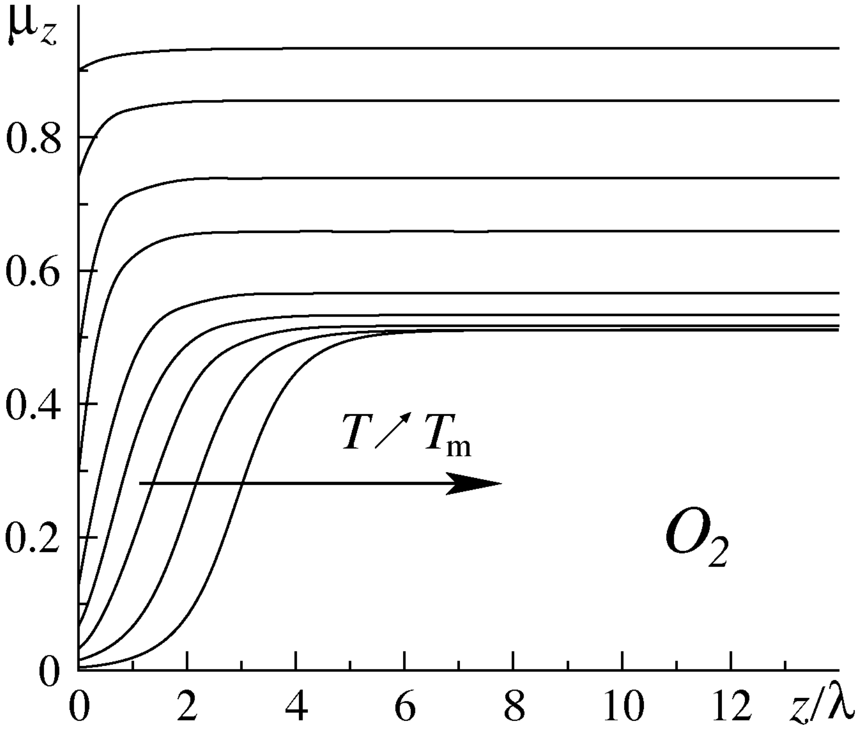

Figure 6.6: Numerical solutions of the order parameter profile μ_z at the surface, for different values of the external magnetic field at $\Gamma = 2\varepsilon_0 d/T = 25$, corresponding to $T = 0.08\varepsilon_0 d$. At this temperature the bulk melts at $B_\mathrm{m}/B_\lambda \approx 0.1528$. The lines from top to bottom correspond to the magnetic fields with values $B/B_\lambda = 0.01$, 0.05, 0.1, 0.125, 0.145, 0.15, $B_\mathrm{m}/B_\lambda - 10^{-4}$, $B_\mathrm{m}/B_\lambda - 10^{-5}$, $B_\mathrm{m}/B_\lambda - 10^{-6}$. While approaching this value the soliton slides into the bulk (see the bottom three lines). The surface undergoes an O_2 type transition, i.e., μ_0 approaches zero (liquid phase) continuously.

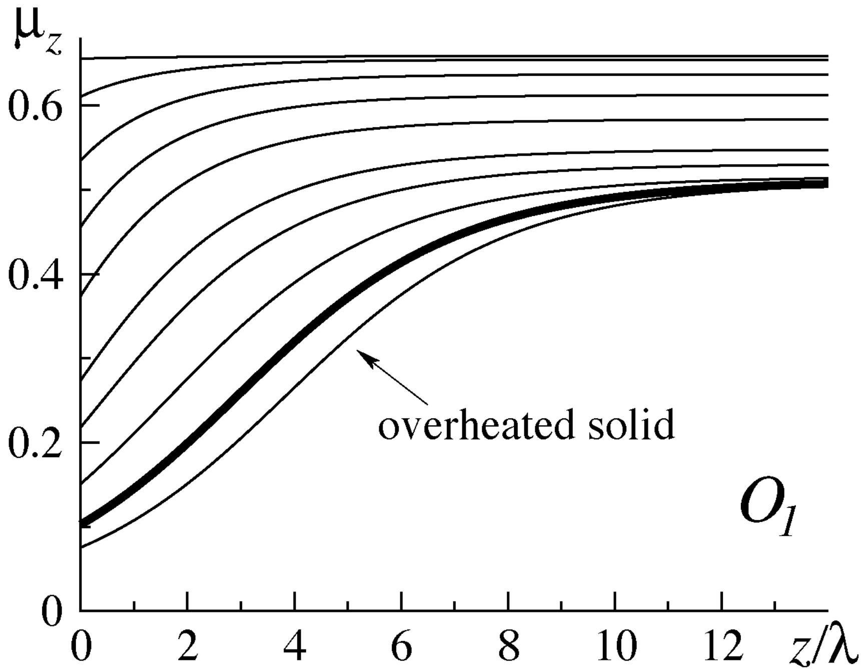

Figure 6.7: Numerical solutions of the order parameter profile μ_z near the surface at $T = 0.33\,\varepsilon_0 d$ ($\Gamma = 6$) for different values of the magnetic field. The freezing field is $B_\mathrm{m}/B_\lambda \approx 0.002396$ (thicker line). The lines from top to bottom correspond to the magnetic fields with values $B/B_\lambda = 0$, 0.0001, 0.0005, 0.001, 0.0015, 0.002, 0.0022, 0.00235, B_m/B_λ, $B_\mathrm{m}/B_\lambda + 10^{-5}$. The order parameter at the surface jumps discontinuously to zero; hence, the surface transition is in the class O_1. In this case, the surface does not preclude the appearance of the overheated solid. Numerically it is possible to obtain a non uniform solution even at magnetic fields $B > B_\mathrm{m}$ larger than the freezing one (cf. lowest thin line), corresponding to a metastable configuration (overheated solid).

sition on the surface eliminates the hysteresis above the melting transition, by preventing the appearance of a metastable overheated solid phase.

In constrast to this scenario, at larger temperatures $T = 0.33\,\varepsilon_0 d > T_{\mathrm{mc}}$ (Fig. 6.7) the surface undergoes a discontinuous transition, although with a reduced jump in comparison with the bulk. Again starting from low magnetic fields (topmost line) the order parameter is constant, due to the smallness of the surface destabilizing potential. Increasing B, the value of μ_0 decreases, still showing a larger suppression than in the bulk. However, the surface potential is not strong enough to push μ_0 to zero and at melting (thick line) the surface still exhibits a finite order parameter. The transition to the homogeneous liquid phase then occurs via a finite jump everywhere, including the surface. This discontinuous transition is compatible with the appearance of the metastable phase. Indeed, numerically it is possible to obtain a non uniform solution even at magnetic fields which are larger than freezing one (lowest line, below the freezing one).

Finally, we check the accuracy of our analytical approach in estimating the location of the multi-critical point $(T_{\mathrm{mc}}, B_{\mathrm{mc}})$. We plot the residual value of the surface order parameter at melting as a function of the temperature in Fig. 6.3, together with the solution of (6.50). For a continuous surface melting transition the order parameter is exactly zero at melting. Numerically, we associate the value $\mu_0 = 0$ to situations where the soliton potential does not show a stable minimum as a function of z_{s} (see Fig. 6.5). Otherwise, we estimate the finite value of μ_0 within the iterative solution of the saddle point equations, which we have described above. The agreement of the numerical and analytical results results is excellent, in particular in the vicinity of the multi-critical point.

6.5 Conclusions

In this chapter, we have analyzed the impact of an *ab*-surface on the melting transition of the pancake vortex lattice. We have used a self-consistent elastic theory to study the stability of the solid phase close to the surface. Whereas both the low and large fields limits are not affected by the presence of the surface, for intermediate fields we found that the lattices on the first layers become unstable below the bulk melting temperature. To obtain a better insight into the problem, we have adapted the DFT-substrate approach of Chapter 5 to include the presence of the surface. We have found that, for intermediate values of the magnetic field, the surface undergoes a continuous melting transition and assists a smooth propagation of the liquid into the bulk. This result reveals the origin of the asymmetric hysteresis at the melting transition observed by Soibel *et al.* [101]: as a consequence of free surfaces which can act as nucleation sites for the liquid phase. Moreover, we have found that at low and large magnetic fields the surface transition turns discontinuous like in the bulk, in agreement with the results of the stability analysis which showed no important effect from the surface in this regime. The surface continuous and discontinuous transitions are separated by a multi-critical point. Whilst a precise location of the high-field multi-critical point goes beyond the limits of validity of our analysis, we have located the low-field multi-critical point by means of an analytical solution of the DFT equations and confirmed numerically the result of the analysis.

An effect which we have not included in our analysis is the impact of the reentrance of the melting line at low magnetic fields. As we have seen in Sec. 2.5, at low magnetic fields the interaction between full *vortex lines* is strongly screened. This leads to a softening of the vortex lattice with exponentially small shear and compression moduli (cf. (2.45)) and to the reentrance of the melting line towards small temperatures. However, our analysis is based on the substrate model which builds on the assumption that the elementary objects are the pancake vortices, which interact logarithmically on all scales. The shear modulus associated with the 2D pancake vortex lattices does not become exponentially small at very low magnetic fields, cf. Eq. (6.19). Thus, it remains unclear if (and how) the substrate model can be extended to study the reentrance of the melting line. Nevertheless, the effect of a surface for very low fields is an interesting question. In fact, in this regime stray magnetic fields produce an algebraic interaction between the tips of the vortex lines (3.38) instead of the exponentially small bulk interaction (2.31). This may lead to a highly unconventional scenario (proposed in [111]) where the tips of the vortex lines on the surface are arranged in a regular lattice while the vortex system is already melted in the bulk. Hence, in this case the surface plays a role which is opposite to the one played in the standard surface melting scenario, since it favors the appearance of the solid instead of the liquid. The impact of this 'surface solidification' on our results remains an interesting open question.

Chapter 7

Conclusions

'Let's assume the solution is another one, then your result is wrong.'

In this thesis, we have discussed the thermodynamic behavior of superconducting systems with a finite number of layers, or more generally, with geometrical constraints. Summarizing, the two major findings of the thesis are: *i)* the finite temperature BKT transition associated with the unbinding of 'fractional-flux' vortices in systems with a finite number of layers (see Chapter 4); *ii)* the complex behavior of surfaces at the melting transition of the vortex lattice, as manifested by the appearance of both surface-melting and surface-non-melting scenarios and the occurrence of multi-critical points at low and large magnetic fields (see Chapter 6).

7.1 Observing fractional-flux vortices

In Chapter 3 we have studied the properties of vortices in systems composed of a finite number N of superconducting layers. While in a single film a vortex binds a whole quantum flux Φ_0, already by adding one additional layer the trapped flux is reduced to half its value $\Phi_0/2$. Increasing the number N of layers, the trapped flux decreases further as Φ_0/N. This reduction in flux has several consequences, the most important being the extension of the logarithmic interaction between fractional-flux vortices to all distances and the appearance of a finite temperature BKT transition associated with the unbinding of pairs of fractional-flux vortices. This transition describes the destruction of the superconducting response in the counterflow channel and can be traced experimentally in transport measurements as proposed in Chapter 4.

Layered superconductors are an example, probably the simplest, of multicomponent superconductors. Recently, several other systems have been put forward as possible realizations of such multicomponent superconductors. Here, we would like to comment these different proposals and their potentiality in revealing fractional flux-vortices in an experiment.

A first example is given by multi-gap superconductors such as MgB_2 [55–57]. For these systems, disconnected sheets of the Fermi surface give rise to distinct superconducting components. Differently from layered superconductors, the components are not geometrically separated but correspond to internal degrees of freedom. In these systems the tunneling of Cooper pairs between the different condensates is not prohibited and, in a generic situation, a finite Josephson coupling remains between the different components. This finite coupling leads to the confinement of vortex–anti-vortex pairs and inhibits their unbinding. Hence, fractional-flux vortices are not easily observed in multi-gap superconductors [61].

A second, more exotic, proposal is metallic hydrogen [62]. At low temperature and under the effect of a high pressure, both electrons and protons are supposed to condensate, giving rise to a two-component superconductor. Tunneling between protonic and electronic components is naturally prohibited and the Josephson coupling is absent. However, the extreme pressure needed to liquify hydrogen is still out of reach for present experimental techniques. Hence, the observation of fractional flux vortices in metallic hydrogen remains only an interesting theoretical proposal.

A major difference of layered superconductors as compared to the other proposals is that the components are separated in space. This implies two advantages: *i)* in artificial systems Josephson coupling can be suppressed (to a large extent) by an appropriate choice of the material parameters and the sample geometry; *ii)* the superconducting components (layers) can be individually accessed in experiments. This second point is the key property that allows to observe fractional-flux vortices. As we have seen the appearance of free fractional-flux vortices is accompanied with the destruction of the counterflow superconducting stiffness, i.e., the ability of carrying currents with opposite orientation in different layers without dissipating energy. To probe the counterflow response it is necessary to access individually the components and to drive opposite currents. This is obviously a more difficult, if not impossible, task to realize in superconductors with multiple intrinsic components.

The appearance of a counterflow superfluid is not specific to layered superconductors. As we have seen in Chapter 4 another example is the bi-layer quantum Hall setup at filling $\nu = 1$. At low temperatures the bi-layer enters an interlayer coherent state, even in the absence of any tunneling between the layers [63]. The properties of this coherent phase has been accessed in the same type of counterflow experiment which we have proposed in the study of the BKT unbinding of fractional-flux vortices [83]. The half-flux vortices in a bi-layer superconductor (existing in one of two layers and with ± vorticity) correspond to merons with a fractionalized charge $\pm e/2$ and ± vorticity [64]; bound neutral meron pairs have their analogue in intralayer vortex–anti-vortex pairs, while bound charged merons correspond to vortex stacks. Similarly to half-flux vortex pairs, meron-pairs are supposed to undergo a BKT transition, leading to the destruction of the interlayer phase coherence. The analogy between the bi-layer superconductor and the bi-layer quantum Hall setup seems an interesting example of a charge–magnetic-flux duality. A more detailed study might unravel further interesting connections between these two different systems.

7.2 Surface melting vs. surface non-melting

In Chapters 5 and 6 we have investigated the melting transition of the vortex lattice, with and without a surface. We have implemented a novel substrate-DFT approach, which, despite of its simplicity, has proven to be a reliable tool to capture the main features of the melting of the pancake vortex system. A particularly interesting result, which we have presented *en passant* in our analysis, is the derivation of the Clausius-Clapeyron relation, which provides a consistent description of the retrograded melting line together with the sign of the density jump across the transition. This derivation requires a constrained free-energy which accounts for the discrete nature of the vortices and proves the thermodynamic consistency of the theory. We would like to emphasize that this derivation is not specific to the vortex system but remains valid for ordinary solids. We have then studied the impact of the surface on the melting transition. We have shown that the surface can undergo both a continuous transition (surface melting) or a discontinuous transition (surface non-melting), depending on the value of the magnetic field. For intermediate fields the surface undergoes a continuous transition and the overheated solid is preempted by the formation of a liquid layer/nucleus at the surface.

In a conventional solid, the structure of the crystal and the interactions are dictated by the chemistry of the material. Hence, for a given material and surface orientation, the surface *either* melts continuously *or* remains solid up to the bulk transition temperature. As we have seen, the vortex system is quite different. The vortex density (and thus the lattice constant and the strength of the vortex interactions) can be varied to a large extent simply by changing the value of the external magnetic field. Hence, the vortex matter defines a highly tunable system and its phenomenology is considerably richer than the one of standard solids. The simultaneous occurrence of both surface melting and surface non-melting scenarios in one material leads to the appearance of multi-critical points and is an example of the consequences of the high tunability of vortex matter.

Finally, we have to point out that our analysis has not exhausted all possible aspects in the discussion of the impact of surfaces on the melting transition. An open issue, which unfortunately cannot be tackled within the framework of our DFT-substrate analysis, is how the surface non-melting scenario is modified at extremely low fields by the reentrance of the melting line. Simple arguments [111] show that the surface can stabilize the solid phase, leading to a highly non-conventional ‘surface solidification’. A full quantitative description of this effect is missing and remains an interesting subject for future investigations.

Appendix A

RG equations for the bi-layer

A.1 Derivation of the RG equations

Here we discuss the derivation of Eqs. (4.5) and (4.22) within a simple linear response theory. The analysis generalizes the one of Ref. [70] by including the effects of magnetic screening. We will use the language of the two-dimensional Coulomb gas and describe the pancake (anti) vortices as positive (negative) charges $(-)\sqrt{\varepsilon_0 d}$. This analogy is exact for log-interacting particles and thus for the distances at which the function q remains constant. Given the long plateau of the screening function q and the relatively short crossover, we will make use of the properties of the 2D Coulomb gas in all our analysis. We first concentrate on the effect of fluctuating vortex–anti-vortex pairs. In the language of the 2D Coulomb gas, magnetic screening acts as a first scale dependent dielectric function which modifies the Coulomb interaction between oppositely charged vortices as in (4.2). Thermally activated pairs produce a downwards renormalization of the force strength

$$\tilde{F}(R) = \frac{2\varepsilon_0 d q(R)}{\epsilon(R)R}, \tag{A.1}$$

where the *total* dielectric constant is

$$\varepsilon(R)/q(R) = 1 + 4\pi\chi(R), \tag{A.2}$$

and $\chi(R)$ is the susceptibility of all dipoles of size smaller than R. We can write

$$\chi(R) = \int_0^R R' dR' d\theta \, dn(R', \theta)\alpha(R'), \tag{A.3}$$

where $dn(R,\theta)$ the density of pairs of size R and orientation θ (it has dimensions of length^{-4}) and $\alpha(R)$ is the polarizability of a single dipole of size R, which is

$$\alpha(R) = \frac{\varepsilon_0 d}{2T} R^2. \tag{A.4}$$

The polarizability is not modified by the inter-particle interaction and, therefore, by the screening factor $q(R)$. In fact, the vortex interaction derives from the Lorentz force $(-\Phi_0 j/c)$ acting on the vortex core, thus no factor q enters in the analysis at this point. The dipole density

$$dn(R',\theta) = \frac{y_0^2 e^{-\tilde{V}(R)/T}}{\xi^4} \tag{A.5}$$

depends self-consistently on the renormalised interaction energy of (4.4) and thus on $q(R)$. Combining (A.4) and (A.5) in (A.3), one finds ($K_0 = \varepsilon_0 d/T$, $K(R) = K_0/\varepsilon(R)$ and $l = \ln(R/\xi)$)

$$\frac{K^{-1}(l)}{q(l)} = K_0^{-1} + 4\pi^3 y_0^2 \int_0^l dl' q(l') e^{4l' - 2\pi \int_\xi^{l'} dl'' K(l'') q(l'')}. \tag{A.6}$$

Defining the auxiliary function y as in (4.6), we obtain the set of differential equations (4.5) for $K(l)$ and $y(l)$ by taking the derivative with respect to l and neglecting terms of order q'.

We can account for the fluctuating free vortex stacks in a similar analysis; the new dielectric function reads

$$\varepsilon(R)/q(R) = 1 + 4\pi\chi(R) + 4\pi\chi_{\mathrm{s}}(R), \tag{A.7}$$

where $\chi_{\mathrm{s}}(R)$ is the susceptibility of all free stacks whose pancake vortices are moved apart to a distance smaller than R. The density $dn_{\mathrm{s}}(R,\theta)$ stems from the total energy needed to create two vortices in opposite layers

$$V_{\mathrm{s}}(R) = E_{\mathrm{s}} + V_{\mathrm{p-p}}(R), \tag{A.8}$$

where E_{s} is the self energy of a straight vortex stack. The average distance between two free stacks is always larger than the effective penetration length $\xi_{\mathrm{s}} \gg \lambda_{\mathrm{eff}}$. Hence, vortex stacks contribute appreciably to ϵ only at $R \gg \lambda_{\mathrm{eff}}$ and behave essentially like vortex–anti-vortex pairs $(1 - q(R \gg \lambda_{\mathrm{eff}}) \approx q(R \gg \lambda_{\mathrm{eff}}) \approx 1/2)$. As a result, the vortex-stack polarizability reads $\alpha_{\mathrm{s}}(R) = \alpha(R) = \varepsilon_0 d R^2/2T$ and from Eq. (A.7) one obtains the scaling relations Eqs. (4.22).

A.2 Alternative derivation

The derivation of the scaling equations presented in Sec. A.1 requires rather uncontrolled approximations which remain implicit within the language of the 2D Coulomb gas. Here, we report an equivalent and more systematic derivation, which is based on a real space renormalization analysis of the partition function of the vortex system. Neglecting scales smaller than the correlation length ξ, we can accurately describe the system as particles (of size ξ) with the interaction of Eq. (4.2). Assuming an overall vortex neutrality, we can write the partition function in the grand-canonical ensemble [112],

$$Z = \sum_{N=0}^{\infty} \frac{y_\xi^{2N}}{(N!)^2} \int_{D_1, D_2, \ldots, D_{2N-1}, D_{2N}} \prod_{i=1}^{2N} \frac{d^2 r_i}{\xi^2} e^{-\beta H}, \tag{A.9}$$

where D_i is the volume available to the i-th vortex

$$D_i = V - \sum_{j<i} d_j, \tag{A.10}$$

and d_j is the disk of radius ξ centered around the j-th vortex. The Hamiltonian reads

$$-\beta H = -\frac{\beta}{2} \sum_{i \neq j} p_i p_j V(|\mathbf{r}_i - \mathbf{r}_j|) \tag{A.11}$$

where p_i is the charge (± 1) of the vortex i. The total number of particles is $2N$, N with positive charge (odd indices) and N negative (even indices). The basic renormalization group step consists in integrating out the effects of one small vortex pair of size $[\xi, \xi + \delta\xi]$, thus going from a system of $2N$ particles to $2(N-1)$ particles with a modified interaction. Increasing the short distance cut-off, we approximate

$$\begin{aligned} \int_{D_1 \ldots D_{2N}} \prod_{i=1}^{2N} \frac{d^2 r_i}{\xi^2} &\approx \int_{D'_1 \ldots D'_{2N}} \prod_{i=1}^{2N} \frac{d^2 r_i}{\xi^2} \\ &+ \frac{1}{2} \sum_{i \neq j} \int_{D'_1 \ldots \check{D}_k \ldots \check{D}_j \ldots D'_{2N}} \prod_{k \neq i,j} \frac{d^2 r_k}{\xi^2} \int_{d_j} \frac{d^2 r_i}{\xi^2} \int_{D_j} \frac{d^2 r_j}{\xi^2}, \end{aligned} \tag{A.12}$$

where contributions of order higher than $\delta\xi$ are neglected and D'_i is defined like D_i but with an increased short distance cut-off $\xi + \delta\xi$. In the second term of Eq. (A.12) we use the decomposition of the Hamiltonian

$$\begin{aligned}\sum_{k\neq l} V(|\mathbf{r}_k-\mathbf{r}_l|) &\approx 2\sum_{k\neq i,j} p_i(\mathbf{r}_i-\mathbf{r}_j)\cdot\nabla V(\mathbf{r}_k-\mathbf{r}_i)+\\ &+\sum_{k,l\neq i,j} V(|\mathbf{r}_k-\mathbf{r}_l|), \qquad (A.13)\end{aligned}$$

where we have expanded linearly the potential and used $V(\xi)=0$ (cf. Eq. (4.2)). Combining terms, one obtains

$$\begin{aligned}Z=\sum_{N=0}^{\infty}\frac{y_\xi^{2N}}{(N!)^2}\int_V\prod_{i=1}^{2N}\frac{d^2r_i}{\xi^2}e^{-\beta H}\times \qquad (A.14)\\ \Big(1+y_\xi^2\int\frac{d^2r_id^2r_j}{\xi^2\ \ \xi^2}\exp\Big[2\sum_k(\mathbf{r}_i-\mathbf{r}_j)\cdot\nabla V(\mathbf{r}_k-\mathbf{r}_i)\Big]\Big).\end{aligned}$$

Expanding the last exponential (it's argument is of order $\delta\xi$), the linear term is odd and vanishes. The quadratic term after partial integration can be written

$$2\pi\frac{L^2}{\xi^2}\delta\ell-2\pi\int\frac{d^2r}{\xi^2}\sum_{k,l}V(|\mathbf{r}_k-\mathbf{r}|)\nabla^2V(|\mathbf{r}_k-\mathbf{r}|)\delta\ell, \qquad (A.15)$$

where we have introduced the quantity $\delta\ell=\delta\xi/\xi$. In the description of the modified interaction enters the following expression

$$I(\mathbf{x})=\int d^2\mathbf{r}V(|\mathbf{x}-\mathbf{r}|)\nabla^2V(r). \qquad (A.16)$$

In order to close the scaling scheme, we implement an adiabatic approximation for the interaction, neglecting terms of order $q'(l)$ and write $\nabla^2V(\mathbf{r})=2\pi[q(\xi)\delta^{(2)}(\mathbf{r})+q'(r)/2\pi r]\approx 2\pi q(\xi)\delta^{(2)}(\mathbf{r})$. The approximation is valid for slowly varying functions $q(r)$ and, thus, when $\xi_\mathrm{p}\ll\lambda_\mathrm{eff}$ or $\xi_\mathrm{p}\gg\lambda_\mathrm{eff}$. Within the adiabatic approximation one obtains $I(\mathbf{x})=2\pi q(\xi)V(x)$ and the functional shape of the interaction is preserved in each RG step. The scaling analysis then continues in the standard way, the short distance cut-off is increased to $\xi+\delta\xi$, and the starting partition function is recovered once we define

$$q_{\ell+\delta\ell}(R)=q_\ell(R)-(2\pi)^2q_\ell(\xi)q_\ell(R)y_\ell^2\delta\ell, \qquad (A.17)$$

and

$$y_{\ell+\delta\ell}=y_\ell+2y_\ell\delta\ell+y_\ell q_\ell(\xi)\delta\ell+O(y^3). \qquad (A.18)$$

Finally, we find a new renormalised system that is described by a new interaction $q_\ell(R)$ and a modified fugacity y_ℓ. Within the adiabatic approximation we can write $q_\ell(R) = q(R)K_\ell/K_0$ and we recover the recursion relations Eq. (4.5).

A.3 Solution of the RG equations

The scaling equation can be solved exactly (cf. Ref. [71]). The solution of a trajectory which passes through the point (K_0^{-1}, y_0) (with $q = 1/2$) reads

$$y^2(K^{-1}) = \frac{2}{\pi^3}\Big[(K^{-1} - K_0^{-1}) - \frac{\pi}{4}\ln\frac{K^{-1}}{K_0^{-1}}\Big] + y_0^2. \tag{A.19}$$

Integrating the first of Eqs. (4.5), we can extract the correlation length l_{hf}. In the critical region, the result is

$$\begin{aligned} l_{\mathrm{hf}} &\approx l_{\mathrm{eff}} + \frac{1}{2\sqrt{(2\pi\bar{y})^2 - (4\bar{K}^{-1}/\pi - 1)^2}} \times \\ &\times \Big(\frac{\pi}{2} - \arctan\frac{4\bar{K}^{-1}/\pi - 1}{\sqrt{(2\pi\bar{y})^2 - (4\bar{K}^{-1}/\pi - 1)^2}}\Big), \end{aligned} \tag{A.20}$$

which close to the left separatrix the standard KT yields the result

$$l_{\mathrm{hf}} \approx l_{\mathrm{eff}} + \frac{\pi}{2\sqrt{(2\pi\bar{y})^2 - (4\bar{K}^{-1}/\pi - 1)^2}} \tag{A.21}$$

and $l_{\mathrm{hf}} = l_{\mathrm{eff}} + 1/(4\pi\bar{y}) \approx l_{\mathrm{eff}} + 1/(4\pi\bar{y}^{(2)})$ at the right separatrix. On the right of the separatrix one finds, after straightforward integration,

$$\begin{aligned} l_{\mathrm{hf}} &\approx l_{\mathrm{eff}} + \frac{2\bar{K}^{-1}}{\pi\sqrt{(4\bar{K}^{-1}/\pi - 1)^2 - (2\pi\bar{y})^2}} \times \\ &\times \ln\frac{4\bar{K}^{-1}/\pi - 1 + \sqrt{(4\bar{K}^{-1}/\pi - 1)^2(2\pi\bar{y})^2}}{2\pi\bar{y}}, \end{aligned} \tag{A.22}$$

which connects smoothly with Eq. (A.20) on the right separatrix. For $4\bar{K}^{-1}/\pi - 1 \gg \bar{y}$, one obtains

$$l_{\mathrm{hf}} \sim l_{\mathrm{eff}} + \frac{1}{2 - \pi\bar{K}/2}\ln\frac{1}{\bar{y}}, \tag{A.23}$$

which is Eq. (4.14).

Appendix B

Calculation of the core energy

Connecting the results of the scaling analysis of Chapter 4 with experimentally accessible quantities requires a precise estimate of the vortex self-energy. Many different terms contribute to the core energy E_c and a complete account demands a numerical study of the Ginzburg-Landau equations. A thorough analysis of the problem for a bulk line vortex was performed in Ref. [32], where the total line energy was calculated

$$\varepsilon_{\mathrm{v}} = \varepsilon_0 \Big(\ln \frac{\lambda}{\xi} + 0.5 \Big). \tag{B.1}$$

Defining $\varepsilon_{\mathrm{v}}(R)$ as the self-energy of a vortex due to contributions up to a distance R from the vortex center, we can extract the core line energy from the correction to the leading logarithmic term when $\xi \ll R \ll \lambda$, i.e., $\varepsilon_{\mathrm{v}}(R) = \varepsilon_{\mathrm{c}} + \varepsilon_0 \ln(R/\xi)$. In this range the effects of magnetic screening are negligible and the result remains valid also for Pearl and pancake vortices (with arbitrary layer number N). Hence, only the condensation energy and the corrections of the kinetic term due to currents close to ξ enter in evaluation of ε_{c}. Instead of calculating ε_{c} directly one can use the result in Ref. [32] and subtract the contributions arising from distances larger than R, $\varepsilon^{>}(R)$, from the total energy. Being far from the core, the condensate density has approached its asymptotic value and the London theory is applicable. Accounting for both contributions from currents and fields one gets [30]

$$\varepsilon^{>}(R) = \varepsilon_B + \varepsilon_j^{>}(R) = \varepsilon_0 \Big(\ln \frac{\lambda}{R} + 0.12 \Big), \tag{B.2}$$

where $\varepsilon_B \approx 0.5\varepsilon_0$ is the total contribution from the magnetic fields and $\varepsilon_j^{>}(R) = \varepsilon_0[\ln(\lambda/R) - 0.38]$ is the contribution from currents at distances larger than R. Finally, we obtain $\varepsilon_{\mathrm{v}}(R) = \varepsilon_{\mathrm{t}} - \varepsilon^{>} = \varepsilon_0[\ln(R/\xi) + 0.38]$ and

$$\varepsilon_{\mathrm{c}} = 0.38\,\varepsilon_0. \tag{B.3}$$

Moreover, by using the results in Ref. [32] we can estimate each of the contributions which combine into ε_{c}. Summarizing, we have the condensation energy $\varepsilon_1 = (\varepsilon_0/2)\int(1-f^2)^2\,RdR = 0.5\varepsilon_0$ ($f = |\psi|/|\psi_\infty|$ is the modulus of the order parameter relative to the asymptotic value), kinetic currents due to variations of the modulus $\varepsilon_2 = \varepsilon_0\int f'^2 RdR = 0.56\varepsilon_0$, from these we can extract the remaining kinetic term $\varepsilon_3 = \varepsilon_0(\ln R/\xi - 0.4) = \varepsilon_0\ln(R/\alpha\xi)$, with $\alpha \approx 1.4$, which coincides with the result of Clem [113].

Appendix C

Gradient expansion

C.1 Kernel in Fourier space

In this appendix we prove the validity of the gradient expansion (5.69) for the DFT free energy in the low-field regime. We start from the expression of the bulk free-energy (5.68)

$$\frac{\delta\omega[\mu_z]}{T} = \int \frac{dz}{d}\frac{\delta\omega^{\mathrm{2D}}_{\mathrm{sub}}(\mu_z)}{T} + \frac{3}{2}\int \frac{dzdz'}{d^2}\bar{c}_{z-z'}(\mu_z - \mu_{z'})^2 \tag{C.1}$$

and calculate the saddle point equation

$$-6\int \frac{dz'}{d}\bar{c}_{z-z'}(\mu_z - \mu_{z'}) = \frac{d}{d\mu}\Big(\frac{\delta\omega^{\mathrm{2D}}_{\mathrm{sub}}(\mu_z)}{T}\Big), \tag{C.2}$$

which has to be compared with the corresponding equation coming from the approximated local theory (5.71)

$$\ell^2\frac{d^2\mu_z}{dz^2} = \frac{d}{d\mu}\Big(\frac{\delta\omega^{\mathrm{2D}}_{\mathrm{sub}}(\mu_z)}{T}\Big). \tag{C.3}$$

The bulk kernel (5.65) reads

$$\bar{c}_z = \bar{c}^{\mathrm{2D}}d\delta(z) + \bar{\alpha}\bar{f}_z, \tag{C.4}$$

where $\bar{f}_z = \exp(-G_+|z|)$ and $\bar{\alpha} \equiv \alpha(G) = \pi\bar{\rho}\Gamma d/G^2\lambda^2 G_+$. Note that the first δ-term in (C.4) does not contribute to the non local term in the free energy (C.1).

The difference between the two left-hand side terms of (C.2) and (C.3) is more conveniently analyzed in Fourier space. In the case of the local theory, the second derivative term is clearly diagonal in Fourier space and its components read

$$\ell^2 k^2 \mu_k = \frac{12\bar{\alpha}k^2}{dG_+^3}\mu_k, \tag{C.5}$$

where we have used the definition (5.70) of ℓ. Considering now the full theory, the left hand side of (C.2) is also diagonal in Fourier space

$$6(\bar{c}_k - \bar{c}_{k=0})\mu_k = \frac{12\bar{\alpha}k^2}{dG_+(k^2+G_+^2)}\mu_k = \frac{\ell^2 k^2}{1+(k/G_+)^2}\mu_k. \tag{C.6}$$

From the comparison of (C.6) with (C.5) it becomes clear that for small wavenumbers $k \ll G_+$, i.e., for variations on scales larger than $1/G_+$, the gradient expansion approximates well the full non local theory. Therefore, one needs only to compare the typical length of the soliton $\sim \ell$ with the size of the kernel $1/G_+$. In Fig. C.1 (upper), we show the product ℓG_+ as a function of $\Gamma = 2\varepsilon_0 d/T$. The length ℓ is larger than G_+, for $\Gamma \lesssim 70$, proving that for large values of Γ the gradient expansion is not justified. For small values of Γ the soliton varies on a scale which is larger than $1/G_+$ and the gradient expansion provides an accurate approximation to the full non-local theory. In fact, expanding (C.6) to second order, we can estimate the error as few percents $(k/G_+)^2 \approx 1/(4\ell G_+)^2 < 0.02$ (where we used $\ell_\mathrm{e} \approx 4\ell$, cf. (5.75)). To confirm this analysis we have solved numerically the integral equation (C.2) imposing the boundary conditions $\mu_{z\to-\infty} = 0$ and $\mu_{z\to\infty} = \mu_\mathrm{sol}$. The results for different values of Γ are plotted in Fig. C.1, together with the soliton of the approximated local theory (thicker line). We have rescaled the z axis in units of the elastic length ℓ. As expected, for low values of Γ we obtain a perfect collapse of the data. On the other hand, for large Γ the kink in the non-local theory is much sharper than the soliton in the local theory and, therefore, the gradient expansion approximates poorly the exact result. Finally, we can estimate that the gradient expansion approximates well the non-local theory for $\Gamma \lesssim 50$, which corresponds to $T \gtrsim 0.04\,\varepsilon_0 d$ and $B \lesssim 0.5\,B_\lambda$.

C.2 Linearised saddle-point equation

For small values of μ_z, we can expand the potential in the RHS of the equation (C.2). Hence, we write, cf. (6.39),

$$\frac{d}{d\mu}\Big(\frac{\delta\omega^{\mathrm{2D}}_{\mathrm{sub}}(\mu_z)}{T}\Big) \approx 6(1-\bar{c}_c)\mu_z, \tag{C.7}$$

where we consider the system at melting, i.e., $c^{\mathrm{2D}}_{\mathrm{sub}} = \bar{c}_c$ to make a clear connection with the discussion in Sec. 6.3.2. Inserting (C.7) and (C.6) in (C.2), we obtain the equation of 'motion' in Fourier space

$$-\ell^2 k^2\Big[1+\frac{6(1-\bar{c}_c)}{(\ell G_+)^2}\Big]\mu_k = 6(1-\bar{c}_c)\mu_k. \tag{C.8}$$

We can transform this equation back to real space

$$(1+r)\ell^2\frac{d^2\mu_z}{dz^2} = 6(1-\bar{c}_c)\mu_z, \tag{C.9}$$

where like in Eq. (6.44) we have defined the parameter $r = dG_+(1-\bar{c}_c)/2\bar{\alpha} = 6(1-\bar{c}_c)/(G_+\ell)^2$. The higher derivatives which are neglected in the gradient expansion produce a small renormalization of the elastic term $(1+r)\approx 1$ as compared to (C.3).

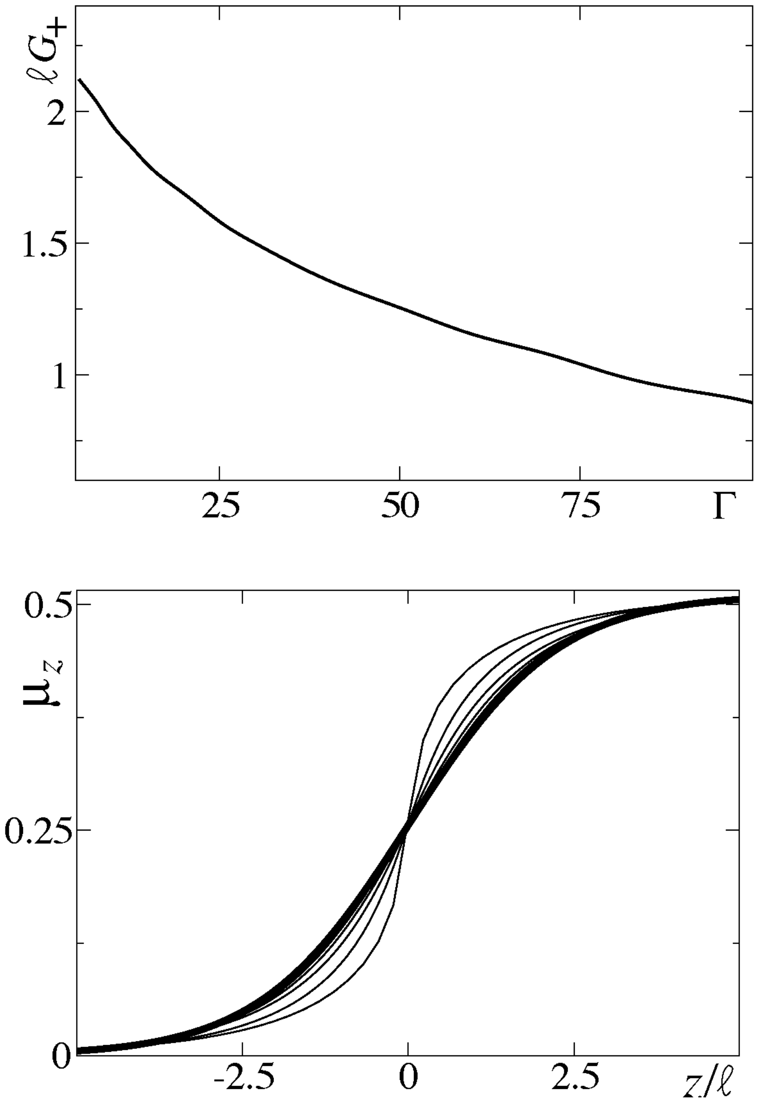

Figure C.1: Upper: plot of the ratio between ℓ and kernel extension $1/G_+$ as a function of $\Gamma = 2\varepsilon_0 d/T$. Lower: comparison of the soliton derived within the local approximation (thicker line) with the results of the full non-local theory for different values of $\Gamma = 6, 40, 80, 100, 130$. For $\Gamma = 6$, upon rescaling z in units of ℓ, the soliton collapses on the solution of the local approximation. Little deviations are present at $\Gamma = 40$ (first distinguishable line in the plot), at which however the soliton is still well approximated by the gradient expansion. At higher Γ's (the most visible lines correspond to $\Gamma = 80, 100, 130$) the difference is appreciable: the full non-local theory leads to a modified shape of the soliton with a much shaper interface.

Bibliography

[1] J. G. Bednorz and K. A. Müller, Z. Phys. **64** (1986).

[2] G. Blatter, M. V. Feigel'man, V. B. Geshkenbein, A. I. Larkin, and V. M. Vinokur, Rev. Mod. Phys. **66**, 1125 (1994).

[3] A. Buzdin and D. Feinberg, J. Phys. France **51**, 1971 (1990).

[4] M. V. Feigel'man, V. B. Geshkenbein, and A. I. Larkin, Physica C **167**, 177 (1990).

[5] J. R. Clem, Phys. Rev. B **43**, 7837 (1991).

[6] J. M. Kosterlitz and D. J. Thouless, J. Phys. C **6**, 1181 (1973).

[7] V. L. Berezinskii, Sov. Phys. JETP **32**, 493 (1971).

[8] A. A. Abrikosov, Sov. Phys. JETP **5**, 1174 (1957).

[9] G. Eilenberger, Phys. Rev. **164**, 628 (1967).

[10] B. A. Huberman and S. Doniach, Phys. Rev. B **43**, 950 (1979).

[11] D. S. Fisher, Phys. Rev. B **22**, 1190 (1980).

[12] D. R. Nelson, Phys. Rev. Lett. **60**, 1973 (1988).

[13] A. Houghton, R. A. Pelcovits, and A. Sudbø, Phys. Rev. B **40**, 6763 (1989).

[14] E. H. Brandt, Phys. Rev. Lett. **63**, 1106 (1989).

[15] L. I. Glazman and A. E. Koshelev, Phys. Rev. B **43**, 2835 (1991).

[16] S. Sengupta, C. Dasgupta, H. R. Krishnamurthy, G. I. Menon, and T. V. Ramakrishnan, Phys. Rev. Lett. **67**, 3444 (1991).

[17] M. J. W. Dodgson, A. E. Koshelev, V. B. Geshkenbein, and G. Blatter, Phys. Rev. Lett. **84**, 2698 (2000).

[18] V. Pudikov, Physica C **212**, 155 (1993).

[19] R. G. Mints, V. G. Kogan, and J. R. Clem, Phys. Rev. B **61**, 1623 (2000).

[20] J. R. Clem, cond-mat/0408371 (2004).

[21] A. De Col, V. Geshkenbein, and G. Blatter, Phys. Rev. Lett. **94**, 097001 (2005).

[22] R. Lipowsky, Phys. Rev. Lett. **49**, 1575 (1982).

[23] J. W. M. Frenken and J. F. van der Veen, Phys. Rev. Lett. **54**, 134 (1985).

[24] U. Tartaglino, T. Zykova-Timan, F. Ercolessi, and E. Tosatti, Physics Reports - Review Section of Physics Letters **411**, 291 (2005).

[25] T. V. Ramakrishnan and M. Yussouff, Phys. Rev. B **19**, 2775 (1979).

[26] T. V. Ramakrishnan, Phys. Rev. Lett. **48**, 541 (1982).

[27] P. S. Cornaglia and C. A. Balseiro, Phys. Rev. B **61**, 784 (2000).

[28] V. L. Ginzburg and L. D. Landau, Zh. Eksperim. i. Teor. Fiz. **20**, 1064 (1950).

[29] J. Bardeen, L. N. Cooper, and J. R. Schrieffer, Phys. Rev. **108**, 1175 (1957).

[30] M. Tinkham, *Introduction to Superconductivity 2nd ed.*, McGraw-Hill Book Co, Singapore, 1996.

[31] G. Blatter and V. B. Geshkenbein, *The Physics of Superconductors*, volume 1, K. H. Bennenmann and K. Emerson, Springer, Berlin, 2003.

[32] C. R. Hu, Phys. Rev. B **6**, 1756 (1972).

[33] E. H. Brandt, J. Low Temp. Phys. **26**, 735 (1977).

[34] V. K. Tkachenko, Zh. Eksp. Theor. Fiz. **29**, 1763 (1969).

[35] A. Sudbø and E. H. Brandt, Phys. Rev. B **43**, 10482 (1991).

[36] E. Zeldov et al., Nature **375**, 373 (1995).

[37] A. Schilling et al., Nature **382**, 791 (1996).

[38] W. E. Lawrence and S. Doniach, *Proceedings of the twelfth International Conference on Low Temperature Physics, Kyoto*, page 361, E. Kanda, Keigaku, Tokyo, 1971.

[39] B. D. Josephson, Phys. Lett. **1**, 251 (1962).

[40] S. Colson et al., Phys. Rev. Lett. **90**, 137002 (2003).

[41] H. Fangohr, A. E. Koshelev, and M. J. W. Dodgson, Phys. Rev. B **67**, 174508 (2003).

[42] J. M. Caillol, D. Levesque, J. J. Weis, and L. P. Hansen, J. Stat. Phys. **28**, 325 (1982).

[43] J. Pearl, Appl. Phys. Lett. **5**, 65 (1964).

[44] J. Pearl, J. Appl. Phys. **37**, 4139 (1966).

[45] G. Carneiro and E. H. Brandt, Phys. Rev. B **61**, 6370 (2000).

[46] J. S. Langer and V. Ambegaokar, Phys. Rev. **164**, 198 (1967).

[47] D. R. Nelson and J. M. Kosterlitz, Phys. Rev. Lett. **39**, 1201 (1977).

[48] D. R. Nelson and B. I. Halperin, Phys. Rev. B **19**, 2457 (1979).

[49] J. Bardeen and M. J. Stephen, Phys. Rev. **140**, 1197A (1965).

[50] S. N. Artemenko, I. G. Gorlova, and Y. I. Latyshev, JETP Lett. **49**, 655 (1989).

[51] A. M. Kadin, K. Epstein, and A. M. Goldman, Phys. Rev. B **27**, 6691 (1983).

[52] A. T. Fiory and A. F. Hebard, Phys. Rev. B **28**, 5075 (1983).

[53] J. V. José, L. P. Kadanoff, S. Kirkpatrick, and D. R. Nelson, Phys. Rev. B **16**, 1217 (1977).

[54] M. R. Beasley, J. E. Mooij, and T. P. Orlando, Phys. Rev. Lett. **42**, 1165 (1979).

[55] Y. Tanaka, Phys. Rev. Lett. **88**, 017002 (2002).

[56] E. Babaev, Phys. Rev. Lett. **89**, 067001 (2002).

[57] E. Babaev, Nucl. Phys. B **686**, 397 (2004).

[58] S. Sachdev, Phys. Rev. B **45**, 389 (1992).

[59] J. P. Rodriguez, Phys. Rev. B **49**, 9831 (1994).

[60] G. E. Volovik, *The universe in a helium droplet*, Springer, 2002.

[61] D. Gorokhov, cond-mat/0502083 (2005).

[62] E. Babaev, A. Sudbø, and N. W. Ashcroft, Nature **431**, 666 (2004).

[63] X. G. Wen and A. Zee, Phys. Rev. Lett. **69**, 1811 (1992).

[64] K. Moon et al., Phys. Rev. B **51**, 5138 (1995).

[65] I. Giaever, Phys. Rev. Lett. **15**, 825 (1965).

[66] J. W. Ekin, B. Serin, and J. R. Clem, Phys. Rev. B **9**, 912 (1974).

[67] J. W. Ekin and J. R. Clem, Phys. Rev. B **12**, 1753 (1975).

[68] B. Horovitz, Phys. Rev. B **47**, 5947 (1993).

[69] J. M. Kosterlitz, J. Phys. C **7**, 1046 (1974).

[70] A. P. Young, Phys. Rev. B **19**, 1855 (1979).

[71] P. Minnhagen, Rev. Mod. Phys. **59**, 1001 (1987).

[72] Y. Saito, Z. Phys. B **32**, 75 (1978).

[73] M. D. Sherrill, Phys. Rev. B **7**, 1908 (1973).

[74] J. R. Clem, Phys. Rev. B **12**, 1742 (1975).

[75] B. I. Halperin and D. R. Nelson, J. Low Temp. Phys. **36**, 599 (1979).

[76] P. G. de Gennes, *Superconductivity of Metals and Alloys*, Addison-Wesley Publishing Company, 1966.

[77] P. L. Gammel, L. F. Schneemeyer, and D. J. Bishop, Phys. Rev. Lett. **66**, 953 (1991).

[78] F. Tafuri, J. R. Kirtley, P. G. Medaglia, P. Orgiani, and G. Balestrino, Phys. Rev. Lett. **92**, 157002 (2004).

[79] P. W. Anderson, J. Phys. Chem. Solids **11**, 26 (1959).

[80] A. I. Larkin and Y. N. Ovchinnikov, J. Low Temp. Phys. **34**, 409 (1979).

[81] E. V. Thuneberg, J. Kurkijärvi, and D. Rainer, Phys. Rev. B **29**, 3913 (1984).

[82] M. Kellogg, I. B. Spielman, J. P. Eisenstein, L. N. Pfeiffer, and K. West, Phys. Rev. Lett. **88**, 126804 (2002).

[83] M. Kellogg, J. P. Eisenstein, L. N. Pfeiffer, and K. W. West, Phys. Rev. Lett. **93**, 036801 (2004).

[84] A. H. MacDonald, Phyisica (Amsterdam) **298B**, 129 (2001).

[85] K. Yang and *et al.*, Phys. Rev. Lett. **72**, 732 (1994).

[86] H. Fertig, Phys. Rev. B **40**, 1087 (1989).

[87] S. M. Girvin, Proc. 11th international conf. on recent progress in many-body theories, in *Advances in Quantum Many-Body Theory*, edited by R. Bishop, T. Brandes, K. Gernoth, N. Walet, and Y. Xian, World Scientific, 2001.

[88] E. Babaev, L. D. Fadeev, and A. J. Niemi, Phys. Rev. B **65**, 100512 (2002).

[89] G. Blatter, V. B. Geshkenbein, A. Larkin, and H. Nordborg, Phys. Rev. B **54**, 72 (1996).

[90] M. J. W. Dodgson, V. B. Geshkenbein, M. V. Feigel'man, and G. Blatter, cond-mat/0007072 (2000).

[91] G. I. Menon, C. Dasgupta, H. R. Krishnamurthy, T. V. Ramakrishnan, and S. Sengupta, Phys. Rev. B **54**, 16192 (1996).

[92] B. B. Laird, J. D. McCoy, and A. D. J. Haymet, J. Chem. Phys. **87**, 5449 (1987).

[93] P. M. Chaikin and T. C. Lubensky, *Principle of condensed matter physics*, Cambridge University Press, United Kingdom, 1995.

[94] J. P. Hansen and I. R. McDonald, *Theory of Simple Liquids*, Academic Press, London, 1986.

[95] Y. Singh, Physics Reports **207**, 351 (1991).

[96] S. Tyagi, Phys. Rev. E **70** (2004).

[97] J. Chakrabarti, H. R. Krishnamurthy, and A. K. Sood, Phys. Rev. Lett. **73**, 2923 (1994).

[98] A. D. J. Haymet and D. W. Oxtoby, J. Chem. Phys. **74**, 2559 (1981).

[99] D. W. Oxtoby and A. D. J. Haymet, J. Chem. Phys. **76**, 6262 (1982).

[100] Y. Fasano, M. D. Seta, M. Menghini, H. Pastoriza, and F. de la Cruz, PNAS **102**, 3898 (2005).

[101] A. Soibel et al., Nature **406**, 282 (2000).

[102] A. R. Ubbelohde, *The Molten State of Matter*, Wiley, New York, 1978.

[103] L. Pietronero and E. Tosatti, Solid State Commun. **32**, 255 (1979).

[104] A. Trayanov and E. Tosatti, Phys. Rev. Lett. **59**, 2207 (1987).

[105] A. Trayanov and E. Tosatti, Phys. Rev. B **38**, 6961 (1988).

[106] R. Ohnesorge, H. Löwen, and H. Wagner, Phys. Rev. E **50**, 4801 (1994).

[107] R. Lipowsky and W. Speth, Phys. Rev. B **28**, 3983 (1983).

[108] A. De Col, V. B. Geshkenbein, G. I. Menon, and G. Blatter, Physica C **404**, 119 (2004).

[109] A. De Col, G. I. Menon, V. B. Geshkenbein, and G. Blatter, Phys. Rev. Lett. **96**, 177001 (2006).

[110] V. Mineev and K. Samokhin, *Introduction to unconventional superconductivity*, Gordon Breach, Amsterdam, 1999.

[111] D. A. Huse, Phys. Rev. B **46**, 8621 (1992).

[112] S. Pierson, Phys. Rev. B **51**, 6663 (1995).

[113] J. R. Clem, J. Low Temp. Phys. **18**, 427 (1974).

List of Publications

6 A. De Col, G.I. Menon, V.B. Geshkenbein, and G. Blatter,
"Surface melting of the vortex lattice",
Phys. Rev. Lett. **96**, 177001 (2006).

5 A.A. Abdumalikov Jr, V.V. Kurin, C. Helm, A. De Col, Y. Koval, and A.V. Ustinov,
"Nonlocal electrodynamics of long ultra-narrow Josephson junctions: Experiment and theory",
cond-mat/0411573.

4 A. De Col, V.B. Geshkenbein, and G. Blatter,
"Dissociation of vortex stacks into fractional-flux vortices",
Phys. Rev. Lett. **94**, 097001 (2005).

3 A. De Col, V.B. Geshkenbein, G.I. Menon, and G. Blatter,
"Surface effects on the pancake vortex phase diagram",
Physica C **404**, 119 (2004).

2 A. De Col and T.B. Liverpool,
"Statistical mechanics of double helical polymer",
Phys. Rev. E **69**, 061907 (2004).

1 S. Ciccariello and A. De Col,
"Zero-temperature perturbative calculation of the magnetic susceptibility of the free fermion system",
Eur. J. Phys. **22**, 629 (2001).

Curriculum Vitae

Personal Data

Name: Alvise De Col
Date of Birth: February 3, 1977 (Venezia, Italy)
Nationality: Italian citizen

Education

1983-1996	Primary and Secondary school in Venezia (Italy)
1996	Final degree: Diploma di Maturità Classica
1996-2001	Undergraduate studies in physics at the University of Padova (Italy)
2000-2001	Exchange student at Imperial College, London (UK)
2001	Master thesis on “Statistical Mechanics of double helical polymers” under the supervision of Dr. T.B. Liverpool
2001-2005	Graduate studies at the Institute of Theoretical Physics at ETH-Zürich under the supervision of Prof. G. Blatter

Acknowledgments

I would like to express my gratitude to my supervisor Gianni Blatter for betting on an atypical (= definitely non-swiss) student the day he accepted me as his graduate student. He initiated this thesis in a very rich and interesting field, which from time to time I found a little bit too mature. In spite of my misgivings, the results that have come out of the project he proposed me have been surprisingly beautiful. I enjoyed the tempo and the style of the scientific (and non-scientific) discussions we had, despite of the long queuing time outside his office. I am particularly indebted to him for giving me the opportunity to present my results at many conferences all around the world and the freedom to work often in Leiden. I also wish to express my gratitude to Dima Geshkenbein for critically reviewing my calculations, for always pointing out old papers of russian physicists related to my work, and for all the imaginary chess games we fought (and the ones we did not play). I profited a lot from his critical insights in physics, his magical skills in solving integrals, and his historical erudition. A special thank goes to Erio Tosatti for co-refereeing this thesis and for his interest in my work.

I wish to thank Christian Helm for his neverending patience shown in answering all my questions and for carefully reading the manuscript of this thesis. It is also a great pleasure to thank Matthew Dodgson for stimulating discussions and for providing me a numerical code of his still disputed 2V-SCHA method. An important contribution to the results of this thesis has come out of the discussions with Gautam Menon during his short visit at ETH. I profited a lot from his expertise on classical density functional theory. I am very grateful to Wim van Saarloos for giving me the opportunity to work often at the Lorentz Instituut. I also would like to thank Valery Pokrovsky, John Clem, and Cristiane de Morais Smith for inviting me at Texas A&M, Iowa State University, and University of Utrecht. A particular thank goes to John Clem for the lovely dinner in his wonderful house in Ames.

I wish to express my gratitude to all members of Gianni's group: Christian, Fabian, Helmut, Jérôme, and Sebi. I doubt that anybody will ever beat our time-outs. For a lucky set of circumstances I started my Ph.D. together with a group of colleagues which immediately became good and close friends. I am particularly indebted to Jérôme for being my personal german teacher and adviser (those coffees have been definitely well spent); Paolo for the very long discussions and the superb dinners (even if you will never convince me that one should put mascarpone on a pizza); Igor for handing in *this* thesis on my behalf and for his fine taste in the choice of the movies for our cinema nights ('come on'); Martin for showing me the best side of Switzerland. Furthermore, I wish to thank Carlo, Christoph, Leni, Matze, Michele, Philippe, Simon, Sam, Slavo, all my other Ph.D. colleagues, Denise, Etusch, and Irene for the nice time together at the ITP. I hope that the new Ph.D. generation will be able to reproduce the pleasant atmosphere of these years.

It is not possible to name all the people with whom I shared unforgettable moments in these four years. Still, I would like to thank my flatmate Léon and all my friends here in Zürich, in Leiden, in Venice, and in Padova (among them I have to mention the *famiglia arroganti* and relatives).

I am also very grateful to my parents and my grandmother for their moral support over the last four years, for having encouraged me to undertake this wonderful experience abroad, and for always showing an unselfish trust in me and in my choices.

I would like to dedicate these last words to my desert rose, Chiara. Neither english nor any other language can express my gratitude and my love. I will rather let the loud and strong dutch wind which is blowing outside talk on my behalf, it reminds me of you...

Als Zarathustra aber allein war, sprach er also zu seinem Herzen:
"Sollte es denn möglich sein! Dieser alte Heilige hat in seinem Walde
noch Nichts davon gehört, dass Gott tot ist!"

F. W. Nietzsche